COUPLED THERMO-ELASTOHYDRODYNAMIC ANALYSIS OF A BUMP-TYPE COMPLIANT FOIL JOURNAL BEARING

by

SERDAR AKSOY

Submitted to the Graduate School of Engineering and Natural Sciences
in partial fulfillment of
the requirements for the degree of
Doctor of Philosophy

SABANCI UNIVERSITY

August 2014

COUPLED THERMO-ELASTOHYDRODYNAMIC ANALYSIS OF A BUMP-TYPE COMPLIANT FOIL JOURNAL BEARING

APPROVED BY:

Assoc. Prof. Mahmut F. AKŞİT *(Thesis Advisor)* ....

Assoc. Prof. Serhat YEŞILYURT ....

Assoc. Prof. Mehmet YILDIZ ....

Assoc. Prof. Güllü KIZILTAŞ ....

Prof. Dr. Yahya DOĞU ....

DATE OF APPROVAL: ....

COUPLED THERMO-ELASTOHYDRODYNAMIC ANALYSIS OF A BUMP-TYPE COMPLIANT FOIL JOURNAL BEARING

Serdar AKSOY

Mechatronics, PhD. Dissertation, 2014

Thesis Advisor: Assoc. Prof. Mahmut F. AKŞİT

Keywords: Elasto-Hydrodynamic Analysis, Reynolds Equation, Aerodynamic Bearings, Fluid-Structure Interaction (FSI), Gas Turbine

ABSTRACT

This work presents a fully coupled thermo-elastohydrodynamic analysis of a bump-type compliant foil journal bearing. The operational characteristics of compliant foil bearings have been evaluated under different operating conditions. Even though some experimental research data are available in literature, extended thermo-hydrodynamic analysis is required to better understand and optimize the system performance at the design level. The presented comprehensive model benchmarked to experiment data will help enable the widespread usage in novel turbomachinery applications. The proposed model predicts three-dimensional thermal, structural and hydrodynamic performance of a bump-type compliant foil bearing. The model couples finite element analysis of the structural deformation and hyrodynamic pressure to a finite difference code for film temperature. The Augmented-Lagrangian contact model and advanced thermal contact modeling is applied. The model involves complete bearing mechanism as well as the interacting section of the shaft with the bearing. Nickel-based superalloys are used as bearing material and temperature dependent thermo-mechanical properties are defined in the solver. The thermal growth of the shaft, foil structure, bearing sleeve, and centrifugal growth of the shaft are considered. The model captures the physics very well and could be utilized to design more advanced bearings. The predictions of the proposed model are benchmarked to published experimental data and a reasonable correlation is obtained. Parametric study is conducted for various shaft speeds and loading conditions to predict thermal and structural performance. Derivation of governing momentum and energy equations, mechanical and thermal contact models, finite element and finite difference formulations are given in detail.

KAYMALI ESNEK FOLYO YATAKLARIN TERMO-ELASTOHİDRODİNAMİK AKIŞKAN-KATI ETKİLEŞİMLİ ANALİZİ

Serdar AKSOY

Mekatronik, Doktora Tezi, 2014

Tez Danışmanı: Doç. Dr. Mahmut F. AKŞİT

Anahtar kelimeler: Elasto-Hidrodinamik Analiz, Reynolds Denklemi, Aerodinamik Yataklar, Akışkan-Katı Etkileşimi, Gaz Türbini

ÖZET

Esnek folyo yatakların operasyonal kabiliyetleri çok farklı çalışma şartlarında gösterilmiştir. Literatürde deneysel birçok çalışma bulunamasına rağmen yatakların dizayn aşamasında geliştirilmesi ve optimize edilmesi için kapsamlı termal-hidrodinamik analizlere ihtiyaç bulunmaktadır. Deney sonuçlarıyla doğrulanmış modeller geliştirilmesi bu sistemlerin yeni turbomakinelerde uygulanmasını yaygınlaştıracaktır. Bu çalışmada birinci nesil bir kaymalı esnek folyo yatağın üç boyutlu termal, yapısal ve hidrodinamik performansını tahmin etmek üzere termo-elastohidrodinamik bir model geliştirilmiştir. Yapısal deformasyon ve hidrodinamik basınç sonlu elemanlar metoduyla çözülerek sonlu farklar metoduyla film sıcaklığını tespit için geliştirilen kod ile birleştirilmiştir. Augmented-Lagrangian mekanik temas ve ileri seviye termal kontak modelleri uygulanmıştır. Yatak mekanizmasının tamamı ve şaftın yatak ile etkileşen kısmı modele dahil edilmiştir. Yatak ve şaft malzemeleri olarak nikel-tabanlı süper alaşımlar seçilerek sıcaklığa bağımlı malzeme bilgileri çözücüye tanıtılmıştır. Şaft ve yatak sisteminin termal ve merkezkaç genleşmeleri çözüme dahil edilmiştir. Geliştirilen model folyo yatakların gerçek fiziğini iyi bir şekilde tahmin ederek ileri seviye yatak tasarımlarında kullanılabilecektir. Önerilen modelden elde edilen tahminler literatürdeki deneysel sıcaklık ölçümleriyle kıyaslanmış ve aralarında kabul edilebilir uyum gözlemlenmiştir. Farklı şaft hızları ve yükleme koşulları için termal ve yapısal performansı tahmin etmek üzere parametrik çalışma yapılmıştır. Momentum ve enerji denklemleri, mekanik ve termal kontak modelleri, sonlu elemanlar ve sonlu farklar metotlarında uygulanan formulasyonlar detaylarıyla açıklanmıştır.

Say: “Are those equal, those who know and those who do not know? It is those who are endued with understanding that receive admonition” (The Holy Quran, 39:9)

A learned guide should be a sheep, not a bird. A sheep gives its lamb milk, while a bird gives its chick regurgitated food. (The Letters, Bediuzzaman Said Nursî)

ACKNOWLEDGEMENT

I would like to thank my advisor, Dr. Mahmut F. Aksit for his guidance, enthusiasm and support throughout my study. His words of encouragement are greatly appreciated. Over the years I have worked with him he always motivated and pushed me to aim higher. Thank members of my advisory committee for their recommendations and comments.

I am grateful to my colleagues in SDM R&D for their closeness and support. I would like to thank Dr. Murat Ozmusul for his support and motivation.

My deepest gratitude is to my parents Perihan and Celal Aksoy who trusted, supported and motivated me during all my life.

Finally, I am very grateful to my lovely family for their patience and motivation during my uncountable work hours. I hope my children Bahadır Said, Reyhan and Ali Zübeyir will achieve always better than me. I specially thank to my wife. She was always with me in my hard times.

I would like to thank Mr. Yousef Jameel who showed his generousity by funding me for 4 years of my study.

The partial graduate scholarship provided by TUBITAK is greatly appreciated.

TABLE OF CONTENTS

1 INTRODUCTION 1
  1.1 Motivation 1
    1.1.1 The Prominent Characteristics of CFB in Turbomachinery 2
  1.2 Operating Principles of Foil Bearings 8
    1.2.1 Structure of Compliant Foil Bearing 10
  1.3 Problem Statement and Scientific Contribution 12
  1.4 Literature Survey 14
    1.4.1 Isothermal Models 15
    1.4.2 Thermal Models 18
2 FOIL BEARING STRUCTURE 23
  2.1 Description of Foil Bearing Geometry 23
    2.1.1 Foil Bearing Geometry used in FEA Model 26
  2.2 Material Properties 29
  2.3 Finite Element Grid Generation 31
    2.3.1 Shear Locking 31
    2.3.2 Mesh Dependency Study 33
3 THEORETICAL BACKGROUND 37
  3.1 Derivation of 4-point Finite Difference Approximation 37
  3.2 Derivation of Reynolds Equation for Hydrodynamic Pressure Estimation 39
    3.2.1 Order of Magnitude Analysis 42
    3.2.2 Non-dimensionalization Process for Reynolds Equation 45
    3.2.3 Finite Difference Approximation and Solution Approach 46
    3.2.4 Solving Reynolds Equation by FEM 50
      3.2.4.1 The Effect of shaft thermal and centrifugal expansion to bearing clearance 50
      3.2.4.2 No-Slip boundary condition 52
  3.3 Derivation of the Bulk Energy Transport Equation for Film Temperature 53
    3.3.1 Derivation of the Bulk-flow Transport Equation 55
    3.3.2 Heat Convection Coefficient Models 57
    3.3.3 Non-Dimensionalization of Solution Parameters 58
    3.3.4 Finite Difference Formulation for Temperature Nodes 59
  3.4 Underlying Equations for Structural Deformation 60

3.5 Mechanical Contact Formulation: Augmented Lagrangian Penalty Method ... 62
3.6 Thermal Contact Formulation: Cooper-Mikic-Yovanovich Correlation 66
4 NUMERICAL SOLVER PROPERTIES 73
4.1 Finite Element Model for Fluid-Structure Interaction (FSI) Model Including Shaft Heat Transfer 73
4.1.1 Structural Boundary Conditions for FSI Problem 74
4.1.2 Thermal Boundary Conditions 76
4.1.3 Solver Configurations 79
4.1.3.1 PARDISO direct solver 79
4.1.3.2 Nonlinear solver: Double Dogleg 80
4.2 Finite Difference Code for Film Temperature 82
4.2.1 The Flowchart of Finite Difference Code 85
4.3 Coupling FEA and FDM 90
5 RESULTS AND DISCUSSION 92
5.1 Model Validation: TEHD Model Predictions versus Experimental Data 92
5.2 Performance Parameters Evaluation 98
5.2.1 Hydrodynamic Parameters 98
5.2.1.1 Pressure field 98
5.2.1.2 Film thickness 106
5.2.1.3 Fluid velocity 111
5.2.2 Thermal Parameters 114
5.2.2.1 Temperature distribution 115
5.2.2.2 Thermal contact properties 123
5.2.3 Structural Parameters 125
5.2.3.1 Deformation 125
5.2.3.2 Stress 133
5.2.3.3 Mechanical contact properties 138
6 CONCLUSION 140
7 REFERENCES 145
APPENDIX A: Temperature Dependent Material Properties 154
A.1 Inconel X-750 154
A.2 Inconel 718 157

LIST OF FIGURES

Figure 1.1: F-14 Foil Bearing ACM (Developed by AiResearch) [5] 7

Figure 1.2: F-16 Foil Bearing ACM (Developed by AiResearch) [5] 7

Figure 1.3: Section view for NASA turbocharger supported by journal and thrust foil bearings [7] 8

Figure 1.4: Basic scheme of a compliant foil bearing 10

Figure 2.1: First generation compliant foil bearings a) Leaf type foil bearing, b) Bump type foil bearing [80] 24

Figure 2.2: Gen II bump-type foil journal bearing [80] 24

Figure 2.3: Gen III bump-type foil journal bearing [80] 25

Figure 2.4: Foil bearing assembly and detailed view for bumps and topfoil 26

Figure 2.5: Foil bearing and shaft geometry from isometric view (Due to the axial symmetry front half of the system is displayed) 27

Figure 2.6: Bumpfoil geometry from isometric view 27

Figure 2.7: Geometry parameters for a single bump 28

Figure 2.8: Bump numbering convention for the CFB model 28

Figure 2.9: Deformation of material subjected to bending moment *M* [86] 31

Figure 2.10: The deformation of a linear element subjected to bending moment *M* [86]. 32

Figure 2.11: Deformation of a quadratic element subjected to bending moment *M* [86]. 33

Figure 2.12: Grid structure for a) Mesh 1 b) Mesh 2 c) Mesh 3 d) Mesh 4 33

Figure 2.13: Topfoil deformation for different meshes 34

Figure 2.14: The mesh generated for foil bearing model. The elements are second-order hexagonal mesh 35

Figure 2.15: The quality index of the mesh is a useful measure the appropriateness of the mesh for the analysis 36

Figure 3.1: Coordinate system for the converging film between stationary bearing surface and rotating shaft surface 40

Figure 3.2: Eccentric position of the shaft during operation under a given load and related parameters......49
Figure 3.3: An example illustrating a typical configuration for thin-film flow [90]......50
Figure 3.4: Thermal expansion of the Inconel 718 shaft with respect to temperature......51
Figure 3.5: Shaft centrifugal growth with respect to the shaft speed for Inconel 718 shaft material. Shaft outer diameter is 50 mm and wall thickness, $ts = Ro - Ri$ is 2.5 mm......52
Figure 3.6: Coordinate systems and heat transfer in the film......56
Figure 3.7: The penetration of the source boundary to the destination surface if contact formulation is not defined properly (Reprinted from [96])......63
Figure 3.8: Asymmetric contact pair definition (Reprinted from [96])......63
Figure 3.9: The contact pair definition for foil bearing model according to the listed guidelines......64
Figure 3.10: The penetration distance measurement in a contact pair [94]......65
Figure 3.11: The penetration distance is used to calculate the penalized contact pressure by using spring analogy......66
Figure 3.12: Asperity contact parameters reprinted from [102]......68
Figure 4.1: Bumps are fixed at specific regions to provide adequate stiffness distribution for expected pressure profile......74
Figure 4.2: The coordinate system for foil bearing assembly and the shaft......75
Figure 4.3: The model is symmetric in axial direction and the symmetry boundaries are shown as highlighted......75
Figure 4.4: The detailed view of the underlying bump geometry......76
Figure 4.5: Schematic representation of radial heat flow paths in CFB......76
Figure 4.6: Schematic representation of axial heat flow paths in CFB and shaft...77
Figure 4.7: A portion of the computational grid for the two-dimensional thermal model of the film gap. The nodes are ordered in the natural row-wise.......83
Figure 4.8: An illustration for thermal mixing conditions within the film between trailing and leading edges of top foil......84
Figure 4.9: Typical temperature distribution in a) Topfoil b) Shaft......84

Figure 4.10: Typical a) Hydrodynamic pressure distribution and b) Film thickness in a foil bearing 85

Figure 4.11: The flowchart of the Finite Difference Code to solve for film gap temperature 87

Figure 4.12: Non-symmetrical sparse matrix for fluid film temperature............... 89

Figure 4.13: Flow diagram for coupled TEHD analysis including FDM and FEA 91

Figure 5.1: Schematic view of the thermocouple locations and numbering convention of the bumps. The model is axially symmetric in the center and the locations at the edges are identical. 93

Figure 5.2: Comparison of the film temperatures prediction at bearing center and edges for various shaft speeds. The comparison is performed for the radial load of 222 N. The dashed lines belong to the TEHD model whereas the continuous lines are for experimental data taken from Ref. [59]. 93

Figure 5.3: Prediction of the film temperatures at the bearing center and edge with respect to the radial load. The data are taken for the shaft speed of 40 krpm. The dashed lines belong to the TEHD model whereas the continuous lines are for experimental data taken from Ref. [59].. 94

Figure 5.4: Prediction of the film temperatures at the bearing center and edge with respect to the shaft speed. The data are taken for the radial load of 133 N. The dashed lines belong to the TEHD model whereas the continuous lines are for experimental data taken from Ref. [59]... 95

Figure 5.5: Prediction of the film temperatures at the bearing center in thermocouple location of #1 with respect to the radial load. The data are taken for various shaft speeds. The dashed lines belong to the TEHD model whereas the continuous lines are for experimental data taken from Ref. [59] 96

Figure 5.6: Predictions for the film pressure in the mid-plane of the bearing surface in tangential direction for different loading conditions. The shaft speed is 40 krpm... 99

Figure 5.7: Predictions for the gradient of the film pressure in the mid-plane of the bearing surface in tangential direction for different loading conditions. The shaft speed is 40 krpm. The second figure displays the critical section along the circumferential position between 125 to 175 deg. 100

Figure 5.8: Predicted pressure fields on bearing surface of the CFB for different static radial loads. The results are given for the shaft speed of 30 krpm. The radial loads are a) 44 N b) 89 N c) 133 N d) 178 N e) 222 N. The units are in Pascal [Pa]. 101

Figure 5.9: Predictions for the film pressure in the mid-plane of the bearing surface in tangential direction for different shaft speeds. The static radial load is 133 N. The second figure displays the critical section along the circumferential position between 125 to 175 deg. 102

Figure 5.10: Predictions for the gradient of the film pressure in the mid-plane of the bearing surface in tangential direction for different shaft speeds. The static radial load is 133 N. The second figure displays the critical section along the circumferential position between 125 to 175 deg. 103

Figure 5.11: Predicted pressure fields on the bearing surface of the CFB for different shaft speeds. The results are given for the static radial load of 133 N. The shaft speeds are a) 20 krpm b) 30 krpm c) 40 krpm d) 50 krpm. The units are in Pascal. 104

Figure 5.12: Comparison of the predicted pressure fields on bearing surface of the a) THD model b) Rigid bearing c) Isothermal. The results are given for the shaft speed of 30 krpm and the static radial load of 133 N. 105

Figure 5.13: Comparison of the predictions for the film pressure in the mid-plane of the bearing surface in tangential direction for the TEHD model, isothermal model and rigid bearing. The results are given for the shaft speed of 30 krpm and the static radial load of 133 N. 106

Figure 5.14: Predictions for the film thickness in the mid-plane of the bearing surface in tangential direction for different loading conditions. The shaft speed is 40 krpm. The second figure displays the critical section along the circumferential position between 125 to 175 deg. 107

Figure 5.15: Predictions for the film thickness in the mid-plane of the bearing surface in tangential direction for different shaft speeds. The static radial load is 133 N. The second figure displays the critical section along the circumferential position between 150 to 200 deg. 108

Figure 5.16: Comparison for the film thickness in the mid-plane and the edge of the bearing surface in tangential direction for shaft speed of 40 krpm and radial load of 178 N. 109

Figure 5.17: Comparison for film thickness predictions in the mid-plane for the TEHD, isothermal model and rigid bearing. The speed is 30 krpm and load 133 N. 110

Figure 5.18: Comparison for film thickness predictions in the mid-plane for a) TEHD b) Rigid bearing c) Isothermal. The speed is 30 krpm and load 133 N. 111

Figure 5.19: Predicted average fluid velocity distribution in the film gap of the CFB for static radial load of 133 N and shaft speed of 30 krpm. The unit is in meters per second [m/s]. 112

Figure 5.20: Predictions for the average fluid velocity in the mid-plane of the bearing surface in tangential direction for different loading conditions. The shaft speed is 40 krpm. The second figure displays the critical section along the circumferential position between 150 to 200 deg. 113

Figure 5.21: Predictions for the average fluid velocity in the mid-plane of the bearing surface in tangential direction for different shaft speeds. The radial load is 133 N. 114

Figure 5.22: Predicted temperature gradient distribution on the CFB including the sleeve. The shaft speed is 30 krpm and the static radial load is 133 N. The unit is in degree Celsius per millimeter [degC/mm]. 115

Figure 5.23: Predicted temperature distribution on the CFB including the sleeve. The shaft speed is 30 krpm and the static radial load is 133 N. The unit is in Celsius. 116

Figure 5.24: The relation between hydrodynamic film pressure, film thickness and surface temperature. The parameters are given in non-dimensional forms for the sake of comparison. The shaft speed is 40 krpm. The static radial load is 222 N. 117

Figure 5.25: Predictions for the film temperature in the mid-plane of the bearing surface in tangential direction for different loading conditions. The shaft speed is 40 krpm. The second figure displays the critical section along the circumferential position between 150 to 200 deg. 118

Figure 5.26: Predictions for the gradient of the film temperature in the mid-plane of the bearing surface in tangential direction for different loading conditions. The shaft speed is 40 krpm. 119

Figure 5.27: Predictions for the film temperature in the mid-plane of the bearing surface in tangential direction for various shaft speed conditions. The static radial load is 133 N. 119

Figure 5.28: Predictions for the gradient of the film temperature in the mid-plane of the bearing surface in tangential direction for various shaft speed conditions. The static radial load is 133 N. 120

Figure 5.29: Predicted temperature distribution on the shaft. The shaft speed is 30 krpm and the static radial load is 133 N. The unit is in degree Celsius. 121

Figure 5.30: Predicted temperature gradient distribution on the shaft geometry. The shaft speed is 30 krpm and the static radial load is 133 N. The unit is in degree Celsius per millimeter. 121

Figure 5.31: Predicted convective heat flux distribution on the CFB including the sleeve. The shaft speed is 30 krpm and the static radial load is 133 N. The unit is in Watt per meter square [W/m^2]. 122

Figure 5.32: Estimated convective heat transfer coefficient on the bearing surface. The shaft speed is 30 krpm and the static radial load is 133 N. The unit is in [W/(m^2K)]. 122

Figure 5.33: Illustration of the thermal contact resistances in topfoil-bump and bump-sleeve contact regions 124

Figure 5.34: Predicted thermal conductance coefficients for the contact surfaces between the bumps and the sleeve surface. The shaft speed is 30 krpm and the static radial load is 133 N. The unit is in [W/(m^2K)]. 124

Figure 5.35: Predicted thermal conductance coefficient for the contact surfaces between the bumps and the topfoil surface. The shaft speed is 30 krpm and the static radial load is 133 N. The unit is in [W/(m^2K)]. 125

Figure 5.36: Total deformation of the bearing surface and underlying bump structure. The bump movement into the leading edge by sweeping between the topfoil structure and sleeve surface is displayed in the zoom image. The deformation is magnified with a scale factor of 20 to observe clearer. The shaft

speed is 30 krpm and the static radial load is 133 N. The unit is in micrometers. 126

Figure 5.37: The deformation of the bearing surface and underlying bump structure from isometric view. The shaft speed is 30 krpm and the static radial load is 133 N. The unit is in micrometers. 127

Figure 5.38: The deformation of the bearing in axial direction. The shaft speed is 30 krpm and the static radial load is 133 N. The unit is in micrometers............128

Figure 5.39: The deformation of the topfoil surface in radial direction from isometric view. The shaft speed is 30 krpm and the static radial load is 133 N. The unit is in micrometers. 128

Figure 5.40: Radial deformation of the topfoil near weld region of the trailing edge. The y-direction shows the radial direction whereas the z-direction indicates the axial direction. The shaft speed is 30 krpm and the static radial load is 133 N. 129

Figure 5.41: Comparison of the radial deformation of the topfoil in the midplane and edge in radial direction. The shaft speed is 30 krpm and the static radial load is 133 N...130

Figure 5.42: The radial deformation of the topfoil in the midplane for various shaft speeds. The static radial load is 133 N. The second figure displays the critical section along the circumferential position between 150 to 200 deg................131

Figure 5.43: The radial deformation of the topfoil in the midplane for various radial loads. The shaft speed is 30 krpm. The second figure displays the critical section along the circumferential position between 150 to 200 deg. 132

Figure 5.44: Von Mises stress distribution on the bumps and contact regions. The shaft speed is 30 krpm and the static radial load is 133 N. 133

Figure 5.45: The stress concentration in welded regions of the topfoil and bump structure. The shaft speed is 30 krpm and the static radial load is 133 N......134

Figure 5.46: Von Mises stress on topfoil in the midplane for various shaft speeds. The radial load is 133 N. The second figure displays the critical section along the circumferential position between 150 to 200 deg.......................................135

Figure 5.47: Von Mises stress distribution on topfoil in the bearing midplane for various radial loads. The shaft speed is 30 krpm. The second figure displays the critical section along the circumferential position between 150 to 200 deg...137

Figure 5.48: Predictions for the contact pressure on some contact surfaces between the topfoil and bumps in axial direction starting from the bearing center towards front edge. Numbering convention of the bumps are already given in previous sections. The shaft speed is 30 krpm and the radial load is 133 N...139
Figure 5.49: Predictions for the contact gaps on some contact surfaces between the topfoil and bumps in axial direction starting from the bearing center towards front edge. Numbering convention of the bumps are already given in previous sections. The shaft speed is 30 krpm and the static radial load is 133 N. 139

LIST OF TABLES

Table 1.1: Comparison of compliant foil bearings to conventional bearing types [6] 6

Table 2.1: Foil bearing model parameter list 29

Table 2.2: Chemical Composition, % for Inconel® X750 [83] 30

Table 2.3: Mesh details 33

Table 2.4: Detailed mesh parameters for selected mesh structure 35

Table 4.1: Heat flow paths for the CFB and shaft 79

Table 5.1: Complete list of the prediction of the film temperatures for all locations with respect to the increasing radial load and various shaft speeds. The experimental data taken from Ref. [59] is given in blue and the predictions are in orange columns. 97

NOMENCLATURE

A_{app}	apparent contact area [m^2]
A_{con}	contact area [m^2]
A_{rcon}	relative real contact area [m^2]
c	Nominal clearance [m]
c_p	specific heat capacity of fluid [J/(kg.K)]
$\mathbf{C}$	4th order elasticity tensor
D	diameter [m]
$\mathbf{D}$	elasticity matrix
D_{avg}	average gas particle diameter [nm] (0.37 nm for air)
$D_{s\text{-}i}$	shaft inner diameter [m]
$D_{sl\text{-}i}$	sleeve inner diameter [m]
$D_{sl\text{-}o}$	sleeve outer diameter [m]
d_g	gap distance [m]
E	Youngs modulus [Pa]
e	eccentricity [m]
e	enthalphy [J]
F	load [N]
F_B	body force [N/m^3]
F_{base}	force affecting the topfoil surface [N]
F_{def}	Deformation gradient matrix
F_{wall}	force affecting the moving shaft [N]
f_p	user defined normal penalty factor multiplier
g	gravitational accelaration [m/s^2]
h(x,y)	fluid film thickness [m]
H_B	Brinell hardness
H_b	the distance of bearing surface to reference plane
h_c	constriction conductance [$W/(m^2.K)$]
h_{conv}	convective heat flux coefficient [$W/(m^2.K)$]
h_g	gap conductance [$W/(m^2.K)$]
h_s	convective heat flux coefficient of shaft surface [$W/(m^2.K)$]
h_{joint}	joint conductance [$W/(m^2.K)$]
h_{max}	maximum film thickness [μm]
h_{mesh}	minimum mesh size for destination boundary
h_r	radiative conductance [$W/(m^2.K)$]
h_{nc}	natural convection coefficient [$W/(m^2.K)$]
h_{tf}	convective heat flux coefficient of topfoil surface [$W/(m^2.K)$]
h_w	the distance of journal surface to reference plane [μm]
H_μ	microhardness
k	thermal conductivity [W/(m.K)] or changed node index in FDM
$k_{contact}$	effective thermal conductivity of the joint [W/(m.K)]
k_B	Boltzmann constant $1.3806488 \times 10^{-23}$ [$m^2.kg/(s^2.K)$]
L	bearing length [m]
L_{bf}	bump length [m]
M	bending moment
m(x)	the source point function in a augmented Lagrangian contact
m	effective absolute mean asperity slope or node number in circumferential direction
M_g	gas parameter
$\mathbf{n}$	surface normal
n	air mol weight [kg] or node number in axial direction
n_{ref}	reference plane normal
n_{spot}	contact spot density
P_g	gas pressure [Pa]

H_{bf}	bump height [m]
P_a	ambient pressure (101 [kPa])
p_n	user defined normal penalty factor
q''_s	Shaft surface heat flux [W/(m^{2}K)]
q''_{tf}	Topfoil surface heat flux [W/(m^{2}K)]
R	radius [m]
$R_{bf\text{-}sl}$	thermal resistance between bumpfoil and sleeve [(m^{2}K)/W]
R_{gc}	universal gas constant [kJ/(mol.K)]
$R_{s\text{-}i}$	shaft inner radius [m]
$R_{s\text{-}o}$	shaft outer radius [m]
$R_{tf\text{-}bf}$	thermal resistance between topfoil and bumpfoil [(m^{2}K)/W]
S_{bf}	bump pitch [m]
S_c	centrifugal expansion of the shaft [m]
s_k	Newton step
S_{th}	thermal expansion of the shaft [m]
T	temperature [K or degC]
t	time [s]
T_a	ambient temperature (293.15 [K])
t_{bf}	bump foil thickness [m]
T_{cool}	cooling flow temperature [K]
T_{gap}	gap temperature [K]
th_s	shaft wall thickness [m]
T_n	normal contact pressure
T_{np}	penalized contact pressure
T_{ref}	reference temperature [K]
T_{sm}	shaft mean temperature [K]
T_t	friction traction vector
U	shaft surface velocity [m/s]
u_{base}	topfoil surface velocity in x direction [m/s]
u(x,y,z,)	film velocity in x-direction [m/s]
û	internal energy [J]
V	volume [m^3]
P	pressure [Pa]
v(x,y,z,)	film velocity in y-direction [m/s]
v_{wall}	shaft surface velocity in y direction [m/s]
v_{base}	topfoil surface velocity in y direction [m/s]
$W_{elastic}$	elastic energy [J]
W_{stored}	total stored energy
w(x,y,z,)	film velocity in z-direction [m/s]
$W_{x,y}$	load capacity [N]
z(x)	finite difference function
Z_{bf}	bump foil plain segment
Δx	finite increment in x-direction [m]
Δy	finite increment in y-direction [m]
ΔY	the distance between contacting surfaces [m]

Greek Letters

Γ	gas mean free path [μm]
Λ_B	bearing compressibility number
Π	thermal mixing parameter
Ψ	relative mean plane seperation
α	thermal expansion coefficient
$\boldsymbol{\alpha}$	thermal expansion tensor
β	gas property parameter (1.65 for air)
γ	total strain tensor
$\dot{\gamma}$	strain rate tensor
δ	some small value
ε	eccentricity ratio
ε_{err}	error rate for two consecutive iteration
ε_{ref}	reference for eccentricity ratio
ζ	ratio of the molecular weight of gas and solid
η	thermal accommodation parameter
θ	circumferential angle
κ	squeeze number
λ	molecular mean free path [μm]
μ	dynamic viscosity [Pa.s]
μ_a	air viscosity in ambient conditions (1.9e-5 [Pa.s])
ν	Poisson ratio
ξ	viscous dissipation [W.kg/m^3]
ρ	density [kg/m^3]
σ	stress [Pa]
σ'	von Mises effective stress [Pa]
τ_{ij}	shear stress
$\boldsymbol{\tau}$	shear stress tensor
φ	attitude angle
χ	effective rms surface roughness [μm]
ψ	constriction parameter
ω	angular speed [rad/s]
$\nabla \mathbf{U}$	deformation rate tensor
ϵ	relative contact spot size

Abbreviations

ACM	Air Cycle Machine
AMB	Active Magnetic Bearing
BLAS	Basic Linear Algebra Subprograms
BRU	Brayton Rotating Unit
CFB	Compliant Foil Bearing
CFD	Computational Fluid Dynamics
CLA	Center-line average
CMY	Cooper-Mikic-Yovanovich correlation
CP	Cauchy Point
deg	Degrees
degC	Degree Celsius
DOF	Degree of freedom
FDM	Finite Difference Method
FE	Finite Element
FEA	Finite Element Analysis
FEM	Finite Element Method
Fr	Froude Number
FSI	Fluid Structure Interaction
Gen	Generation
Kn	Knudsen number
LE	Leading Edge
LHS	Left Hand Side
Lit.	Literature
ND or Non-Dim	Non-dimensional
NS	Navier-Stokes
Nu	Nusselt number
PARDISO	Parallel Direct Solver
Pr	Prandtl number
Re	Reynolds number
RHS	Right Hand Side
RMS	Root mean square
TC Loc.	Thermocouple locations
TE	Trailing Edge
TEHD	Thermo Elasto Hydrodynamics
THD	Thermo Hydrodynamics

Subscripts

a	ambient
b	bearing
bf	bumpfoil
cool	coolant
d	down
f	film gap
fl	fluid
g	gas
i	inner or tangential direction index in FDM
j	journal or axial direction index in FDM
leading	leading edge
L	length
nc	Natural convection
o	outer
p	point
ref	reference
s	shaft
sf	surface
sl	sleeve
tf	topfoil
trailing	trailing edge
u	up
v	volume
x	x direction
y	y direction
z	z direction
0	initial

Superscripts

k	iteration number
n	normal
t	traction

1 INTRODUCTION

1.1 Motivation

The machines that transfer energy between an operating fluid and a rotating structure are called as turbomachinery. All types of turbines including gas, steam and wind turbines, compressors, blowers, pumps and mills could be given as examples of this type of machinery. For instance, a gas turbine converts the thermal energy extracted from combustion gas of a hydrocarbon fuel into mechanical energy by rotating a shaft through turbine blades. The bearings are the main support and positioning mechanism of the rotating components for every type of turbomachinery. Different type of bearings perform various tasks in a turbomachine. Thrust bearings serve as axial positioners, journal or roller bearings support the rotor in radial direction whereas angular contact bearings can accomplish both tasks. The essential targets of bearing design are longer service life, improved reliability and efficiency. The critical factors and parameters that shape the bearing design can be listed as follows [1],

1. Radial/axial or combined load capacity
2. Shaft surface speed
3. Operating temperature
4. Lubrication method and lubricant type
5. Demanded service life
6. Reliability against failure
7. Shaft arrangements or misalignment
8. Mounting and dismounting method
9. Vibration and noise level
10. Environmental conditions

Oil-lubricated shaft support components, based on fluid film and rolling-element type bearings, have been an industrial standard for centuries and have served the community successfully. Their reliable and sufficient performance even at extreme loading conditions, and proven long service life have enabled them to prevail in most mechanical systems. Commonly used systems include internal combustion engines, power plant turbines, fluid compressors and electric motors. During long-term productive research period, development and experience have resulted in well-established and acknowledged principles for successful applications and innumerable specific designs of these machine elements for particularly challenging applications [2]. This positive experience with conventional rotor support technologies, however, concealed the crucial role of rotor support technologies in the overall success and performance of rotating systems. When novel machinery forced the limits beyond the norm with respect to rotor speed, temperature or other factors, it is better conceived that closer attention must be devoted to the rotor support system including the consideration of alternate bearing technologies. To illustrate the recent requirements for support systems, in propulsion and stationary power generation areas [3], the bearing lubrication at the hot section (turbine side) requires very complicated oil-lubrication system and cooling devices to extend the life of the ball bearings. Future aircraft engines and weapon systems require breakthrough bearing system with much higher operating temperature than current oil-lubricated bearings. The maximum operating temperatures of various synthetic oils are about 250°C [4], and the temperature limit is one of the most significant factors that hinders the design of more efficient turbines. Replacing the radial bearings of the gas turbines with air-lubricated bearings can eliminate the complicated oil lubrication circuit at the hot sections while allowing the design of environment-friendly high efficient turbines. Compliant air foil bearings (CFB) have been recognized as one of the most promising air bearings for the aforementioned applications.

1.1.1 The Prominent Characteristics of CFB in Turbomachinery

The use of foil bearings in turbomachinery has various advantages compared to the conventional rotor support technologies. The salient features of foil bearings are explained below in detail.

Improved Reliability: Machines supported by foil bearings are more reliable because fewer parts are utilized to support the rotating components and there is no required lubrication and oil feeding system. During steady operation, hydrodynamic pressure generated in the air/gas film prevents the bearing surface from physical contact with the shaft and thus, ideally no wear occurs at this state. The bearing surface comes into contact with the shaft surface only when the machine starts and stops. During this transient regime, special coatings developed for foil bearings to limit the wear rate.

No Requirement for Scheduled Maintenance: Due to the elimination of the oil lubrication system, there is no need to check and replace the lubricant in foil bearing supported machines. This reduces the operating costs for long term.

Soft Failure: Because of the compliant structure and low operation clearances inherent in foil bearing design and assembly, if a bearing failure occurs, the bearing foils confine the shaft assembly from excessive displacement such that the damage is most often limited to the bearings and shaft surface. The shaft may be re-used as before or can be repaired. Damage to the other hardware is expected to be minimal and fixable during overhaul.

Environmental Sustainability: Foil bearings are inherently resistant to external disturbances like foreign substance ingestion. Large-sized particles could not enter into the bearing flow path because of tighter operating clearance between the shaft and the bearing. Smaller particles are rapidly flushed out of the bearing by means of cooling stream. This capability of foil bearings to endure against contamination eliminates the requirement for a filtering system.

High Speed Operation: The efficiency of most turbomachinery such as compressor, turbine, and turbocharger are improving as the rotor speed has been increased. Foil bearings allow these machines to operate at higher speeds without any theoretical limitation as with ball bearings due to the centrifugal effects or as in oil-lubricated bearings due to the excessive shear heating of oil film. In fact, due to the hydrodynamic improvement, they have a higher load capacity as the speed increases.

Low and High Temperature Capabilities: Many oil lubricants cannot operate at very high temperatures without breaking down due to the phenomena called as shear-thinning. At low temperature, the viscosity of oil lubricants increases drastically and prevents stable operation. Foil bearings, however, operate efficiently at severely high temperatures, as well as at cryogenic temperatures because dynamic viscosity of air does not get affected from temperature change significantly.

Process Fluid Operations: Foil bearings enable operation with various kinds of process fluids including helium, xenon, refrigerants, liquid oxygen and liquid nitrogen. For applications in vapor cycles, the refrigerant can be used to cool and support the foil bearings without the need for oil lubricants that can contaminate the system and reduce efficiency [5].

A comparison for foil bearings to the conventional bearing systems is presented in Table 1.1.

Property	**Compliant Foil Bearing (CFB)**	**Oil-lubricated Bearing**	**Rolling Element Bearing**	**Active Magnetic Bearing (AMB)**
Maximum Operating Speed at Bearing Surface (Bore) for Radial Bearing	Essentially unlimited, 150 to 225 m/s is fairly typical	Generally 75 to 105 m/s or less	Equal to a surface speed of 52 to 157 m/s	180 m/s for typical materials, 200 m/s for special alloys
Minimum Required Operating Speed	Yes, application dependent	Yes, application dependent	None	None
Load Capacity and Typical Projected Area Loads	Low to moderate 50 to 100 psi (0.68 MPa) for radial 25 to 35 psi (0.2 to 0.25 MPa) for thrust	Potentially very high 100 to 450 psi (0.68 to 3.1 MPa) for radial 250 to 500 psi (1.7 to 3.4 MPa) for thrust	Moderate to high	Low to moderate 100 psi (0.68 MPa)
Short term overload capability	Limited	Substantial	Good	Limited

Bearing Operating Temperature Range	Cryogenic to 650˚C +	Varies with construction and lubricant, but most babbitt surfaced industrial bearings operate in the range of 32 to 82˚C, and alarm by 120˚C	-30 to 230˚C	-180 to 540˚C claimed by developers
Power Loss	Radial very low, thrust moderate	Can be significant	Generally low to moderate	Generally very low
Oil Free	Yes	No	No	Yes (although backup bearings could be grease lubricated)
Misalignment Capability	Low to moderate	Moderate, depends on construction	Very low (highly loaded angular contact) to moderate (spherical roller)	Moderate
Auxiliary Systems	Source of a limited amount of low pressure "cooling" air	Pumps, coolers, filters	Nothing for grease lubricated bearings, ranging to pumps, filters, etc. for oil-jet lube at high speeds and loads	Control system electronics, auxiliary bearings, generally some amount of cooling air
Radial Envelope requirement	Length in range of 0.5 to 2x shaft diameter, D_o in range of 1.25 to 2 times diameter	Length in range of 0.5 to 2x shaft diameter, D_o in range of 1.25 to 2 times diameter, plus lube oil system	Length in range of 0.2 to 0.5x shaft diameter, D_o in range of 1.5 to 2 times diameter, plus lube oil system	Length in range of 1 to 2x shaft diameter, D_o in range of 1.5 to 4 times diameter, plus electronics if external

Weight	Generally the lightest option	Generally pretty heavy when pumps, filters, piping etc. considered along with the actual bearings	Relatively light	Moderate including electronics
Stiffness	Low	Moderate to high	High	Depends on tuning, generally are tuned soft
Damping	Low to moderate	Generally High	Very Low	Moderate to high depending on tuning and system dynamics
Shock Tolerance	Good	Very Good	Moderate	Can be poor

Table 1.1: Comparison of compliant foil bearings to conventional bearing types [6]

During the last 25 years, significant progress has been achieved by utilizing foil bearings in turbomachinery. The reliability of the machines using foil bearings has increased over tenfold in comparison to those with rolling bearings. Air Cycle Machine (ACM) are serving for cabin pressurization, heating and cooling in aircrafts for many years. Almost every new ACM on military and civil aircrafts are supported by foil bearings, and the old systems already built with rolling element bearings are replaced with foil air bearings to improve reliability and overall performance. Some examples of ACMs developed for military aircrafts by AiResearch are displayed in Figure 1.1 and Figure 1.2. The section view of a turbocharger developed by NASA by using journal and thrust foil bearings is illustrated in Figure 1.3. Many machines with working fluids other than air, such as helium, xenon, refrigerants, liquid oxygen and liquid nitrogen, have been built and successfully tested [5].

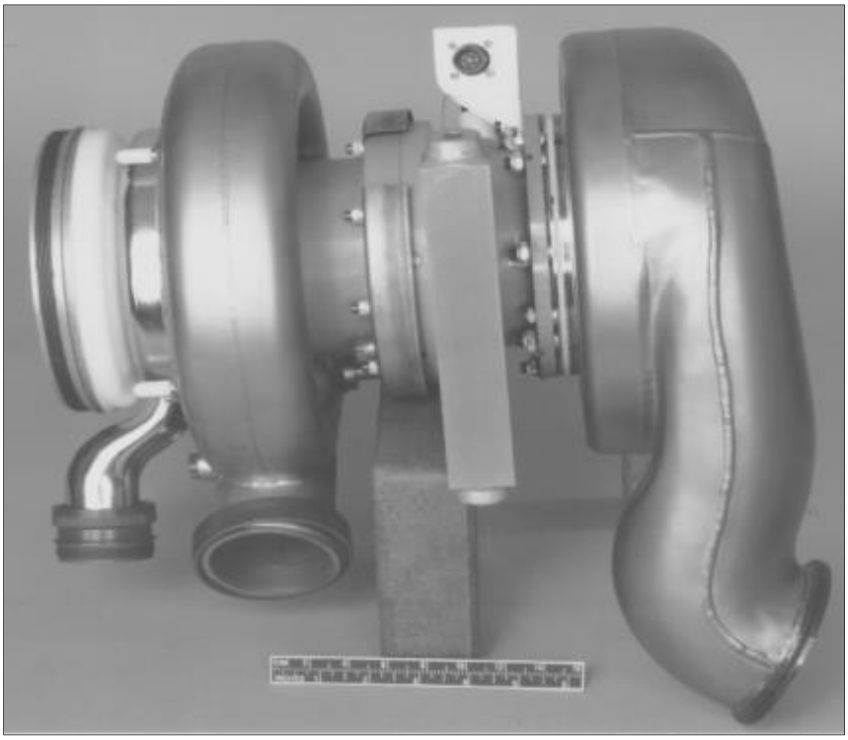

Figure 1.1: F-14 Foil Bearing ACM (Developed by AiResearch) [5]

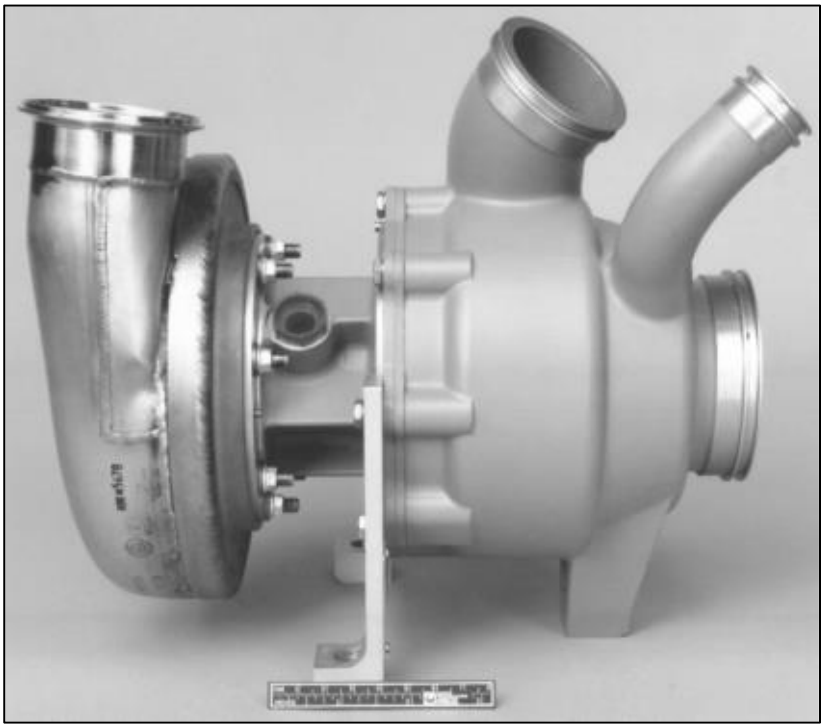

Figure 1.2: F-16 Foil Bearing ACM (Developed by AiResearch) [5]

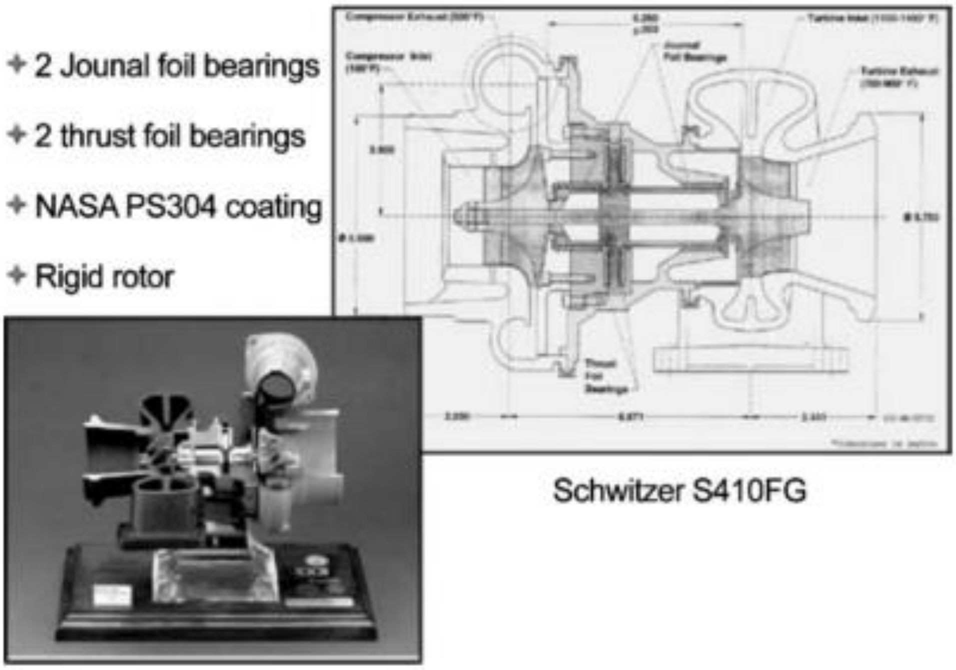

Figure 1.3: Section view for NASA turbocharger supported by journal and thrust foil bearings [7]

1.2 Operating Principles of Foil Bearings

Compliant foil gas bearings are a class of hydrodynamic bearings that use ambient gas as their operating fluid and hence does not require any additional lubrication circuit. The hydrodynamic pressure is generated between the moving shaft surface and flexible bearing surface called as *topfoil surface* typically formed of numerous layers of sheet metal foils. To support radial or axial loads, foil bearings can be configured as journal or thrust bearings as in conventional oil-lubricated technologies. The main behavior of a shaft supported by foil-gas bearing is that it floats on a self-generated fluid film during normal operation but experiences a short-term dry sliding contact during low speed operation at start-up and shut-down periods. The bearing geometry and the fluid film thickness are shaped according to the equilibrium between the hydrodynamic film pressure, and the deformation of the topfoil surface with its bumpy underlying spring support structure [8]. Dynamic rotor movements or vibrations during operation induce fluctuations in the film pressure and results in small motions in the foils. The sliding contact mechanism due to the relative motions of the foil structures improves the overall damping capability of the bearing system [9]. From this point of view, one can acknowledge a foil bearing both a supporting bearing mechanism and a damper system that reduces undesired oscillations by dissipating the energy through Coulomb friction. By means of the compliant structure, the bearing accommodates itself to thermal and mechanical distortions much more effectively than any other supporting technologies. These outstanding features of foil-gas bearings have long been known by many researchers and engineers. Gross [10] referred to these features in 1969 by stating that *"Foil bearings were evolved to minimize instability problems, reduce manufacturing tolerances and permit adaptation of the bearing to changes in shaft diameter caused by centrifugal force or temperature gradients. The fluid film between the shaft and the foil is likely to have a greater stiffness than the foil itself"*. The succeeding forty years of intensive research and development in foil bearings have greatly supported Gross' summary and must be considered first when adapting foil bearings into new turbomachinery. On the otherside, foil bearings have a significant drawback of lower load capacity and dynamic properties due to the low viscosity of air compared to oil lubricants. This brings both assets and difficulties to the systems established using such rotor supports. The main benefit of gas bearings is the elimination of the lubrication system combined with the capability to operate at higher speeds and temperatures. The primary difficulty is to develop novel machine designs that can utilize the advantage of the performance characteristics of foil bearings while compensating their performance shortcomings [11]. Foil bearings offer very modest load capacity, stiffness and damping compared to conventional support systems. One can expect stiffness and damping of a foil bearing to be an order-of-magnitude lower than a similar size oil-lubricated bearing. On the other hand, friction can be lower especially at high rotational speeds and foil bearings have no intrinsic DN speed limitations, as do rolling-element type bearings. Foil bearing load capacity is heavily influenced by speed as well. At high speeds, foil-gas bearings exhibit comparable or even higher load capacity than rolling-element bearings but have limited capability at low speeds [12]. These characteristics of foil-gas bearings dictate that their successful application occurs when a rotor system is designed around the bearing capabilities in contrast to the current common practice of first designing the aero-components, determining speeds and loads from which the rotor design and bearing requirements follow [11].

The operational feasibility of the compliant foil bearing for small scaled gas turbines has been demonstrated for different temperature, load, vibration and load conditions at speeds exceeding 700,000 rpm, temperatures exceeding 650˚C, and loads approaching 4200 N [13, 14]. Foil bearings have been applied to ACMs [15], industrial compressors [16], turboexpanders [17], turbochargers [18], cryocoolers, cryogenic pumps, and other systems operating at extreme environments [19, 20].

1.2.1 Structure of Compliant Foil Bearing

Figure 1.4 demonstrates the schematic of a typical bump-type foil journal bearing. Foil bearing consists of three main parts namely top foil, corrugated bumps and bearing housing. This twofold structure providing stiffness and damping to the system makes foil bearing unique. Compliant support structure of the bearing can be made of more than one corrugated bump foil. This flexible structure improves dynamic properties of the bearing. The compliant bumps can deform under load due to the hydrodynamic pressure and form the converging wedge between the shaft and bearing surface without being affected much from speed and temperature variations. Furthermore, shaft growth due to the centrifugal and thermal effects, and thermal and mechanical deformations of the bearing housing are compensated without significant performance loss thanks to the compliant mechanism [21].

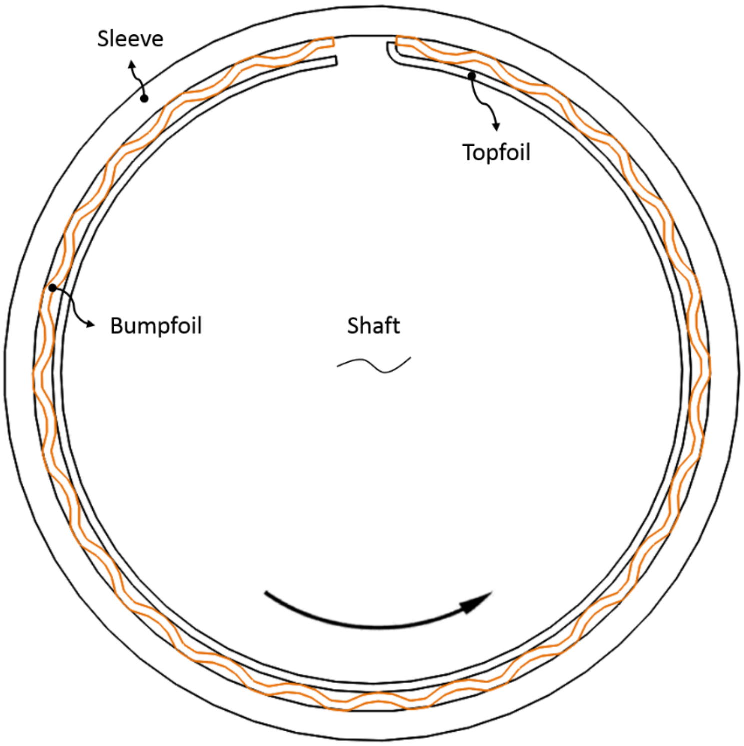

Figure 1.4: Basic scheme of a compliant foil bearing

Typically, nickel-based alloys coated with soft film are used as top and bump foil material. The coating film abrades during start/stop cycles to accommodate itself to foil geometry distortions. The foil is not coated at elevated temperatures but the shaft is treated with solid lubricant coatings. Top foil provides required smooth surface to the lubricant to create hydrodynamic pressure with relative motion of the shaft surface. The behavior of bumps can be easily considered as a spring-damper system that supports the topfoil for desirable stiffness and damping. The relative motion of bumps with respect to the topfoil and housing during operation dissipates the vibration based energy due to the friction and supplies additional damping to the system. This characteristic behavior of foil bearing also improves its accommodation of thermal, and centrifugal expansions as well as misaligned assembly that results in more stable operation capability of the system.

Another commonly used type of foil bearing is so-called multiple leaf-type bearing. In multiple leaf CFB, the compliance is achieved by bending of staggered structural foils and the dry-friction at the contact lines defines the operational characteristics [22]. In corrugated bump CFB, bump-strip layers supporting a thin top foil render an adjustable support. In this type of bearing, dry-friction effects arising between the bumps and topfoil, and the bumps and the bearing inner surface provide the energy dissipation or damping characteristics [23]. The published literature note that multiple leaf CFB are not the best supports in high performance turbomachinery, primarily because of their inherently low load capacity. A corrugated bump type CFB fulfills most of the requirements of highly efficient oil-free turbomachinery, with demonstrated ultimate load capacity up to 680 kPa (100 psi) [24]. The forced performance of a CFB depends upon the material properties and geometrical configuration of its support structure (the top foil and bump strip layers), as well as the hydrodynamic film pressure generated within the bearing clearance. In particular, the underlying support structure dominates the static and dynamic performance of heavily loaded CFB especially at high speeds [25]. For example, due to the elastic deflection of the bump strip layers, the operation film thickness remains almost constant compared to the shaft eccentricity. The overall stiffness mainly depends on the softer support structure, rather than the gas film, which “hardens” as the shaft speed and applied load increase. Material hysteresis and dry-friction dissipation mechanisms between the bumps and top foil, as well as between the bumps and the bearing inner surface, appear to enhance the bearing damping [26].

1.3 Problem Statement and Scientific Contribution

Due to the considerations stated above, the interest in oil-free gas turbine engines for both terrestrial power generation and propulsion including space applications is steadily increasing. The required load and speed capacity for more efficient high speed turbine designs severely challenge conventional rolling element bearing arrangements. Furthermore, an external lubrication system is required for the bearings, unless the process fluid can be used as lubricant. The oil lubricated hydrodynamic bearings is not much more appealing either. More advanced lubrication systems are required for this type of bearings. A considerable power loss also occurs due to the high viscous dissipation inherent in liquid lubricants. In addition, an advanced sealing system with its losses, leakage, and other environmental concerns is required due to the presence of a lubrication system.

The rotor system can be simplified greatly by eliminating the lubrication mechanism. That will reduce overall system weight, and advance system performance. However, at high speeds and temperatures, gas bearing will also need to accommodate itself centrifugal and thermal growth as well as vibration conditions in order to prevent ultimate failure. Hence, the bearing surfaces should be sufficiently compliant to provide required operation region for the shaft [21].

The lubricant used in foil bearing applications is usually air that has a superior performance at elevated temperatures in terms of viscosity compared to the oil based lubricants. However, that property may result in thermal instability with increasing temperature. In addition, some limitations exist for the foil bearings due to the material property changes under some operation circumstances. The foils soften at high temperatures and the stiffness drops rapidly. The most crucial problem faced in experiments at high speeds or overload conditions is the high local temperature gradient that causes wavy deformation of the foil surface and catastrophic failure of the bearing [27]. Another important concern in terms of the thermal management is the weak conduction rate of the bearing due to the thin foil structure. The contact between the topfoil and bumps occurs at localized small areas that resists effective heat removal from the system. Inappropriate thermal management due to insufficient cooling and inapropriate coating may produce ultimate deterioration of the rotor-bearing system.

Even though experimental research data are available in open literature, extended thermo-hydrodynamic analysis is required to better understand and optimize the system performance at the design level. Comprehensive modeling of CFB calibrated with relevant test data will help enable the widespread use of CFB in novel turbomachinery applications, such as hybrid fuel cell-turbine power systems and micro-engines recharging battery packs for clean hybrid electric vehicles [13].

Conventional models remain rather simplified as they include the bumps only as an equivalent stiffness uniformly distributed around the bearing circumference. More complex models couple directly the elastic deformations of the top foil to the bump mechanism as well as to the hydrodynamics of the gas film but by considerably simplifying the structural model. In the structure of an actual bump foil bearing, the role of the top foil is to generate air film force when the journal rotates. Therefore, it is important that bending stiffness of the top foil is sufficiently high to endure the pressure. However, the portions of the topfoil surface that are not in contact with the bumps have practically little stiffness and deflect more when exposed to hydrodynamic pressure. In many previous studies, this deflection of the top foil was ignored. Therefore, extraction of the damping characteristics due to the top foil deflection was impossible. However, the top foil deflecting phenomenon which is called as sagging radically affects the overall behavior of the bearing, and it is observed by many researchers during post-experimental investigation of bearing components.

The model explained in this work couples the structural deformation of the underlying structure with hyrodynamic pressure generated in the film gap by solving the Reynolds Equation and Duhamel-Hooke’s relation for structural deformation that are directly coupled by utilizing a commercial Finite Element Analysis (FEA) code. The bending effects of the top foil are also investigated, considering energy dissipation due to deflection of top foil and bump foil. Furthermore, it accounts for temperature change in the film due to the viscous dissipation and compressibility of the fluid by solving the bulk flow energy equation using a custom written direct solver based on Finite Difference Method (FDM) that is iteratively coupled to the main FEA code. The physical contacts between bearing assembly components are modeled by utilizing Augmented-Lagrangian contact model. The thermal contact is also included in the model with an advanced approach called Cooper-Mikic-Yovanovich (CMY) correlation. The model involves complete bearing mechanism as well as the shaft section interacting with bearing. Temperature distribution over the shaft due to the generated heat in the film is integrated to the model. The thermal growth of the shaft, foil structure, bearing sleeve, and centrifugal growth of the shaft are also considered. From this aspect, this model is the most complete and advanced model in open-literature for a bump-type compliant foil journal bearing that provides a deep insight into the structural and thermal characteristics of a CFB during steady-state operation. The proposed model is validated via the temperature measurements available in the literature. The effects of the shaft speed and static radial loading on hydrodynamic, thermal and structural properties including pressure distribution, velocity profile, film thickness, temperature distribution, thermal contact properties, deformation of topfoil and bumps, von Mises stress distribution and mechanical contact properties are investigated in detail.

1.4 Literature Survey

The foil gas bearings were invented during a research for faster magnetic tape recording. Recording performance was suffering due to the elevation of the recording head and floating of the tape. Underlying physics behind this phenomenon was first recognized by an IBM engineer Baumeister [28] and called it as “foil bearing problem” by inspiring from studies on flexible bearing technology. Gross developed the mathematical model of foil bearing problem to apply this issue to the bearing systems of high speed machines. The work done by Gross is extended to nuclear reactors that require high speed coolers and compression turbines [29]. These systems do not compensate contaminants that may occur due to oil lubricants and thus, requires a clean bearing mechanism. Furthermore, operating temperatures and speeds of these systems are considerably high. Taking these into account, Gross and his colleagues succeeded to develop a 15 kW Brayton rotating unit (BRU) supported by foil bearings. During the initial phase of BRU design, rigid gas bearings are utilized, and significant problems including instability and vibrations are faced due to inadequate performance of these bearings with respect to the thermal and centrifugal transients. The problems are greatly eliminated when foil bearings are replaced as supporting system. This positive achievement triggered an extensive conversion for bearing components of power conversion systems developed by NASA involving turboexpanders, auxiliary power units (APU) and ACM [29]. Foil bearings are adapted to ACMs by Garret-AiResearch to provide cabin pressurization in aircrafts in the late 1960s [30]. This integration improved cabin pressurization without scheduled maintenance and lubrication system requirement as well as solving the oil filtering problem that was a common issue in 1950s and the 1960s. Development of bump-type foil bearings for fighter jets by Mechanical Technologies Inc. and Hamilton Standard bring the design one step further.

To operate the foil bearings at elevated temperatures, solid lubricant coatings should be applied properly. Significant amount of studies are performed by NASA and most of these works are released to open literature to share the fundamental technology advancements [7]. The first thriving engine of Capstone is developed during the beginning of 90s by exploiting NASA reports on special high temperature foil bearing coatings [31]. The company continued to extent its product portfolio in the following years and had sold over 4000 units all over the world.

The requirement for more robust and more reliable turbomachinery in different areas including cryogenic turbopumps forced foil bearing technology steadily progress. Several experiments are conducted with various fluids to unveil the cryogenic performance of foil bearings until basic design parameters are determined. Nowadays, foil bearings are commercially applied to many cryogenic turbopumps and turbocompressors [32].

Foil bearings are essentially designed for bearing mechanism of lightly loaded systems. However, it is also attempted to support heavier rotors on foil bearings which eventually cause new challenges like limited damping capability, higher start torque requirement and limited loading capacity at low speeds because of accelerated wear [33]. To improve the loading and damping capacity especially at low speeds, foil bearings are hybridized either by magnetic or hydrostatic bearings [34].

1.4.1 Isothermal Models

Outstanding structural properties of foil bearings make them unique and advantageous over other bearings. If a foil bearing is carefully designed, it will have suitable compliance that enables higher tolerance to assembly misalignments, erroneous manufacturing, thermal and centrifugal expansions [5, 35]. Additionally, friction between the elements of the bearing structure results in improved damping properties of the bearing [35].

On the other side, the relatively complex bearing structure and the interactions between the bearing elements complicates modeling of the foil bearing. Coupled fluid-structure interaction solution techniques have to be applied to obtain a reasonable output in terms of understanding the underlying operation mechanism of foil bearings. The hydrodynamic flow profile and resulting bearing deformations are interacting with each other. Therefore, foil bearing system becomes a highly non-linear and iterative problem in which various parameters from different physics should be considered.

In early studies for modeling foil bearing stiffness behavior, researchers modeled the bumps as independent simple springs, and did not consider the interaction between the bumps [25, 36, 37]. The structural stiffness of the bumps are calculated by Walowit [38] by applying the circular beam equation with plane strain assumption. Throughout this study, friction in between bumps and housing or bumps and top foil is ignored for the sake of simplicity. Heshmat et al. [25, 39, 40] numerically analyzed the bump foil bearing by using Walowit’s equation for bump stiffness. They detailed the bearings static load performance. In this study, bump foil is assumed to be an elastic foundation. They solved compressible Reynolds equation to calculate the flow profile in the hydrodynamic film between journal and top foil surfaces. The film pressure is coupled to the local deflection of the corrugated bumps in this approach. The effect of the top foil structure is completely eliminated in this simple model and the elastic displacement is assumed to be proportional to the local pressure difference. Another significant parameter comes with this approach is the structural compliance coefficient of the bumps that depends on foil thickness, geometric shape and material properties. This simple but useful model is known as *simple elastic foundation model* and utilized in many works. The load carrying capacity and bearing loss torque is calculated by means of FDM. The study reveals that for the same air film thickness distribution, foil bearings have greater load capacity compared to the rigid gas bearings. Peng and Carpino [40, 41] calculated the linearized stiffness and damping force coefficients of CFBs by using finite difference formulations. They solve the Reynolds equation simultaneously by combining equivalent stiffness of fluid film and structural bump. The thin compliant foil is positioned on top of the corrugated bumps. The equivalent viscous damping in an excitation cycle of the journal was estimated by assuming that the dissipated energies due to the dry-friction between contacting pairs of bump-topfoil and bump-housing are equal. They also proved that this equivalent viscous damping increased the overall stiffness and damping of the bump foil bearing. In a following study [42], Peng and Carpino applied finite element perturbation approach to calculate the bearing stiffness and damping coefficients. The effects of the membrane, bending and elastic foundation as well as the viscous damping due to the Coulomb friction are considered in the structural model. The fluid film is assumed to be simplified isothermal ideal gas. They concluded that the dynamic coefficients of the foil bearing are affected by the stiffness of the foil membrane. They also note that finite element approach significantly contributes to the accuracy of the overall analysis. Carpino et al. [43-46] have improved the computational models by including the details of membrane and bending effects of the top foil, and integrating the elastic deformation of the sub-foil structure. In [43, 44], the FEA models for the gas film and the foil structure are coupled in an iterative scheme via the pressure field. Furthermore, Refs. [45, 46] introduced a more advanced finite element formulation that covers membrane and bending stresses in a cylindrical shell coupled through moment, tension, curvature, and strain expressions. Their analysis combines the hydrodynamic film pressure and the structural deformation of the top and bump foils in a single finite element model. Their predictions successfully captures the irregular distribution of the pressure and film thickness due to foil detachment in the exit region of the gas film. Heshmat et al. [47] predict the static load performance of thrust CFBs by coupling the finite element model of the structure generated in a commercial code to the finite difference formulation of the film hydrodynamics. The predictions are in a good agreement to the test measurements. Lee et al. [48] developed a computational model integrating the foil structure and fluid film. The structural FEA models for the top foil and corrugated bump geometry are coupled to the hydrodynamic film pressure model. The predictions for minimum bearing film thickness, attitude angle, and force coefficients are presented. In another study, Le Lez and his colleagues developed two new models. In the first model [49], they employed a commercial finite element analysis package to solve the problem numerically. In the second model [50], they proposed an analytic formula in which the bump foil-top foil assembly is replaced with a network of interconnected springs. The experimental data and the predictions are comparable for both models. DellaCorte and Valco [51] developed a useful estimation guideline for the load capacity of air-lubricated foil journal bearings by utilizing the experimental data in literature. In this study, bearings are categorized as three different design generations with respect to the underlying bump geometry and related stiffness performance of the bearings. The details of each model are explained in the following sections. Radil et al. [52] illustrated the strong correlation between the load capacity of CFB and operating bearing clearance. Due to the thermal and centrifugal expansions of the journal during operation, the clearance is largely unknown for foil bearings. In a succeeding study, Radil et al. [53] evaluated three different thermal management techniques for foil bearings. They indicated that the cooling performance of each method are distinct. The analysis performed by Kim and San Andrés [54] is revised by including the impact of the assembly preload [55] in the model. They also implemented an analytical method to estimate load capacity, minimum film thickness and stiffness coefficients during operation at elevated shaft speeds. They found that the underlying bump foil geometry substantially dictates the load capacity, stiffness behavior and structural deformation of a CFB. In a more recent study, San Andres and Kim [56] compared one-dimensional and two dimensional finite element models for topfoil geometry to predict the static and dynamic load performance of the bearing. The deformation of the topfoil is coupled to the film pressure through a global stiffness matrix during calculations. The predicted results for attitude angle and minimum film thickness for various static loads are compared to the literature. They found that the minimum film thickness for a given load is overestimated at bearing midplane and underestimated at bearing edges using two dimensional FEA model. Interestingly, the 1D top foil model yields more conforming results to the published experimental data in literature.

1.4.2 Thermal Models

Salehi et al. [57] performed the first study to characterize thermal properties of gas foil bearings by utilizing the simple elastic foundation model [25] to resolve bump deformation. The Couette flow approximation is applied to simplify the energy equation by neglecting the work done by pressure such that the energy and Reynolds equations are uncoupled. Their analysis calculates only the circumferential temperature distribution at the bearing mid-plane. The axial temperature distribution is assumed to linearly decrease towards the bearing edges. To predict the temperature increase of the cooling stream, the inlet and outlet temperatures of the flow are measured during tests. The peak temperatures are measured in the direction of the radial load. The measurements also demonstrate that the temperature increases as the rotor speed and static load increase. A comparison of the predicted temperature-rise of the cooling flow to the experimental measurement shows good agreement with a deviation of ~20 %. Peng and Khonsari [58] proposed more advanced THD model to predict the performance of the CFB at steady state conditions. The foil structure is represented by simple elastic foundation whereas coupled Reynolds and thermal energy transport equations solved simultaneously for prediction of the gas film pressure and temperature fields. The heat convection coefficients on surrounding surfaces are obtained by means of the cooling flow thermal state. The thermal resistance of the topfoil structure is also defined in the thermal model. However, the heat flux towards the shaft and sleeve which is a significant source of heat dissipation mechanism of the thermal system is ignored. In addition, their model allows sub-ambient pressure values which is not realistic, as suction flows from the bearing side edges occurs. According to the predictions, temperature distribution in axial direction is almost uniform. Furthermore, the load capacity of the bearing improves due to the increase of air viscosity with respect to temperature rise. Their temperature predictions are in a good agreement with experiments. On the other hand, Radil and Zeszotek [59] found that load capacity of a CFB decreases almost 30% when temperature has increased from 25ºC to 650ºC. To improve the accuracy of the predictions, thermo-mechanical properties of the structural components need to be calculated. Paulsen et al. [60] developed a mathematical approach by using linear perturbation theory to compare the difference between isothermal and thermal models for three different foil bearing geometries. To simplify the model, they did not includ the heat flux along the axial and circumferential directions of the housing and shaft that causes an overprediction for the temperatures. Feng and Kaneko [61] presented a THD analysis of multi-wound foil bearing by utilizing Lobatto point quadrature to solve for energy equation. Reynolds equation, the foil elastic deflection, and the energy equation are solved in an iterative procedure until convergence achieved. They compared the results in Ref. [59] to benchmark their models. In a succeeding study [62], they implemented Lobatto point quadrature algorithm in a sparse mesh to reduce the computational cost of the analysis. The deflection of the foil geometry is modeled as link-spring structure and thermal growth of the bumps are also included into the model. The temperature predictions agree well with test data in Ref. [59]. San Andres and Kim [63] developed a 2D THD model which predicts the heat transfer only in radial direction. To further simplify the model, they presumed the cooling flow as heat sink with constant temperature. Their model does not account heat convection between bump foils and cooling air either. However, the results are in a good agreement with the experimental data from Ref. [59] by adjusting the unknown parameters like mixing ratio, bearing clearance, bump geometry etc. Kim, et al. [64] investigated the effects of different mixing models in bearings. Kim and San Andres [65] measured rotor response with foil bearings cooled by pressurized side flow. They benchmarked the measurements for onset speeds of instability and whirl sub-synchronous frequency to the predictions with a computational model. Sim and Kim [66] developed a 3D THD model for compliant flexure pivot tilting pad gas bearings. The model predicts the rotor and pad temperatures, as well as the gas film temperature, simultaneously preserving global thermal balance when sufficient thermal boundary conditions for the bearing housing and rotor ends far away from the bearing edges are defined. Lee and Kim [67] extended the study in Ref. [66] by introducing detailed thermal models of foil structures and cooling channels formed by bump foil geometry. Thermal contact resistance coefficients between top foil and bearing sleeve, and between bump foil and bearing sleeve were experimentally measured and included into the model. Similar to the work in Ref. [66], this work also investigates the 3D THD characteristics of CFB considering global energy balance of the film flow with surrounding components by solving generalized Reynolds equation, 3D energy equation, and heat balance equation simultaneously. Thermal expansion of top/bump foils, rotor, and bearing sleeve, as well as shaft centrifugal expansion are also considered in the model. A model simulation was implemented to correlate with experimental data for CFB temperature published in Ref. [59]. Even though the model includes relatively detailed physics of the problem, it does not account for the deflection of the topfoil geometry. Talmage and Carpino [68] proposed a coupled model to illustrate the significance of temperature effects and thermal distortion in the foil structure while using thermal and pressure models that incorporate the outstanding features of a gas-lubricated foil journal bearing. Sim and Kim [69] presented an enhanced version of the THD analysis presented in Ref. [66] by adding analytic thermal contact formulation for the bumps and numerical inlet flow mixing models. The proposed model demonstrates the characteristics of the inlet flow mixing and determines the thermal mixing parameter. The model predictions are also validated by comparing to the experimental test data in Ref. [70]. San Andres and Kim [56] compared 1D and 2D finite element models to estimate the static and dynamic load capacity of foil bearing. The deformation of the topfoil structure is coupled to Reynolds equation through a global stiffness matrix. It is found that predictions in 1D model are closer to the experimental data, but 2D model overestimates the minimum film thickness at the bearing center. Another interesting 3-D THD model presented by Kim et al. [71] in a recent work for a three-pad foil journal bearing and surrounding components including the shaft. The temperature profile of the inlet region is determined through a simple computational fluid dynamics (CFD) model using a commercial software. The dynamic performance of the bearing at elevated temperatures is also measured by using linear perturbation method. They found that due to the softening of the components at high temperature, the stiffness and damping coefficients decrease compared to the values at room temperature. Kim and San Andres [72] used the thermal energy transport model presented in Ref. [63] to simulate the temperature of a CFB at moderately high temperature. The effectiveness of the developed thermal management system is evaluated by comparing the predictions to the experimental measurements. The shaft motions are also investigated to identify the critical speeds at elevated temperatures. According to the measurements, they figured out that the critical speed hardly increases as temperature rises. Lee and Kim [73] presented another 3D THD model for double-acting foil thrust bearings considering cooling effect of the thrust runner disc by the cooling air plenum. Kim et al. [74] compared simulated THD performance of a three-pad CFBs with a single pad circular CFB for different cooling air pressures. Their results indicate that for lightly loaded cases, the three-pad CFBs have lower temperature than single pad bearing. Lee et al. [75] further advanced their 3D THD model to predict transient thermal behavior of three-pad radial air foil bearings. Their model incorporates transient energy equations for gas film and all main bearing components like top foil, bump foils, housing, and shaft and gas film to predict transient evolution of the foil bearing temperature during operation. The predictions yield good agreement with the experimental data. In a more recent study, Paouris et al. [76] proposed a finite element model for a hydrostatic foil bearing to solve coupled incompressible Reynolds equation and foil deformation by using shell elements in an iterative scheme. To better predict the thermal properties, a simple finite element model is developed for the cooling channel in-between bumps. The model does not account for material non-linearities but simulates sagging of the topfoil between the bumps well.

Furthermore, using shell elements to solve for deformation causes shear locking problem that is explained in the following sections.

2 FOIL BEARING STRUCTURE

2.1 Description of Foil Bearing Geometry

Figure 2.1 shows the configuration of a “first generation” bump type CFB. The CFB consists of a thin topfoil and a series of corrugated bump strip supports. The *leading edge* of the thin foil is free, and the foil *trailing edge* is welded to the bearing housing. Beneath the top foil, a bump structure is laid on the inner surface of the bearing. The smooth surface of the top foil is supported by a series of bumps acting as springs, which make the bearing compliant. The bump strip provides a tunable structural stiffness. Damping arises due to material hysteresis and dry-friction between the bumps and topfoil, and between the bumps and the bearing inner surface.

Foil gas bearing technology evolved from rigid gas bearings as a means to overcome physical limitations that resulted from operating a bearing using low viscosity fluids and modest self- generated hydrodynamic fluid film pressures, namely the inability to tolerate misalignment and distortion and a lack of adequate damping and stability. By incorporating thin sheet metal foils in place of rigid bearing surface both compliance and coulomb friction damping capabilities were added to the bearing. The flexibility of the geometry influenced directly by the fluid film pressure gives rise to improved performance and more complexity in terms of bearing modeling. These characteristics were recognized early during the development progress of foil bearings. Despite the challenges that are faced for performance prediction, foil bearings followed a fairly routine experimentally driven development path.

First Generation Bearings

A 1967 gas bearing symposium, held in London, highlighted the concept of using several leafs of foil cantilevered to form a foil bearing [77]. This concept was turned into the first practical foil bearing developed by industry for air cycle machines used for cabin pressurization [78]. With this approach, the limited hydrodynamic gas film pressure was not utilized to overcome foil tension forces found in earlier tape type bearings. Other bending dominated designs based upon small corrugations in underlying bump foils soon followed [79]. These first generation foil bearings are illustrated in Figure 2.1.

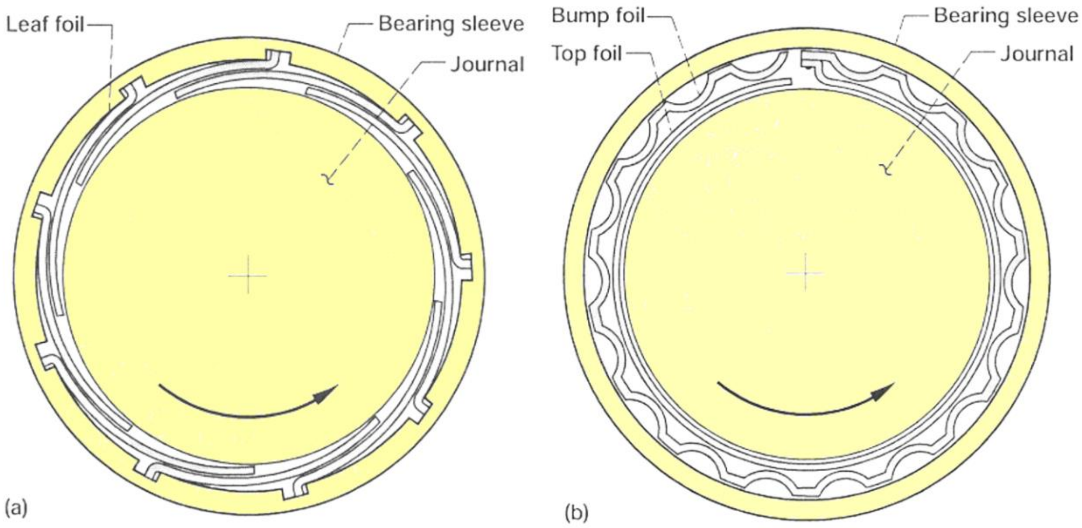

Figure 2.1: First generation compliant foil bearings a) Leaf type foil bearing, b) Bump type foil bearing [80]

Second Generation Bearings

Following the commercialization of first generation bending dominated bump and leaf foil bearings in ACM's, several new designs were developed in which the elastic bearing substructure was tailored to accommodate hydrodynamic phenomena such as edge leakage and environmental conditions like misalignment and gravitational load biases. These second generation foil bearings are shown in Figure 2.2 [81]. Second generation bearings showed double load capacity as compared to that of first generation designs and made possible the development of bearing for more demanding applications such as cryogenic turboexpanders.

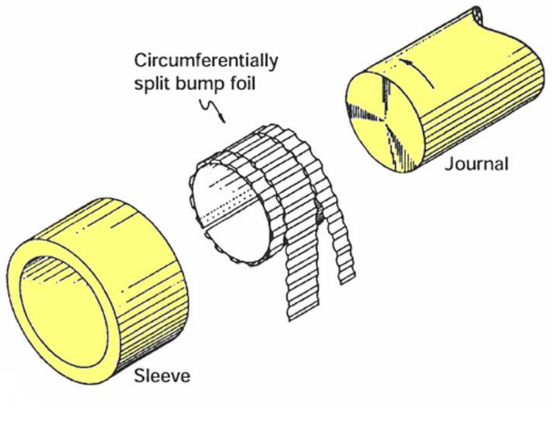

Figure 2.2: Gen II bump-type foil journal bearing [80]

Third Generation Bearings

In the late 1980’s and early 1990’s Heshmat pioneered the development of third generation of foil bearings (Figure 2.3) in which the elastic foundation stiffness was tailored in more than one direction [82]. Employing multiple bump spring layers and circumferentially slit support foils, these Generation III bearings enabled the tuning of the bearing structural stiffness and damping properties. Gen III bearings display improved dynamic properties and load capacities nearly double Gen II designs. Since that time, others have developed alternative approaches to achieve similar structural design freedoms

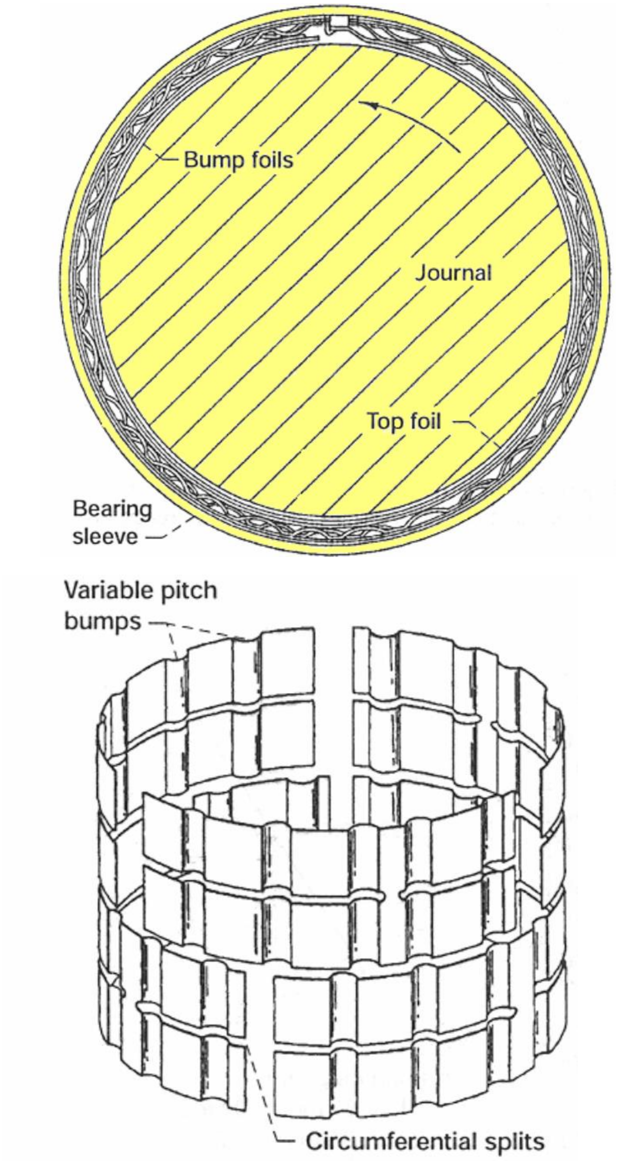

Figure 2.3: Gen III bump-type foil journal bearing [80]

2.1.1 Foil Bearing Geometry used in FEA Model

A bump-type foil journal bearing (Figure 2.4) similar to the design illustrated in Figure 2.1 is used in the presented TEHD analysis. The bearing design parameters are given in Table 2.1. The topfoil consists of a single sheet welded to the sleeve from the trailing edge and the leading edge remains free. It is neither preferred nor necessary to model the full length of the shaft in axial direction which would increase the number of degree of freedoms (DOF) in finite element model drastically. The modeled portion of the free part of the shaft is elongated one-bearing length in both directions as shown in Figure 2.5.

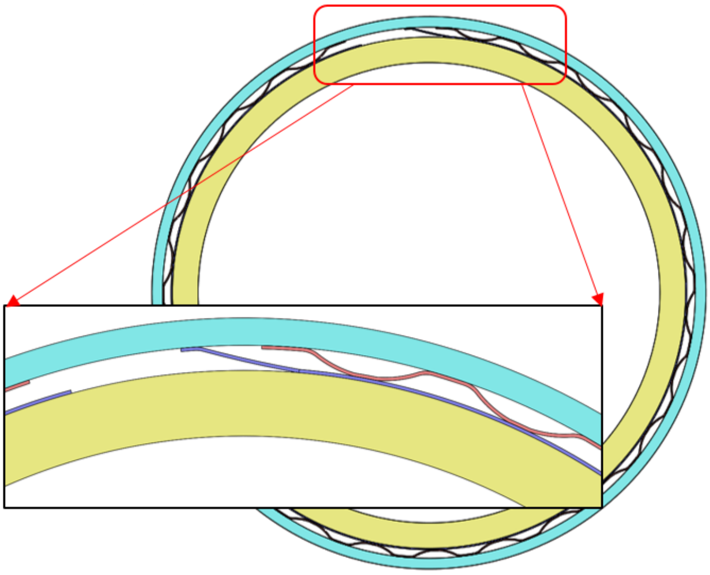

Figure 2.4: Foil bearing assembly and detailed view for bumps and topfoil

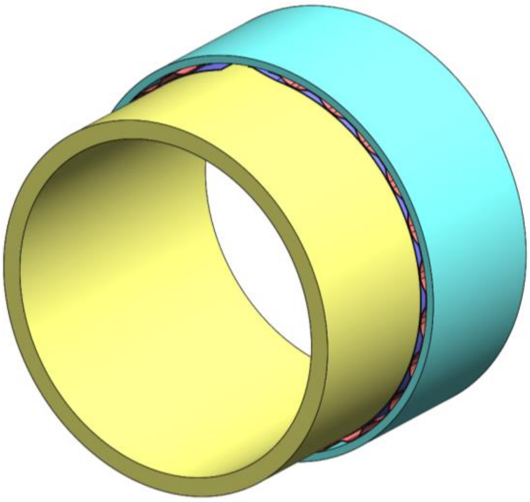

Figure 2.5: Foil bearing and shaft geometry from isometric view (Due to the axial symmetry front half of the system is displayed)

The simple bumpy structure displayed in Figure 2.6 reduces the possibility for the bumps to slide in axial direction due to the irregular hydrodynamic pressure distribution on bearing surface.

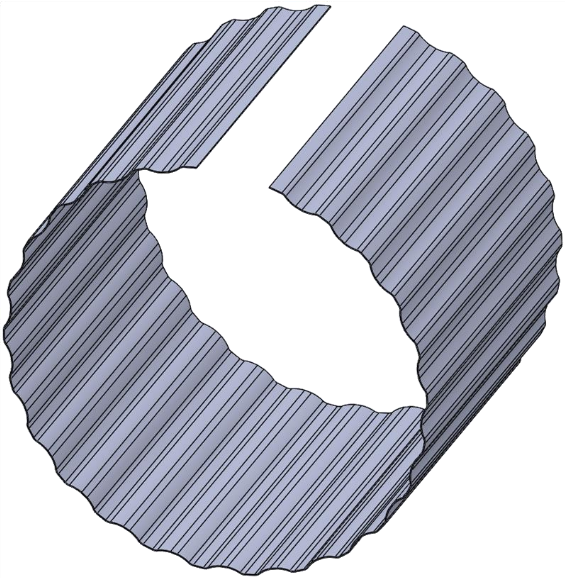

Figure 2.6: Bumpfoil geometry from isometric view

The head section of the bumps are modeled as plain geometry as depicted in Figure 2.7 to reduce the contact pressure and related stress concentration. If the bumps would be modeled fully round as in conventional approach, the contact between the bumps and topfoil would be a line contact which would result in very high stress concentration. This will cause rapid failure of the bumps either due to the low-cycle fatigue during start-stop cycles or high-cycle fatigue because of the vibration and transient motion during operation. Most significantly, it would improve the convergence performance of TEHD model during contact formulations.

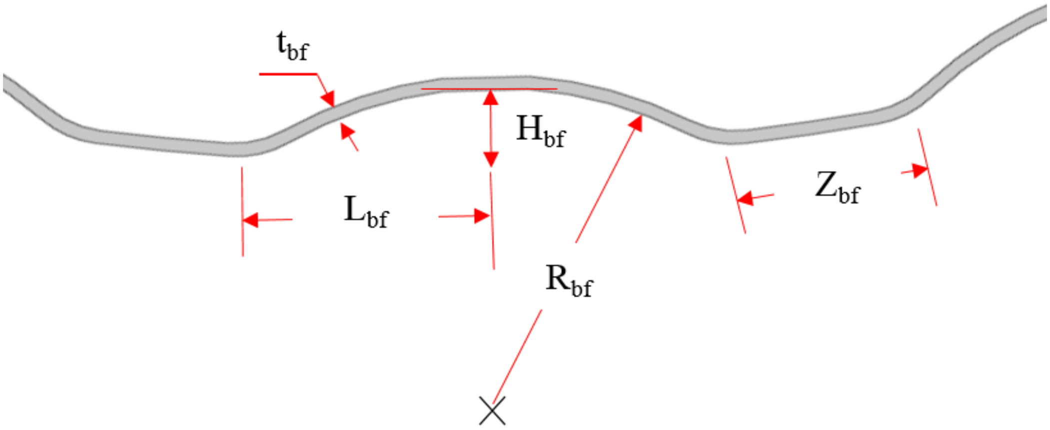

Figure 2.7: Geometry parameters for a single bump

The model includes 24 equally aligned bumps in circumferential direction which corresponds to one bump per 14.16˚. The numbering convention of the bumps is shown in Figure 2.8. The shaft diameter and the bearing length are determined according to the experimental work published by Radil and Zeszotek [59] to benchmark the predictions in TEHD model to the measurements in that study. However, they did not give details for the foil material or bump geometry. The remaining bearing parameters are obtained from the study of San Andres and Kim [63] in which they present this information according to the assumptions based on industry experience. The sleeve outer diameter is defined arbitrarily because it would not affect the solution considerably.

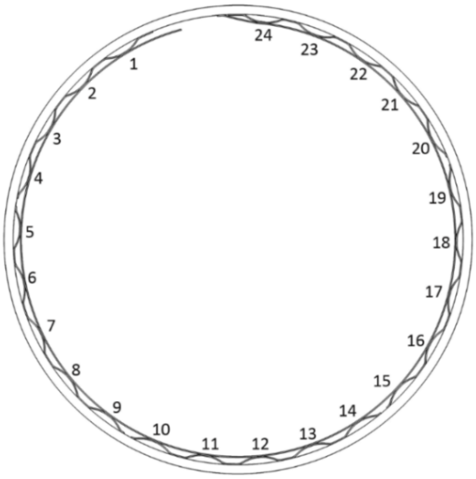

Figure 2.8: Bump numbering convention for the CFB model

CFB Parameters	**SI Units**
Number of bumps	24
Bearing inner diameter, D	50 mm
Bearing axial Length, L	41 mm
Nominal clearance, c	20 µm
Bump foil plain segment, Z_{bf}	1.8082 mm
Bump length, L_{bf}	2.5 mm
Bump foil thickness, t_{bf}	127 µm
Bump height, H_{bf}	0.70 mm
Bump pitch, $S_{bf}=2L_{bf}+Z_{bf}$	6.30 mm
Bearing angle covered by bumps	340˚
Shaft inner diameter, D_{s-i}	45 mm
Shaft outer diameter, $D_{s-o}=D-2c$	49.96 mm
Shaft axial length, L_s	82 mm
Sleeve inner diameter, D_{sl-i}	51.91 mm
Sleeve outer diameter, D_{sl-o}	54 mm

Table 2.1: Foil bearing model parameter list

2.2 Material Properties

The commonly used material for corrugated sheet metal and smooth foil is a special nickel-chromium alloy called INCONEL® X-750 due to its superior spring properties at elevated temperatures. It is a precipitation-hardenable alloy used for its resistance against corrosion and oxidation, and high strength up to temperatures over 700˚C. Alloy X-750 has satisfactory properties down to cryogenic temperatures. The chemical composition of this alloy is given in the Table 2.2.

Nickel (plus Cobalt)	70.00 min.
Chromium	14.0-17.0
Iron	5.0-9.0
Titanium	2.25-2.75
Aluminum	0.40-1.00
Niobium (plus Tantalum)	0.70-1.20
Manganese	1.00 max.
Silicon	0.50 max.
Sulfur	0.01 max
Copper	0.50 max.
Carbon	0.08 max.
Cobalt	1.00 max.

Table 2.2: Chemical Composition, % for Inconel® X750 [83]

Thermal properties including thermal expansion coefficient and thermal conductivity are provided by Special Metals Co. [83]. Effect of temperature on modulus of elasticity, poisson ratio and tensile strength are given in Appendix A. The material properties are defined as piece-wise interpolation polynomials with respect to the temperature to include the effect of temperature.

Inconel® 718 is selected as journal and sleeve material due to common experience and its satisfactory strength at elevated temperatures. Temperature dependent data for the thermal properties like thermal conductivity and thermal expansion coefficient, and the structural properties such as modulus of elasticity and poisson ratio for this material [84] are detailed in Appendix A.

The lubricant used in this work is air. For a perfect ideal gas, physical properties follow a relationship known as the ideal gas law:

$$PV = nR_{gc}T \tag{2.1}$$

where V is the volume occupied by n kg mol of a gas at the absolute temperature, T in Kelvin and R_{gc} is the universal gas constant, $R_{gc}=8.3143\ kJ/(mol.K)$.

The dynamic viscosity is one the most significant material property that designates the flow profile in the wedging film. The viscosity of a fluid is dominated by the combined effect of intermolecular forces and momentum transfer between molecules.

The viscous properties of a liquid primarily governed by intermolecular forces whereas the momentum transfer is more effective in gases. Increasing temperature causes a decline in dynamic viscosity in liquids since it weakens intermolecular forces. On the other hand, as temperature increases, momentum transfer between gas molecules increases due to increased number of molecular collisions. Therefore, the dynamic viscosity of gases increases with temperature, which allows higher load capacity at elevated operation temperatures. There are several emprical relations to estimate the viscosity of gases with respect to the temperature.

2.3 Finite Element Grid Generation

The mesh resolution and mesh element quality are significant measures to verify the quality of a finite element model. Low mesh resolution or improper element formulation are the main sources of inaccurate results and convergence problems in FEA studies. Generating a well-organized mesh is very critical to obtain valuable output and accurate predictions. Before going into analysis directly, the element quality should be checked in terms of distortion (warpage), aspect ratio, minimum and maximum allowable angles, skewness and the Jacobian number.

2.3.1 Shear Locking

One of the critical problems that may cause underprediction of foil deformation is shear locking which is a problem with all fully integrated first order solid elements [86]. Shear locking causes the elements to behave too stiff in bending. Consider a small piece of material in a structure subjected to pure bending. The material will distort as illustrated in Figure 2.9.

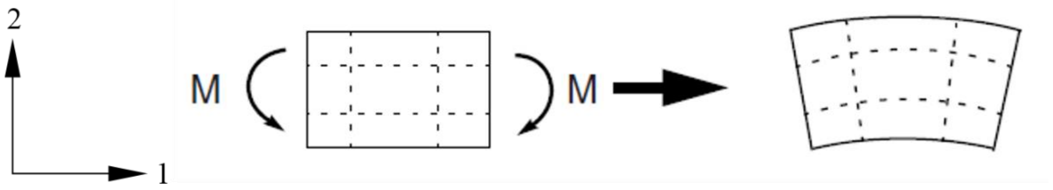

Figure 2.9: Deformation of material subjected to bending moment *M* [86]

Figure 2.10: The deformation of a linear element subjected to bending moment *M* [86].

The lines that are initially parallel to the horizontal axis will take a constant curvature, and the lines through the thickness of the material remain straight. The angle between the horizontal and vertical lines remains at 90˚. However, the edges of a linear element cannot curve, hence, if the small piece of material is modeled by using a single linear element, edges of the deformed shape will be a straight as shown in Figure 2.10.

The dotted lines are representing the integration points over the element. The upper line has increased length, indicating that the direct stress in the direction 1, σ_{11}, is tensile. On the other hand, the length of the lower dotted line is decreased indicating that σ_{11} is compressive. Assuming displacements are very small, direct stress in direction 2 is zero at all integration points. These are expected results for a small material subjected to pure bending. However, the angle between the vertical and horizontal lines, which was 90˚, has changed. This shift indicates that the shear stress, σ_{12}, at these points is not zero. This additional stress appears due to inability of element edges to curve. It also means that strain energy is generated in the element under bending deformation such that the overall deflections will be less than actual case.

Shear locking merely affects the linear elements, and for the quadratic elements it is not a problem since their edges are able to curve when bending moment is applied as shown in Figure 2.11. However, even quadratic elements will exhibit some locking if they are distorted too much or if the applied bending stress has a gradient. Thus, the generated mesh must be free of distorted elements and the order of the elements should be at least second order [86].

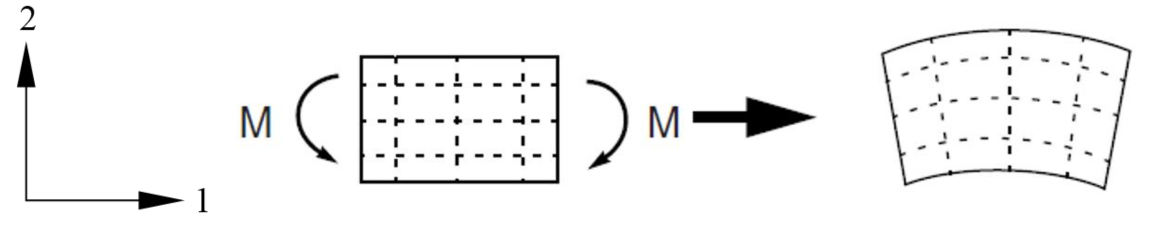

Figure 2.11: Deformation of a quadratic element subjected to bending moment *M* [86].

2.3.2 Mesh Dependency Study

The effect of grid resolution on model accuracy is investigated in this section. The model is run with isothermal conditions. The shaft speed is 30 krpm and the radial static load is 60 N for all cases. The properties of the selected mesh structures are given in Table 2.3. The detailed view of the meshes are illustrated in Figure 2.12.

Mesh Number	Mesh 1	Mesh 2	Mesh 3	Mesh 4
Number of elements	14,900	28,800	41,086	60,640
Total number of DOF	610,303	966,631	1,671,593	2,447,586

Table 2.3: Statistics for the meshes used in the mesh dependency analysis

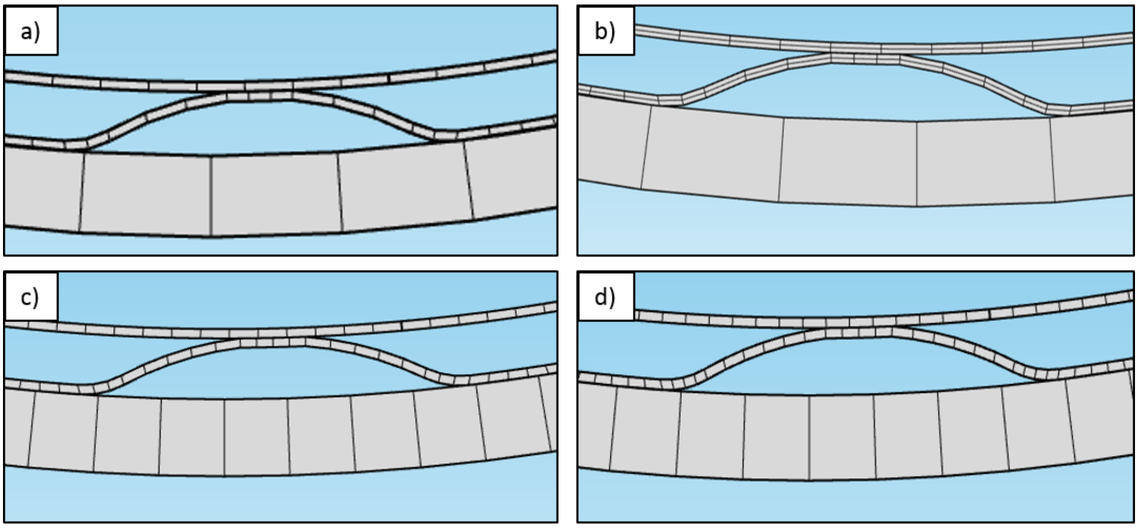

Figure 2.12: Grid structure for a) Mesh 1 b) Mesh 2 c) Mesh 3 d) Mesh 4

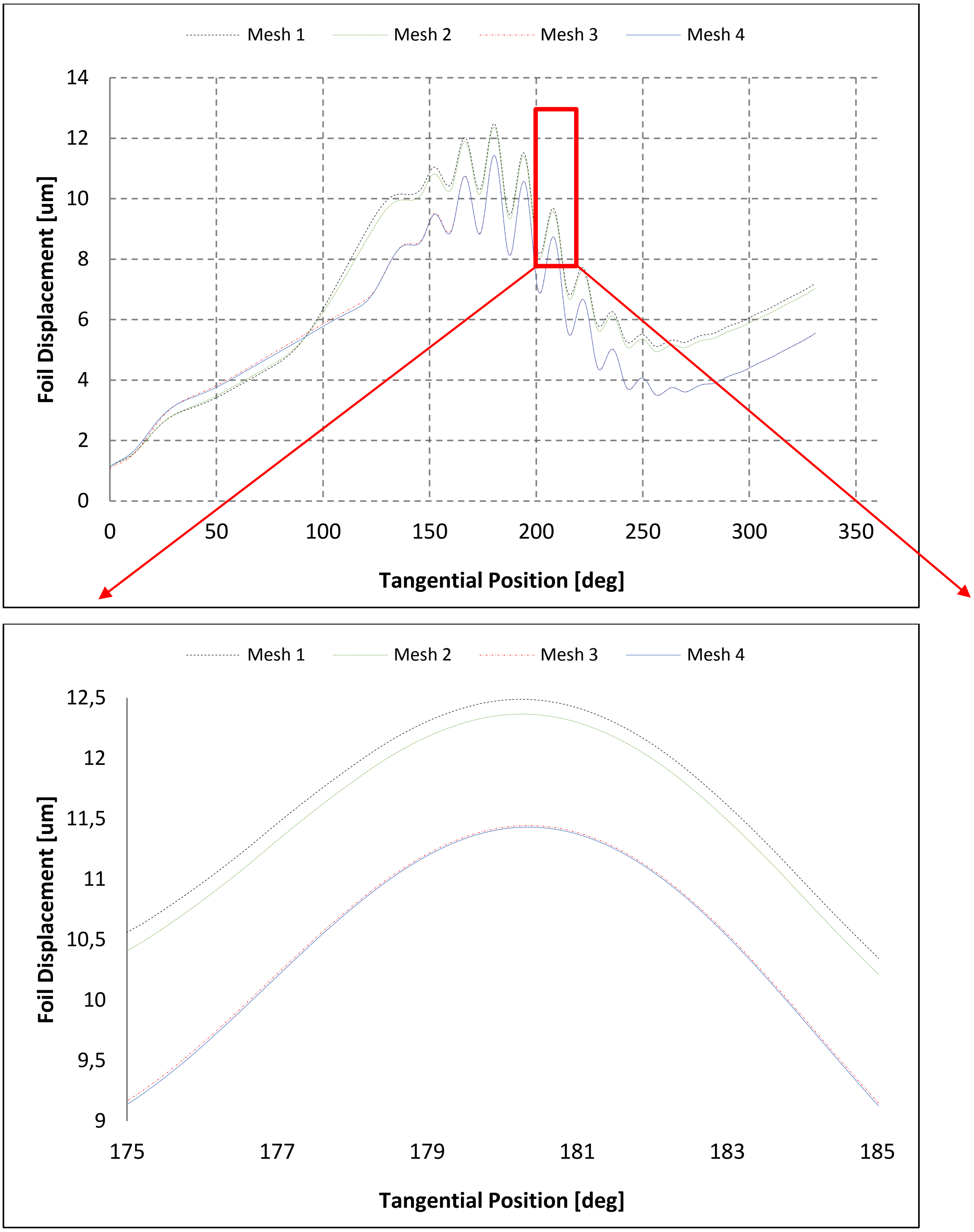

Figure 2.13: Topfoil deformation for different meshes

The deformation of the topfoil with different mesh structure is investigated to observe the dependency of the analysis to the mesh resolution. As seen in Figure 2.13, the deformation profile is changing slightly as the mesh resolution changes. However, the change becomes negligible after some point. Hence, it is decided that the mesh resolution is sufficient to capture the physics of the problem accurately.

Element type	2nd Order Hexahedral elements
Number of elements	66,586
Average element quality	0.3741
Total number of DOF	1,866,904
Number of DOF for film pressure	53,202
Number of DOF for displacement field	1,671,453
Number of DOF for temperature	133,608
Number of DOF for contact pressure	8,640

Table 2.4: Detailed mesh parameters for selected mesh structure

The detailed information for the selected mesh structure is listed in Table 2.4. Selected mesh structure is given in Figure 2.14. The critical regions are meshed finer to capture the physics of the problem more accurately. The high quality mesh grid at contact surfaces which are the most critical regions due to higher momentum and heat flux are shown in Figure 2.15. This figure demonstrates the quality index of the elements estimated according to the several quantities including aspect ratio, element Jacobian, distortion, skewness and orthogonality. The low quality elements are avoided in this model to improve convergence performance and accuracy of the results.

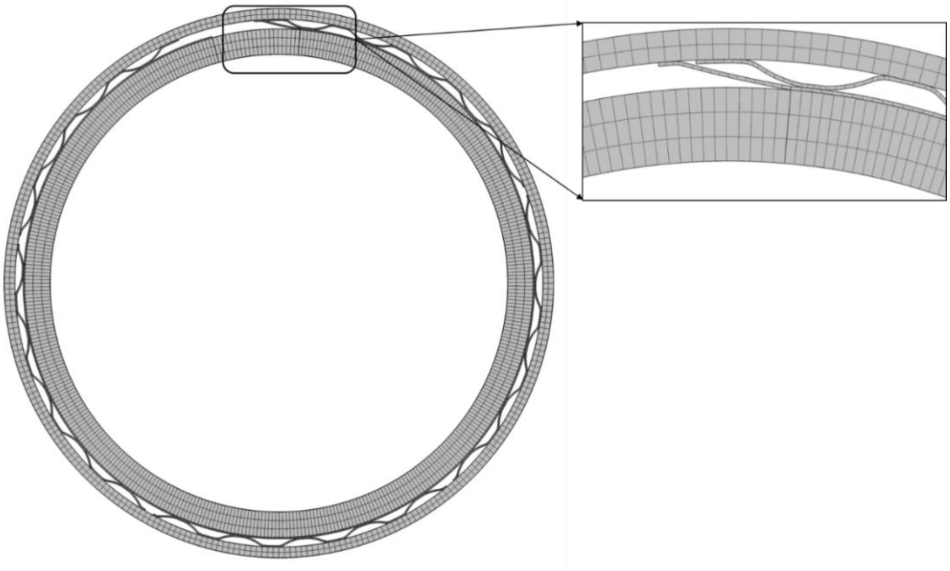

Figure 2.14: The mesh generated for foil bearing model. The elements are second-order hexagonal mesh

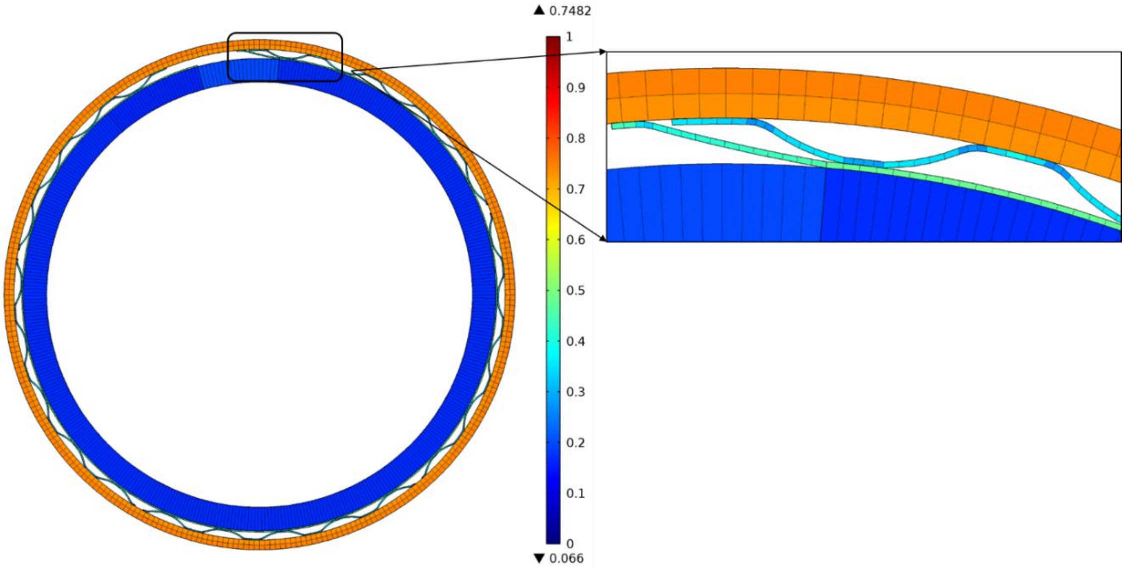

Figure 2.15: The quality index of the mesh is a useful measure the appropriateness of the mesh for the analysis

3 THEORETICAL BACKGROUND

This chapter discusses theoretical fundamentals of foil bearing TEHD model. The aim here is to apply this knowledge to develop a physically realistic and computationally robust solution algorithm. For this purpose, we will cover all governing equations step-by-step to build a suitable format to be used in the developed algorithm. The three basic governing laws; the conservation of mass, momentum, and energy are discussed in detail to deduce useful forms for parameters including flow velocity, pressure, temperature, load and deformation. Formal derivations of these equations from the very basics of thermodynamic laws will not be repeated here. In addition to conservation laws, theoretical background for structural deformation, contact algorithms and thermal contact behavior are also explained in separate sections, for the sake of completeness. Finally, a new 4-point finite difference approximation is proposed to improve the convergence performance of the solver. Non-dimensionalization techniques to normalize the Reynolds' and energy equations are given in related sections. Order of magnitude analysis to determine the relatively significant terms is carried out to simplify the equations.

3.1 Derivation of 4-point Finite Difference Approximation

The aim of the finite difference method is essentially to approximate solutions to differential equations by replacing the derivatives in the differential equations with finite difference approximations. This formulation gives large but finite algebraic systems of equations that can be solved via a specially written code [87]. We want to derive a two-sided finite difference approximation to $z(\bar{x})$ based on some given set of points in the neighborhood. Taylor series can be used to find an appropriate formulation by means of the method of undetermined coefficients. To improve the accuracy and easy convergence, unsymmetric backward-skewed 4-point approximation is used. Taylor series expansion is as follows,

$$
\begin{aligned}
z(\bar{x}+\delta) &= z(\bar{x}) + \delta z'(\bar{x}) + \frac{1}{2}\delta^2 z''(\bar{x}) + \frac{1}{6}\delta^3 z'''(\bar{x}) + O(\delta^4) \\
z(\bar{x}-\delta) &= z(\bar{x}) - \delta z'(\bar{x}) + \frac{1}{2}\delta^2 z''(\bar{x}) - \frac{1}{6}\delta^3 z(\bar{x}) + O(\delta^4) \\
z(\bar{x}-2\delta) &= z(\bar{x}) - 2\delta z'(\bar{x}) + \frac{1}{2}(2\delta)^2 z''(\bar{x}) - \frac{1}{6}(2\delta)^3 z'''(\bar{x}) + O(\delta^4)
\end{aligned}
\tag{3.2}
$$

For $z'(\bar{x})$ approximation function can be defined as,

$$
z'(\bar{x}) = m_1 z(\bar{x}) + m_2 z(\bar{x}-\delta) + m_3 z(\bar{x}+\delta) + m_4 z(\bar{x}-2\delta)
\tag{3.3}
$$

By using the expanded terms, the function becomes:

$$
\begin{aligned}
z'(\bar{x}) = (m_1+m_2+m_3+m_4)z(\bar{x}) &+ (-m_2+m_3-2m_4)\delta z'(\bar{x}) \\
&+ \frac{(m_2+m_3+4m_4)}{2}\delta^2 z''(\bar{x}) \\
&+ \frac{(m_2-m_3-8m_4)}{6}\delta^3 z'''(\bar{x})
\end{aligned}
\tag{3.4}
$$

where $m_1, m_2, m_3\ and\ m_4$ are coefficients. The coefficients of each term for a first order derivative will form following equation system:

$$
\begin{aligned}
(m_1+m_2+m_3+m_4) &= 0 \\
(-m_2+m_3-2m_4) &= {}^{1}/_{\delta} \\
\frac{(m_2+m_3+4m_4)}{2} &= 0 \\
\frac{(m_2-m_3-8m_4)}{6} &= 0
\end{aligned}
\tag{3.5}
$$

By using matrix algebra, the equation system can be solved easily. The approximation for a first order derivative with unsymmetric backward-skewed 4-point approximation becomes;

$$
z'(\bar{x}) = \frac{z(\bar{x})}{2\delta} - \frac{z(\bar{x}-\delta)}{\delta} + \frac{z(\bar{x}+\delta)}{3\delta} + \frac{z(\bar{x}-2\delta)}{6\delta}
\tag{3.6}
$$

The approximation for partial derivatives of temperature can be expressed as;

$$
\begin{aligned}
\frac{\partial T}{\partial x} &= \frac{T_{i,j}}{2\Delta x} - \frac{T_{i-1,j}}{\Delta x} + \frac{T_{i+1,j}}{3\Delta x} + \frac{T_{i-2,j}}{6\Delta x} \\
\frac{\partial T}{\partial y} &= \frac{T_{i,j}}{2\Delta y} - \frac{T_{i,j-1}}{\Delta y} + \frac{T_{i,j+1}}{3\Delta y} + \frac{T_{i,j-2}}{6\Delta y}
\end{aligned}
\tag{3.7}
$$

Similar approach is used to calculate the approximation for second-order derivatives. The equation system for this case becomes;

$$\begin{gathered}(m_1 + m_2 + m_3 + m_4) = 0 \\ (-m_2 + m_3 - 2m_4) = 0 \\ \frac{(m_2 + m_3 + 4m_4)}{2} = {}^{1}\!/_{\delta^2} \\ \frac{(m_2 - m_3 - 8m_4)}{6} = 0\end{gathered} \tag{3.8}$$

The approximation with 4-points is identical to a central difference approach as,

$$z''(\bar{x}) = \frac{z(\bar{x} + \delta) - 2z(\bar{x}) + z(\bar{x} - \delta)}{\delta^2} \tag{3.9}$$

Second-order partial derivatives for temperature are expressed as in the following form,

$$\begin{gathered}\frac{\partial^2 T}{\partial x^2} = \frac{T_{i+1,j} - 2T_{i,j} + T_{i-1,j}}{\Delta x^2} \\ \frac{\partial^2 T}{\partial y^2} = \frac{T_{i,j+1} - 2T_{i,j} + T_{i,j-1}}{\Delta y^2}\end{gathered} \tag{3.10}$$

Partial derivatives in the governing conservation equations are replaced by these approximations as presented in the coming sections to make the equation systems appropriate for a computational solution.

3.2 Derivation of Reynolds Equation for Hydrodynamic Pressure Estimation

The derivation of the classical Reynolds equation based on the work of Osborne Reynolds [88] is discussed in this section. It provides an insight into fluid behavior in bearing lubricant films. If this equation is solved appropriately, one can find pressure distribution in a bearing with an arbitrary film shape [89]. Once the pressure profile is obtained, all remaining bearing performance parameters including load capacity, friction force, flow rates etc. can be estimated. Throughout this analysis, it is assumed that the fluid is a Newtonian type, the flow is laminar and steady, and variation of the pressure and temperature across the film is negligible. Furthermore, the inertia and body force terms are also assumed to be negligible. Due to physics of the thin film geometry, all these assumptions are considered proper and commonly used in lubrication problems. The governing equations for conservation of mass (continuity) and conservation of momentum (Navier-Stokes (NS) equation) for a domain as in Figure 3.1 are given respectively as:

$$\frac{\partial \rho}{\partial t} + \nabla.(\rho V) = 0 \tag{3.11}$$

$$\rho \frac{DV}{Dt} = F_B - \nabla P + \nabla.\tau_{ij} \tag{3.12}$$

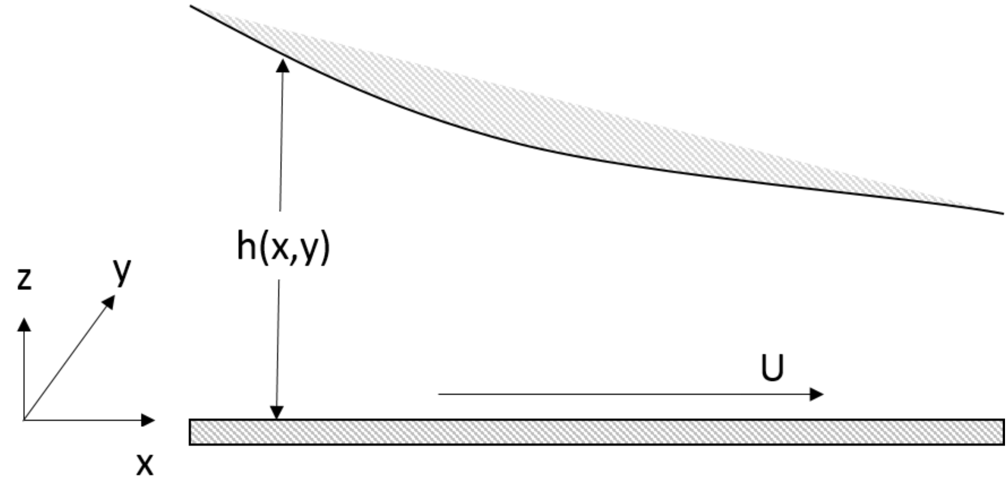

Figure 3.1: Coordinate system for the converging film between stationary bearing surface and rotating shaft surface

In Cartesian coordinates, conservation of momentum equations for 3D takes the following form corresponding to the *x*, *y*, and *z* directions, respectively:

x-Momentum

$$\rho\left(\frac{\partial u}{\partial t} + u\frac{\partial u}{\partial x} + v\frac{\partial u}{\partial y} + w\frac{\partial u}{\partial z}\right) = \left(\frac{\partial}{\partial x}\tau_{xx} + \frac{\partial}{\partial y}\tau_{yx} + \frac{\partial}{\partial z}\tau_{zx}\right) - \frac{\partial P}{\partial x} + F_{Bx} \tag{3.13}$$

y-Momentum

$$\rho\left(\frac{\partial v}{\partial t} + u\frac{\partial v}{\partial x} + v\frac{\partial v}{\partial y} + w\frac{\partial v}{\partial z}\right) = \left(\frac{\partial}{\partial x}\tau_{xy} + \frac{\partial}{\partial y}\tau_{yy} + \frac{\partial}{\partial z}\tau_{zy}\right) - \frac{\partial P}{\partial y} + F_{By} \tag{3.14}$$

z-Momentum

$$\rho\left(\frac{\partial w}{\partial t}+u\frac{\partial w}{\partial x}+v\frac{\partial w}{\partial y}+w\frac{\partial w}{\partial z}\right)=\left(\frac{\partial}{\partial x}\tau_{xz}+\frac{\partial}{\partial y}\tau_{yz}+\frac{\partial}{\partial z}\tau_{zz}\right)-\frac{\partial P}{\partial z}+F_{Bz} \qquad (3.15)$$

The relationship between the shear stress and strain rate for a Newtonian fluid is given as

$$\tau=\mu\dot{\gamma} \qquad (3.16)$$

where μ is the fluid viscosity and strain rate tensor is defined by following relation,

$$\dot{\boldsymbol{\gamma}}=\nabla\cup+(\nabla\cup)^{T} \qquad (3.17)$$

where τ, $\dot{\boldsymbol{\gamma}}$, $\nabla\cup$, $(\nabla\cup)^{T}$ are shear stress tensor, strain rate tensor, deformation rate tensor and transpose of deformation rate tensor, respectively. The deformation and shear stress tensors can be expressed in matrix form in Cartesian coordinates as follows,

$$\nabla\cup=\begin{bmatrix}\frac{\partial u}{\partial x} & \frac{\partial v}{\partial x} & \frac{\partial w}{\partial x}\\ \frac{\partial u}{\partial y} & \frac{\partial v}{\partial y} & \frac{\partial w}{\partial y}\\ \frac{\partial u}{\partial z} & \frac{\partial v}{\partial z} & \frac{\partial w}{\partial z}\end{bmatrix} \qquad (3.18)$$

$$\tau=\begin{bmatrix}\tau_{xx} & \tau_{xy} & \tau_{xz}\\ \tau_{yx} & \tau_{yy} & \tau_{yz}\\ \tau_{zx} & \tau_{zy} & \tau_{zz}\end{bmatrix} \qquad (3.19)$$

Normal stress components are,

$$\tau_{xx}=\sigma_{xx}=2\mu\frac{\partial u}{\partial x};\ \ \tau_{yy}=\sigma_{yy}=2\mu\frac{\partial v}{\partial y};\ \ \tau_{zz}=\sigma_{zz}=2\mu\frac{\partial w}{\partial z} \qquad (3.20)$$

Shear stress components are,

$$\begin{aligned}\tau_{xy}&=\tau_{yx}=\mu\left(\frac{\partial u}{\partial y}+\frac{\partial v}{\partial x}\right);\\ \tau_{xz}&=\tau_{zx}=\mu\left(\frac{\partial u}{\partial z}+\frac{\partial w}{\partial x}\right);\end{aligned} \qquad (3.21)$$

$$\tau_{yz} = \tau_{zy} = \mu\left(\frac{\partial w}{\partial y} + \frac{\partial v}{\partial z}\right);$$

Applying the stress components to Navier-Stokes, equations take following form,

$$\rho\left(\frac{\partial u}{\partial t} + u\frac{\partial u}{\partial x} + v\frac{\partial u}{\partial y} + w\frac{\partial u}{\partial z}\right) = \mu\left(\frac{\partial^2 u}{\partial x^2} + \frac{\partial^2 u}{\partial y^2} + \frac{\partial^2 u}{\partial z^2}\right) - \frac{\partial P}{\partial x} + F_{Bx}$$

$$\rho\left(\frac{\partial v}{\partial t} + u\frac{\partial v}{\partial x} + v\frac{\partial v}{\partial y} + w\frac{\partial v}{\partial z}\right) = \mu\left(\frac{\partial^2 v}{\partial x^2} + \frac{\partial^2 v}{\partial y^2} + \frac{\partial^2 v}{\partial z^2}\right) - \frac{\partial P}{\partial y} + F_{By} \tag{3.22}$$

$$\rho\left(\frac{\partial w}{\partial t} + u\frac{\partial w}{\partial x} + v\frac{\partial w}{\partial y} + w\frac{\partial w}{\partial z}\right) = \mu\left(\frac{\partial^2 w}{\partial x^2} + \frac{\partial^2 w}{\partial y^2} + \frac{\partial^2 w}{\partial z^2}\right) - \frac{\partial P}{\partial z} + F_{Bz}$$

3.2.1 Order of Magnitude Analysis

To simplify the equations and to eliminate the terms that are relatively not significant, an order of magnitude analysis is conveyed. The change of the velocity terms over film thickness in z-direction is much more dramatic compared to the remaining directions as shown in the following comparison:

$$\frac{\partial^2}{\partial x^2} \sim \frac{1}{D^2}, \frac{\partial^2}{\partial y^2} \sim \frac{1}{L^2} \ll \frac{\partial^2}{\partial z^2} \sim \frac{1}{h^2}$$

$$\Longrightarrow \frac{\partial^2 u}{\partial z^2} \;\&\; \frac{\partial^2 v}{\partial z^2} \gg other\ velocity\ components \tag{3.23}$$

Since the film thickness is very small compared to other dimensions, the pressure almost does not change over film thickness:

$$\frac{\partial P}{\partial z} \ll \frac{\partial P}{\partial x} \& \frac{\partial P}{\partial y} \tag{3.24}$$

The system is assumed to be in steady-state such that:

$$\frac{\partial u}{\partial t} = \frac{\partial v}{\partial t} = \frac{\partial w}{\partial t} = 0 \tag{3.25}$$

The flow in film thickness direction is immaterial, and thus, *w=0*. The NS equations take the following simpler form:

$$\rho\left(u\frac{\partial u}{\partial x}+v\frac{\partial u}{\partial y}\right)=\mu\left(\frac{\partial^2 u}{\partial z^2}\right)-\frac{\partial P}{\partial x}$$
$$\rho\left(u\frac{\partial v}{\partial x}+v\frac{\partial v}{\partial y}\right)=\mu\left(\frac{\partial^2 v}{\partial z^2}\right)-\frac{\partial P}{\partial y} \tag{3.26}$$

Let us compare inertial terms with viscous terms,

$$\frac{\rho\left(u\frac{\partial u}{\partial x}\right)}{\mu\left(\frac{\partial^2 u}{\partial z^2}\right)}\sim\frac{\rho U.{}^{U}/_{D}}{\mu\left({}^{U}/_{c^2}\right)}=\frac{\rho U}{\mu}\left(\frac{c^2}{D}\right)=\frac{\rho UD}{\mu}\left(\frac{c}{D}\right)^2 \tag{3.27}$$

For a typical case we work on,

$$D=0.05m,\qquad \frac{c}{D}\cong 16x10^{-8},\qquad U\approx 50\frac{m}{s},\qquad \rho=1.2\frac{kg}{m^3},$$
$$\mu=2x10^{-5}Pa.s$$

$$\frac{\rho UD}{\mu}\left(\frac{c}{D}\right)^2=\frac{1.2(kg/m^3)x50(m/s)x0.05m}{2x10^{-5}(N/m^2)s}16x10^{-8}\cong 0.024 \tag{3.28}$$

Therefore, we can conclude that viscous terms are more dominant than inertial terms in this study. Contribution of gravitational force is,

$$F_{By}=\rho g \tag{3.29}$$

When inertia forces are compared to gravitational force, dimensionless Froude Number, *Fr* becomes as,

$$\frac{\rho\left(u\frac{\partial u}{\partial x}\right)}{\rho g}\sim\frac{\rho U.{}^{U}/_{\pi D}}{\rho g}=\frac{U^2}{\pi Dg}=Fr\cong\frac{(50)^2}{3.14x0.05x9.81}\approx 162 \tag{3.30}$$

Apparently, body forces due to gravity are also negligible compared to inertial forces. Comparison of the pressure terms with respect to the inertial forces gives dimensionless Euler Number, *Eu*,

$$\frac{\partial P/\partial x}{\rho\left(u\frac{\partial u}{\partial x}\right)}\sim\frac{P_a/\pi D}{\rho U.{}^{U}/_{\pi D}}=\frac{P_a}{\rho U^2}=Eu\cong\frac{\frac{1x10^5N}{m^2}}{1.2x(50)^2}=33.33 \tag{3.31}$$

This implies that contribution of the pressure forces is much greater than inertial forces and must be considered in conjunction with viscous forces as shown in the following comparison of pressure and viscous forces;

$$\frac{\mu\left(\frac{\partial^2 u}{\partial z^2}\right)}{\partial P/\partial x} = \frac{\mu\left({}^{U}/_{c^2}\right)}{P_a/\pi D} = \frac{\mu U \pi D}{P_a c^2} = \Lambda_B \cong \frac{2x10^{-5}x50x3.14x0.05}{1x10^5 x(2x10^{-5})^2} \approx 1.96 \tag{3.32}$$

The non-dimensional term, Λ_B here is the bearing compressibility number and commonly used in bearing analysis as a performance criteria. The comparison reveals that pressure and viscous forces are both significant in a typical hydrodynamic bearing problem. By using the relations above, NS equations take the following simpler form,

$$\begin{gathered} 0 = \mu\left(\frac{\partial^2 u}{\partial z^2}\right) - \frac{\partial P}{\partial x} \\ 0 = \mu\left(\frac{\partial^2 v}{\partial z^2}\right) - \frac{\partial P}{\partial y} \end{gathered} \tag{3.33}$$

Assuming no-slip wall boundary condition, laminar flow profile and $\mu \neq \mu(z)$, boundary conditions for NS equations can be defined as

$$\begin{gathered} u = U \ @\ z = 0 \\ u = 0 \ @\ z = h(x,y) \\ v = 0 \ @\ z = 0 \\ v = 0 \ @\ z = h(x,y) \end{gathered} \tag{3.34}$$

To solve for fluid velocities *u* and *v*, the equations from 0 to h(x,y) is integrated in z-direction and velocity profiles become as,

$$\begin{gathered} u = \frac{1}{2\mu}\frac{\partial P}{\partial x} z^2 + C_1 z + C_2 \\ v = \frac{1}{2\mu}\frac{\partial P}{\partial y} z^2 + C_3 z + C_4 \end{gathered} \tag{3.35}$$

Applying boundary conditions specified above,

$$\begin{gathered} u = \frac{1}{2\mu}\frac{\partial P}{\partial x}(z^2 - zh) + U\left(1 - \frac{z}{h}\right) \\ v = \frac{1}{2\mu}\frac{\partial P}{\partial y}(z^2 - zh) \end{gathered} \tag{3.36}$$

The first terms on the right hand side of the equations are Poiseuille flow terms indicating the effect of pressure on velocity. The second term of u shows the Couette flow effect because of the relative surface velocity difference between shaft and bearing surfaces.

Now, we can plug the resulting equations into the continuity equation. In the Cartesian coordinate system, the continuity equation takes the following form,

$$\cancelto{}{\frac{\partial \rho}{\partial t}} + \frac{\partial(\rho u)}{\partial x} + \frac{\partial(\rho v)}{\partial y} + \cancelto{}{\frac{\partial(\rho w)}{\partial z}} = 0 \tag{3.37}$$

Integration of continuity equation with respect to z yields,

$$\frac{\partial}{\partial x}\left(\frac{\rho h^3}{\mu}\frac{\partial P}{\partial x}\right) + \frac{\partial}{\partial y}\left(\frac{\rho h^3}{\mu}\frac{\partial P}{\partial y}\right) = 6U\frac{\partial(\rho h)}{\partial x} \tag{3.38}$$

For the ideal gas property of air, incompressible steady state Reynolds Equation gets the following form,

$$\frac{\partial}{\partial x}\left(\frac{Ph^3}{\mu T}\frac{\partial P}{\partial x}\right) + \frac{\partial}{\partial y}\left(\frac{Ph^3}{\mu T}\frac{\partial P}{\partial y}\right) = 6U\frac{\partial}{\partial x}\left(\frac{Ph}{T}\right) \tag{3.39}$$

By using the relations below, Reynolds equation can be defined in a different more useful form for this problem,

$$\frac{\partial P^2}{\partial x} = 2P\frac{\partial P}{\partial x}, \qquad \frac{\partial P^2}{\partial y} = 2P\frac{\partial P}{\partial y} \tag{3.40}$$

$$\frac{1}{2}\frac{\partial}{\partial x}\left(\frac{h^3}{\mu T}\frac{\partial P^2}{\partial x}\right) + \frac{1}{2}\frac{\partial}{\partial y}\left(\frac{h^3}{\mu T}\frac{\partial P^2}{\partial y}\right) = 6U\frac{\partial}{\partial x}\left(\frac{Ph}{T}\right) \tag{3.41}$$

3.2.2 Non-dimensionalization Process for Reynolds Equation

In engineering analysis, normalizing the terms in governing equations provides an insight to the behavior of the problem. To non-dimensionalize the Reynolds equation following relations are applied,

$$\begin{gathered}\bar{x} = \frac{x}{\pi D}, \qquad \bar{y} = \frac{y}{L}, \qquad \bar{u} = \frac{u}{U}, \qquad \bar{T} = \frac{T}{T_a}, \qquad \overline{T_x} = \frac{\overline{\Delta T}}{\overline{\Delta x}} = T_x\frac{\pi D}{T_a}, \\ \overline{T_y} = \frac{\overline{\Delta T}}{\overline{\Delta y}} = T_x\frac{L}{T_a}, \qquad \bar{\mu} = \frac{\mu}{\mu_i}, \qquad \bar{P} = \frac{P}{P_a}, \qquad \overline{P_x} = \frac{\overline{\Delta P}}{\overline{\Delta x}} = P_x\frac{\pi D}{P_a},\end{gathered} \tag{3.42}$$

$$\bar{P}_y = \frac{\overline{\Delta P}}{\overline{\Delta y}} = P_y \frac{L}{P_a}, \qquad \bar{h} = \frac{h}{c}$$

After inserting non-dimensional terms, Reynolds Equation becomes

$$\Rightarrow \frac{1}{2} \frac{\partial}{\partial \bar{x} \pi D} \left(\frac{\bar{h}^3 c^3}{\mu \bar{T} T_a} \frac{\partial \bar{P}^2 {P_a}^2}{\partial \bar{x} \pi D} \right) + \frac{1}{2} \frac{\partial}{\partial \bar{y} L} \left(\frac{\bar{h}^3 c^3}{\mu \bar{T} T_a} \frac{\partial \bar{P}^2 {P_a}^2}{\partial \bar{y} L} \right) = 6U \frac{\partial}{\partial \bar{x} \pi D} \left(\frac{\bar{P} P_a \bar{h} c}{\bar{T} T_a} \right) \tag{3.43}$$

$$\Rightarrow \frac{c^3 {P_a}^2}{2\mu (\pi D)^2 T_a} \frac{\partial}{\partial \bar{x}} \left(\frac{\bar{h}^3}{\bar{T}} \frac{\partial \bar{P}^2}{\partial \bar{x}} \right) + \frac{c^3 {P_a}^2}{2\mu L^2 T_a} \frac{\partial}{\partial \bar{y}} \left(\frac{\bar{h}^3}{\bar{T}} \frac{\partial \bar{P}^2}{\partial \bar{y}} \right) = \frac{6 U P_a c}{\pi D T_a} \frac{\partial}{\partial \bar{x}} \left(\frac{\bar{P} \bar{h}}{\bar{T}} \right) \tag{3.44}$$

$$\Rightarrow \frac{\partial}{\partial \bar{x}} \left(\frac{\bar{h}^3}{\bar{T}} \frac{\partial \bar{P}^2}{\partial \bar{x}} \right) + \left(\frac{\pi D}{L} \right)^2 \frac{\partial}{\partial \bar{y}} \left(\frac{\bar{h}^3}{\bar{T}} \frac{\partial \bar{P}^2}{\partial \bar{y}} \right) = 12 \Lambda_B \frac{\partial}{\partial \bar{x}} \left(\frac{\bar{P} \bar{h}}{\bar{T}} \right) \tag{3.45}$$

By applying the derivatives and assuming that T(x,y) is constant for pressure step during iterative solution,

$$\begin{aligned} & 3\bar{h}^2 \frac{\partial \bar{h}}{\partial \bar{x}} \bar{P} \frac{\partial \bar{P}}{\partial \bar{x}} + \bar{h}^3 \left(\frac{\partial \bar{P}}{\partial \bar{x}} \right)^2 + \bar{h}^3 \bar{P} \frac{\partial^2 \bar{P}}{\partial \bar{x}^2} \\ & \qquad + \left(\frac{\pi D}{L} \right)^2 \left[3\bar{h}^2 \frac{\partial \bar{h}}{\partial \bar{y}} \bar{P} \frac{\partial \bar{P}}{\partial \bar{y}} + \bar{h}^3 \left(\frac{\partial \bar{P}}{\partial \bar{y}} \right)^2 + \bar{h}^3 \bar{P} \frac{\partial^2 \bar{P}}{\partial \bar{y}^2} \right] \\ & \qquad = 6 \Lambda_B \left(\bar{P} \frac{\partial \bar{h}}{\partial \bar{x}} + \bar{h} \frac{\partial \bar{P}}{\partial \bar{x}} \right) \end{aligned} \tag{3.46}$$

Dividing both sides by $\bar{h}^3 \bar{P}$ we get,

$$\begin{aligned} & \frac{3}{\bar{h}} \frac{\partial \bar{h}}{\partial \bar{x}} \frac{\partial \bar{P}}{\partial \bar{x}} + \frac{1}{\bar{P}} \left(\frac{\partial \bar{P}}{\partial \bar{x}} \right)^2 + \frac{\partial^2 \bar{P}}{\partial \bar{x}^2} + \left(\frac{\pi D}{L} \right)^2 \left[\frac{3}{\bar{h}} \frac{\partial \bar{h}}{\partial \bar{y}} \frac{\partial \bar{P}}{\partial \bar{y}} + \frac{1}{\bar{P}} \left(\frac{\partial \bar{P}}{\partial \bar{y}} \right)^2 + \frac{\partial^2 \bar{P}}{\partial \bar{y}^2} \right] \\ & \qquad = 6 \Lambda_B \left(\frac{1}{\bar{h}^3} \frac{\partial \bar{h}}{\partial \bar{x}} + \frac{1}{\bar{h}^2 \bar{P}} \frac{\partial \bar{P}}{\partial \bar{x}} \right) \end{aligned} \tag{3.47}$$

3.2.3 Finite Difference Approximation and Solution Approach

By using the finite difference approximation derived in previous sections for partial derivative terms, Eq. 3.47 could be expressed as,

$$
\begin{aligned}
&\frac{3}{h_{i,j}}\left(\frac{h_{i,j}}{2\Delta x}-\frac{h_{i-1,j}}{\Delta x}+\frac{h_{i+1,j}}{3\Delta x}+\frac{h_{i-2,j}}{6\Delta x}\right)\left(\frac{P_{i,j}}{2\Delta x}-\frac{P_{i-1,j}}{\Delta x}+\frac{P_{i+1,j}}{3\Delta x}+\frac{P_{i-2,j}}{6\Delta x}\right)\\
&\qquad+\frac{1}{P_{i,j}}\left(\frac{P_{i,j}}{2\Delta x}-\frac{P_{i-1,j}}{\Delta x}+\frac{P_{i+1,j}}{3\Delta x}+\frac{P_{i-2,j}}{6\Delta x}\right)^2+\left(\frac{P_{i+1,j}-2P_{i,j}+P_{i-1,j}}{\Delta x^2}\right)\\
&+\left(\frac{\pi D}{L}\right)^2\left[\frac{3}{h_{i,j}}\left(\frac{h_{i,j}}{2\Delta y}-\frac{h_{i,j-1}}{\Delta y}+\frac{h_{i,j+1}}{3\Delta y}+\frac{h_{i,j-2}}{6\Delta y}\right)\left(\frac{P_{i,j}}{2\Delta y}-\frac{P_{i,j-1}}{\Delta y}+\frac{P_{i,j+1}}{3\Delta y}+\frac{P_{i,j-2}}{6\Delta y}\right)\right.\\
&\qquad+\frac{1}{P_{i,j}}\left(\frac{P_{i,j}}{2\Delta y}-\frac{P_{i,j-1}}{\Delta y}+\frac{P_{i,j+1}}{3\Delta y}+\frac{P_{i,j-2}}{6\Delta y}\right)^2\\
&\qquad\left.+\left(\frac{P_{i,j+1}-2P_{i,j}+P_{i,j-1}}{\Delta y^2}\right)\right]
\end{aligned}
\tag{3.48}
$$

Let us define the left and right hand side of the Eq. 3.48 by *LHS* and *RHS* respectively as follows,

$$
LHS=\left(\frac{P_{i+1,j}-2P_{i,j}+P_{i-1,j}}{\Delta x^2}\right)+\left(\frac{\pi D}{L}\right)^2\left(\frac{P_{i,j+1}-2P_{i,j}+P_{i,j-1}}{\Delta y^2}\right)
\tag{3.49}
$$

$$
\begin{aligned}
RHS=6\Lambda_B&\left(\frac{1}{{h_{i,j}}^3}\left(\frac{h_{i,j}}{2\Delta x}-\frac{h_{i-1,j}}{\Delta x}+\frac{h_{i+1,j}}{3\Delta x}+\frac{h_{i-2,j}}{6\Delta x}\right)\right.\\
&\left.+\frac{1}{{h_{i,j}}^2P_{i,j}}\left(\frac{P_{i,j}}{2\Delta x}-\frac{P_{i-1,j}}{\Delta x}+\frac{P_{i+1,j}}{3\Delta x}+\frac{P_{i-2,j}}{6\Delta x}\right)\right)\\
&-\frac{3}{h_{i,j}}\left(\frac{h_{i,j}}{2\Delta x}-\frac{h_{i-1,j}}{\Delta x}+\frac{h_{i+1,j}}{3\Delta x}+\frac{h_{i-2,j}}{6\Delta x}\right)\left(\frac{P_{i,j}}{2\Delta x}-\frac{P_{i-1,j}}{\Delta x}\right.\\
&\left.+\frac{P_{i+1,j}}{3\Delta x}+\frac{P_{i-2,j}}{6\Delta x}\right)-\frac{1}{P_{i,j}}\left(\frac{P_{i,j}}{2\Delta x}-\frac{P_{i-1,j}}{\Delta x}+\frac{P_{i+1,j}}{3\Delta x}+\frac{P_{i-2,j}}{6\Delta x}\right)^2\\
&-\left(\frac{\pi D}{L}\right)^2\left[\frac{3}{h_{i,j}}\left(\frac{h_{i,j}}{2\Delta y}-\frac{h_{i,j-1}}{\Delta y}+\frac{h_{i,j+1}}{3\Delta y}+\frac{h_{i,j-2}}{6\Delta y}\right)\left(\frac{P_{i,j}}{2\Delta y}\right.\right.\\
&\left.-\frac{P_{i,j-1}}{\Delta y}+\frac{P_{i,j+1}}{3\Delta y}+\frac{P_{i,j-2}}{6\Delta y}\right)\\
&\left.+\frac{1}{P_{i,j}}\left(\frac{P_{i,j}}{2\Delta y}-\frac{P_{i,j-1}}{\Delta y}+\frac{P_{i,j+1}}{3\Delta y}+\frac{P_{i,j-2}}{6\Delta y}\right)^2\right]
\end{aligned}
\tag{3.50}
$$

Boundary conditions for pressure distribution are,

$$\begin{gathered} P(0,y) = P_a \\ P\left(\theta_{leading}, y\right) = P_a \\ P(x,L) = P_a \\ \frac{\partial P}{\partial y}\Big|_{y=0} = 0 \end{gathered} \tag{3.51}$$

To solve for $P_{i,j}$ RHS is evaluated by using initial values of eccentricity ratio and pressure. Then the equation is solved iteratively for pressure. After convergence is achieved film thickness is updated by using current eccentricity. If the generated bearing load is not sufficient to carry the applied load, eccentricity ratio is increased with a small increment until lifting load is satisfied or reached to a previously defined minimum film thickness after that physical contact is assumed to occur between the top foil and the shaft surfaces. Typically, under relaxation is used to improve the convergence especially at large bearing compressibility numbers and eccentricity ratio. The film thickness is updated in each iteration as follows,

$$\bar{h}^{k+1} = 1 + \left(\varepsilon_{ref} + \Delta\varepsilon^{k}\right)\cos(\theta - \Delta\varphi^{k}) + \delta_f \tag{3.52}$$

where $\Delta\varepsilon$ is the change of the eccentricity due to the deformation of the top foil and $\Delta\varphi$ is the change of the attitude angle, δ_f is thickness change in the film due to deformation and superscript k gives the iteration number. The resulting non-dimensional bearing loads are calculated by integrating the generated hydrodynamic pressure over the top foil surface as,

$$\begin{gathered} W_x = \int_{-1}^{1}\int_{0}^{2\pi} (P-1) cos\theta d\theta dy \\ W_y = \int_{-1}^{1}\int_{0}^{2\pi} (P-1) sin\theta d\theta dy \\ W = \sqrt{{W_x}^2 + {W_y}^2} = \frac{W}{P_a RL} \end{gathered} \tag{3.53}$$

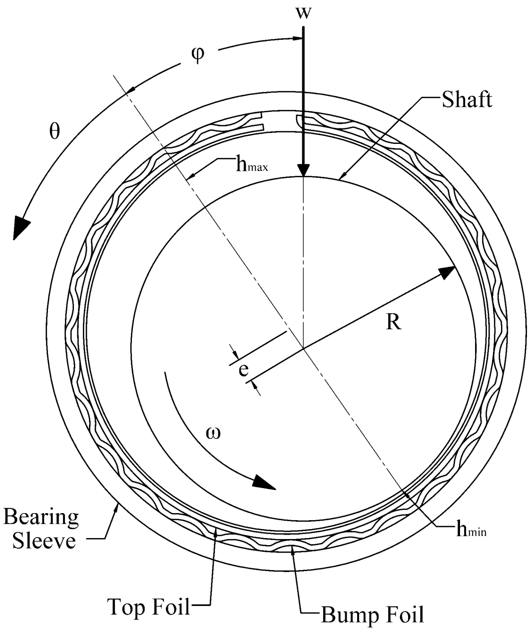

Figure 3.2: Eccentric position of the shaft during operation under a given load and related parameters

The attitude angle displayed in Figure 3.2 is calculated by taking the ratio of the bearing loads as,

$$tan\varphi = -\frac{W_y}{W_x} \tag{3.54}$$

The updates for the attitude angle is calculated as,

$$\Delta\varphi^k = atan\left(\frac{-W_y{}^k}{W_x{}^k}\right) - atan\left(\frac{-W_y{}^{k-1}}{W_x{}^{k-1}}\right) \tag{3.55}$$

The change of the attitude angle is taken into account by rotating the coordinate frame according to that angle which provides force balance by eliminating the horizontal force terms. The following rotation matrix is used to apply the change of the attitude angle,

$$\begin{bmatrix} x' \\ y' \\ z' \end{bmatrix} = \begin{bmatrix} \cos(\varphi + \pi/2) & sin(\varphi + \pi/2) & 0 \\ -sin(\varphi + \pi/2) & cos(\varphi + \pi/2) & 0 \\ 0 & 0 & 1 \end{bmatrix} \begin{bmatrix} x \\ y \\ z \end{bmatrix} \tag{3.56}$$

3.2.4 Solving Reynolds Equation by FEM

The derivation of the Reynolds Equation starting from the general momentum equations and finite difference formulation for an iterative solver is presented in the previous section. However; for TEHD model developed in this work, Reynolds Equation is solved by using commercial software capable of solving fluid structure interaction and thin film flows successfully by utilizing direct solvers. A typical system where hydrodynamic lubrication/lift is expected is illustrated in Figure 3.3 below.

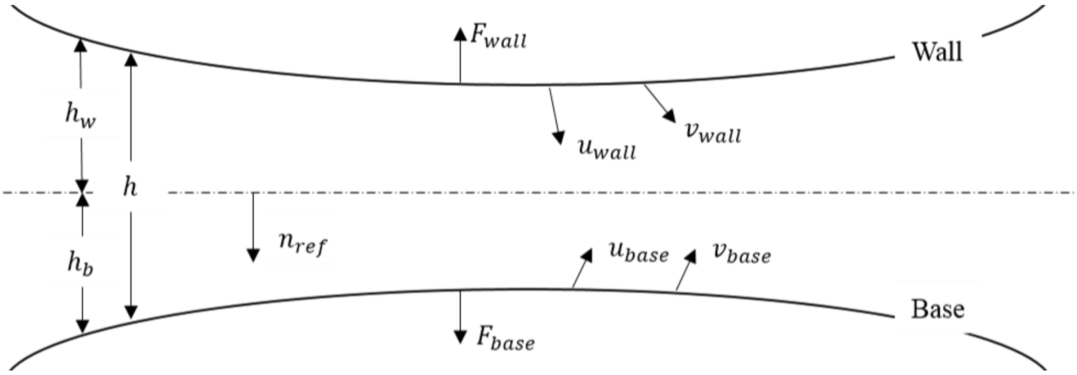

Figure 3.3: An example illustrating a typical configuration for thin-film flow [90]

The air film applies two kinds of forces to the shaft and the top foil. At initial state, both structures are surrounded by ambient gas. Due to the relative movements of the structures, hydrodynamic film pressure develops inside the gap. The normal force affecting the moving shaft is $F_{wall}^{n} = -\boldsymbol{n_{ref}} P_a$. The tangential force on the moving wall is the viscous drag force of the air F_{wall}^{t}, which resists the rotation of the structure. In our problem, the viscosity of the air is so small, such that tangential force due to viscous friction could be easily eliminated [90].

3.2.4.1 The Effect of shaft thermal and centrifugal expansion to bearing clearance

The load capacity of a CFB occurs in excess of the nominal bearing clearance due to compliant structure. In fact, the nominal clearance in a CFB is not well-defined because the topfoil surface is in contact with shaft surface at start-up. In that sense, the bearings are preloaded to minimize the film gap between topfoil and shaft surface, and applying an initial torque to the shaft. The expansion of the shaft due to thermal and centrifugal effects contributes to bearing clearance during operation where c = $c_0 - S_{th} - S_c$. For a hollow shaft, the thermal expansion is defined as,

$$S_{th} \approx \alpha(R_o - R_i)(T_{sm} - T_a) \tag{3.57}$$

where α is the thermal expansion coefficient of the shaft material and T_{sm} is mean shaft temperature. The linear expansion is depicted in Figure 3.4. The centrifugal growth of the shaft, S_C is a function of its geometry and material properties [63] as in the following relation,

$$S_c = \frac{R_o \rho_s \omega^2}{8E_s}\left\{(1 - \upsilon_s)A_1 + (1 - \upsilon_s)A_2 - (1 - {\upsilon_s}^2){R_o}^2\right\} \tag{3.58}$$

where

$$A_1 = (R_o^2 + R_i^2)(3 + \upsilon_s), \qquad A_2 = R_i^2(3 + \upsilon_s) \tag{3.59}$$

and $E_s, \upsilon_s, and\ \rho_s$ are the shaft material elastic modulus, Poisson ratio, and density, respectively. Figure 3.5 shows the predicted centrifugal growth with respect to increasing speed for an Inconel 718 shaft. The plot reveals the quick growth of outer shaft diameter for a thin walled structure. The bearing designer must consider this behavior of the shaft to prevent failure due to seizure, as mentioned in Ref. [27].

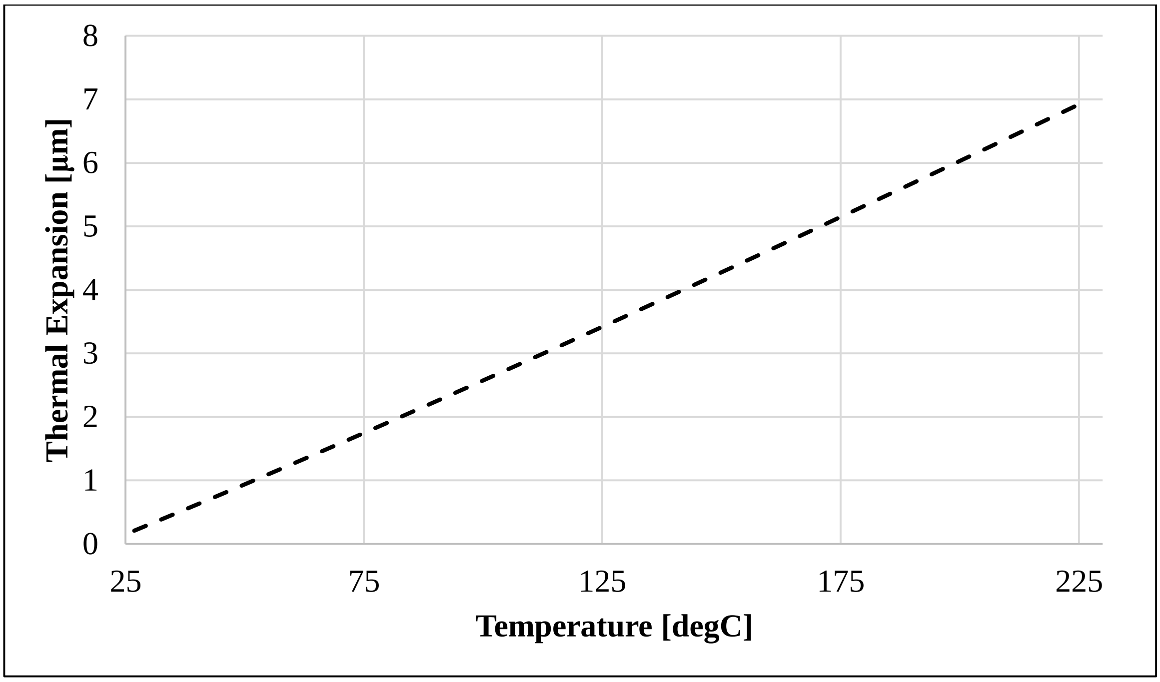

Figure 3.4: Thermal expansion of the Inconel 718 shaft with respect to temperature

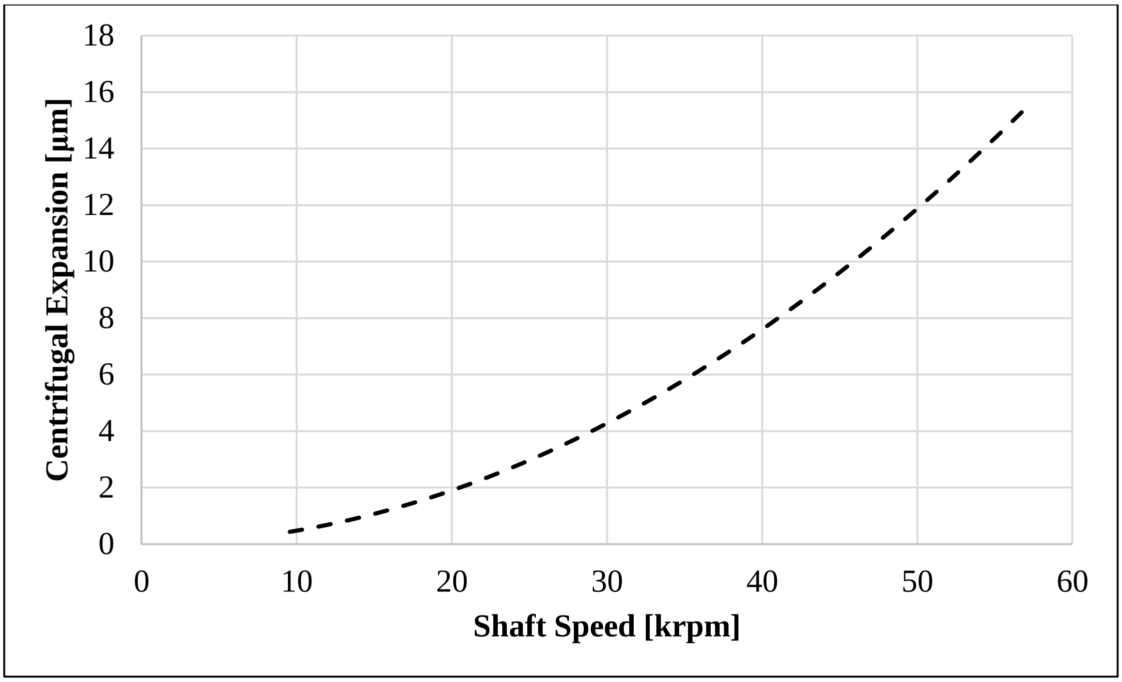

Figure 3.5: Shaft centrifugal growth with respect to the shaft speed for Inconel 718 shaft material. Shaft outer diameter is 50 mm and wall thickness, $t_s = R_o - R_i$ is 2.5 mm

3.2.4.2 No-Slip boundary condition

The aspect ratio between the film thickness and remaining bearing dimensions in lubrication problems is always very large. Since the film thickness is very thin, the inertial effects in the fluid can be ignored compared to the viscous effects as discussed before. Additionally, the pressure and temperature can be assumed constant through the film thickness depth for the same reason. Due to small curvature of the channel for a thin film gap, it is assumed that the channel boundaries are parallel to each other. With these assumptions, the fluid problem in the bearing gap described by NS equations reduces to the Reynolds equation in the channel boundary as explained previously. Another crucial measure to validate the Reynolds equation is the squeeze number, κ [89].

$$\kappa = \frac{12\mu L^2 \omega}{P_a {h_0}^2} \tag{3.60}$$

For the Reynolds equation to describe the flow problem properly, κ must be much smaller than unity. For typical values of, μ=2e-5 Pa.s, L=100 mm, ω=1500 rad/s, P_a=101 kPa, h_0=10 μm, κ becomes around 0.0035 which is far beyond the critical value of one.

The Reynolds equation assumes that continuum flow holds such that the mean free path of the gas molecules is relatively small compared to the film thickness. The continuum condition is determined by calculating the Knudsen number, $Kn=\lambda/h$, where λ represents the molecular mean free path of operating fluid. The continuum assumption for the governing equation holds only when $Kn < 0.01$. Physical meaning of the mean free path is the distance travelled by a gas particle between two consecutive collisions. Hence; if the film thickness is sufficiently narrow, the mean free path becomes on the same order with film thickness. Slip flow occurs between the lubricating surfaces when $0.01<Kn<15$. Fully developed molecular flow occurs when Kn is increased beyond 15 [91].

The common lubricant in foil bearings is air whose mean free path is 0.064 μm in room conditions. Typical minimum film thickness encountered in foil bearing applications is around 7-8 μm. The Knudsen number becomes Kn=0.064/7=0.00914. For most applications, continuum flow holds. However, in some cases film thickness becomes less than 6 μm, and Reynolds equation must be modified for slip flow condition. For the sake of generality, continuum flow is assumed throughout this work.

3.3 Derivation of the Bulk Energy Transport Equation for Film Temperature

The first law of thermodynamics for a differential element of fluid is stated as conservation of energy [89]. It shows the equilibrium between the total energy of a system, which consists of internal, kinetic and potential energies, and the energy added to and the work done by the system. The terms in left-hand side of Eq. (3.61) are called as convective terms because they represent relative motion of the fluid to the boundaries. The first term in right hand side expresses the energy transfer rate by means of conduction. In the scope of this study, this term is converted to a convection term in bulk flow equation. Second term in right hand side presents the rate of work done by the differential fluid volume in expansion or compression. The last term represents the rate of viscous energy dissipated as heat due to shear effect and called as viscous dissipation that contributes to elevating the temperature of the fluid. The energy equation is defined as follows,

$$\rho \frac{De}{Dt} = \nabla.(k\nabla T) + \frac{DP}{Dt} + \xi \tag{3.61}$$

where e is enthalphy defined as,

$$e = \hat{u} + {}^{P}\!/_{\rho} => De = c_p(T)DT \tag{3.62}$$

In Cartesian coordinates, assuming $c_p \neq c_p(T)$ energy equation can be expressed as,

$$\begin{gathered}\rho c_p\left(u\frac{\partial T}{\partial x} + v\frac{\partial T}{\partial y} + w\frac{\partial T}{\partial z}\right) \\ = k\frac{\partial^2 T}{\partial x^2} + k\frac{\partial^2 T}{\partial y^2} + k\frac{\partial^2 T}{\partial z^2} + u\frac{\partial P}{\partial x} + v\frac{\partial P}{\partial y} + w\frac{\partial P}{\partial z} \\ +\mu\left[2\left(\frac{\partial u}{\partial x}\right)^2 + 2\left(\frac{\partial v}{\partial y}\right)^2 + 2\left(\frac{\partial w}{\partial z}\right)^2 \right. \\ \left. + \left(\frac{\partial v}{\partial x} + \frac{\partial u}{\partial y}\right)^2 + \left(\frac{\partial w}{\partial y} + \frac{\partial v}{\partial z}\right)^2 + \left(\frac{\partial u}{\partial z} + \frac{\partial w}{\partial x}\right)^2\right]\end{gathered} \tag{3.63}$$

As in the conservation of momentum equation,

$$\frac{\partial u}{\partial z} \& \frac{\partial v}{\partial z} \gg other\ velocity\ components \tag{3.64}$$

The relation between pressure components are also same as given in Eq. 3.14. Since the film thickness is very small, the conduction in radial direction through gas film is much higher compared to circumferential and axial directions,

$$k\frac{\partial^2 T}{\partial z^2} \gg \ k\frac{\partial^2 T}{\partial x^2} \ \& \ k\frac{\partial^2 T}{\partial y^2} \tag{3.65}$$

When this relation is applied, the conductive terms in circumferential and axial directions drop and the energy equation takes the following simpler form,

$$\rho c_p\left(u\frac{\partial T}{\partial x} + v\frac{\partial T}{\partial y}\right) = k\frac{\partial^2 T}{\partial z^2} + u\frac{\partial P}{\partial x} + v\frac{\partial P}{\partial y} + \mu\left[\left(\frac{\partial u}{\partial z}\right)^2 + \left(\frac{\partial v}{\partial z}\right)^2\right] \tag{3.66}$$

where the last term in the left hand side is called as viscous dissipation,

$$\xi = \mu\left[\left(\frac{\partial u}{\partial z}\right)^2 + \left(\frac{\partial v}{\partial z}\right)^2\right] \tag{3.67}$$

Remember the velocity components are calculated as,

$$u = \frac{1}{2\mu}\frac{\partial P}{\partial x}(z^2 - zh) + U\left(1 - \frac{z}{h}\right)$$

$$v = \frac{1}{2\mu}\frac{\partial P}{\partial y}(z^2 - zh) \tag{3.68}$$

Let us define the partial derivative terms as follows for the sake of simplicity,

$$\frac{\partial P}{\partial x} = P_x, \qquad \frac{\partial P}{\partial y} = P_y, \qquad \frac{\partial T}{\partial x} = T_x, \qquad \frac{\partial T}{\partial y} = T_y \tag{3.69}$$

The gradients of the velocities across film thickness become as follows:

$$\frac{\partial u}{\partial z} = \frac{1}{2\mu}P_x(2z - h) - \frac{U}{h} \tag{3.70}$$

$$\frac{\partial v}{\partial z} = \frac{1}{2\mu}P_y(2z - h) \tag{3.71}$$

The square of equations (3.70) and (3.71) are also used. They are calculated as,

$$\left(\frac{\partial u}{\partial z}\right)^2 = \left(\frac{1}{2\mu}P_x(2z - h)\right)^2 - \frac{U}{h.\mu}P_x(2z - h) + \frac{U^2}{h^2} \tag{3.72}$$

$$\left(\frac{\partial v}{\partial z}\right)^2 = \left(\frac{1}{2\mu}P_y(2z - h)\right)^2 \tag{3.73}$$

The viscous dissipation can be represented in simpler form as in,

$$\xi = \frac{a^2}{4\mu}\left(P_x^2 + P_y^2\right) - \frac{U.a}{h}P_x + \frac{U^2}{h^2}\mu \tag{3.74}$$

where following relations are used to reduce the complexity of the equations;

$$a = (2z - h), \qquad b = (z^2 - zh), \qquad d = (1 - \frac{z}{h}) \tag{3.75}$$

3.3.1 Derivation of the Bulk-flow Transport Equation

Integration across the film thickness of the steady state thermal energy transport equation gives the bulk-flow equation for transport of gas film [63]. Integrating each term by $\int_0^h dz$,

$$\int_0^h a.dz = 0, \quad \int_0^h a^2.dz = \frac{h^3}{3}, \quad \int_0^h b.dz = -\frac{h^3}{6}, \quad \int_0^h d.dz = \frac{h}{2} \tag{3.76}$$

$$\int_0^h (uT_x + vT_y).dz = -\frac{h^3}{12\mu}(P_xT_x + P_yT_y) + \frac{Uh}{2}T_x \tag{3.77}$$

$$\int_0^h (uP_x + vP_y).dz = -\frac{h^3}{12\mu}(P_x^2 + P_y^2) + \frac{Uh}{2}P_x \tag{3.78}$$

$$\int_0^h \xi.dz = \frac{h^3}{12\mu}(P_x^2 + P_y^2) + \frac{U^2}{h}\mu \tag{3.79}$$

The relation between conditions in the boundary layer and the convection heat transfer can be illustrated as in Figure 3.6.

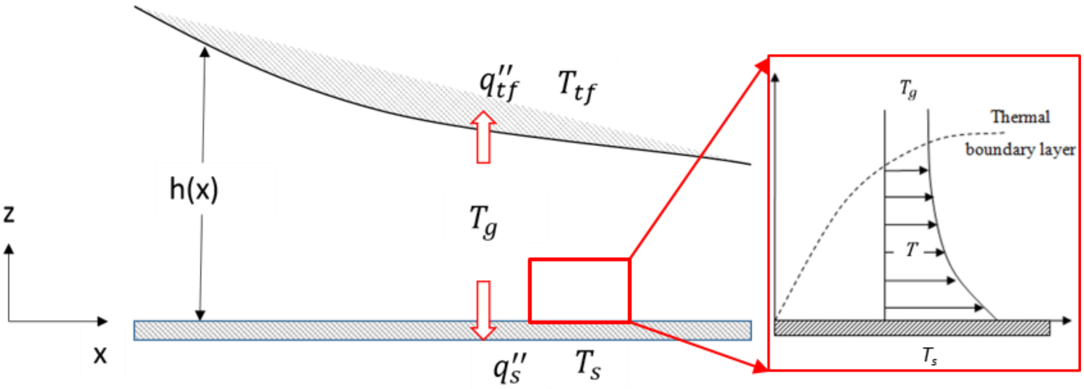

Figure 3.6: Coordinate systems and heat transfer in the film

The local heat flux can be obtained by applying Fourier’s law as follows:

$$q''_{sf} = -k_f \frac{\partial T}{\partial z}|_{z=0} \tag{3.80}$$

The subscription, *sf* refers the surface heat flux because there is no fluid motion and energy transfer at the surface except conduction [92]. Newton’s law of cooling gives the heat flux as,

$$q''_{sf} = h(T_s - T_a) \tag{3.81}$$

Combining Equations (3.80) and (3.81) convective heat flux coefficient, h_{conv} becomes,

$$h_{conv} = \frac{-k_f \, {\partial T}/{\partial z}\,|_{z=0}}{T_s - T_a} \tag{3.82}$$

By using the relation between convection and conduction coefficients at boundary surfaces, integration of the conductive term across film thickness could be expressed as

$$\int_0^h k\frac{\partial^2 T}{\partial z^2}.dz = k\frac{\partial T}{\partial z}|_0^h = k\frac{\partial T}{\partial z}|_{z=h} - k\frac{\partial T}{\partial z}|_{z=0} \tag{3.83}$$
$$\Rightarrow h_s(T_s - T_g) - h_{tf}(T_g - T_{tf})$$

Final form of the bulk flow equation for transport of gas film becomes,

$$\Rightarrow \rho c_p\left[-\frac{h^3}{12\mu}(P_xT_x + P_yT_y) + \frac{U.h}{2}T_x\right]$$
$$= h_s(T_s - T) + h_{tf}(T_{tf} - T) + \frac{U.h}{2}P_x + \frac{U^2}{h}\mu \tag{3.84}$$

3.3.2 Heat Convection Coefficient Models

The heat convection coefficients for heat flux from the gas film into the journal outer surface and topfoil inner surface calculated by using the Reynolds-Colburn analogy which defines the relation between fluid friction and heat transfer [93]. The Nusselt number, *Nu* is defined by:

$$Nu_L = \frac{h_{tf}h}{k_g} = 0.664 {Re_L}^{1/2} Pr^{1/3} \tag{3.85}$$

where *Pr* is the Prandtl number and *Re$_L$* is Reynolds number expressed respectively as

$$Pr = \frac{c_p\mu}{k_G} \tag{3.86}$$

$$Re_L = \frac{\rho u_\infty h}{\mu} \tag{3.87}$$

From here convection coefficients become as follows:

$$h_{tf} = h_s = \rho u_\infty c_p 0.664 {Re_L}^{-1/2} Pr^{-2/3} \tag{3.88}$$

There are several approaches to define conductivity and dynamic viscosity of gases with respect to the temperature. Throughout this work following relations are selected for air conductivity and dynamic viscosity [68]:

$$k_g = 7.4x10^{-5}T_g + 4.25x10^{-3} \tag{3.89}$$

$$\mu = 1.4566x10^{-6}{T_g}^{0.5}\left(1 + {}^{110.33}\!/_{T_g}\right)^{-1} \tag{3.90}$$

3.3.3 Non-Dimensionalization of Solution Parameters

Similar normalization procedure performed to derive the dimensionless form of Reynolds equation. Following normalization relations are applied to the parameters in bulk-flow energy equation:

$$\begin{gathered}
\bar{x} = \frac{x}{\pi D}, \qquad \bar{y} = \frac{y}{L}, \qquad \bar{u} = \frac{u}{U}, \qquad \bar{T} = \frac{T}{T_a}, \qquad \overline{T_x} = \frac{\overline{\Delta T}}{\overline{\Delta x}} = T_x\frac{\pi D}{T_a}, \\
\overline{T_y} = \frac{\overline{\Delta T}}{\overline{\Delta y}} = T_x\frac{L}{T_a}, \qquad \bar{\mu} = \frac{\mu}{\mu_i}, \qquad \bar{P} = \frac{P}{P_a}, \qquad \overline{P_x} = \frac{\overline{\Delta P}}{\overline{\Delta x}} = P_x\frac{\pi D}{P_a}, \\
\overline{P_y} = \frac{\overline{\Delta P}}{\overline{\Delta y}} = P_y\frac{L}{P_a}, \qquad \bar{h} = \frac{h}{c}
\end{gathered} \tag{3.91}$$

By using the non-dimensional parameters in left hand side (LHS) and right hand side (RHS), the Eq. (3.84) takes the following form:

$$LHS = -\rho c_p\left[-\frac{\bar{h}^3c^3}{12\bar{\mu}\mu_i}\left(\bar{P}_x\frac{P_a}{\pi D}\bar{T}_x\frac{T_a}{\pi D} + \bar{P}_y\frac{P_a}{L}\bar{T}_y\frac{T_a}{L}\right) - \bar{T}_x\frac{T_a}{\pi D}\frac{U\bar{h}c}{2}\right] \tag{3.92}$$

$$RHS = T_a(h_sT_s + h_{tf}T_{tf}) - \bar{T}T_a(h_s + h_{tf}) + \frac{U.c.P_a}{2\pi D}\bar{h}\bar{P}_x + \frac{U^2\bar{\mu}\mu_i}{\bar{h}c} \tag{3.93}$$

Multiplying both sides with $\frac{2\pi D}{\rho c_p U T_a c}$, *LHS* and *RHS* become:

$$LHS = \frac{-c^2P_a}{6\mu_i\pi DU}\frac{\bar{P}_x\bar{T}_x\bar{h}^3}{\bar{\mu}} + \bar{T}_x\bar{h} + \frac{-c^2P_a\pi D}{6\mu_iL^2U}\frac{\bar{P}_y\bar{T}_y\bar{h}^3}{\bar{\mu}} \tag{3.94}$$

$$RHS = \frac{2\pi D}{\rho c_p U c}\left[h_s(\bar{T}_s - \bar{T}) + h_{tf}(\overline{T_{tf}} - \bar{T})\right] + \frac{1}{\rho c_p T_a}\left(P_a . \bar{h} . \bar{P}_x + \frac{2\pi D U \mu_i \bar{\mu}}{\bar{h} c^2}\right) \tag{3.95}$$

Let us define additional parameters to reduce the number of terms, and to further simplify the equations for coding,

$$a_1 = \frac{-c^2 P_a}{6\mu_i \pi D U}, \qquad a_2 = \frac{-c^2 P_a \pi D}{6\mu_i L^2 U}, \qquad a_3 = \frac{h_s 2\pi D}{\rho c_p U c}, \qquad a_4 = \frac{h_{tf} 2\pi D}{\rho c_p U c}, \qquad a_5 = \frac{P_a}{\rho c_p T_a}, \qquad a_6 = \frac{2\pi D U \mu_i}{\rho c_p T_a c^2} \tag{3.96}$$

The bulk-flow equation now takes the following simpler form:

$$\Rightarrow a_1 \frac{\bar{P}_x \bar{T}_x \bar{h}^3}{\bar{\mu}} + \bar{T}_x . \bar{h} + a_2 \frac{\bar{P}_y \overline{T_y} \bar{h}^3}{\bar{\mu}} + (a_3 + a_4)\bar{T} = a_3 \bar{T}_s + a_4 \bar{T}_{tf} + a_5 \bar{h} . \bar{P}_x + a_6 \frac{\bar{\mu}}{\bar{h}} \tag{3.97}$$

3.3.4 Finite Difference Formulation for Temperature Nodes

The 4-point backward-skewed finite difference formulation explained in previous sections is applied to approximate the partial derivatives of temperature except in symmetry plane where Neumann boundary condition is approximated with backward difference.

$$a_1 \frac{\bar{P}_x \bar{h}^3}{\bar{\mu}\overline{\Delta x}}\left(\frac{T_{i,j}}{2} - T_{i-1,j} + \frac{T_{i+1,j}}{3} + \frac{T_{i-2,j}}{6}\right) + a_2 \frac{\bar{P}_y \bar{h}^3}{\bar{\mu}\overline{\Delta y}}\left(\frac{T_{i,j}}{2} - T_{i,j-1} + \frac{T_{i,j+1}}{3} + \frac{T_{i,j-2}}{6}\right) + \frac{\bar{h}}{\overline{\Delta x}}\left(\frac{T_{i,j}}{2} - T_{i-1,j} + \frac{T_{i+1,j}}{3} + \frac{T_{i-2,j}}{6}\right) + (a_3 + a_4) T_{i,j} = F \tag{3.98}$$

Collecting the coefficients of same finite difference nodes together,

$$T_{i,j}\left(a_1 \frac{\bar{P}_x \bar{h}^3}{2\bar{\mu}\overline{\Delta x}} + a_2 \frac{\bar{P}_y \bar{h}^3}{2\bar{\mu}\overline{\Delta y}} + \frac{\bar{h}}{2\overline{\Delta x}} + a_3 + a_4\right) + T_{i-1,j}\left(-a_1 \frac{\bar{P}_x \bar{h}^3}{\bar{\mu}\overline{\Delta x}} - \frac{\bar{h}}{\overline{\Delta x}}\right) + T_{i+1,j}\left(-{}^{c_1}/_{3}\right) + T_{i-2,j}\left(-{}^{c_1}/_{6}\right) + T_{i,j-1}\left(-a_2 \frac{\bar{P}_y \bar{h}^3}{\bar{\mu}\overline{\Delta y}}\right) + T_{i,j+1}\left(-{}^{c_4}/_{3}\right) + T_{i,j-2}\left(-{}^{c_4}/_{6}\right) = F \tag{3.99}$$

where

$$c_0 = a_1\frac{\overline{P}_x\overline{h}^3}{2\overline{\mu}\overline{\Delta x}} + a_2\frac{\overline{P}_y\overline{h}^3}{2\overline{\mu}\overline{\Delta y}} + \frac{\overline{h}}{2\overline{\Delta x}} + a_3 + a_4;\ \ c_1 = -a_1\frac{\overline{P}_x\overline{h}^3}{\overline{\mu}\overline{\Delta x}} - \frac{\overline{h}}{\overline{\Delta x}};$$
$$c_2 = -{}^{c_1}\!/_3;\ \ c_3 = -{}^{c_1}\!/_6 \tag{3.100}$$
$$c_4 = -a_2\frac{\overline{P}_y\overline{h}^3}{\overline{\mu}\overline{\Delta y}};\ \ c_5 = -{}^{c_4}\!/_3;\ \ c_6 = -{}^{c_4}\!/_6$$

The final compact form of the non-dimensional energy equation in finite difference formulation becomes as,

$$c_0T_{i,j} + c_1T_{i-1,j} + c_2T_{i+1,j} + c_3T_{i-2,j} + c_4T_{i,j-1} + c_5T_{i,j+1} + c_6T_{i,j-2} = F \tag{3.101}$$

3.4 Underlying Equations for Structural Deformation

Total Lagrangian formulation is used for structural analysis in COMSOL Multiphysics for both small and finite deformations. This means that rather than the current position in space, the computed stress and deformation state is always referred to the material configuration. Likewise, material properties are always defined for material particles and with tensor components referring to a coordinate system based on the material frame. This brings significant advantage that material properties depending on spatial position can be evaluated just once for the initial material configuration and do not change though the solid deforms and/or rotates [94].

The total strain tensor for an elastic material could be defined in terms of the displacement gradient components as,

$$\varepsilon_{ij} = \frac{1}{2}\left(u_{j,i} + u_{i,j}\right) \tag{3.102}$$

The stress tensor is related to the strain tensor and temperature by the Duhamel-Hooke's law as follows,

$$\sigma = \sigma_0 + C\colon[\varepsilon - \varepsilon_0 - \boldsymbol{\alpha}\Delta T] \tag{3.103}$$

where C denotes the 4th order elasticity tensor, ":" stands for the double-dot tensor product, σ_0 and ε_0 are initial stresses and strains, $\Delta T=T-T_{ref}$, and $\boldsymbol{\alpha}$ is the thermal expansion tensor. The elastic energy by using the tensor components expressed as,

$$W_{elastic} = \sum_{i,j,m,n} \frac{1}{2} C_{ijmn}(\varepsilon_{ij} - \varepsilon_{ij}^{0} - \alpha_{ij}\Delta T)(\varepsilon_{mn} - \varepsilon_{mn}^{0} - \alpha_{mn}\Delta T) \tag{3.104}$$

The strain tensor could be written by using the symmetry in matrix form as,

$$\begin{bmatrix} \varepsilon_x & \varepsilon_{xy} & \varepsilon_{xz} \\ \varepsilon_{xy} & \varepsilon_y & \varepsilon_{yz} \\ \varepsilon_{xz} & \varepsilon_{yz} & \varepsilon_z \end{bmatrix} \tag{3.105}$$

Stress and thermal expansion tensors are also similarly represented as in the following matrices:

$$\begin{bmatrix} \sigma_x & \sigma_{xy} & \sigma_{xz} \\ \sigma_{xy} & \sigma_y & \sigma_{yz} \\ \sigma_{xz} & \sigma_{yz} & \sigma_z \end{bmatrix}, \quad \begin{bmatrix} \alpha_x & \alpha_{xy} & \alpha_{xz} \\ \alpha_{xy} & \alpha_y & \alpha_{yz} \\ \alpha_{xz} & \alpha_{yz} & \alpha_z \end{bmatrix} \tag{3.106}$$

For an isotropic material, the elasticity matrix becomes,

$$D = \frac{E}{(1+\nu)(1-2\nu)} \begin{bmatrix} 1-\nu & \nu & \nu & 0 & 0 & 0 \\ \nu & 1-\nu & \nu & 0 & 0 & 0 \\ \nu & \nu & 1-\nu & 0 & 0 & 0 \\ 0 & 0 & 0 & 0.5-\nu & 0 & 0 \\ 0 & 0 & 0 & 0 & 0.5-\nu & 0 \\ 0 & 0 & 0 & 0 & 0 & 0.5-\nu \end{bmatrix} \tag{3.1076}$$

and the thermal expansion matrix is:

$$\begin{bmatrix} \alpha & 0 & 0 \\ 0 & \alpha & 0 \\ 0 & 0 & \alpha \end{bmatrix} \tag{3.108}$$

The strain conditions for a node are totally defined by the deformation components and their derivatives. The relation between the strain and deformation relies on the relative magnitude of the displacement. Assuming small displacement, the normal and shear strain components are related to the deformation as follows,

$$\begin{gathered} \varepsilon_x = \frac{\partial u}{\partial x}, \qquad \varepsilon_y = \frac{\partial v}{\partial y}, \qquad \varepsilon_z = \frac{\partial w}{\partial z} \\ \varepsilon_{xy} = \frac{1}{2}\left(\frac{\partial u}{\partial y} + \frac{\partial v}{\partial x}\right), \qquad \varepsilon_{yz} = \frac{1}{2}\left(\frac{\partial v}{\partial z} + \frac{\partial w}{\partial y}\right), \qquad \varepsilon_{xz} = \frac{1}{2}\left(\frac{\partial u}{\partial z} + \frac{\partial w}{\partial x}\right) \end{gathered} \tag{3.109}$$

In cases involving combined tensile and shear stresses acting on the same point, it is appropriate to define an effective stress that can represent the stress combination. The distortion energy approach explained in [95] could be utilized to perform this for ductile materials. The von Mises effective stress, σ' is defined as the uniaxial stress that would create the same distortion energy as it is created by the actual combination of applied stresses. The von Mises effective stress, σ' for three dimensional Cartesian system is defined as,

$$\sigma' = \sqrt{\frac{(\sigma_x - \sigma_y)^2 + (\sigma_y - \sigma_z)^2 + (\sigma_z - \sigma_x)^2 + 6(\sigma_{xy}^2 + \sigma_{yz}^2 + \sigma_{zx}^2)}{2}} \qquad (3.110)$$

The nonlinear solver implementation of the equations explained above is based on the principle of virtual work. According to this principle, the sum of virtual work from internal strain is equal to work done by external loads. The total stored energy, W_{stored}, for a linear material from external and internal strains and loads equals:

$$W_{stored} = \int (-\varepsilon : \sigma + \boldsymbol{u}.\boldsymbol{F_v}) \boldsymbol{dv} + \int (\boldsymbol{u}.\boldsymbol{F_s}) \boldsymbol{d\sigma} + \int (\boldsymbol{u}.\boldsymbol{F_L}) \boldsymbol{dl} + \sum_{\boldsymbol{p}} (\boldsymbol{u}.\boldsymbol{F_p}) \qquad (3.111)$$

where F_v, F_s, F_L *and* F_p are body, surface, line and point loads respectively. The principle of virtual work states that $\delta W = 0$ and the solver tries to provide this equation by estimating the displacement, $\boldsymbol{u}$.

3.5 Mechanical Contact Formulation: Augmented Lagrangian Penalty Method

When two separate surfaces touch each other such that they become mutually tangent, they are said to be in contact. In the common physical sense, surfaces that are in contact have these characteristics:

- They do not interpenetrate.
- They can transmit compressive normal forces and tangential friction forces.
- They often do not transmit tensile normal forces.
- They are therefore free to separate and move away from each other.

Physical contacting bodies do not interpenetrate. Therefore, the program must establish a relationship between two surfaces to prevent them from passing through each other in the analysis (Figure 3.7). When the program prevents interpenetration, we say that it enforces contact compatibility[96].

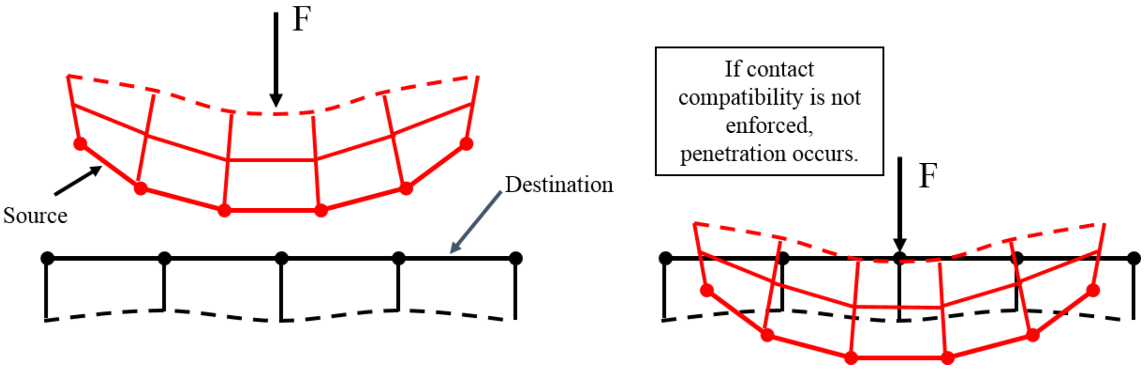

Figure 3.7: The penetration of the source boundary to the destination surface if contact formulation is not defined properly (Reprinted from [96])

The nonlinearity in contact problems occurs due to changing-status of the contact property. That is, the stiffness of the system depends on the contact status whether parts are touching or separated.

In studying the contact between two bodies, one of the surfaces is taken as source surface and the other as destination. For rigid-flexible contact, the source surface is associated with the deformable body and the destination surface must be the rigid surface. For flexible-flexible contact, both source and destination surfaces are associated with deformable bodies. The source and destination surfaces constitute a "Contact Pair". The contact pair is *asymmetric* (source/destination pair). The destination contact domain is constrained not to penetrate the source domain, but not vice versa (Figure 3.8).

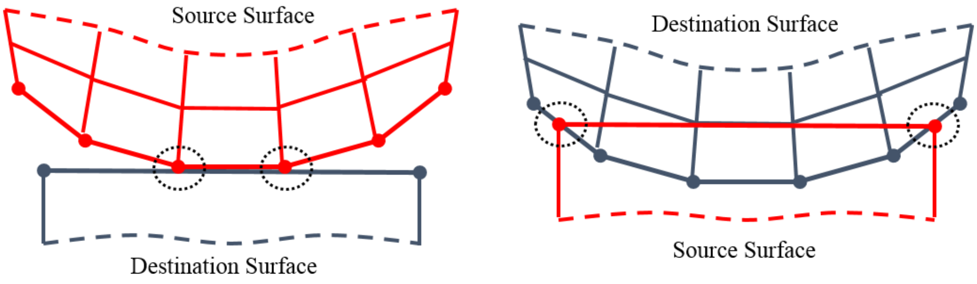

Figure 3.8: Asymmetric contact pair definition (Reprinted from [96])

Here are some guidelines for proper selection of contact surfaces [96]:

- If a convex surface comes into contact with a flat or concave surface, the source should be concave and the destination must be convex rather than the opposite.

- If one surface has a coarse mesh and the other has a fine mesh, the surface with the coarse mesh should be the destination surface.
- If one surface is stiffer than the other, the stiffer surface should be the destination surface.
- If one surface is higher order and the other is lower order, the lower order surface should be the destination surface.
- If one surface is larger than the other, the larger surface should be the destination surface.

The contact pair surfaces for foil bearing THD model is selected according to the recommended guidelines to obtain more accurate results and a better convergence profile. The selected boundaries could be seen in Figure 3.9.

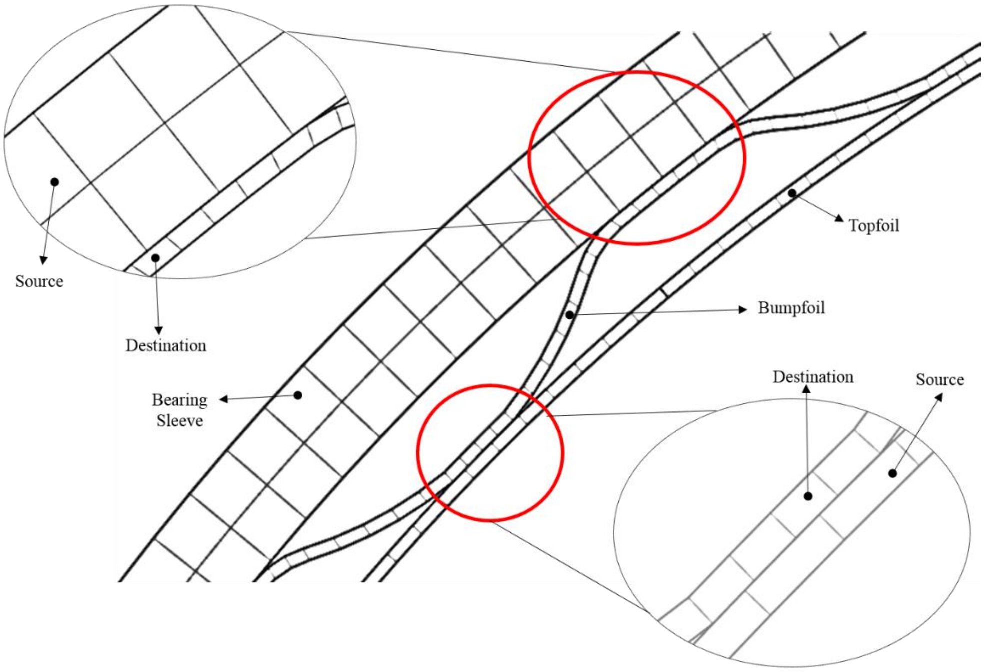

Figure 3.9: The contact pair definition for foil bearing model according to the listed guidelines

The Figure 3.10 indicates where the penetration distance is defined in a contacting pair. The penetration distance is measured along the normal direction of the contact surface (at integration points) to the target surface [97].

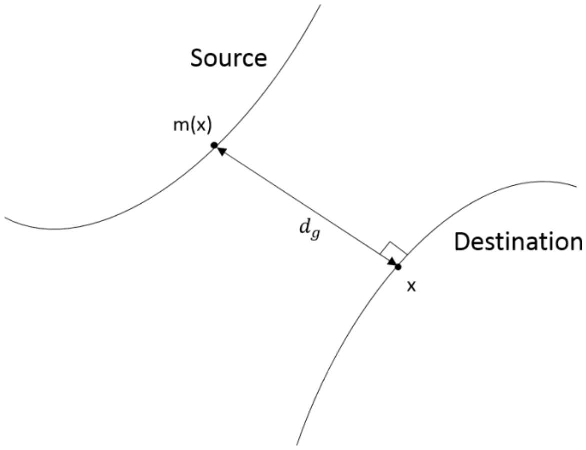

Figure 3.10: The penetration distance measurement in a contact pair [94]

The commerical solver utilizes an *augmented Lagrangian* method to solve contact problems. It means that the software solves the system in a segregated way. The augmented Lagrangian method performs iterative series of penalty updates to find the Lagrange multipliers (i.e., contact tractions). Compared to the penalty method, the augmented Lagrangian method usually leads to better conditioning and is less sensitive to the magnitude of the contact stiffness coefficient. However, in some analyses, the augmented Lagrangian method may require additional iterations, especially if the deformed mesh becomes excessively distorted.

Augmentation components are introduced for the contact pressure, T_n and the components, T_{ti} of the friction traction vector, T_t. An additional iteration level is added where the usual displacement variables are solved separately from the contact pressure and traction variables. The algorithm repeats this procedure until it fulfills a convergence criterion. For the sake of simplicity and better convergence of the problem, frictional components are ignored in this study and left to future work.

In the following equations, $\boldsymbol{F_{def}}$ is the deformation gradient matrix. When looking at expressions evaluated on the destination boundaries, the expression map(E) denotes the value of the expression E evaluated at a corresponding source point.

The penalized contact pressure is defined on the destination boundary by [94]:

$$T_{np} = \begin{cases} T_n - p_n d_g & if\ d_g \leq 0 \\ T_n e^{-\frac{p_n d_g}{T_n}} & otherwise \end{cases} \tag{3.112}$$

where d_g is the gap/distance (Figure 3.11) between the destination and source boundary, and p_n is the user-defined normal penalty factor defined as follows,

$$p_n = f_p \frac{E_{eq}}{h_{mesh}} \tag{3.113}$$

where E_{eq} is the mean of elastic modulus for the source and destination boundaries, h_{mesh} is the minimum mesh size for destination boundary, and f_p is user-defined penalty factor multiplier which is determined by trial-error after several tests.

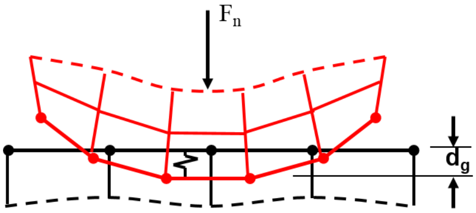

Figure 3.11: The penetration distance is used to calculate the penalized contact pressure by using spring analogy

The definition of the initial contact pressure is another critical issue that influences the convergence of the contact algorithm. To start with a good guess that is in the close vicinity of the final solution enables an easy convergence for the contact problem. Hence, the initial contact pressure is defined as,

$$T_n^0 = \frac{W}{A_{contact}} \tag{3.114}$$

3.6 Thermal Contact Formulation: Cooper-Mikic-Yovanovich Correlation

Modeling thermal contacts are quite intricate due to thermal constriction and heat flux as well as the random distribution of asperities and the unknown boundary condition of micro-contact properties [98]. Several models are developed to predict the contact gap and joint conductance between nominally flat rough surfaces. The models depends on the assumption that the surface asperities have Gaussian height distributions and they are spread over randomly on the contacting surface which has an apparent contact area, A_{app}. A portion of the contacting surface asperities under a mechanical load is illustrated in Figure 3.12. As indicated by dashed lines, each surface has a mean plane, and the distance between them, denoted as ΔY, is related to the apparent contact pressure, the effective surface roughness, χ and plastic or elastic properties of the surfaces.

The surfaces contain irregularities of various orders ranging from shape deviations to irregularities of the order of interatomic distances. Usually, surface roughness relates to the fluctuations in the height of the surface asperities relative to a reference plane. Two essential methods are utilized to characterize the statistical heights of the asperities. These are CLA (center-line average) or arithmetic average and the standard deviation or root mean square (RMS) [99].

$$CLA = \frac{1}{L}\int_{0}^{L} |y(x)|dx \tag{3.115}$$

$$RMS = \sqrt{\frac{1}{L}\int_{0}^{L} y^2(x)dx} \tag{3.116}$$

For Gaussian asperity heights with respect to the mean plane these two measures are related as [100];

$$\chi = \sqrt{\frac{\pi}{2}}.CLA \tag{3.117}$$

Another critical roughness parameter is the absolute mean asperity slope defined as [101]:

$$m = \frac{1}{L}\int_{0}^{L} \left|\frac{dy(x)}{dx}\right| dx \tag{3.118}$$

The effective rms surface roughness and the effective absolute mean asperity slope are defined as follows;

$$\chi = \sqrt{\chi_1^2 + \chi_2^2} \tag{3.119}$$

$$m = \sqrt{m_1^2 + m_2^2} \tag{3.120}$$

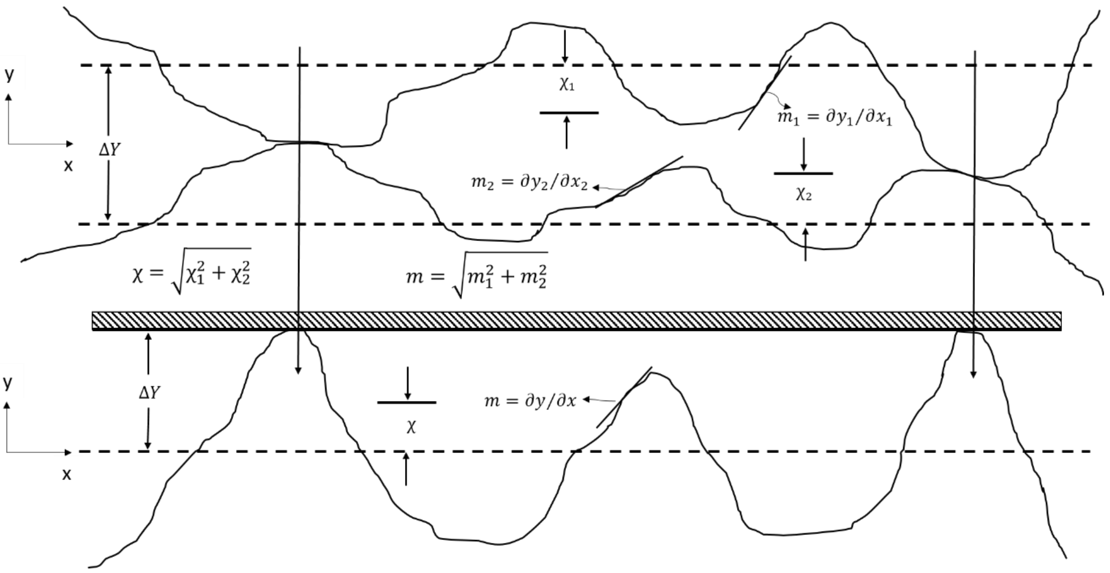

Figure 3.12: Asperity contact parameters reprinted from [102]

For standard foil bearing components, the roughness values are given by Radil et al. [52] as follows,

$$\chi_{topfoil} = \chi_{bumpfoil} = 0.15\ \mu m, \qquad \chi_{sleeve} = 0.1\ \mu m \tag{3.121}$$

Lambert et al. [103] provide the asperity slope with an empirical equation as,

$$m = 0.076\chi^{0.52} \tag{3.122}$$

When roughness parameters are calculated by using these relations, we obtain the numbers as,

$$\begin{aligned} \chi_{tf-bf} &= \sqrt{0.15^2 + 0.15^2} = 0.212\ \mu m \\ m_{tf-bf} &= 0.076x0.212^{0.52} = 0.0339 \\ \chi_{bf-sl} &= \sqrt{0.1^2 + 0.15^2} = 0.18\ \mu m \\ m_{bf-sl} &= 0.076x0.18^{0.52} = 0.0311 \end{aligned} \tag{3.123}$$

The model developed by Yovanovich et al. [104] is valid for isotropic rough surfaces and assumes plastic deformation of the softer of the contacting surface asperities. The model gives three significant geometric parameters at the contact, namely, the relative real contact area, A_{rcon}/A_a, the contact spot density *n*, and the mean contact spot radius r_{con} in terms of the relative mean plane separation which is defined as $\lambda = \Delta Y/\chi$.

The heat flux values at the upside and downside boundaries are determined by the temperature difference according to the following relations:

$$-n_d.(-k_d \nabla T_d) = -h(T_u - T_d)$$
$$-n_u.(-k_u \nabla T_u) = -h(T_d - T_u) \tag{3.124}$$

Three conductance parameters contribute to the joint conductance, h that are the constriction conductance, h_c, comes from the contacting asperity spots, the gap conductance, h_g because of the gas at the gap due to the rough surface property, and the radiative conductance, h_r.

$$h = h_c + h_g + h_r \tag{3.125}$$

When the temperature is less than 600˚C, h_r is relatively small compared to other conductance components and could be neglected for the sake of simplicity since the temperature does not exceed 200˚C for most of the cases presented in this work.

Contact conductance is defined as,

$$h_c = \frac{2n_{spot}r_{con}k_{contact}}{\Psi(\epsilon)}\ [W/m^2K] \tag{3.126}$$

where the effective thermal conductivity of the joint is

$$k_{contact} = \frac{2k_u k_d}{k_u k_d}\ [W/mK] \tag{3.127}$$

and the constriction parameter Ψ, is approximated by

$$\Psi(\epsilon) = (1-\epsilon)^{1.5}\ for\ 0 < \epsilon < 0.3 \tag{3.128}$$

where the relative contact spot size $\epsilon = \sqrt{A_{rcon}/A_a}$.

For assumed plastic deformation of the contacting asperities, following equations are utilized to obtain the contact geometric parameters [101, 104]:

$$\frac{A_{rcon}}{A_a} = \frac{1}{2} erfc\left(\frac{\lambda}{\sqrt{2}}\right) \tag{3.129}$$

$$n = \frac{1}{16}\left(\frac{m}{\chi}\right)^2 \frac{\exp(-\lambda^2)}{erfc\left(\frac{\lambda}{\sqrt{2}}\right)} \tag{3.130}$$

$$r_{con} = \sqrt{\frac{8}{\pi}}\frac{\chi}{m} exp\left(\frac{\lambda^2}{2}\right) erfc\left(\frac{\lambda}{\sqrt{2}}\right) \tag{3.131}$$

$$nr_{con} = \frac{1}{4\sqrt{2\pi}}\frac{m}{\chi} exp\left(\frac{-\lambda^2}{2}\right) \tag{3.132}$$

The correlation for the parameters are as follows,

$$\Rightarrow \frac{A_{rcon}}{A_a} = \exp(-0.8141 - 0.61778\lambda - 0.42476\lambda^2 - 0.004353\lambda^3) \tag{3.133}$$

$$\mathrm{n} = \left(\frac{m}{\chi}\right)^2 \exp(-2.6516 - 0.6178\lambda - 0.5752\lambda^2 - 0.004353\lambda^3) \tag{3.134}$$

$$r_{con} = \frac{\chi}{m}(1.156 - 0.4526\lambda + 0.08269\lambda^2 - 0.005736\lambda^3) \tag{3.135}$$

The relative mean plane separation for plastic deformation is given by

$$\lambda = \sqrt{2} erfc^{-1}\left(\frac{2T_n}{H_\mu}\right) \tag{3.136}$$

where H_μ is the microhardness of the softer of the contacting asperities. The required microhardness value could be obtained from the relative contact pressure T_n/H_μ. The explicit relationship for plastic deformation is defined by Song and Yovanovich [105] as

$$\frac{T_n}{H_\mu} = \left[\frac{T_n}{b_1(1.62\chi/m)^{b_2}}\right]^{1/(1+0.071b_2)} \tag{3.137}$$

where the coefficients b_1 and b_2 are obtained from Vickers microhardness tests. Sridhar and Yovanovich [106] developed correlation equation for Vickers measurements to Brinell hardness, H_B as follows,

$$\frac{b_1}{H_0} = 4 - 5.77\frac{H_B}{H_0} + 4\left(\frac{H_B}{H_0}\right)^2 - 0.61\left(\frac{H_B}{H_0}\right)^3 \tag{3.138}$$

$$b_2 = -0.37 + 0.442\left(\frac{H_B}{b_1}\right) \tag{3.139}$$

where H_0 =3.178 GPa. For similar materials used in the analysis, the coefficients are given by Hegazy [102] as follows,

$$b_1 = 6.271\ GPa, \qquad b_2 = -0.229 \tag{3.140}$$

The contact pressure, T_n is dynamically updated from the contact formulation solutions during Newton-Raphson iterations.

Finally, the contact conductance, h_c is given as,

$$h_c = \frac{mk_{contact}}{2\chi\sqrt{2\pi}} \frac{\exp\left(-\frac{\lambda^2}{2}\right)}{\left[1 - \sqrt{0.5erfc\left(\frac{\lambda}{\sqrt{2}}\right)}\right]^{1.5}} \tag{3.141}$$

For a wide range of λ and T_n/H_μ, the correlation equation is defined by Yovanovich [104] as

$$h_c = 1.25\frac{mk_{contact}}{\chi}\left(\frac{T_n}{H_\mu}\right)^{0.95} \tag{3.142}$$

The gap conductance due to the interstitial fluid could not be neglected for high contact pressure or thermally high conductive fluids. Even though the conductivity of air is very small, due to the small contact area between bumpfoil and topfoil structures, the contact pressure reaches up to 30-40 MPa in some cases. Hence, the gap conductance should be taken into consideration. For the parallel-plate assumption gap conductance due to the air is defined as,

$$h_g = \frac{k_g}{\Delta Y + M_g} \tag{3.143}$$

where k_g is the gas conductivity and M_g is the gas parameter equal to:

$$M_g = \eta\beta\Gamma, \qquad \Gamma = \frac{k_B T_g}{\sqrt{2}\pi {D_{avg}}^2 P_g} \tag{3.144}$$

Here η is the contact thermal accommodation parameter, β is a gas property parameter (equal to 1.65 for air), Γ is the gas mean free path, k_B is the Boltzmann constant, D_{avg} is the average gas particle diameter (equal to 0.37 nm for air), P_g is the gas pressure and T_g is the gap temperature calculated as:

$$T_g = \frac{T_u + T_d}{2} \tag{3.145}$$

Song and Yovanovich [105] developed a correlation for the contact thermal accommodation parameter, η as follows:

$$\eta = exp\left[C_0\left(\frac{T_g - T_0}{T_0}\right)\right]\left(\frac{1.4m_g}{C_1 + 1.4m_g}\right) + \left\{1 - exp\left[C_0\left(\frac{T_g - T_0}{T_0}\right)\right]\right\}\left(\frac{2.4\mu}{(1+\zeta)^2}\right) \tag{3.146}$$

where the ratio of the molecular weight of gas and solid, $\zeta = \frac{1.4m_g}{m_s}$, and the constants C_0 = -0.57, C_1 = 6.8, and T_0 = 273 K. The accommodation parameter, η changes from 0.8414 to 0.7929 when T_g has increased from 300˚K to 400˚K. Thus, for the sake of simplicity we could take a mean value for η as 0.82 without any significant deviation from reality.

4 NUMERICAL SOLVER PROPERTIES

The purpose of the method presented here is to directly couple the finite difference approach for temperature distribution of the lubricant film to the bearing deformation and hydrodynamic flow that are coupled within a single finite element formulation. The model couples the deformation of the underlying foil structure with hyrodynamic pressure generated at the hydrodynamic film by solving Reynolds Equation within a commercial Finite Element Analysis (FEA) code. The bending effects of the top foil were also investigated, considering energy dissipation due to deflection of top foil and bump foil. Furthermore, it accounts for temperature change in the film gap due to the viscous dissipation and compressibility of the fluid by solving the bulk flow energy equation in an in-house routine exploits Finite Difference Method (FDM) that is iteratively coupled to the FEA code. The mechanical contacts between bearing assembly components are modeled with Augmented-Lagrangian penalty method. The thermal contact is also included into the model with an advanced approach called Cooper-Mikic-Yovanovich (CMY) correlation which is discussed in previous sections. The model involves complete bearing mechanism as well as the interacting section of the shaft with the bearing. The thermal growth of the shaft, foil structure, bearing sleeve, and centrifugal growth of the shaft are also taken into account. The details of each section is explained below.

4.1 Finite Element Model for Fluid-Structure Interaction (FSI) Model Including Shaft Heat Transfer

The finite element model presented here couples the hydrodynamic pressure created in the wedging film gap between shaft and topfoil surfaces, and the deformation of the compliant topfoil surface due to this pressure. The code also accounts for conjugate heat transfer mechanisms and related thermal effects on the structure by relating the film temperature to the surrounding surfaces through convective heat transfer model.

Structural and thermal boundary conditions defining the problem is given in following sections. The solver configuration and solution procedure is also detailed below.

4.1.1 Structural Boundary Conditions for FSI Problem

The welded sections of the bumps are displayed in Figure 4.1. The bumps in the neighborhood of the welded regions will have higher stiffness values. The topfoil is welded merely from the trailing edge to enable free deflection. The sleeve is fixed everywhere.

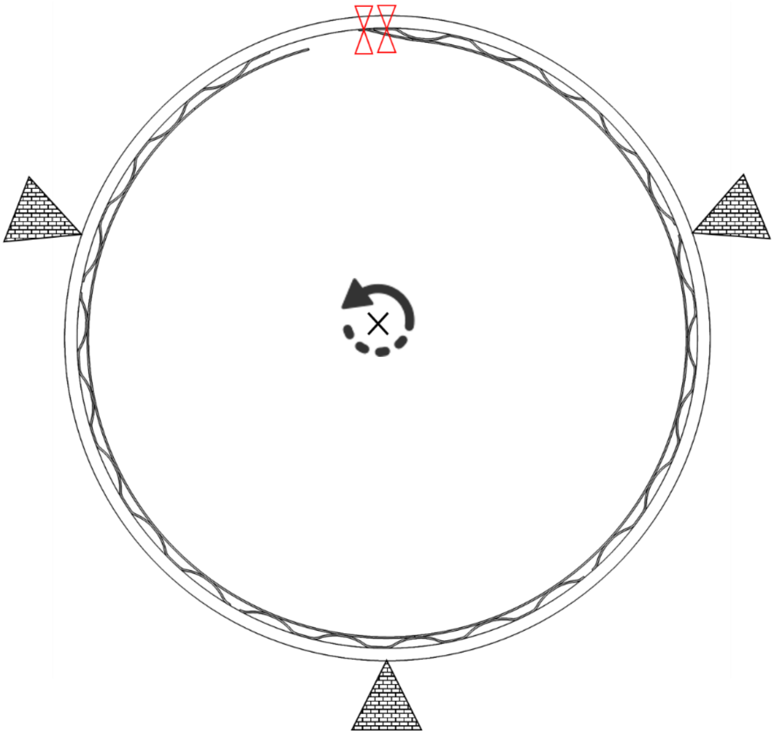

Figure 4.1: Bumps are fixed at specific regions to provide adequate stiffness distribution for expected pressure profile

Cartesian coordinate system is used for the foil bearing assembly and the shaft. The coordinate system is illustrated in Figure 4.2. The x-coordinate axis indicates the circumferential direction, the y-coordinate axis indicates the axial direction and the z axis states for radial direction. Since the radius of the bearing is very large compared to the bump radius and film gap thickness, the cylindrical coordinate system is not preferred for the sake of simplicity.

In the foil bearing assembly, the bump geometry is equivalent in axial direction. Hence, to reduce the computational effort for the problem, the model is assumed to be symmetric in y-direction as shown in Figure 4.3. This will result in more deformation on the bumps that are close to the center because higher pressure load is expected around the center.

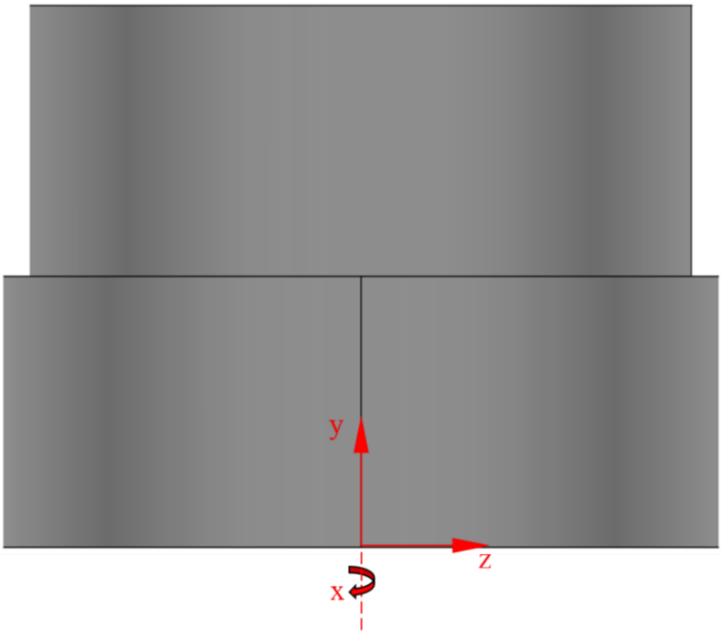

Figure 4.2: The coordinate system for foil bearing assembly and the shaft

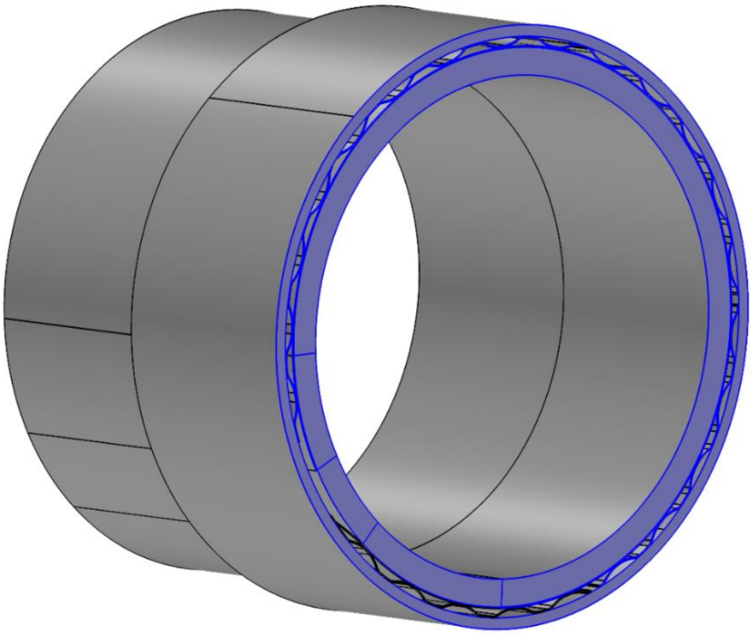

Figure 4.3: The model is symmetric in axial direction and the symmetry boundaries are shown as highlighted

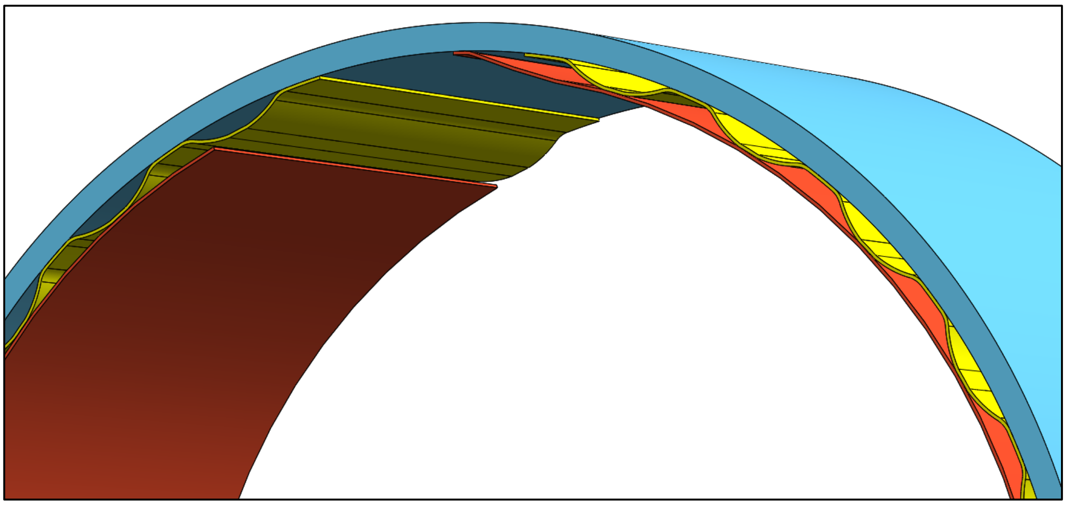

Figure 4.4: The detailed view of the underlying bump geometry

4.1.2 Thermal Boundary Conditions

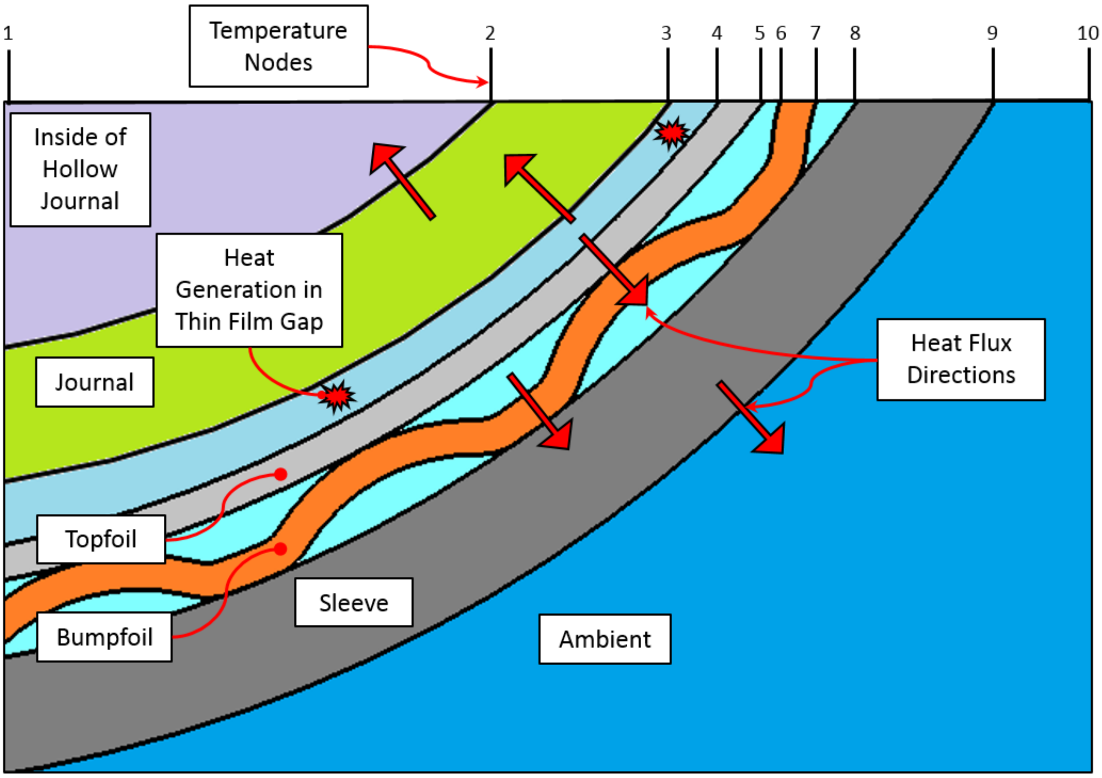

Figure 4.5: Schematic representation of radial heat flow paths in CFB

The proposed model integrates different radial and axial heat flow paths that are listed in Table 4.1. Radial and axial heat flow directions are represented in Figure 4.5 and Figure 4.6, respectively. In the thin film gap between the shaft and the topfoil, heat is generated due to the compressibility of the air and viscous dissipation. Conjugate heat transfer happens between interacting fluid and solid domains. Thermal resistance effects between contacting surfaces, which is explained in previous sections, are also considered during calculation of heat transfer. The released heat is partially absorbed by surrounding components until the system reaches thermal equilibrium. When system comes into steady state, additional heat is removed through convection and conduction to the shaft and topfoil. If a cooling stream inside the hollow shaft exist, it carries out the removed heat from the shaft. Otherwise, heat is removed slowly by natural convection from shaft surfaces that are open to ambient as shown in Figure 4.6.

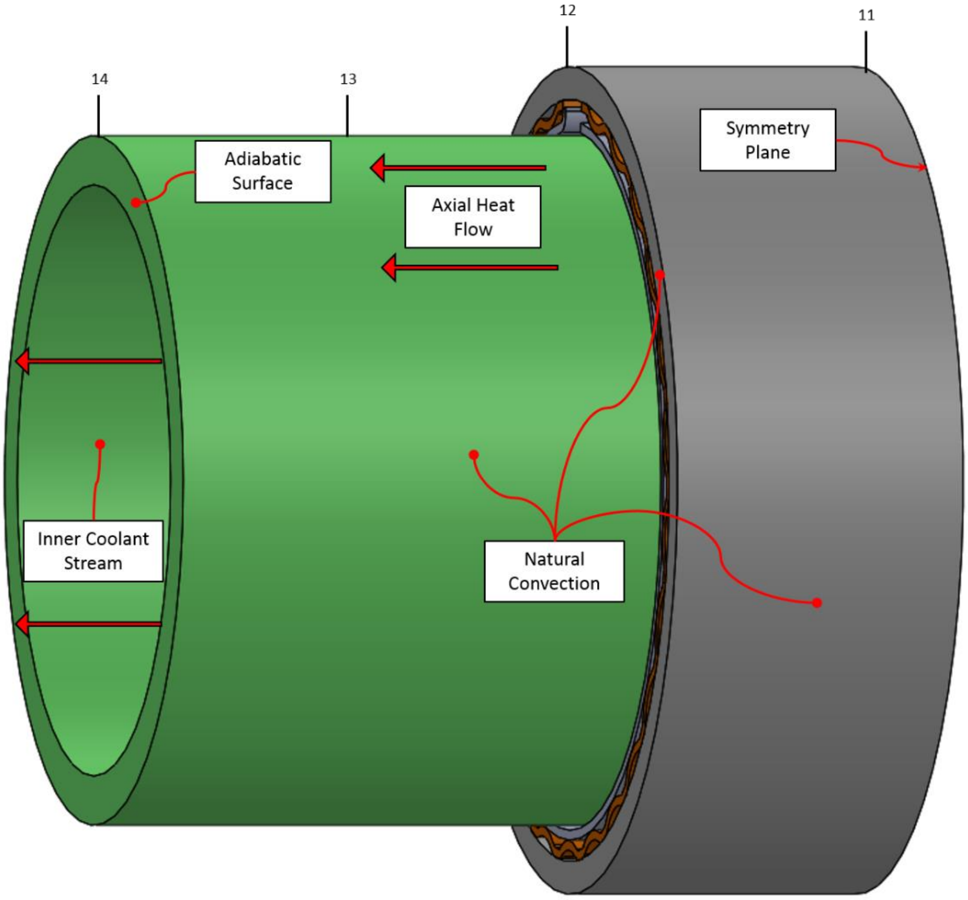

Figure 4.6: Schematic representation of axial heat flow paths in CFB and shaft

Outer surface of the shaft and inner surface of the topfoil are interacting directly with the fluid film. If the transient physical contact at start/stop cycles are ignored, the main heat flow mechanism is convective heat transfer between the fluid in the film gap and surrounding components. The temperature of the fluid, T_g is calculated by finite difference code and applied to the surrounding surfaces by one-to-one mapping method. The calculated temperature values and heat transfer coefficients are exported to a file in harddisk and it is then imported to FEA code as interpolation function for ambient temperature convective heat transfer coefficient.

Temperature Node	**Description**
$\boldsymbol{T_1}$	Ambient or coolant temperature inside the hollow shaft.
$\boldsymbol{T_2}$	Temperature of the inner surface of the shaft. Heat flux is estimated by solving the following equation: $q_2'' = -k_s \frac{\partial T}{\partial z} = h_{13}(T_1 - T_2)$
$\boldsymbol{T_3}$	Temperature of the outer surface of the shaft. Heat flux is defined by equating the conduction and convection from the film: $q_s'' = h_s(T_g - T_3) = -k_s \frac{\partial T}{\partial z}$
$\boldsymbol{T_4}$	Inner surface temperature of topfoil. Heat flux by convection from the film and conduction through foil is defined as: $q_{tf}'' = h_{tf}\left(T_g - T_4\right) -= -k_{tf} \frac{\partial T}{\partial z}$
$\boldsymbol{T_5}$	Outer surface temperature of topfoil. Heat flux through convection from outer cooling stream and conduction to the bumps considered thermal resistance between bumpfoil and topfoil: $q_5'' = h_{cool}(T_{cool} - T_5) + \frac{1}{R_{tf-bf}} \left(\frac{k_{bf} + k_{tf}}{2}\right) \frac{\partial T}{\partial z} = -k_{tf} \frac{\partial T}{\partial z}$
$\boldsymbol{T_6}$	Outer surface temperature of bumpfoil. Heat flux is defined by: $q_6'' = h_{cool}(T_{cool} - T_6) + k_{bf} \frac{\partial T}{\partial z} = \frac{1}{R_{tf-bf}} \left(\frac{k_{bf} + k_{tf}}{2}\right) \frac{\partial T}{\partial z}$
$\boldsymbol{T_7}$	Inner surface temperature of bumpfoil. Heat flux is defined by: $q_7'' = h_{cool}(T_{cool} - T_7) + \frac{1}{R_{bf-sl}} \left(\frac{k_{bf} + k_{sl}}{2}\right) \frac{\partial T}{\partial z} = -k_{bf} \frac{\partial T}{\partial z}$
$\boldsymbol{T_8}$	Inner surface temperature of sleeve. Heat flux is defined by: $q_8'' = h_{cool}(T_8 - T_{cool}) + k_{sl} \frac{\partial T}{\partial z} = \frac{-1}{R_{tf-bf}} \left(\frac{k_{bf} + k_{sl}}{2}\right) \frac{\partial T}{\partial z}$
$\boldsymbol{T_9}$	Outer surface temperature of sleeve. Heat flux is defined by: $q_9'' = h_{sl}(T_a - T_8) = -k_{sl} \frac{\partial T}{\partial z}$
$\boldsymbol{T_{10}}$	Ambient temperature, T_a
$\boldsymbol{T_{11}}$	Symmetry plane temperature where heat flux is defined by:

	$$-\boldsymbol{n}.\left(-k\frac{\partial T}{\partial y}\right)=0$$
$\boldsymbol{T_{12}}$	Front surface temperature of the sleeve. Net heat flux is approximated by: $$-k_{sl}\frac{\partial T}{\partial y}=h_{nc}(T_{12}-T_a)$$
$\boldsymbol{T_{13}}$	Outer surface temperature of the shaft subjected to open air: $$-k_s\frac{\partial T}{\partial y}=h_{nc}(T_{13}-T_a)$$
$\boldsymbol{T_{14}}$	Cross-section surface temperature of shaft: $$-\boldsymbol{n}.\left(-k_s\frac{\partial T}{\partial y}\right)=0$$

Table 4.1: Heat flow paths for the CFB and shaft

4.1.3 Solver Configurations

Fluid-structure interaction with contacting surfaces including Reynolds equation makes the problem highly nonlinear. Moreover, thin structure of the foil over a larger geometry converts the problem to a stiff one. To yield a reasonable output, the analysis must be carefully configured and an optimized solver for this problem must be selected. For this type of problems, COMSOL applies a fully coupled nonlinear solver that uses an affine invariant form of the damped version of Newton's method [107] which is explained in [108]. The linear solver for the intermediate calculations are realized by the parallel sparse direct linear solver PARDISO (Parallel Sparse Direct and Multi-Recursive Iterative Linear Solvers). In the following sections, the solvers are explained in detail.

4.1.3.1 PARDISO direct solver

The PARDISO solver operates on general systems of the form $Ax = b$. To enhance sequential and parallel sparse numerical factorization performance, the underlying algorithm of the solver is based on a Level-3 BLAS update. The BLAS (Basic Linear Algebra Subprograms) are routines that provide standard building blocks for performing basic vector and matrix operations where the Level 1 BLAS perform scalar, vector and vector-vector operations, the Level 2 BLAS perform matrix-vector operations, and the

Level 3 BLAS perform matrix-matrix operations [109]. This system benefits from pipelining parallelism with a combination of left-looking and right-looking supernode techniques. PARDISO is multithreaded parallel solver on platforms that support multithreading [110]. By means of multithreading, the computational time greatly reduces especially if the degree of the freedom in the system is considerably high. The numerical stability and scalability during element factorization is provided by means of supernode pivoting in parallel pivoting methods.

PARDISO calculates the solution of a set of sparse linear equations with multiple right-hand sides, $\boldsymbol{Ax}=\boldsymbol{b}$; using a parallel *LU, LDL* or *LLT* factorization, where $\boldsymbol{A}$ and $\boldsymbol{x}$ are n-by-n matrices and $\boldsymbol{b}$ is n-by-one vector [111]. First of all, the solver computes a symmetric permutation based on either the minimum degree algorithm [112] or the nested dissection algorithm from the METIS package [113] (which is a set of serial programs for partitioning graphs, partitioning finite element meshes, and producing fill reducing orderings for sparse matrices [114]), followed by the parallel left-right looking numerical Cholesky factorization [115]. Diagonal pivoting for symmetric indefinite matrices is used by the solver and an approximation of $\boldsymbol{x}$ is found by forward and backward substitution through iterative refinement. The coefficient matrix is perturbed whenever numerically acceptable pivots cannot be found within a diagonal supernode block. One or two passes of iterative refinement may be required to correct the effect of the perturbations. Furthermore, this method is accurate for large set of matrices from different applications areas as accurate as a direct factorization method that uses complete sparse pivoting techniques [116].

4.1.3.2 Nonlinear solver: Double Dogleg

Numerical methods used to solve for nonlinear optimization problems are iterative. For example, at the k^{th} iteration, a current approximate solution for the problem x_k is available. A new point x_{k+1} is computed by certain techniques, and this process is repeated until the solver converges to an accepted optimum point. The classical conventional methods for optimization problems are line search algorithms like conjugate gradient descent, Newton’s method or Quasi-Newton method. Such an algorithm obtains a search direction in each iteration according to some pre-defined criteria, and searches along this direction to obtain a better optimum point. The search direction is a descent direction, normally computed by solving a sub-problem that approximates the original optimization problem near the current iterate. Thus, there always exist better points along the search direction unless a stationary point is reached.

Trust region algorithms are a class of relatively new algorithms. The trust region approach is strongly related with approximation techniques. An approximate model can be constructed near the current point if a current guess of the solution for the optimization problem exists. The next iteration point is evaluated by using the solution of the approximate model. Actually, most line search algorithms also solve approximate models to determine search directions. However, in a trust region algorithm, the approximate model is selected merely in a region close to the current iteration point. The reason behind this idea is that for general nonlinear functions local approximation models can only fit the original function locally. The region that the approximate model is trusted as a good fit to the original problem is called as the trust region. A trust region is defined normally in a neighborhood centered at the current iterate. The trust region could be adjusted from iteration to iteration according to the quality of the approximation model. If the computations indicate a well approximation to the original problem, the trust region can be expanded. On the other hand, when the approximate model does not work well enough, the trust region should be shrinked.

Due to the bounded nature of the trust region approach, trust region algorithms can use non-convex approximate models. This property brings an advantage to trust region algorithms compared to line search algorithms. Trust region algorithms are thus, reliable and robust, they can be applied to ill-conditioned problems, and they have very strong convergence properties.

Trust region sub-problems are essential to trust region algorithms. Since each iteration of a trust region algorithm requires a solution to a trust region sub-problem, finding an efficient solver for trust region sub-problems is very critical [117]. An efficient method to solve the trust region sub-problems is the so-called *Dogleg method* which was presented by Powell [118]. To find an approximate solution for the sub-problem, i.e., to find $x_{k+1} = x_k + s_k$ such that $\|s_k\| = \Delta_k$, Powell used a path composed of two line segments to approximate s_k. The first line segment runs from the current iteration point to the Cauchy point (which is a point generated by the steepest descent method and solves the quadratic model with the given current values); the second line segment runs from the Cauchy point to the Newton point (next iteration point). Let x_{k+1} be the intersection point of the path and the trust-region boundary. Obviously, $\|x_{k+1} - x_k\| = \Delta_k$. If the Newton step satisfies $\|s_k\| \leq \Delta_k$, the new iterate x_{k+1} becomes the Newton point.

Dennis and Mei [119] proposed that if the point generated by trust region iteration is biased towards the Newton direction, the behavior of the algorithm is further improved. Then we choose a point $\bar{N}$ on the Newton direction, and connect the Cauchy point to $\bar{N}$. The intersection point of the connection line and the trust region boundary is considered as the new iterate x_{k+1}. So, the algorithm follows $x_k \rightarrow CP \rightarrow x_{k+1}^N$ for dogleg, and $x_k \rightarrow CP \rightarrow \bar{N} \rightarrow x_{k+1}^N$ for double dogleg approach [120].

4.2 Finite Difference Code for Film Temperature

The energy equation for the film temperature between the shaft and topfoil is solved by utilizing the finite difference approximation explained in previous sections. The structure of the solution matrix depends on the order chosen to enumerate the unknowns. A 2D domain is required to define the film temperature. Unfortunately, in two space dimensions the structure of the stiffness matrix is not compact, and the nonzero terms cannot be regularly clustered near the main diagonal [87]. The natural rowwise ordering is a good alternative where the unknowns along the bottom row, u_{11}, u_{21}, u_{31}, ... u_{m1}, followed by the unknowns in the second row u_{12}, u_{22}, ..., u_{m2}, and so on, as shown in Figure 4.7. Following index change formula is used to define the node order in the code.

$$k = (j-1)m + i \tag{4.1}$$

The origin is placed on the left corner where x and y axes correspond to the circumferential and axial directions respectively. The boundary conditions for the domain are defined as follows;

$$\begin{gathered} T(0, y) = T_{trailing} \\ T(\theta_{leading}, y) = T_{leading} \\ T(x, L) = T_a \\ \frac{\partial T}{\partial y}|_{y=0} = 0 \end{gathered} \tag{4.2}$$

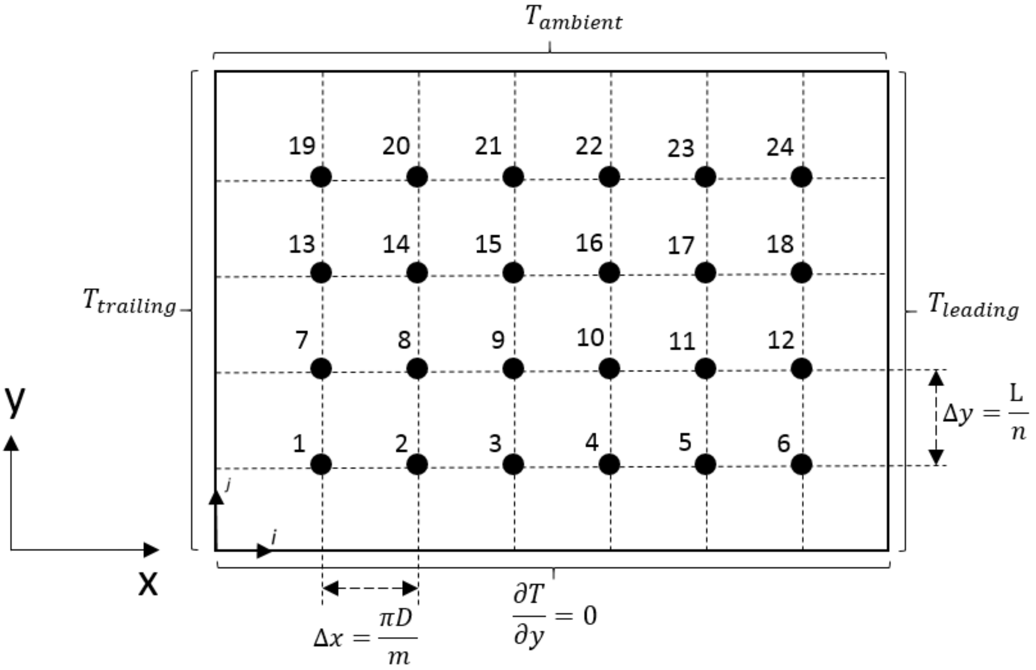

Figure 4.7: A portion of the computational grid for the two-dimensional thermal model of the film gap. The nodes are ordered in the natural row-wise.

Topfoil detachment leads gas film pressure to decrease below ambient pressure [121]. Therefore, fresh cold air is not expected to enter from the axial boundaries into the film. Near the leading edge of the top foil, a thermal mixture between coolant and circulating flows will occur, as shown in Figure 4.8. Mass conservation and energy balances gives the leading edge temperature as

$$T_{leading} = \frac{(1-\Pi)\dot{m}_{trailing}T_{trailing} + \Pi\dot{m}_{cool}T_{cool}}{\dot{m}_{leading}} \tag{4.3}$$

where

$$\dot{m}_{trailing} = \int_0^L (\rho h U)|_{\theta=\theta_{trailing}} dy\,, \qquad \dot{m}_{leading} = \int_0^L (\rho h U)|_{\theta=\theta_{leading}} dy \tag{4.4}$$

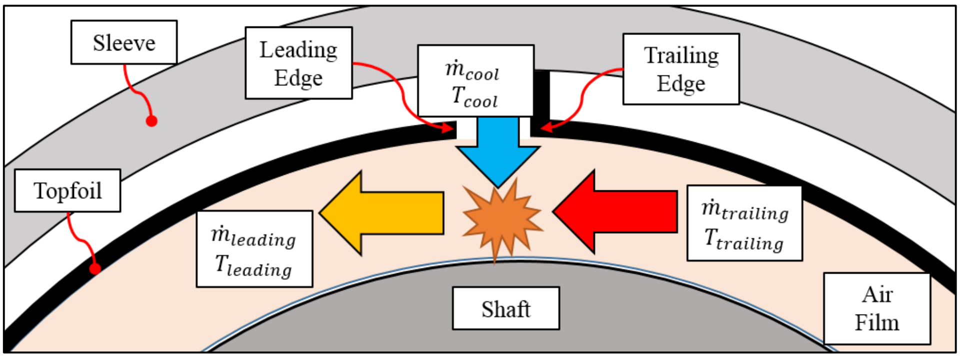

Figure 4.8: An illustration for thermal mixing conditions within the film between trailing and leading edges of top foil

The thermal mixing parameter, Π <1 is determined empirically and it is a function of the externally applied cooling flow and the bearing configuration [63].

Temperature values at trailing and leading edges of the topfoil surface are taken from FEA to the FDM code to define boundary conditions. In addition, the node temperatures of the topfoil and shaft surfaces are included in the FDM solver as explained in Section 3.3. Typical temperature distribution on topfoil and shaft surfaces are given in Figure 4.9.

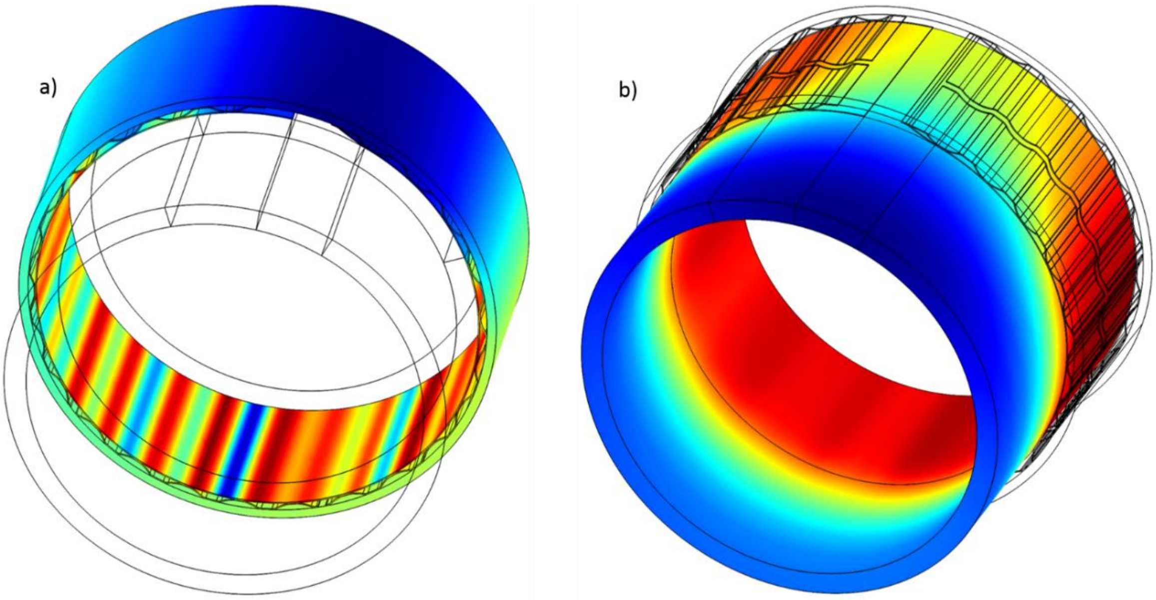

Figure 4.9: Typical temperature distribution in a) Topfoil b) Shaft

There are essentially two different approaches to solve the large linear systems arising from discretizing elliptic equations as in this study. An iterative method starts with an initial guess for the unknowns and attempts to improve the solution via iterative procedure. The code stops when the difference between two consecutive iterations falls below a pre-defined error criteria. Another approach is using a direct method such as Gaussian elimination which yields an exact solution in a finite number of iterations [87]. Iterative methods are more economic in terms of memory storage but less stable for most cases. If adequate storage and efficient elimination techniques are used, direct method provided much more stable solutions in fewer number of iterations. Therefore, direct method is selected due to its superior properties even though it requires more complex coding algorithms and computational resources.

Hydrodynamic pressure distribution and film thickness change over the domain are also included in the solution process. Typical pressure distribution and film thickness change in a foil bearing are displayed in Figure 4.10. They are also exported to the FDM code, and used in calculation of the fluid film temperature.

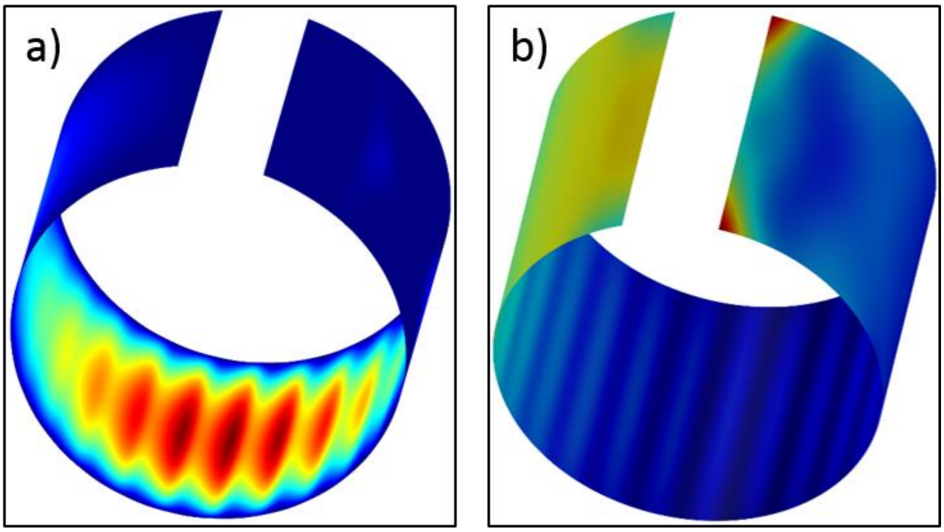

Figure 4.10: Typical a) Hydrodynamic pressure distribution and b) Film thickness in a foil bearing

4.2.1 The Flowchart of Finite Difference Code

The overall flow of the finite difference code is given in Figure 4.11. The code starts by taking the input parameters for the current iteration including hydrodynamic pressure distribution, film thickness change over topfoil surface, temperature distribution on topfoil and shaft surfaces, initial clearance between shaft and topfoil surface, shaft surface speed, trailing and leading edge temperatures. The initialization for parameters involves initial definitions for temperature dependent material properties, geometry dimensions and temporary vectors/matrices. Non-dimensional forms of the solution parameters are used to avoid the matrices to become numerically stiff. The grid numbers are chosen carefully such that the position of the nodes in FDM code exactly corresponds to the nodes in FEA. This is critical because the temperature values of the nodes are assigned to the FEA nodes by using the position information. Another alternative might be using a mapping algorithm which would increase the complexity of the code further, and most probably cause additional instabilities. The code continues with the calculation of the coefficients of the surrounding nodes given in Eq. 3.87. Non-symmetrical sparse stiffness matrix is constructed by using these coefficients as shown in Figure 4.12. The matrix is solved by using LU matrix factorization technique which expresses the stiffness matrix *A* as the product of two essential triangular matrices, one of them a permutation of a lower triangular matrix, ***L*** and the other an upper triangular matrix, ***U*** [122]. To improve the stability of the calculation further, row permutation matrix satisfying the equation ***L*U*=*P*A*** is also utilized.

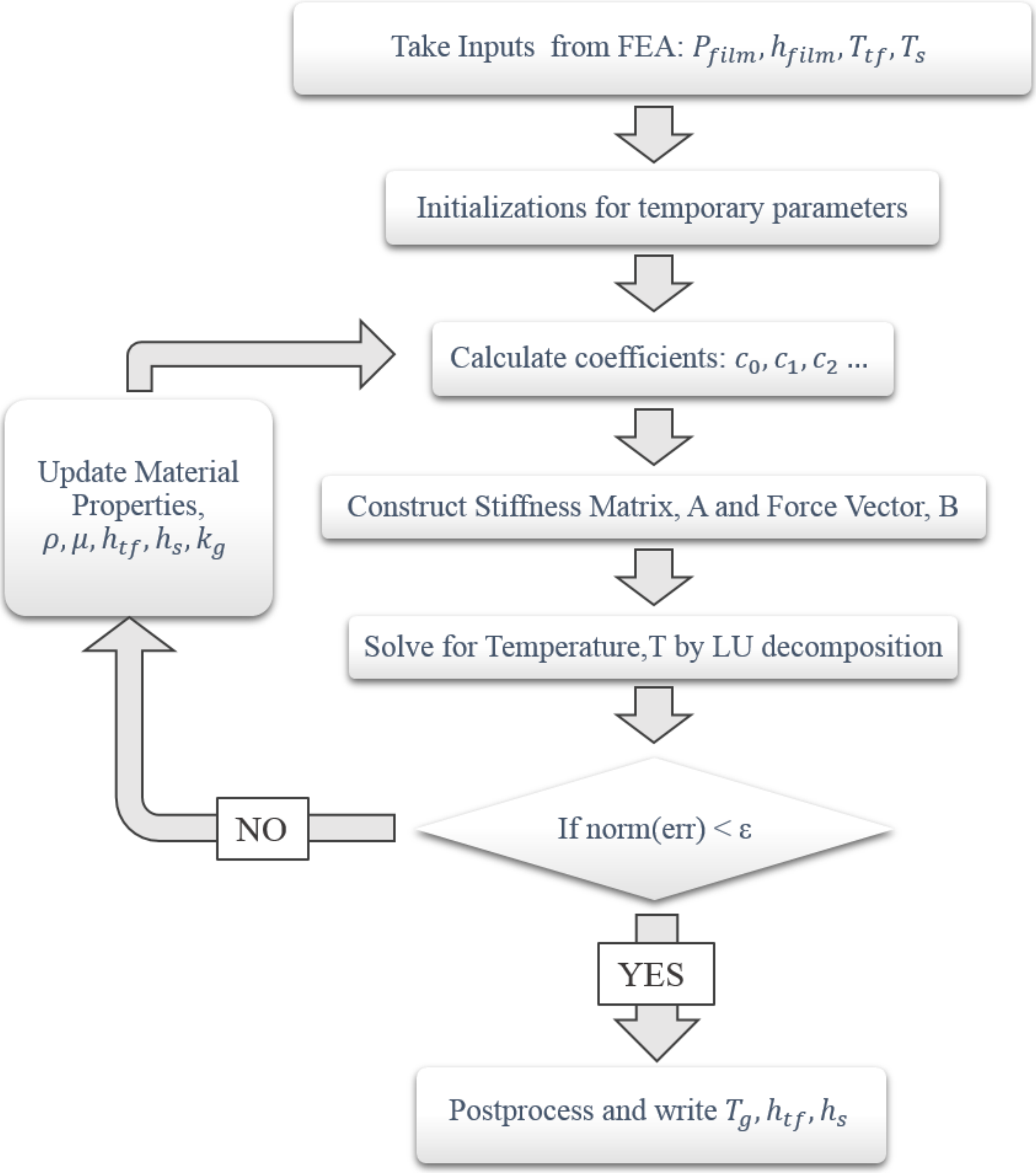

Figure 4.11: The flowchart of the Finite Difference Code to solve for film gap temperature

When the factorization completes, the algorithm checks whether following error criteria is satisfied;

$$\|T^k - T^{k-1}\| = \varepsilon_{err} \tag{4.5}$$

ε_{err} is taken as 0.01 which is sufficient to decide on convergence for film temperature change. If the difference between two consecutive iterations does not satisfy the error criteria, material properties including dynamic viscosity, μ_g, thermal conductivity, k_g and density, ρ_g are updated with respect to the current temperature values for each node. The calculation and required updates keep going until convergence is achieved. When the convergence is obtained, the gas film temperature, T_g and convection coefficients of topfoil and shaft surfaces, $h_{tf,}$, h_j are written to a text file in harddisk. This file is imported by FEA code to estimate the convective heat flux between fluid film and interacting surfaces. The details for this process are explained in the next section.

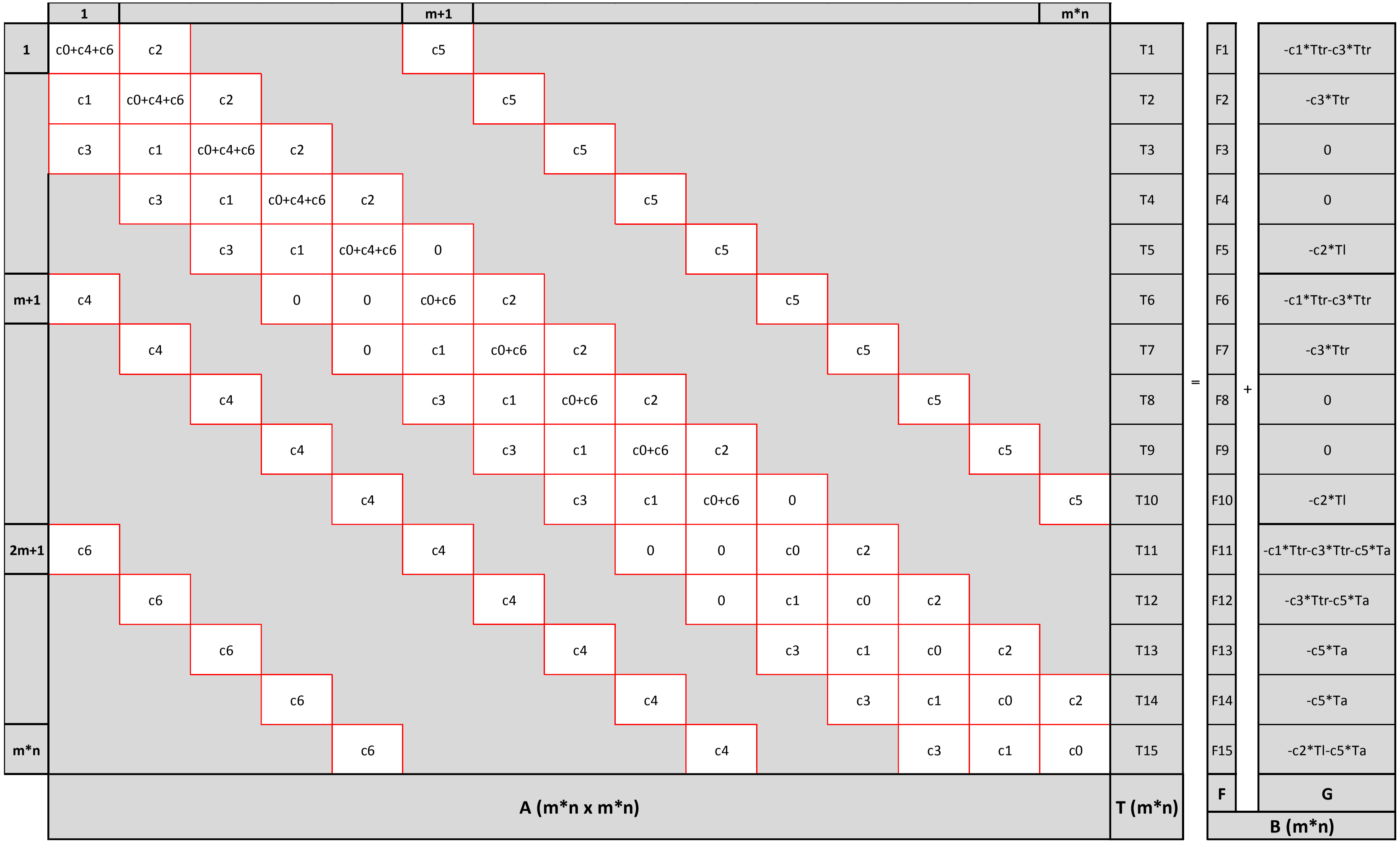

	1					m+1									m*n					
1	c0+c4+c6	c2				c5										T1	=	F1	+	-c1*Ttr-c3*Ttr
	c1	c0+c4+c6	c2				c5									T2		F2		-c3*Ttr
	c3	c1	c0+c4+c6	c2				c5								T3		F3		0
		c3	c1	c0+c4+c6	c2				c5							T4		F4		0
			c3	c1	c0+c4+c6	0				c5						T5		F5		-c2*Tl
m+1	c4			0	0	c0+c6	c2				c5					T6		F6		-c1*Ttr-c3*Ttr
		c4			0	c1	c0+c6	c2				c5				T7		F7		-c3*Ttr
			c4			c3	c1	c0+c6	c2				c5			T8		F8		0
				c4			c3	c1	c0+c6	c2				c5		T9		F9		0
					c4			c3	c1	c0+c6	0				c5	T10		F10		-c2*Tl
2m+1	c6					c4			0	0	c0	c2				T11		F11		-c1*Ttr-c3*Ttr-c5*Ta
		c6					c4			0	c1	c0	c2			T12		F12		-c3*Ttr-c5*Ta
			c6					c4			c3	c1	c0	c2		T13		F13		-c5*Ta
				c6					c4			c3	c1	c0	c2	T14		F14		-c5*Ta
m*n					c6					c4			c3	c1	c0	T15		F15		-c2*Tl-c5*Ta
	A (m*n x m*n)															T (m*n)		F		G
																		B (m*n)		

Figure 4.12: Non-symmetrical sparse matrix for fluid film temperature

4.3 Coupling FEA and FDM

The flow diagram for coupled TEHD solver is displayed in Figure 4.13. The code initiates by solving coupled hydrodynamic pressure and structural deformation in FEA model. The film thickness in Reynolds' Equation is a function of deformation. On the other hand, the deformation is basically calculated by applying hydrodynamic pressure on topfoil surface and also taking thermal effects into account. Hence, the problem is a kind of fully coupled two way fluid-structure interaction (FSI) type. The solution of FEA problem gives the pressure distribution on topfoil surface, film thickness change and temperature distributions both on topfoil and shaft surfaces. These parameters are utilized in FDM to calculate the film temperature by solving the energy equation described in Section 4.2. When film temperature code converges, the temperature of the fluid film and convection coefficients for shaft and topfoil surfaces are exported to a file in harddisk. Actually, there are more obvious ways to connect two softwares such as using special functions that simultaneously solve both code. However, this reduces the speed of the solver drastically and causes unnecessary additional calculations. Thus, an iterative sequential solving methodology is preferred to simplify and accelerate the solver. The exported file is imported by FEA model to be utilized in interpolation functions. Interpolation functions are beneficial to eliminate or reduce the cost for possible problems that may be encountered during exporting the position information of element nodes. These parameters are used to define convection boundary conditions on topfoil and shaft surfaces. FEA code reruns with newly given structural and thermal boundary conditions. The convergence criteria for the solver is the difference of temperature of the fluid film for two consecutive sequential iterations. If the temperature does not change significantly, the solver decides that the analysis is sufficiently converged. If the change is considerable, material properties are updated according to the new temperature values and analysis continues until convergence criteria satisfied.

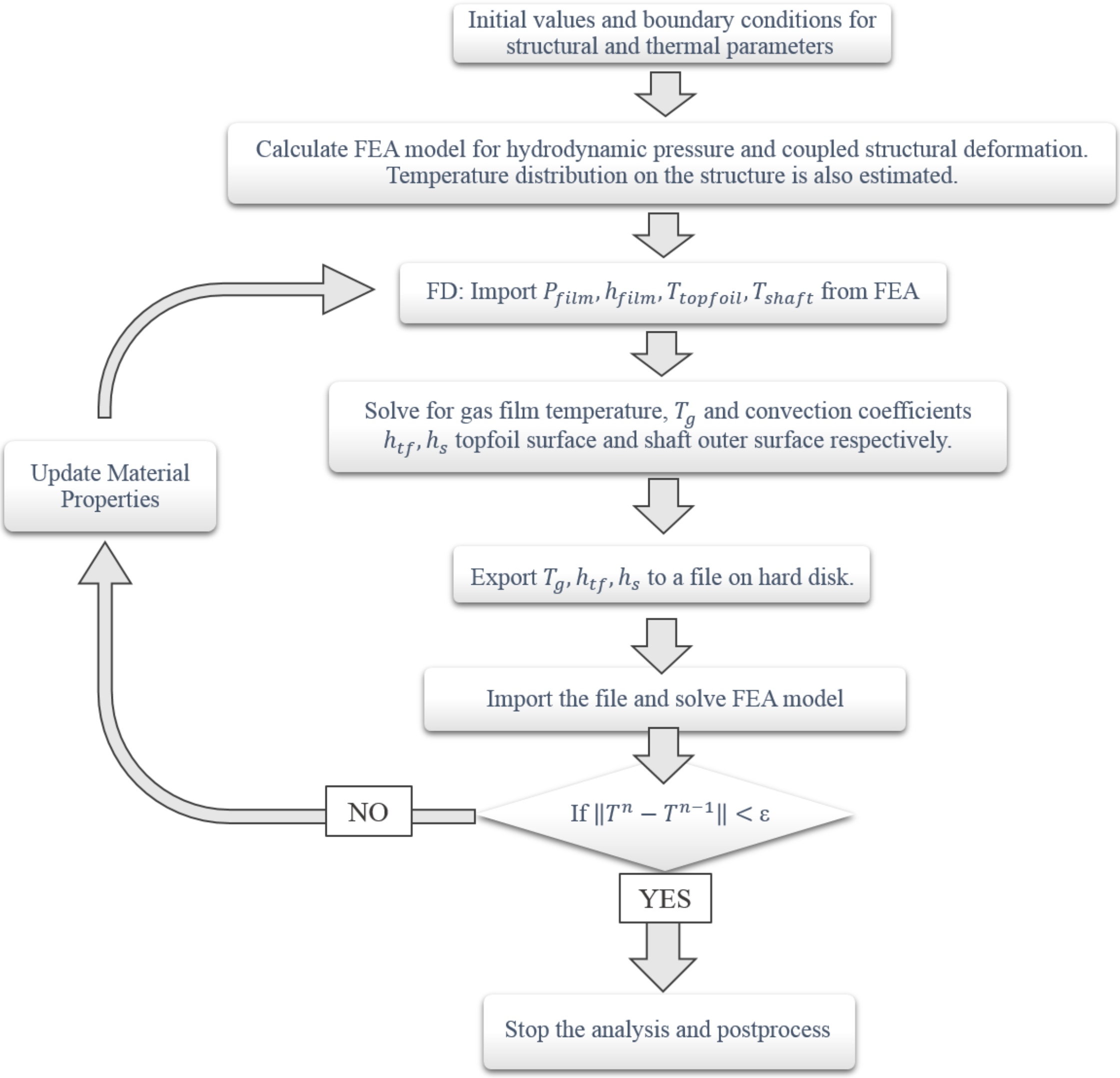

Figure 4.13: Flow diagram for coupled TEHD analysis including FDM and FEA

5 RESULTS AND DISCUSSION

5.1 Model Validation: TEHD Model Predictions versus Experimental Data

The TEHD model developed in this study is benchmarked to the experimental work of Radil and Zeszotek [59] that presented measurements of temperature in a CFB for a number of speed and load conditions. The temperature data is collected by attaching nine K-type thermocouples underneath certain bumps that are in the center and along the bearing edges. The thermocouples are welded to the backside of the contacting region of the bumps to the bearing surface to observe maximum temperatures in the air film. The temperature readings from the TEHD model is performed for similar regions by putting measurement probes in the model as illustrated in Figure 5.1. The axial length of the tested CFB is 41 mm and the diameter is 50 mm. Note however that Ref. [59] does not provide the details for the foil material or the bump strip layers geometry. The assumed parameters for bearing geometry are taken from Ref. [63] and listed in Table 2.1. The material for the bearing is considered to be Inconel X750 which is common for foil bearings due to its superior spring properties especially at elevated temperatures. The shaft material is assumed to be Inconel 718. Temperature dependent material properties for both materials are given in Appendix A.

The tests are conducted for applied static load of increments increasing from 9 N to 222 N. After reaching steady state condition, thermocouples welded beneath certain bumps record metal temperatures. The measurements indicate sudden increase in temperature as the shaft starts to rotate because of the tight assembly clearance. Similarly, as static radial load increases temperature readings steadily increase. Axial temperature gradients are also increasing as the shaft speeds up. The peak temperature measurements are along the bearing midplane independent from tangential position of the bumps.

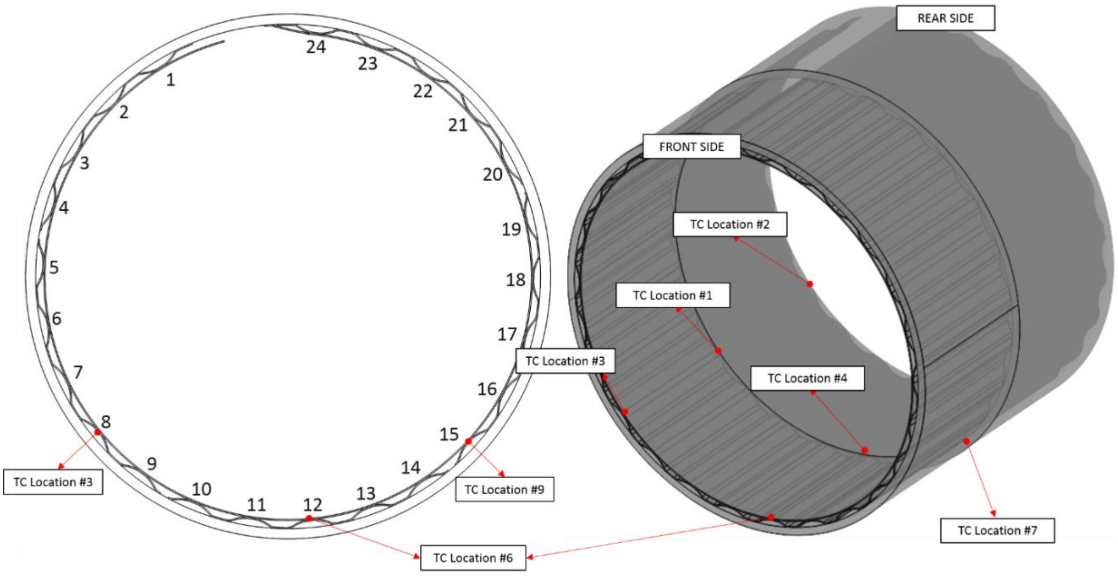

Figure 5.1: Schematic view of the thermocouple locations and numbering convention of the bumps. The model is axially symmetric in the center and the locations at the edges are identical.

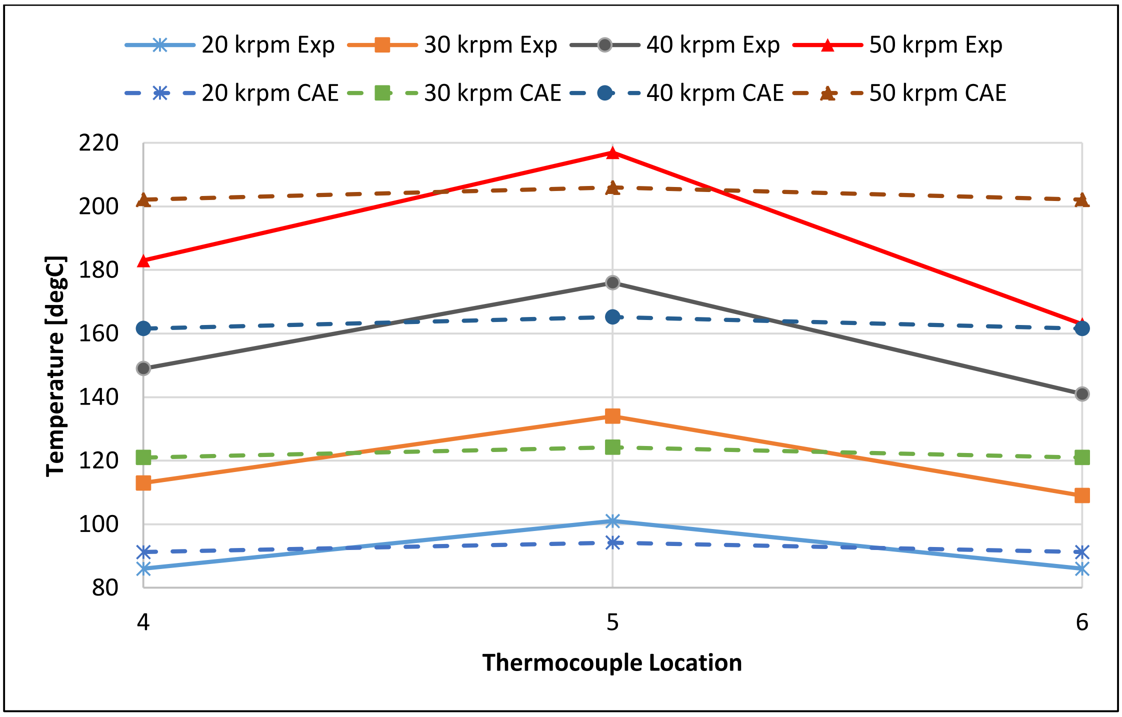

Figure 5.2: Comparison of the film temperatures prediction at bearing center and edges for various shaft speeds. The comparison is performed for the radial load of 222 N. The dashed lines belong to the TEHD model whereas the continuous lines are for experimental data taken from Ref. [59].

Temperature readings from the experiment for thermocouple locations of #4, #5 and # 6 that shows the axial temperature distribution in the vicinity of maximum pressure zone are compared to the results obtained from TEHD model as given in Figure 5.2. The results are in agreement in terms of magnitude except that axial temperature gradient is smaller in the model compared to the test results. The temperature values are higher in the center than the edges independent from the shaft speed. The shaft speed has a drastic effect on temperature increase for all locations. The difference between the model and the test results indicate the transient characteristics of the viscous heating. The steady state model does not capture the transient effects adequately but simulates the average trend very well.

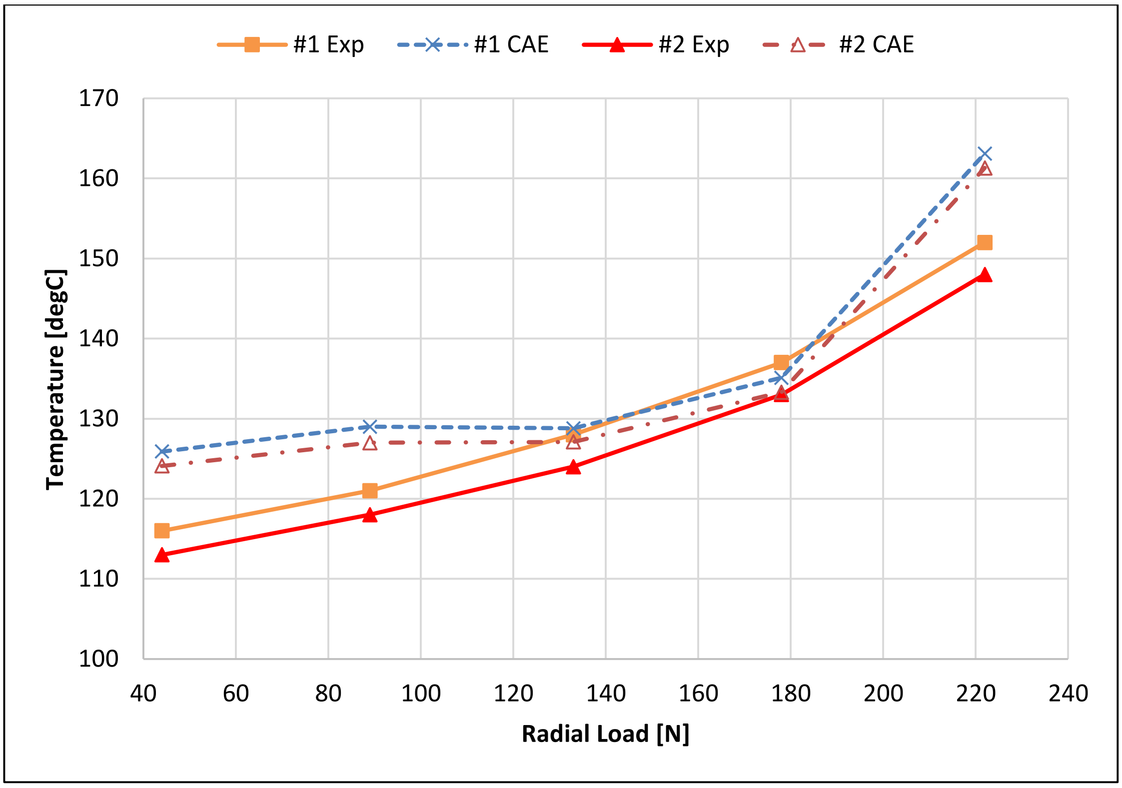

Figure 5.3: Prediction of the film temperatures at the bearing center and edge with respect to the radial load. The data are taken for the shaft speed of 40 krpm. The dashed lines belong to the TEHD model whereas the continuous lines are for experimental data taken from Ref. [59]

The change of the temperature readings at the bearing midplane and bearing edge from the experiment and corresponding values from the TEHD analysis with respect to the increasing radial load is displayed in Figure 5.3. The trend of the temperature increase is parabolic as the applied load increases. The TEHD study predicts slightly higher temperatures than the experiment but captures the behavior very well. The agreement is more obvious for intermediate loading values.

Figure 5.4 depicts the role of the changing shaft speed on bearing surface temperature both at the bearing center and edges. The temperature is increasing quickly as shaft speed increases. Note that temperature nearly doubles when the speed doubles. This is an expected result due to the increasing shear heat effect of the shaft surface due to thin film. Both the predictions and measurements illustrate that the temperature is higher in the bearing center compared to the edges. Another critical observation from this plot is the requirement to an external axial cooling system that would replace the heated circulating fluid with fresh air and prevent a possible failure of the bearing due to thermal runaway. As stated in previous sections, one of the advantages of the foil bearing is its operation capability at very high surface speeds. However, this analysis demonstrates that without an advanced cooling mechanism the bearing could not operate at high speeds due to the rapid heat generation in the fluid film.

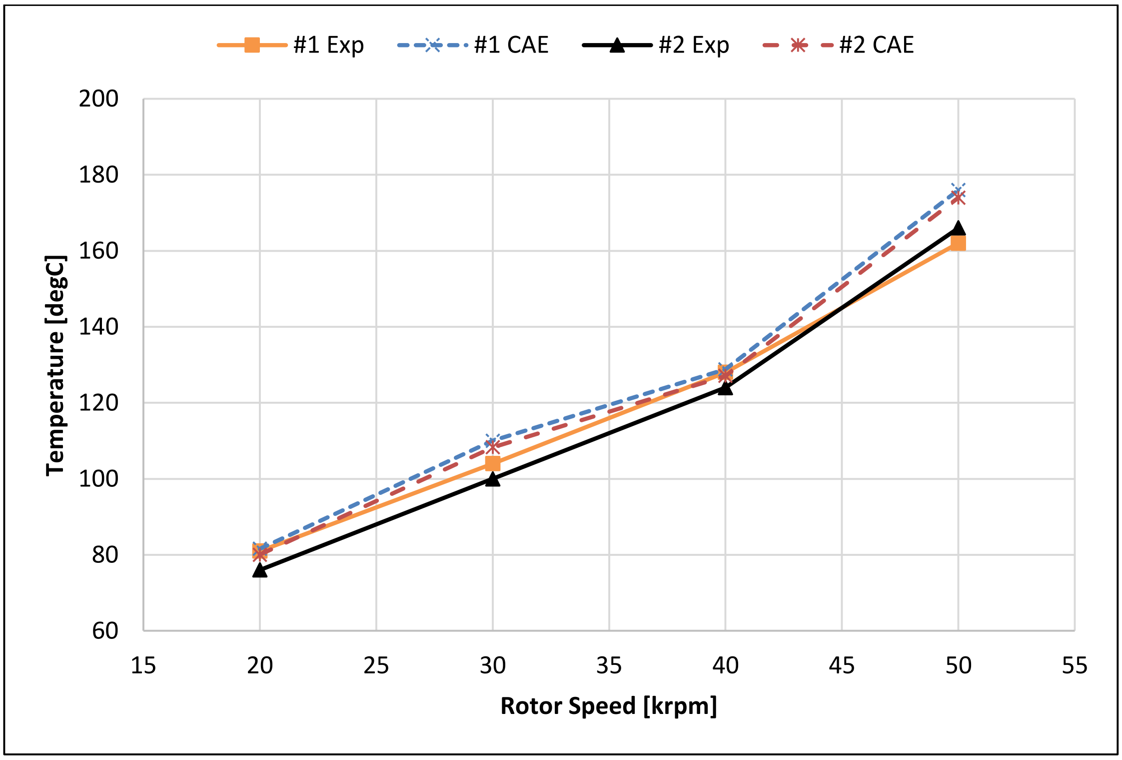

Figure 5.4: Prediction of the film temperatures at the bearing center and edge with respect to the shaft speed. The data are taken for the radial load of 133 N. The dashed lines belong to the TEHD model whereas the continuous lines are for experimental data taken from Ref. [59].

The comparison of the predictions of the TEHD study and measurements from the experiment for the effect of the shaft speed and radial load on temperature increase in the bearing center is given in Figure 5.5. The predicted temperatures correlate favorably with the measurements especially for low speeds but begin to deviate as shaft speed increases. The shaft speed increase contributes to the heating of the bearing surface more than the radial load. Accelerating the shaft 10 krpm results approximately 30˚C temperature increase in bearing center.

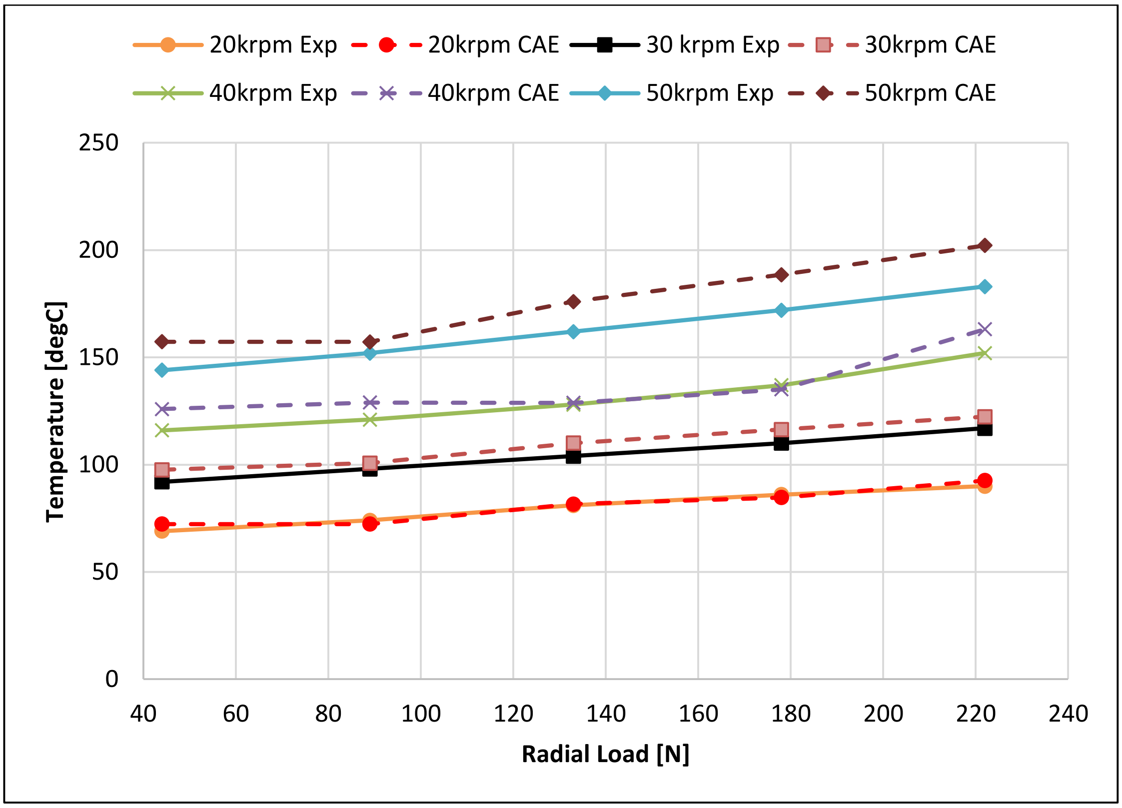

Figure 5.5: Prediction of the film temperatures at the bearing center in thermocouple location of #1 with respect to the radial load. The data are taken for various shaft speeds. The dashed lines belong to the TEHD model whereas the continuous lines are for experimental data taken from Ref. [59]

The complete list for the temperature measurements and corresponding predictions from the TEHD model is presented in Table 5.1 There is a good agreement between the predicted temperatures from the developed TEHD model and measurements from the experiment detailed in Ref. [59]. This benchmark study indicates that the proposed model captures the physics of the CFB under various operation conditions and could be utilized in further investigation of foil bearings.

Shaft Speed	TC Loc.	Radial Load									
		44 N Lit.	44 N CFD	89 N Lit.	89 N CFD	133 N Lit.	133 N CFD	178 N Lit.	178 N CFD	222 N Lit.	222 N CFD
20 krpm	1	69	72.3	74	72.3	81	81.6	86	84.7	90	92.6
	2	65	70.8	70	70.8	76	80	81	83.1	85	90.9
	3	61	70.8	66	70.8	72	80	77	83.1	80	90.9
	4	77	73.6	82	73.9	90	82.9	96	86.4	101	94.2
	5	67	71.4	71	71.2	77	80.6	82	83.5	86	91.2
	6	66	71.4	71	71.2	77	80.6	82	83.5	86	91.2
	7	72	72.9	78	73	86	82.6	92	85.5	97	93.4
	8	65	71.1	69	71.1	76	80.6	81	83.6	84	91.4
	9	61	71.1	65	71.1	72	80.6	77	83.6	81	91.4
30 krpm	1	92	97.6	98	100.7	104	110	110	116.4	117	122.3
	2	88	95.9	94	89.9	100	108.3	106	114.6	112	120.6
	3	79	95.9	83	89.9	89	108.3	94	114.6	100	120.6
	4	106	99.3	112	102.4	119	111.8	126	118.2	134	124.2
	5	90	96.3	96	99.4	102	108.7	108	115	113	121
	6	87	96.3	92	99.4	98	108.7	103	115	109	121
	7	98	98.3	105	101.4	112	110.9	119	117.2	127	123.4
	8	88	96.3	93	99.4	99	108.8	106	115.1	112	121.2
	9	79	96.3	84	99.4	89	108.8	96	115.1	102	121.2
40 krpm	1	116	125.9	121	129	128	128.8	137	135.1	152	163.1
	2	113	124.1	118	127	124	127.1	133	133.3	148	161.3
	3	97	124.1	101	127	107	127.1	114	133.3	127	161.3
	4	136	127.4	141	130.8	149	130.8	160	136.9	176	165.2
	5	114	124.8	119	127.6	126	127.4	134	133.6	149	161.6
	6	107	124.8	111	127.6	118	127.4	127	133.6	141	161.6
	7	125	127	131	129.8	139	129.8	150	136.2	167	164.5
	8	112	124.7	117	127.6	124	127.6	133	133.8	148	162.1
	9	97	124.7	102	127.6	109	127.6	117	133.8	131	162.1
50 krpm	1	144	157.3	152	157.2	162	176	172	188.5	183	202.2
	2	146	155.4	156	155.3	166	174	176	186.4	188	204
	3	117	155.4	124	155.3	132	174	141	186.4	151	204
	4	168	159.2	181	159.2	193	177.9	205	190.4	217	206
	5	146	155.8	154	155.8	162	174.4	172	186.8	183	202.2
	6	128	155.8	136	155.8	143	174.4	154	186.8	163	202.2
	7	156	158.2	166	158.2	177	177	190	189.8	202	205.4
	8	142	156	151	156	160	174.8	171	187.4	181	203
	9	118	156	126	156	134	174.8	144	187.4	154	203

Table 5.1: Complete list of the prediction of the film temperatures for all locations with respect to the increasing radial load and various shaft speeds. The experimental data taken from Ref. [59] is given in blue and the predictions are in orange columns.

5.2 Performance Parameters Evaluation

In the previous section, the TEHD model predictions for temperatures at certain bumps are compared to the readings from the experiment conducted by Radil and Zeszotek [59] in a CFB. Although the details of the bearing geometry, shaft inner diameter and many other test parameters are not given exactly by the researchers, the presented study provides evidence for good correlation between the developed TEHD model and experiments. In the following sections, the behavior of a CFB is investigated for significant parameters including hydrodynamic pressure, film thickness, temperature distribution, thermal gradients, contact properties, thermal contact resistance, stress distribution and deformation characteristics. These are the essential parameters to determine the performance of a foil bearing for various operating conditions and should be clarified before applying this bearing mechanism to a system or machine.

5.2.1 Hydrodynamic Parameters

The basic hydrodynamic or actually aerodynamic parameters for an air foil bearing are film pressure generated due to the relative motion of the bearing and shaft surfaces, the wedging film thickness that is a function of both eccentric position of the shaft and deformation of the compliant bearing surface and fluid velocity in the film gap. These parameters are also utilized commonly to determine the loading capacity of the bearing, reverse torque applied to the shaft because of the viscous shear friction, drag coefficient, power losses and attitude angle.

5.2.1.1 Pressure field

The predictions for the film pressure in the mid-plane of the foil bearing with the given parameters in Table 2.1 are shown in Figure 5.6. The pressure on bearing surface for different loading conditions is compared with respect to the tangential position at a shaft speed of 40 krpm. The gradient of the pressure with same conditions is also given in Figure 5.7. As seen in both figures, pressure values are highly dependent on bump positions and rippling between two consecutive bumps because of the deformation of the topfoil/bearing surface under pressure. The peak values for the pressure are occurring at places contacting with bumps where film thickness is also minimum. This behavior is very specific for foil bearings and cannot be observed in conventional bearings due to their rigid bearing surface. The ripples are damped as the flow is approaching to leading and trailing edges. The magnitude of the pressure gradient is also growing as static radial load is increased. The mean value of the pressure predictions in this study is similar to the results obtained in literature. However, the resolution capability of the proposed model is apparently stronger than the previous analyses. While the previous models estimate the deformation of the bearing surface with a simple elastic formulation, presented model employs the power of finite element method combined with a fine grid of the solution domain as well as simultaneous multi-physics solver approach.

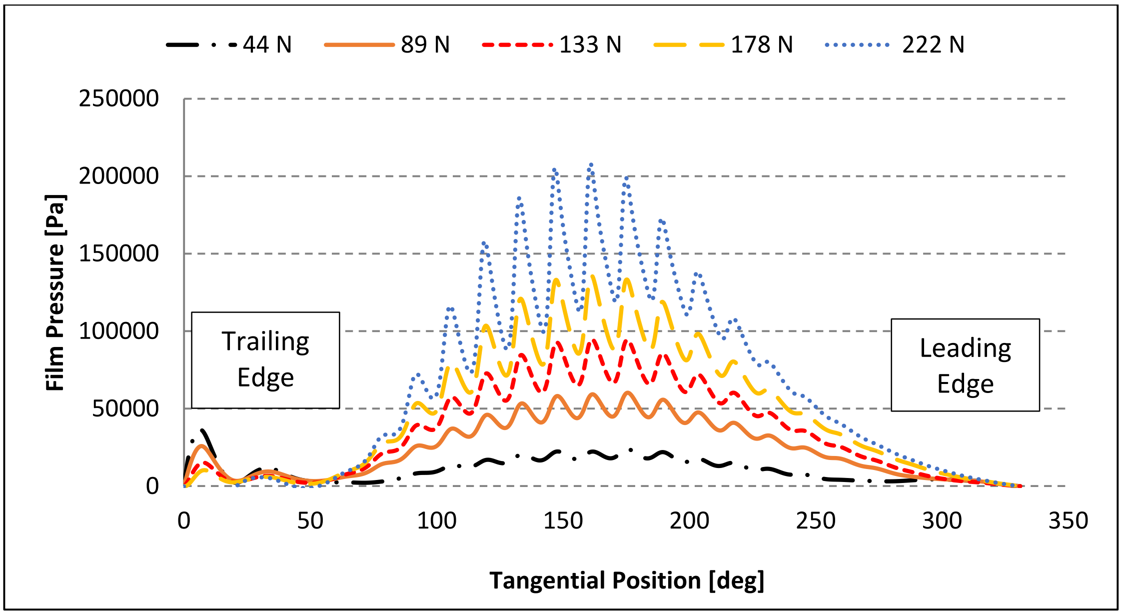

Figure 5.6: Predictions for the film pressure in the mid-plane of the bearing surface in tangential direction for different loading conditions. The shaft speed is 40 krpm.

Note that the pressure gradient is significantly high as radial load is increased and reaches almost 1 bar/mm which may be critical for structural durability of the bearing surface and supporting bumps for long operation periods. This should be investigated in detail to predict possible fatigue failure mechanisms and propose better bearing designs especially for heavily loaded conditions.

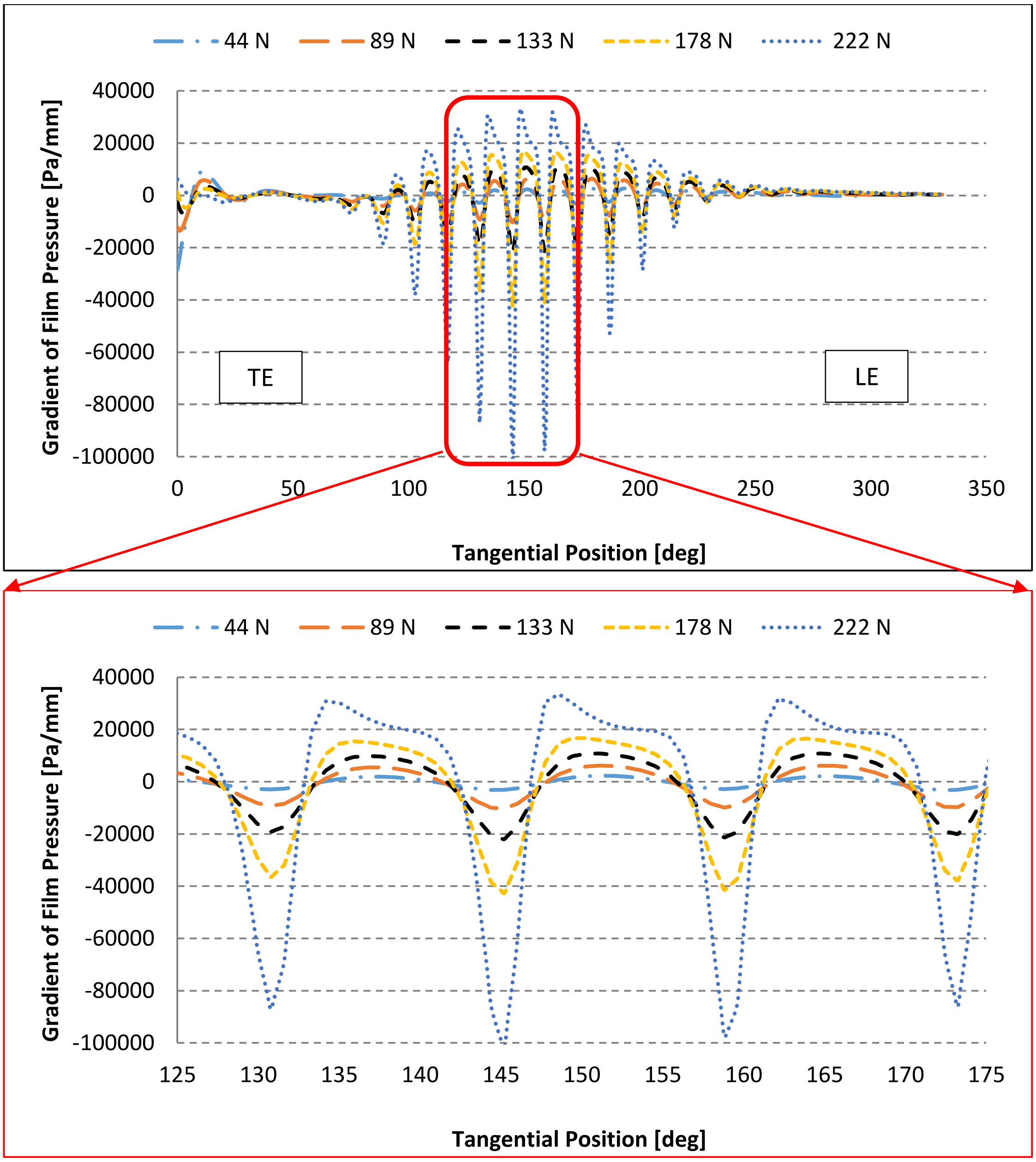

Figure 5.7: Predictions for the gradient of the film pressure in the mid-plane of the bearing surface in tangential direction for different loading conditions. The shaft speed is 40 krpm. The second figure displays the critical section along the circumferential position between 125 to 175 deg.

Figure 5.8 depicts 2D pressure distribution for various radial load conditions at shaft speed of 30 krpm. Although there are several peak points, highest pressures are predicted along the circumferential coordinates of 160 to 175 degrees. The highest pressure values are highly dependent on radial load and increase almost linearly with a slope of 550 to 850 Pa/N. For lightly loaded conditions, high pressure zone constitutes almost continuous characteristics with evenly distributed peaks. On the other hand, as radial load is increased, the pressure region separate into smaller sections with higher pressure peaks and very high pressure gradient. This behavior may cause buckling of the bearing surface under heavily loaded conditions which may eventually result in an ultimate failure of the bearing due to seizure to the shaft surface.

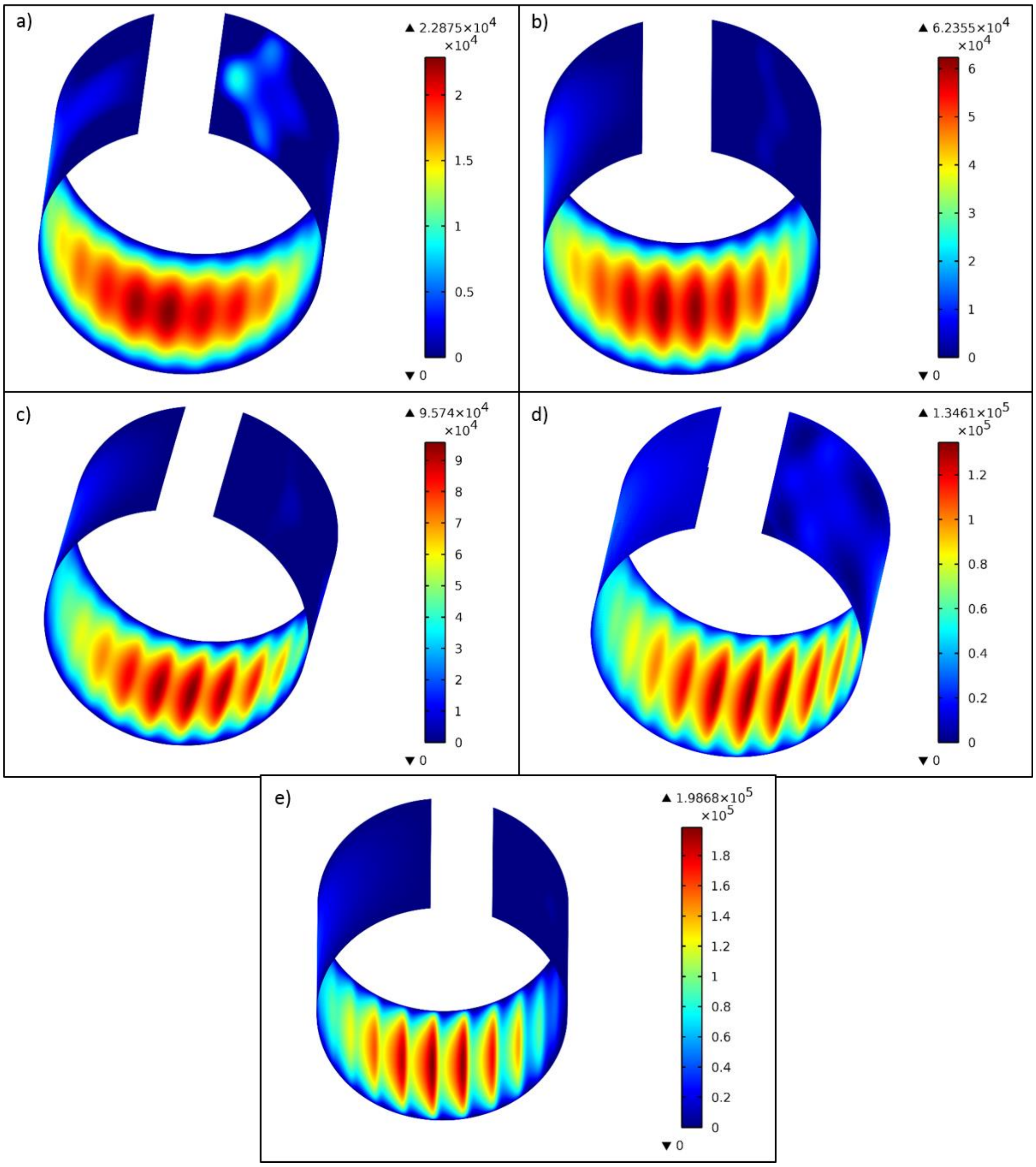

Figure 5.8: Predicted pressure fields on bearing surface of the CFB for different static radial loads. The results are given for the shaft speed of 30 krpm. The radial loads are a) 44 N b) 89 N c) 133 N d) 178 N e) 222 N. The units are in Pascal [Pa].

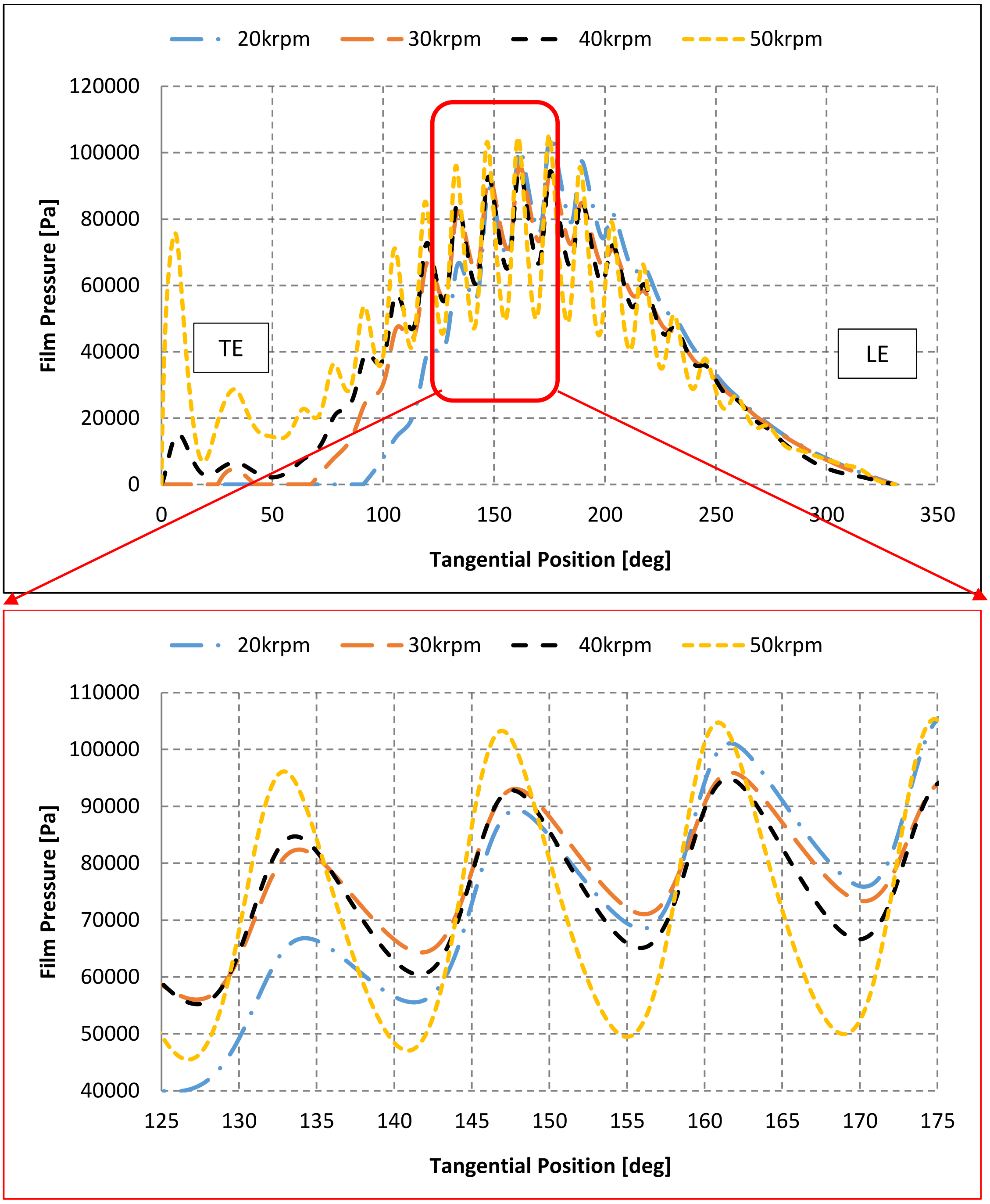

Figure 5.9: Predictions for the film pressure in the mid-plane of the bearing surface in tangential direction for different shaft speeds. The static radial load is 133 N. The second figure displays the critical section along the circumferential position between 125 to 175 deg.

To prevent such conditions, advanced design techniques should be applied to optimize the film pressure distribution on bearing surface. Note that the axial gradient of the pressure is also very high as radial load increases. This might be another source of failure due to the detachment of the topfoil surface from edges that may contact to the shaft surface. The intuitive solution to such problems is adjustment of the stiffness by playing with geometrical dimensions of the supporting bumps. As a matter of fact, new generations of foil bearings are proposed to solve these problems by distributing the bump stiffness with respect to the load conditions and related film pressure such that stiffness is higher where maximum pressure values are expected.

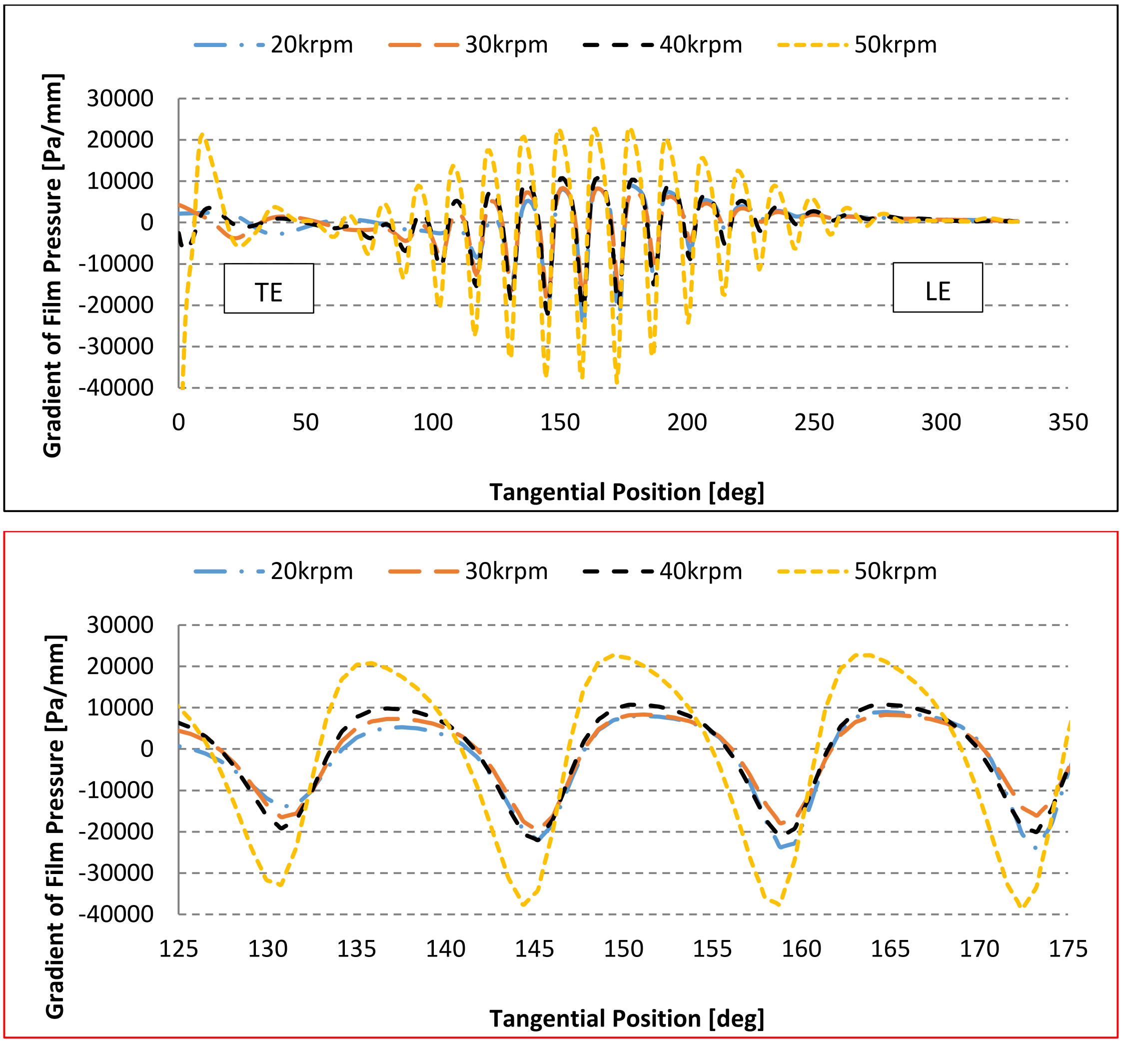

Figure 5.10: Predictions for the gradient of the film pressure in the mid-plane of the bearing surface in tangential direction for different shaft speeds. The static radial load is 133 N. The second figure displays the critical section along the circumferential position between 125 to 175 deg.

The predictions for film pressure distribution in the bearing center along the circumferential direction for different shaft speeds are displayed in Figure 5.9. The static radial load is 133 N for all cases. Although the peak values are very close to each other, the bandwidth of high pressure zone grows as the shaft speed is increased. Furthermore, significant pressure gradients are observed at elevated shaft speeds as shown in Figure 5.10.

The maximum pressure values are almost independent from the shaft speed for the same radial load of 133 N as shown in Figure 5.11. On the other hand, high pressure regions appear when the shaft speed is increased. Note that similar response is observed when the load has increased. The peak values are also predicted along the circumferential coordinates of 160 to 175 degrees.

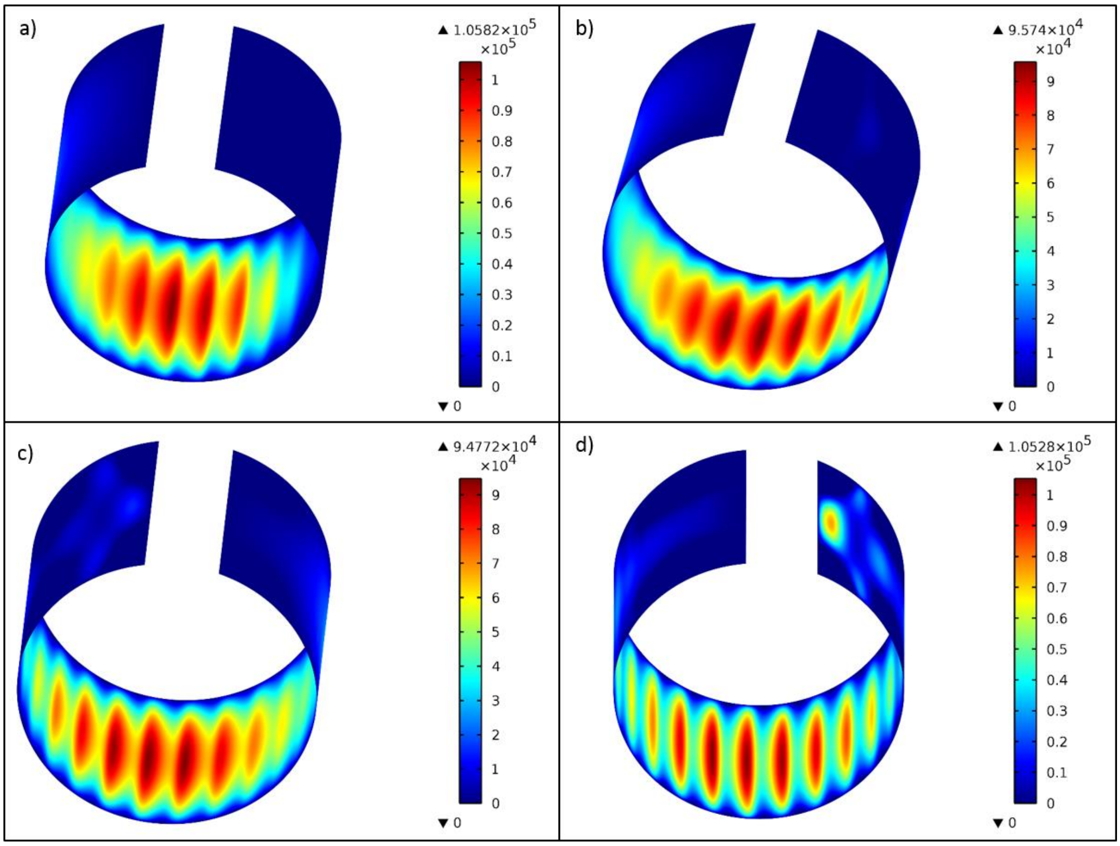

Figure 5.11: Predicted pressure fields on the bearing surface of the CFB for different shaft speeds. The results are given for the static radial load of 133 N. The shaft speeds are a) 20 krpm b) 30 krpm c) 40 krpm d) 50 krpm. The units are in Pascal.

Also note that when the shaft speed reaches to 50 krpm, the pressure locally increases around trailing edge where the topfoil structure is tack welded to the sleeve. As already stated previously, the topfoil structure starts to buckle due to the high pressure gradients and film thickness shrinks as the topfoil surface approaches to the shaft surface. Therefore, the tendency of the topfoil structure to buckle at elevated shaft speeds and/or heavily loaded cases should be carefully examined to prevent ultimate bearing failures by tailoring the design according to the operating conditions.

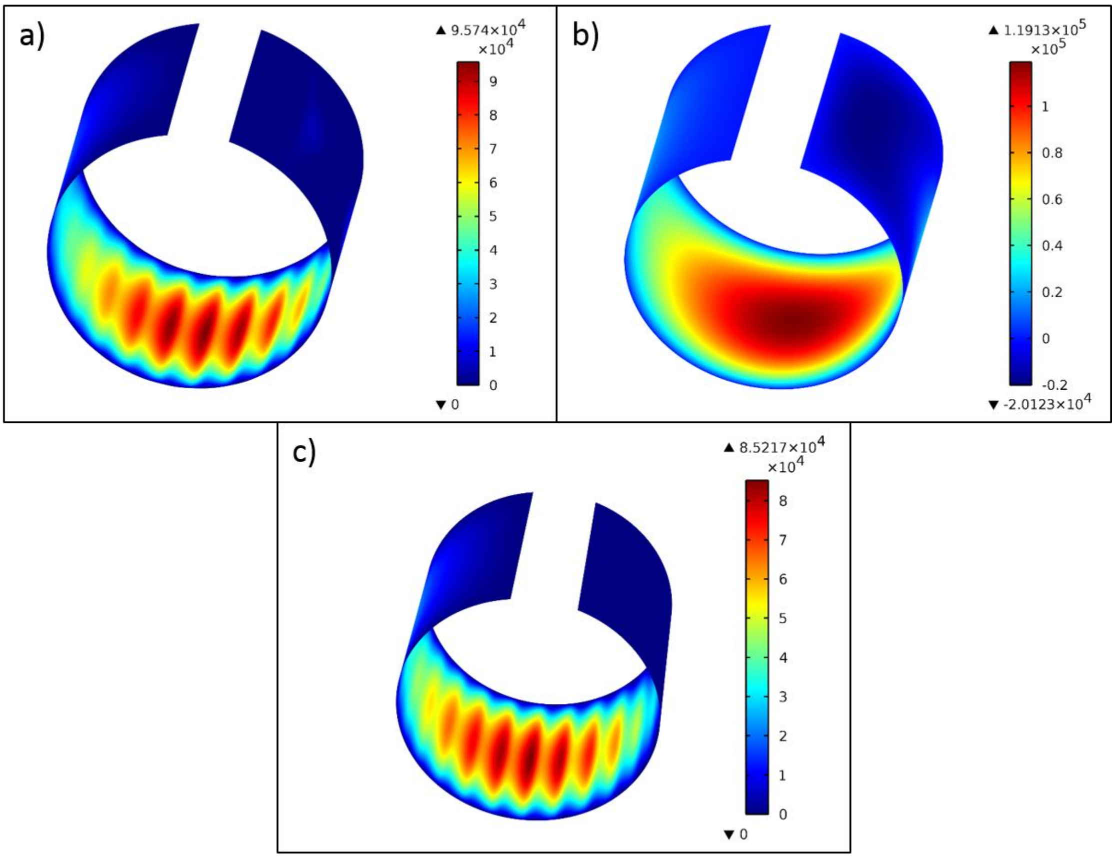

Figure 5.12: Comparison of the predicted pressure fields on bearing surface of the a) THD model b) Rigid bearing c) Isothermal. The results are given for the shaft speed of 30 krpm and the static radial load of 133 N.

The pressure field of the CFB obtained from TEHD model is compared to a rigid bearing and isothermal model for the same foil bearing as displayed in Figure 5.12. The shaft speed is 30 krpm and the radial load is 133 N. The dimensions and operating conditions are identical for all cases except that deformation of the bearing surface is not allowed for rigid bearing model. The isothermal model assumes a constant temperature that is equivalent to ambient temperature. Note that the peak pressure values are higher in a rigid bearing to sustain the radial load. Because the bearing surface is compliant in a foil bearing, it enables deformation under pressure. Therefore, the pressurized region easily extends to relatively larger area than a rigid bearing and the total force exerted in vertical direction is adequate to bear the applied load with a lower film pressure. On the other hand, the isothermal model does not account thermal expansion of bearing components and material property changes in the fluid but the pressure profiles are very similar to each other. The peak pressure predictions in isothermal model is even less than TEHD model.

The predictions for the film pressure at the bearing center is illustrated in Figure 5.13 for TEHD and isothermal models of the foil bearing, and a rigid gas bearing. The radial static load is 133 N and the shaft speed is 30 krpm. The pressure profile is very smooth in a rigid bearing compared to the ripples in foil bearing. Furthermore, the peak pressure is predicted along the circumferential coordinate of 160 deg in rigid bearing whereas it occurs around 175 deg for foil bearing. It also appears that subambient pressure is possible in a rigid bearing but it is not allowed in a foil bearing due to the deflection of the bearing surface.

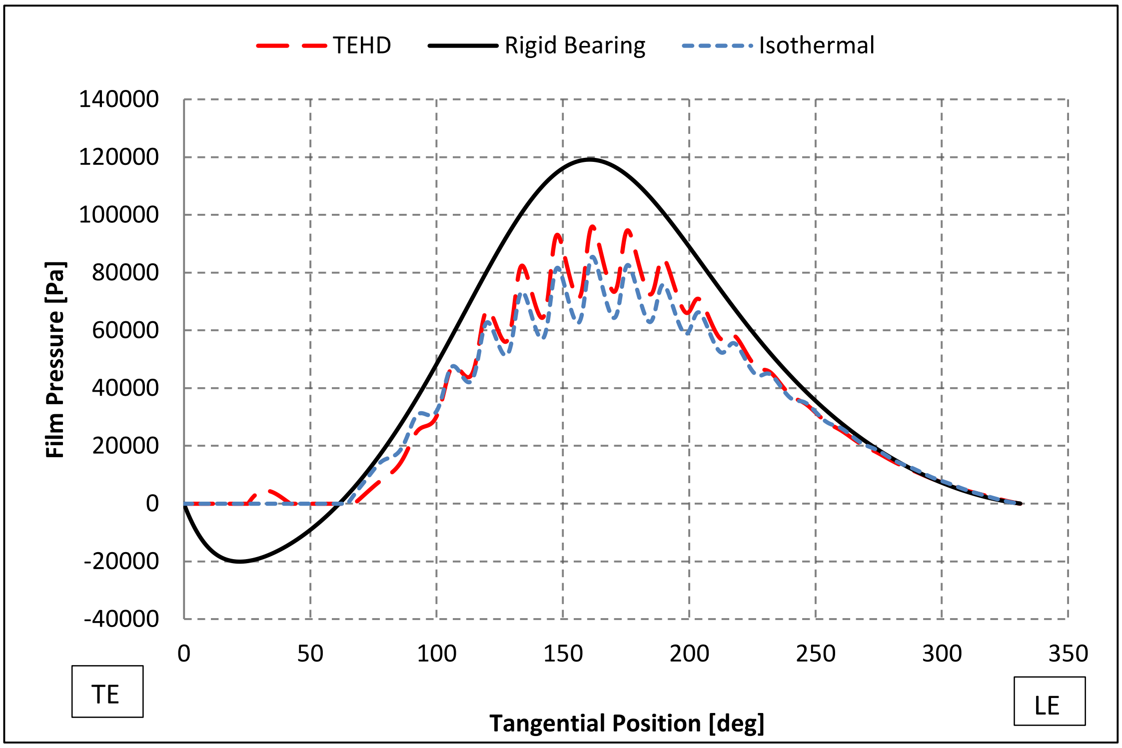

Figure 5.13: Comparison of the predictions for the film pressure in the mid-plane of the bearing surface in tangential direction for the TEHD model, isothermal model and rigid bearing. The results are given for the shaft speed of 30 krpm and the static radial load of 133 N.

5.2.1.2 Film thickness

Film thickness in a foil bearing is a function of both hydrodynamic pressure generated in the film and the deformation of the bearing surface due to this pressure load.

The TEHD model developed in this study considers both effects effectively by solving the hydrodynamic pressure equation (Reynolds Equation) and structural deformation simultaneously.

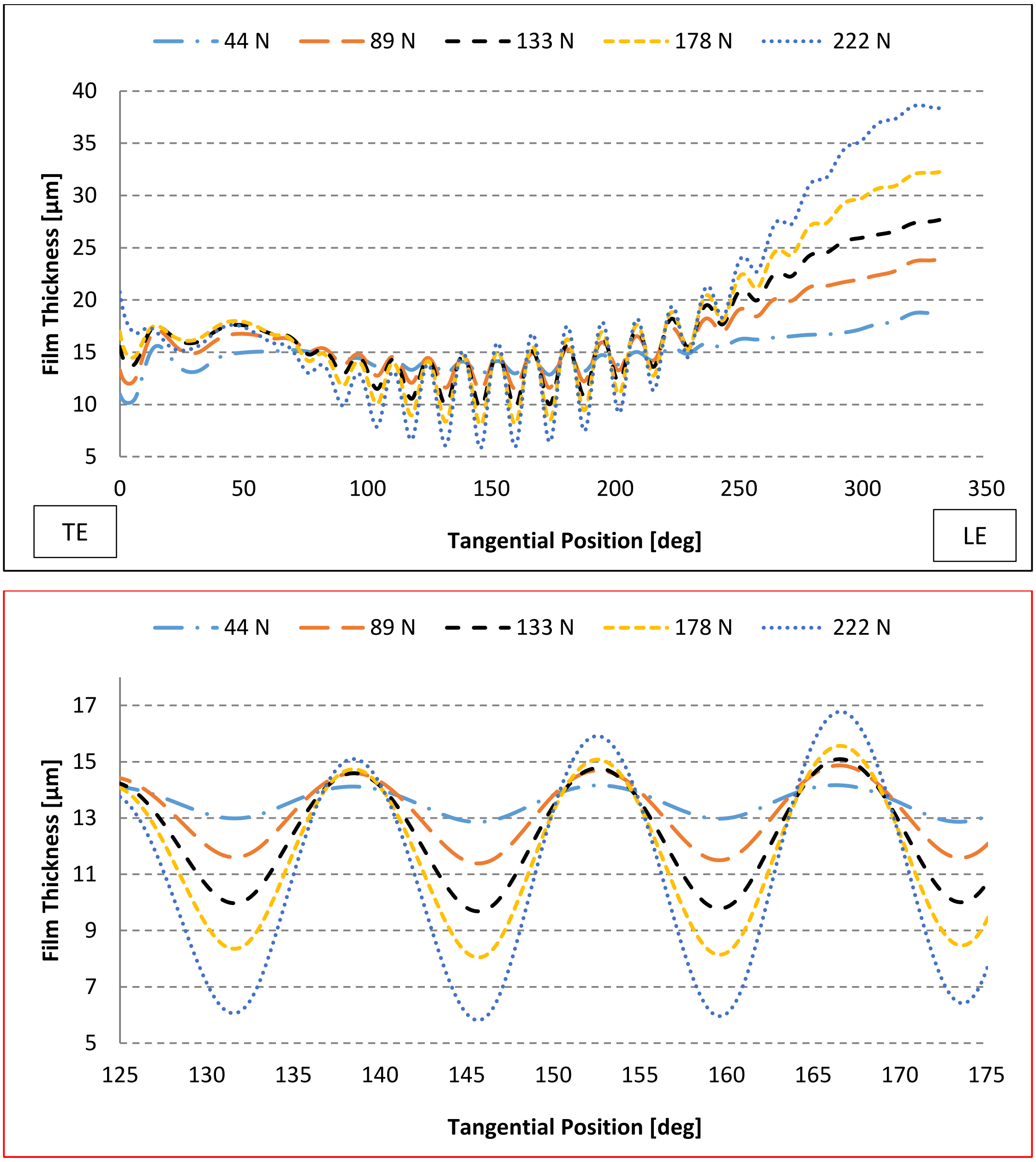

Figure 5.14: Predictions for the film thickness in the mid-plane of the bearing surface in tangential direction for different loading conditions. The shaft speed is 40 krpm. The second figure displays the critical section along the circumferential position between 125 to 175 deg.

Figure 5.14 displays the film thickness change in the mid-plane of the bearing for various loading conditions at the shaft speed of 40 krpm. The wavy distribution of the film thickness is a result of foil deflection between consecutive bumps in a similar fashion of pressure profile. The amplitude of the ripples grows as the load is increased. Minimum film thickness reduces down to 5.8 μm for a static load of 222 N at tangential position of 145 degrees. It is also noteworthy that film thickness increases in the vicinity of leading edge rapidly due to the deflection of the topfoil towards shaft and losing contact from the bumps.

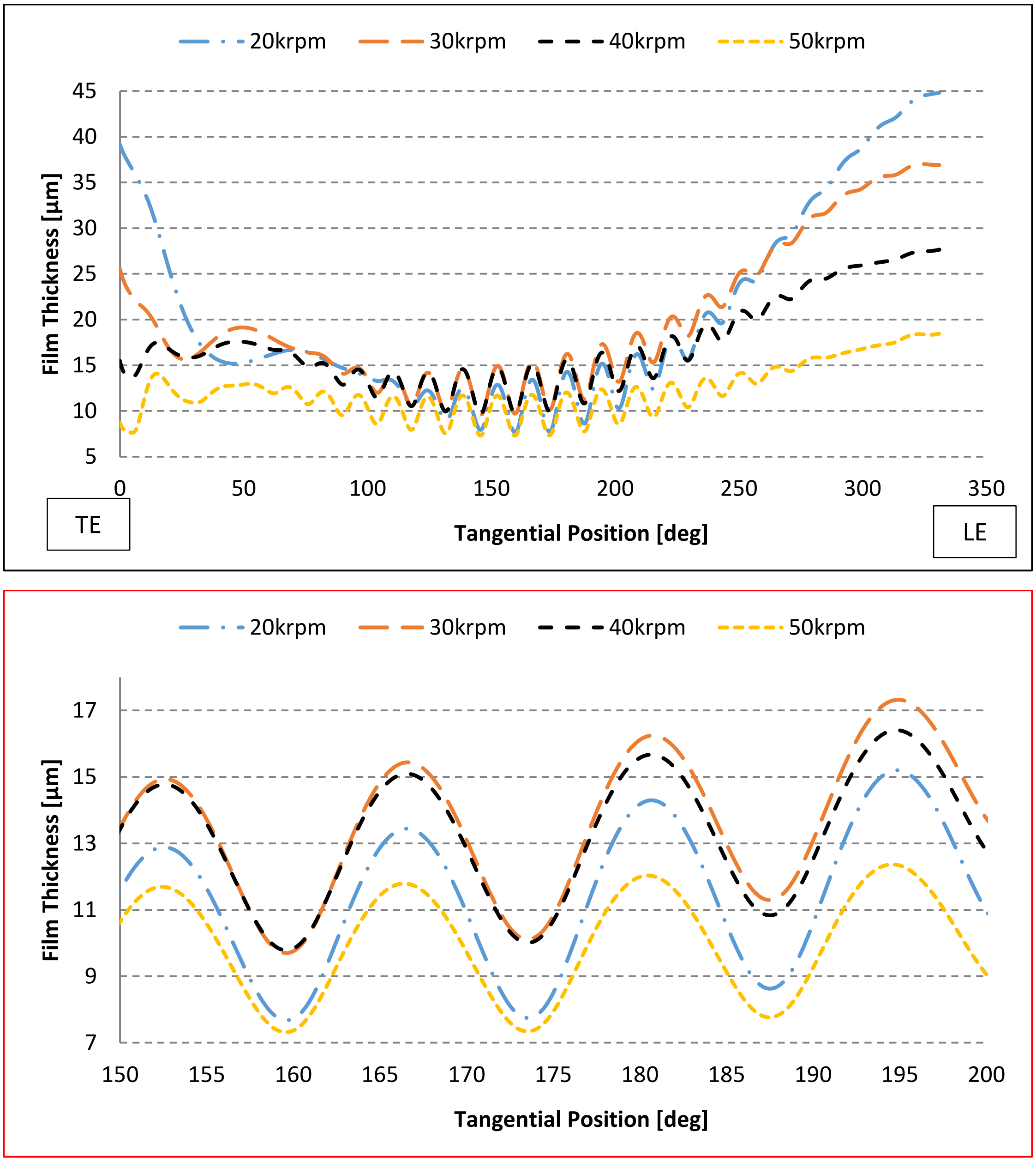

Figure 5.15: Predictions for the film thickness in the mid-plane of the bearing surface in tangential direction for different shaft speeds. The static radial load is 133 N. The second figure displays the critical section along the circumferential position between 150 to 200 deg.

The change of the film thickness in the mid-plane with respect to the shaft speed is illustrated in Figure 5.15. The static radial load is 133 N for all cases. The profile is very similar at maximum pressure region which corresponds to 100 to 200 degrees along the tangential direction but deviates significantly as approached to the edges. Remember from Figure 5.9 that positive pressure is predicted everywhere when the shaft speed is 50 krpm. Hence, film thickness distribution is more balanced at that speed.

On the contrary, pressure is exerted in a smaller region for shaft speed of 20 krpm and film thickness is thin locally in that region and thicker elsewhere. The minimum film thickness predictions at bearing surface mid-plane are 7.67 μm, 9.53 μm, 9.68 μm, and 7.32 μm for shaft speeds of 20, 30, 40, and 50 krpm, respectively.

Film thickness distributions for bearing mid-plane and one of the symmetric edges are compared in Figure 5.16. The shaft speed is 40 krpm and applied radial load is 133 N for this case. The topfoil buckles near trailing and leading edges because of the high pressure at the center. This is why the film thickness grows rapidly at side edges especially when approached to the free standing leading edge.

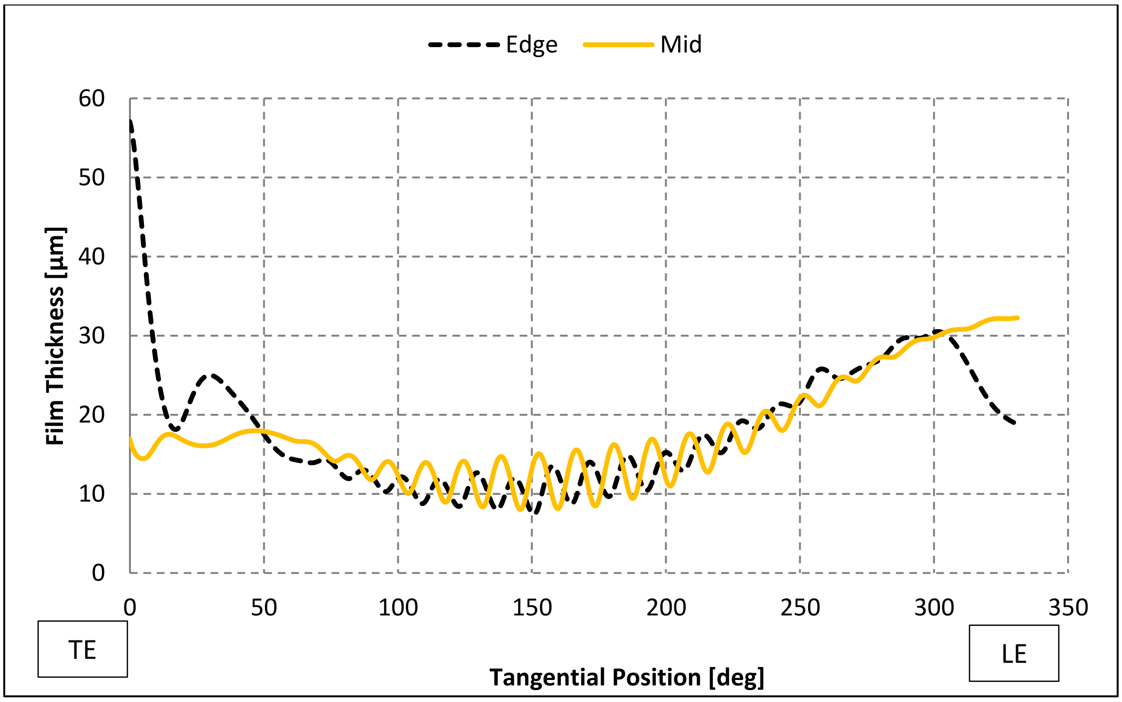

Figure 5.16: Comparison for the film thickness in the mid-plane and the edge of the bearing surface in tangential direction for shaft speed of 40 krpm and radial load of 178 N.

The film thickness predictions acquired from TEHD model are compared to an isothermal model and a rigid bearing in Figure 5.17. The shaft speed is 30 krpm and the radial load is 133 N. The film thickness distribution is very smooth for a rigid bearing in contrast to the ripples in a foil bearing. Minimum film thickness for a rigid bearing is less than a foil bearing due to the higher pressure rates for the same radial load. This indicates that foil bearings could operate under heavier loads without any significant contact problem between the shaft and bearing surfaces due to its compliant mechanism. The predictions for the film thickness in TEHD model is also thicker around leading edge in comparison to the isothermal model which does not take thermal expansions into account. However, the predictions are comparable to each other near high pressure section of the bearing surface. This situation can be observed better in Figure 5.18 where 2-D film thickness distributions are presented for the TEHD and isothermal models, and a rigid bearing.

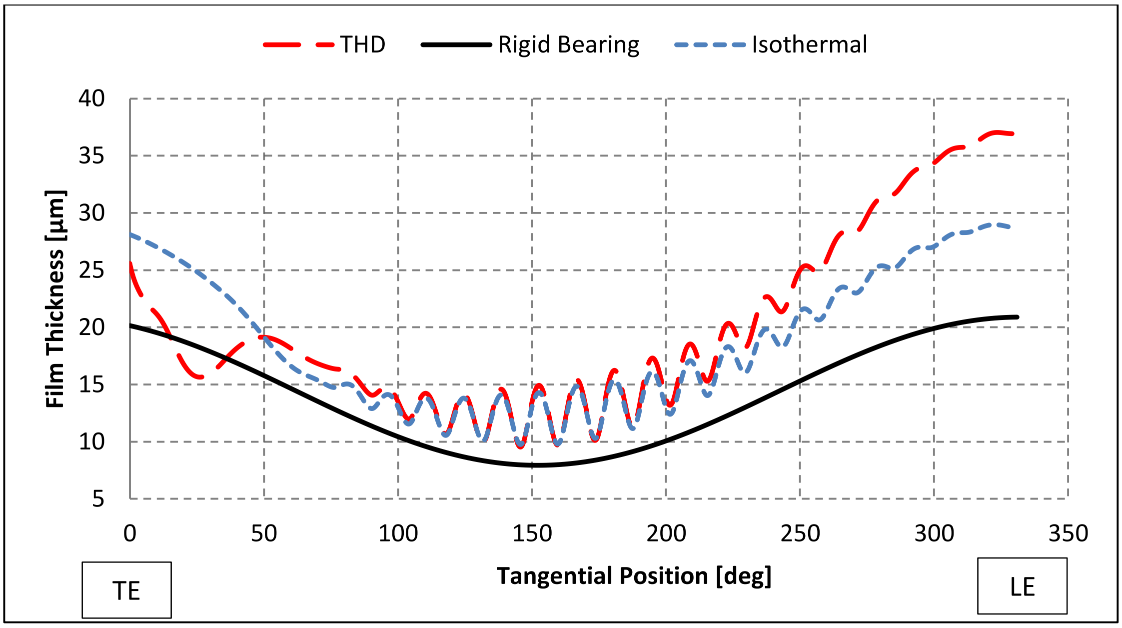

Figure 5.17: Comparison for film thickness predictions in the mid-plane for the TEHD, isothermal model and rigid bearing. The speed is 30 krpm and load 133 N.

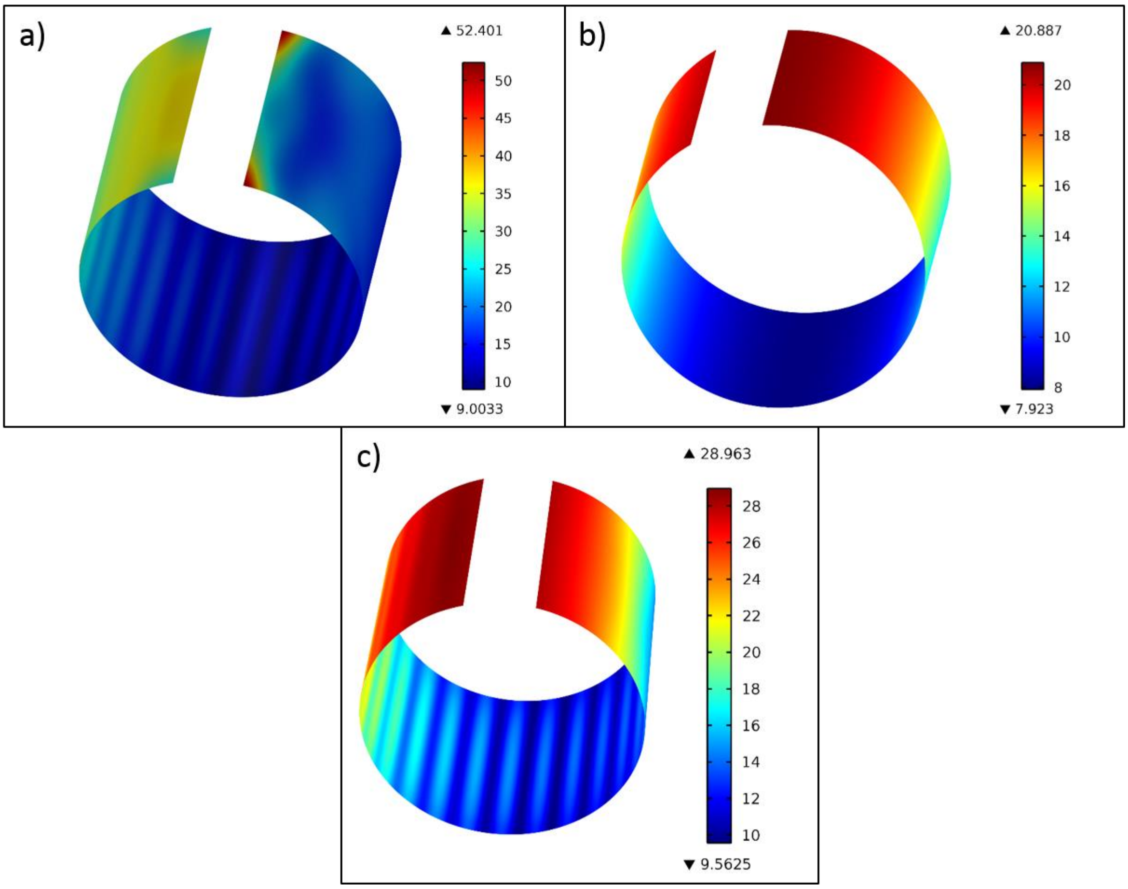

Figure 5.18: Comparison for film thickness predictions in the mid-plane for a) TEHD b) Rigid bearing c) Isothermal. The speed is 30 krpm and load 133 N.

5.2.1.3 Fluid velocity

Figure 5.19 displays average velocity distribution in the hydrodynamic film including both Poiseuille and Couette flow effects for shaft speed of 30 krpm and static radial load of 133 N. The flow accelerates when approaches to bump peaks where film thickness shrinks and a converging gap is created. The film thickness rapidly expands near trailing edge as shown in Figure 5.16. Moreover, the continuity of the flow is disturbed in this region due to the attached edge of the topfoil to the sleeve. Hence, the flow drastically decelerates around this region.

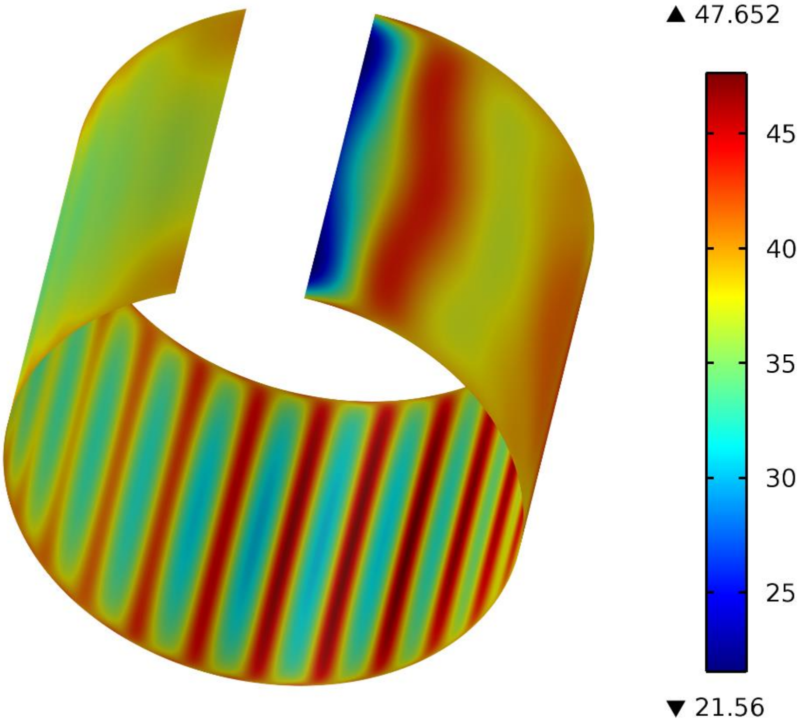

Figure 5.19: Predicted average fluid velocity distribution in the film gap of the CFB for static radial load of 133 N and shaft speed of 30 krpm. The unit is in meters per second [m/s].

The effect of the radial load on average film velocity in the mid-plane of bearing surface is illustrated in Figure 5.20. The shaft speed is taken as 40 krpm for all cases. The flow accelerates when enters the narrow gap between shaft surface and the region on the peaks of the bumps and quickly decelerates as exits from this gap. This behavior is common for all loading conditions but more dramatic for heavily loaded cases because of high pressure gradients and related rapid film thickness change along tangential direction. The velocity magnitudes are less than shaft surface speed for all cases because of averaging of the flow domain. The flow almost converges to the mean value when it is approaching to the leading edge independent from the radial load. However, flow profiles are different around trailing edge due to dissimilar buckling characteristics with respect to loading condition.

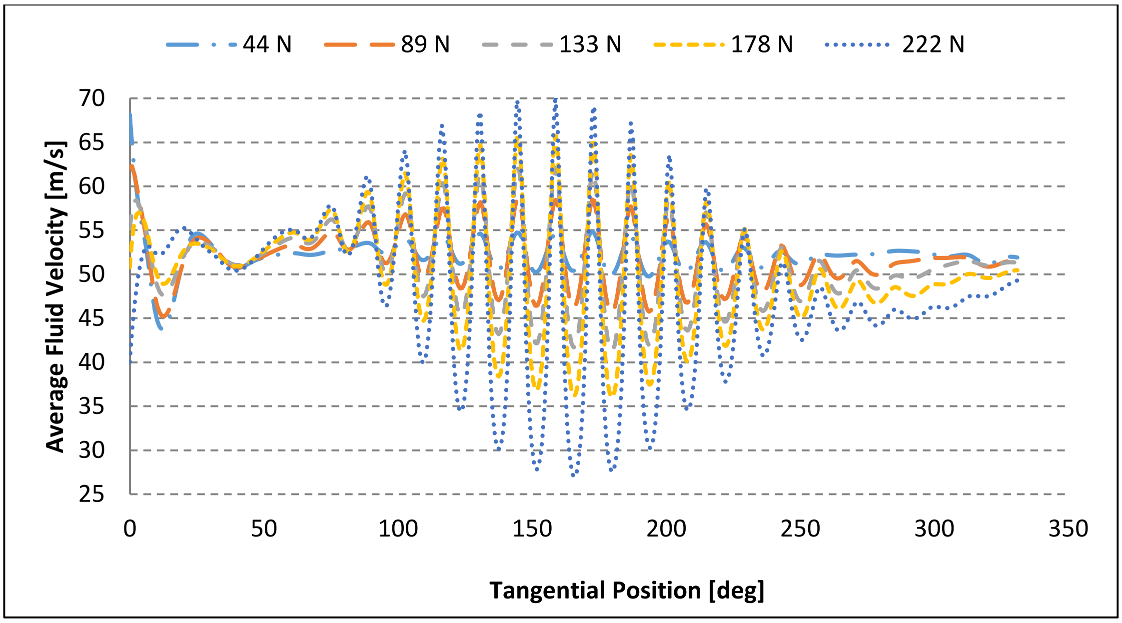

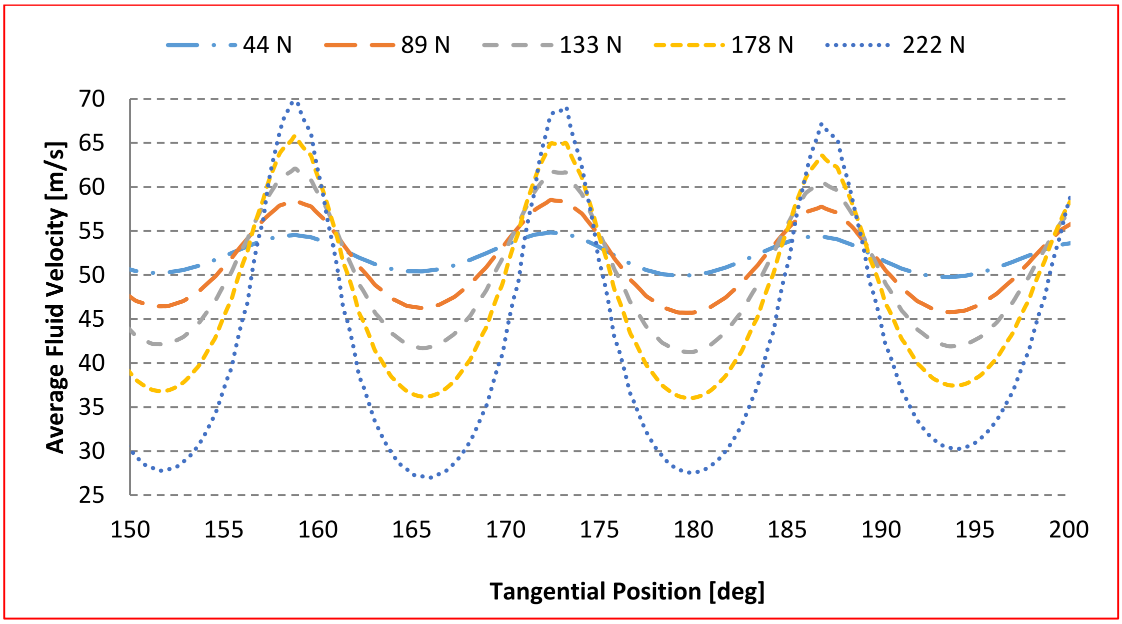

Figure 5.20: Predictions for the average fluid velocity in the mid-plane of the bearing surface in tangential direction for different loading conditions. The shaft speed is 40 krpm. The second figure displays the critical section along the circumferential position between 150 to 200 deg.

Figure 5.21 depicts average film velocity in the bearing center for various shaft speeds. The static radial load is taken as 133 N for all runs. The Couette flow effect due to the changing shaft speed is clearly seen on this plot. As in the previous case, the flow profiles are very similar except in the vicinity of trailing edge. In addition, the portion with wavy flow profile in circumferential direction grows as well as the amplitude of the waves as the shaft speed is increased.

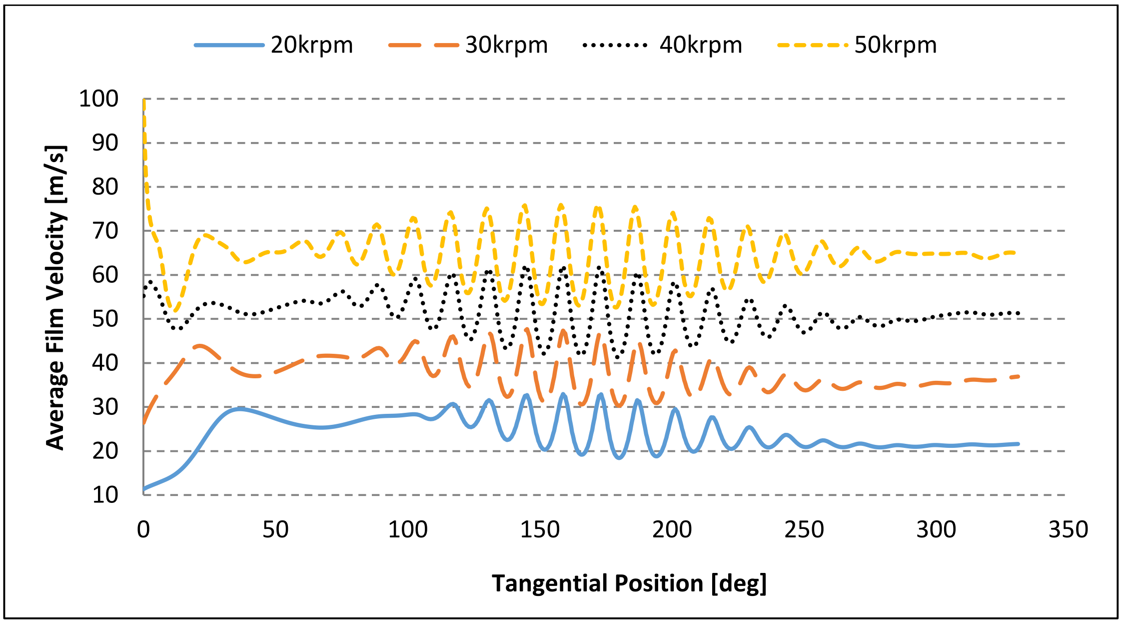

Figure 5.21: Predictions for the average fluid velocity in the mid-plane of the bearing surface in tangential direction for different shaft speeds. The radial load is 133 N.

5.2.2 Thermal Parameters

In this section, thermal properties of the foil bearing acquired from TEHD study are investigated in detail. To develop an effective thermal management system in a foil bearing, all heat flux paths including cooling flow should be considered in the model. The fully coupled TEHD model proposed in this study takes all these aspects into account. Thermal properties of a bearing cover many topics but the main focus is given to temperature distribution, temperature gradients, heat flux paths and thermal contact properties. Temperature is one of the most critical physical properties for this type of bearings because it has implications both on flow domain and surrounding structure. Especially at elevated shaft speeds and heavily loaded cases, temperature directly affects the loading capacity of the bearing and deformation of the underlying structure. Remember that dynamic viscosity of air is a strong function of temperature and steadily increases as temperature goes up. That property would contribute to the load capacity at high temperatures. Furthermore, thermal contact resistance in between contacting elements determines heat flux from the hydrodynamic film towards surrounding medium. The correlation developed by Cooper-Mikic-Yovanovich (CMY), which has been already explained in Section 3.6, is utilized to estimate thermal conductance values.

5.2.2.1 Temperature distribution

The temperature gradient given in Figure 5.22 depicts sudden change of the temperature between two consecutive bumps. The temperature changes more than 8˚C per one millimeter in some regions. This may cause thermal buckling of the topfoil structure, if not managed by an adequate cooling mechanism. Predicted temperatures on bearing components for the shaft speed of 30 krpm and radial load of 133 N are displayed in Figure 5.23. Peak temperature values are predicted in high pressure zone as expected. On the other hand, in the vicinity of the bump peaks temperature begins to drop because of the heat conduction over bumps to the sleeve. More interestingly, temperature declines and begins to climb again before the flow reaches to the section contacting with bumps. Similarly but in reverse direction, temperature continues to increase after leaving the bump and makes a peak point between two consecutive bumps.

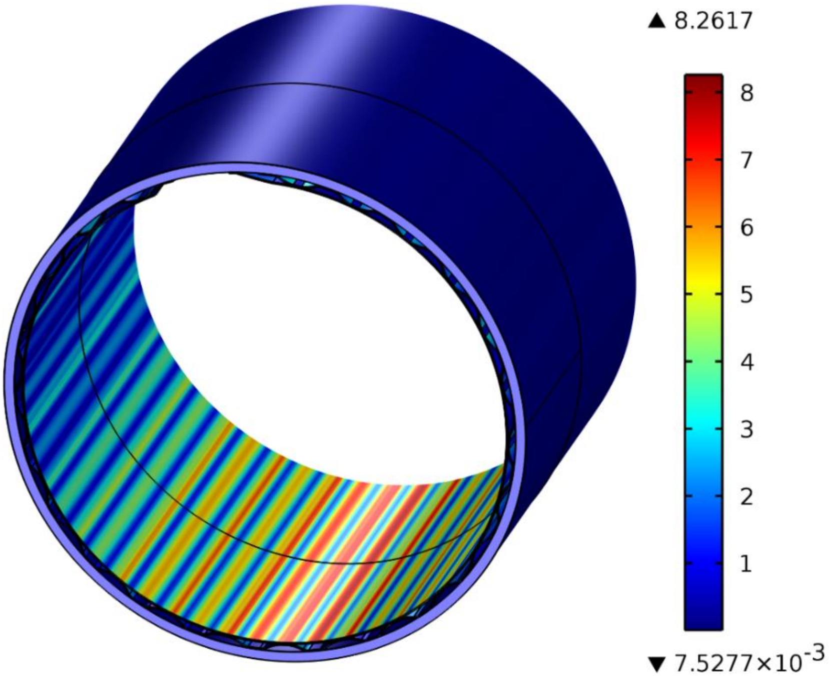

Figure 5.22: Predicted temperature gradient distribution on the CFB including the sleeve. The shaft speed is 30 krpm and the static radial load is 133 N. The unit is in degree Celsius per millimeter [degC/mm].

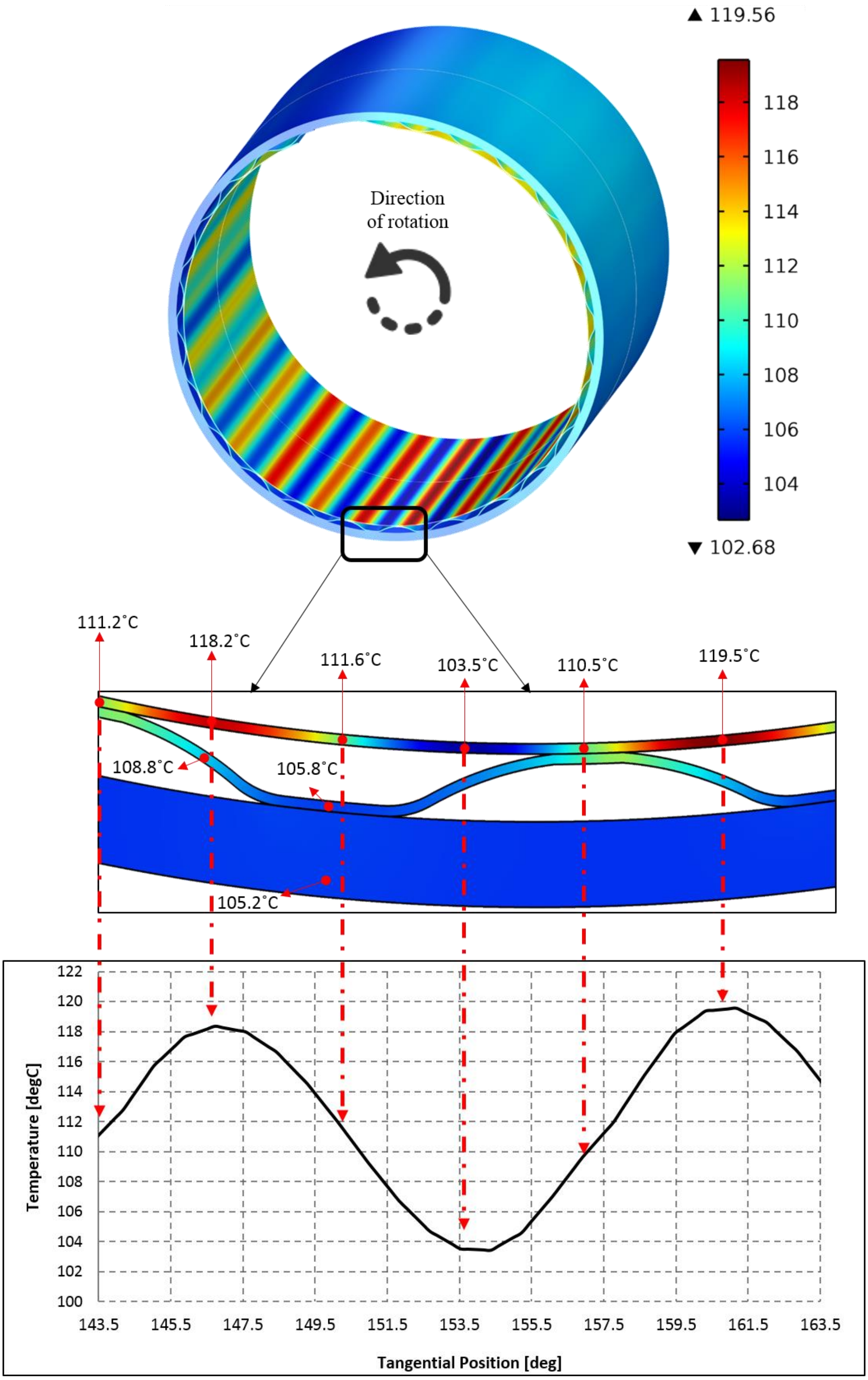

Figure 5.23: Predicted temperature distribution on the CFB including the sleeve. The shaft speed is 30 krpm and the static radial load is 133 N. The unit is in Celsius.

The change of the bearing surface temperature along circumferential direction is given in Figure 5.25 for various loading conditions at a shaft speed of 40 krpm. The temperature values grow as the load increases. The peak temperature predictions are 135, 139, 144, 158 and 178˚C for radial loads of 44, 89, 133, 178, and 222 N, respectively. Note that, the mean temperature increases parabolically when the load increases. As previously explained, the pressure distribution is greatly dependent on applied radial load; however, the gradient of the temperature does not get affected notably from this change, as illustrated in Figure 5.26. Therefore, it can be stated that the temperature profile is essentially determined by convective and conductive heat transfers rather than compressibility effects.

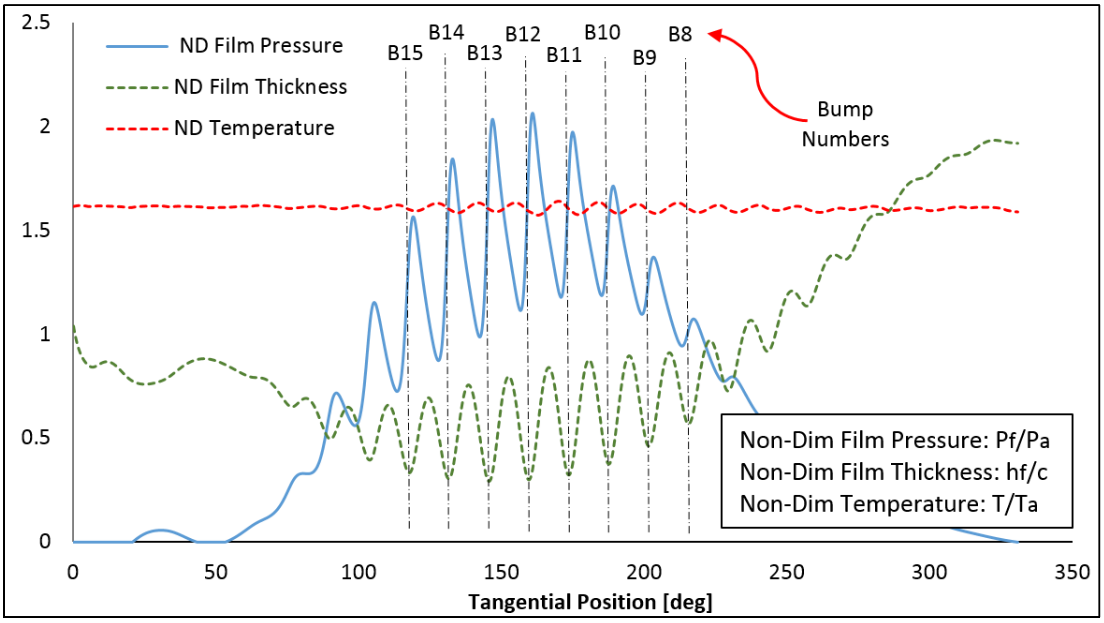

Figure 5.24: The relation between hydrodynamic film pressure, film thickness and surface temperature. The parameters are given in non-dimensional forms for the sake of comparison. The shaft speed is 40 krpm. The static radial load is 222 N.

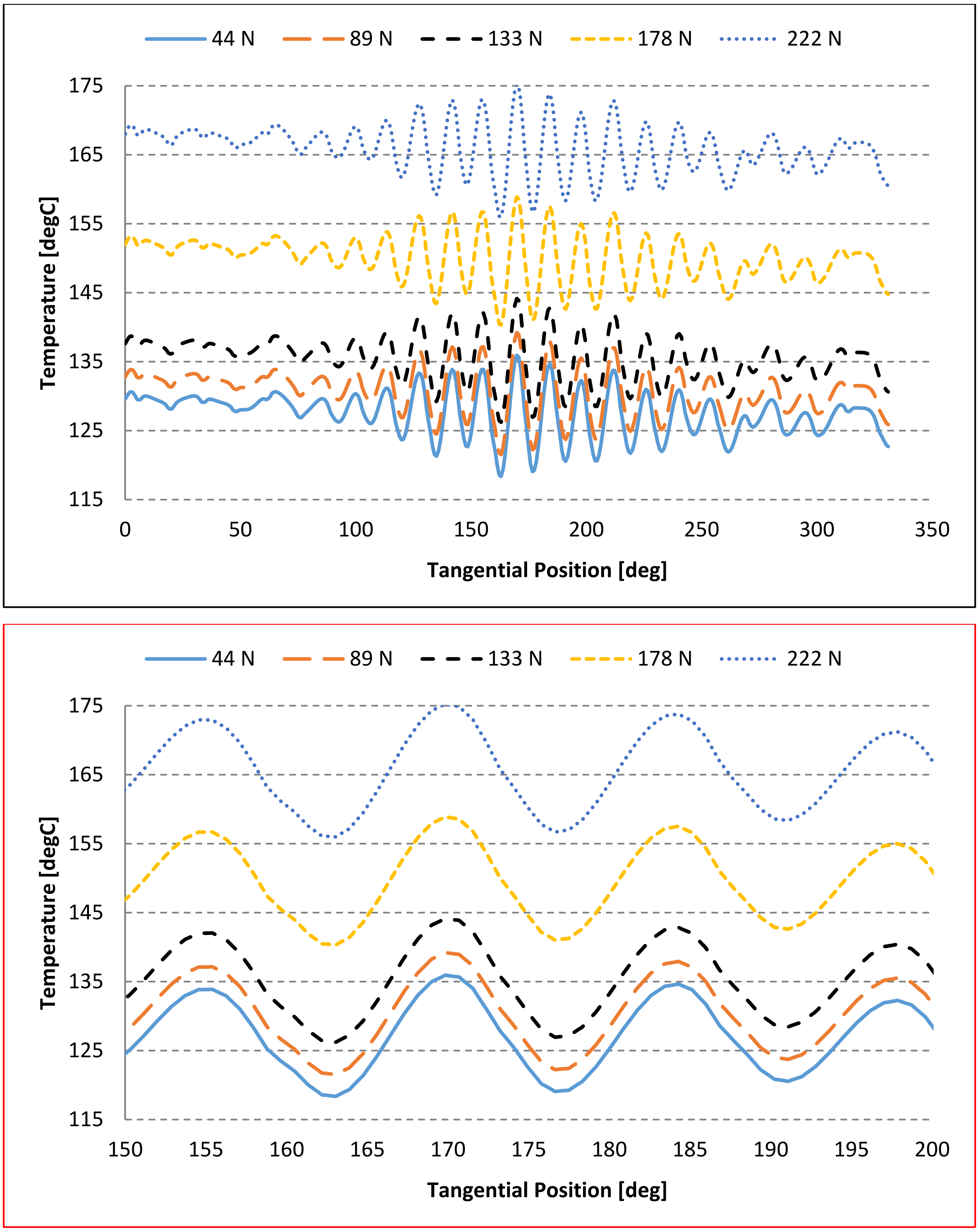

Figure 5.25: Predictions for the film temperature in the mid-plane of the bearing surface in tangential direction for different loading conditions. The shaft speed is 40 krpm. The second figure displays the critical section along the circumferential position between 150 to 200 deg.

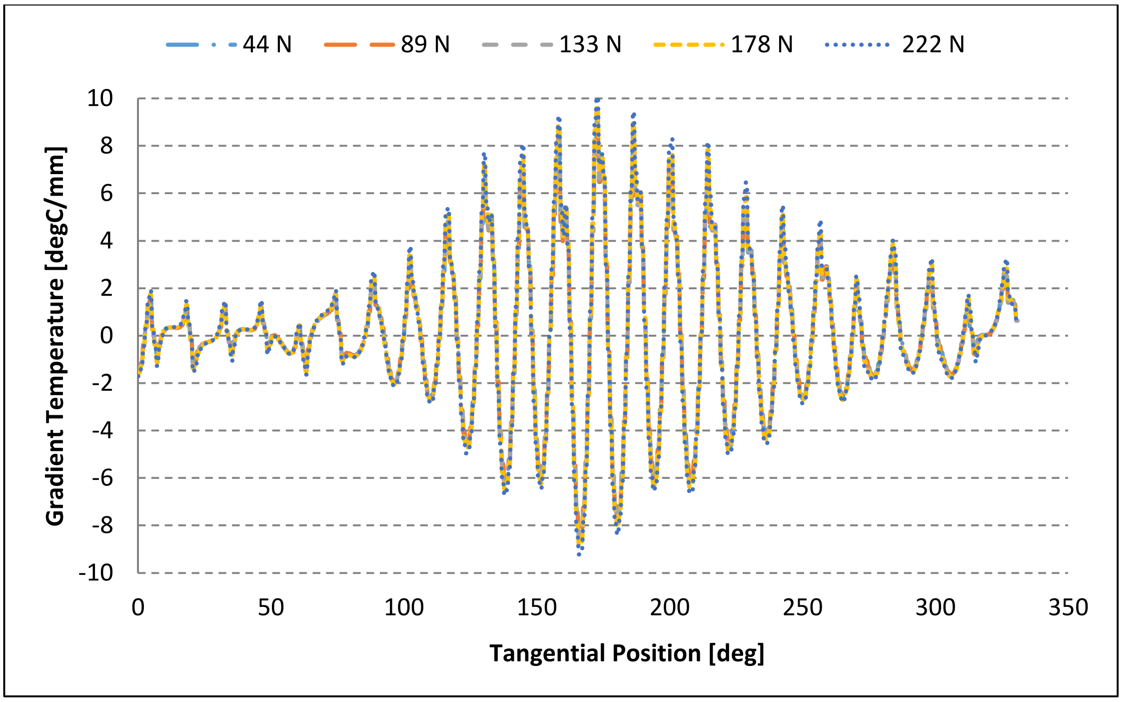

Figure 5.26: Predictions for the gradient of the film temperature in the mid-plane of the bearing surface in tangential direction for different loading conditions. The shaft speed is 40 krpm.

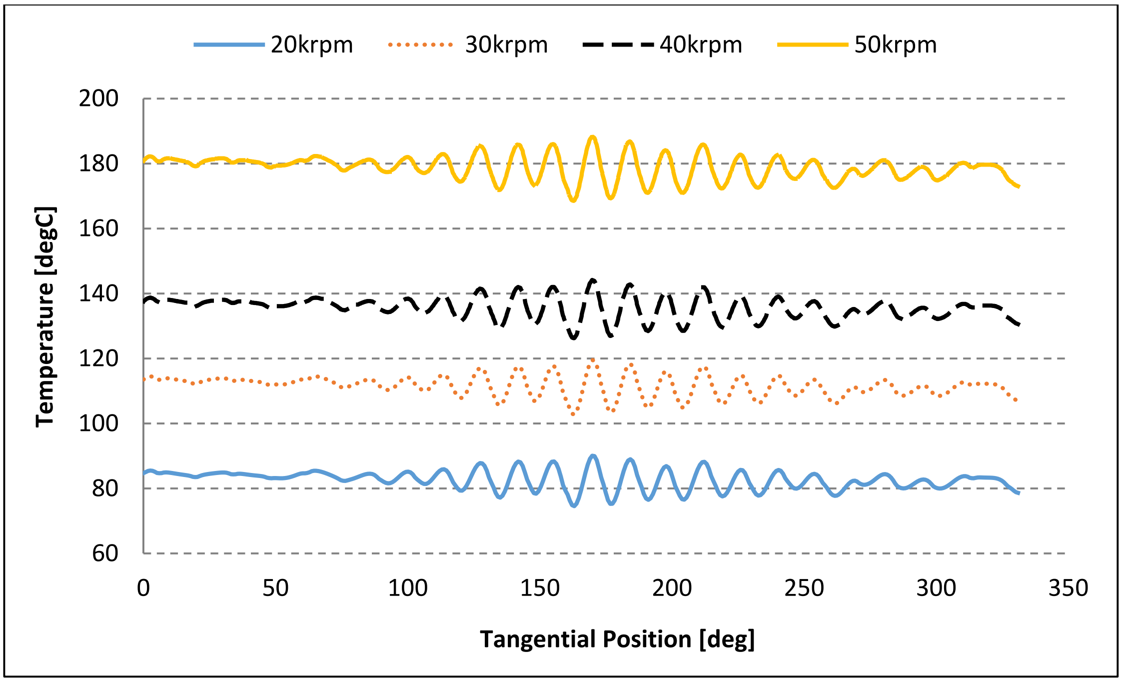

Figure 5.27: Predictions for the film temperature in the mid-plane of the bearing surface in tangential direction for various shaft speed conditions. The static radial load is 133 N.

The change of the topfoil surface temperature in the midplane for various shaft speeds is given in Figure 5.27. The radial load is 133 N for all cases. The mean temperature is almost constant along circumferential direction with a small negative slope towards leading edge. Note that, increase in the shaft speed by 10 krpm causes an increase in the mean temperature 30 to 40˚C which reveals the dominant role of viscous dissipation in heat generation. The peak temperature predictions are 90.1, 119.5, 144.1 and 188.2˚C for shaft speeds of 20, 30, 40, and, 50 krpm respectively. The gradient of temperature for the same cases is displayed in Figure 5.28. Similar to the radial load change, the temperature gradient is almost not affected from the change of shaft speed.

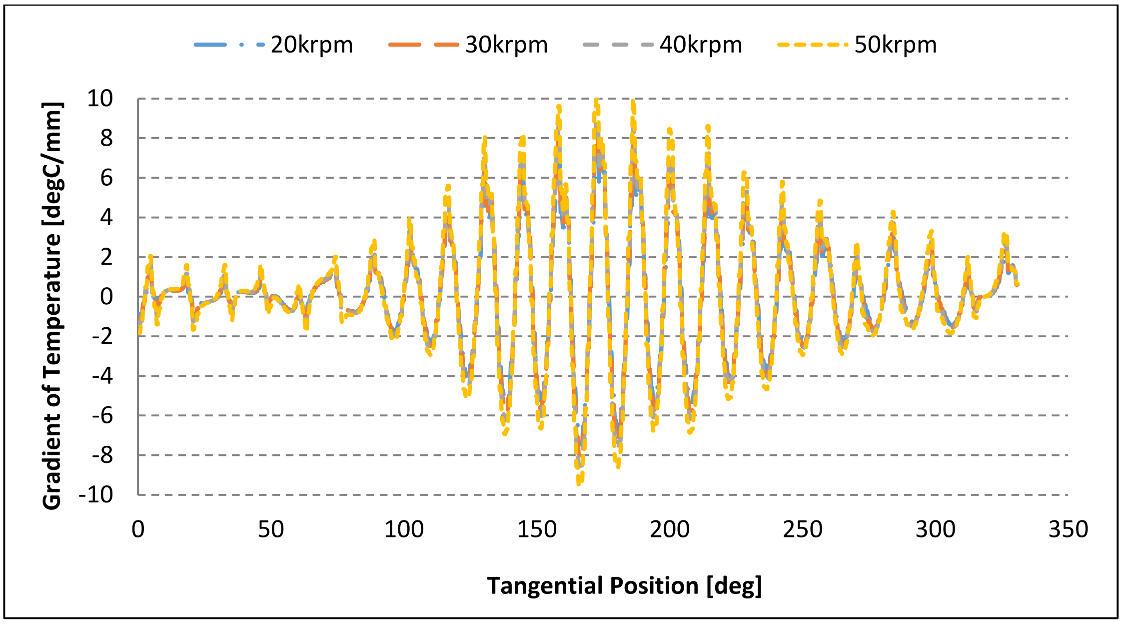

Figure 5.28: Predictions for the gradient of the film temperature in the mid-plane of the bearing surface in tangential direction for various shaft speed conditions. The static radial load is 133 N.

Figure 5.29 depicts predicted temperature distribution on the shaft for a radial load of 133 N and speed of 30 krpm. Flow temperature estimations for the fluid film are mapped to the shaft surface and thus, similar temperature profile is observed in that section. However, the values are slightly lower than the bearing surface due to the higher heat conduction rate over shaft towards free ends. The peak temperature prediction for the bearing surface is 119˚C whereas it is 114.5˚C on shaft surface. Shaft surface temperature drops remarkably outside the bearing region as shown in Figure 5.30. High temperature gradient on the shaft combined with centrifugal effects may cause significant instabilities. Therefore, foil bearing designers must analyze the rotordynamics of the system considering the thermal implications both on the shaft and the bearing.

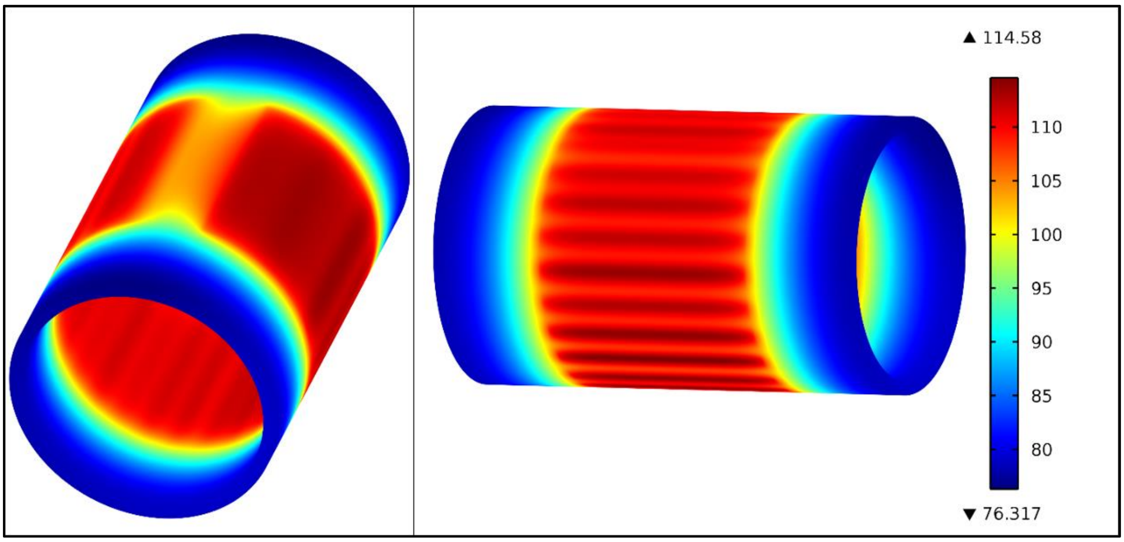

Figure 5.29: Predicted temperature distribution on the shaft. The shaft speed is 30 krpm and the static radial load is 133 N. The unit is in degree Celsius.

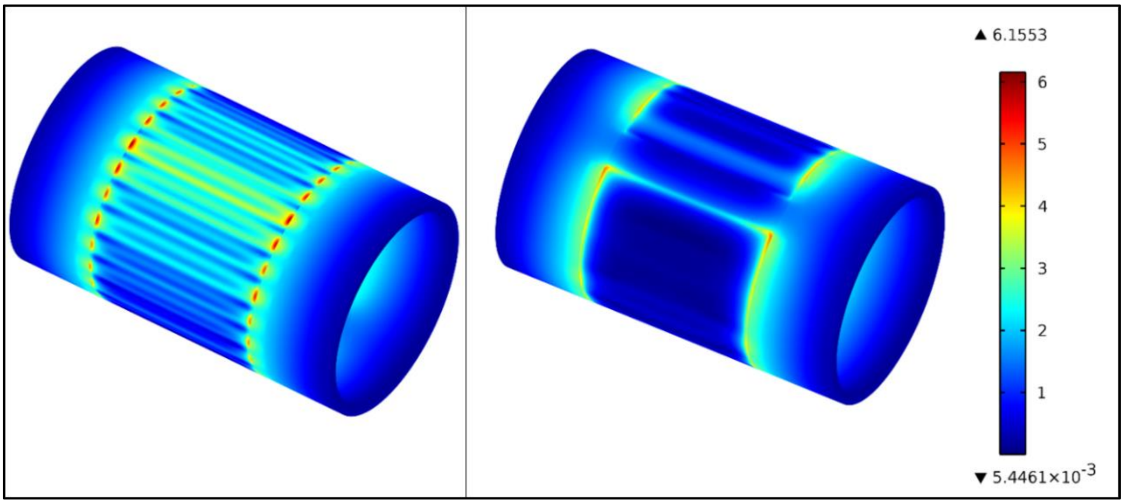

Figure 5.30: Predicted temperature gradient distribution on the shaft geometry. The shaft speed is 30 krpm and the static radial load is 133 N. The unit is in degree Celsius per millimeter.

Convective heat flux distribution on bearing surface for the shaft speed of 30 krpm and radial load of 133 N is displayed in Figure 5.31. The convective heat flux increases as the flow approaches to the bumps due to the acceleration of the flow, and it decreases as the flow exits from the narrow gap in between the bump peaks and shaft surface. The convective heat flux is very strong especially in high pressure zone due to the thin film thickness and high flow velocities.

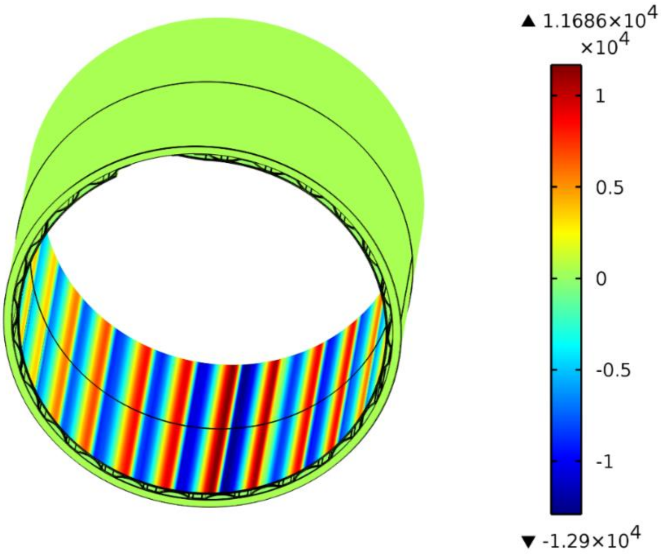

Figure 5.31: Predicted convective heat flux distribution on the CFB including the sleeve. The shaft speed is 30 krpm and the static radial load is 133 N. The unit is in Watt per meter square [W/m^2].

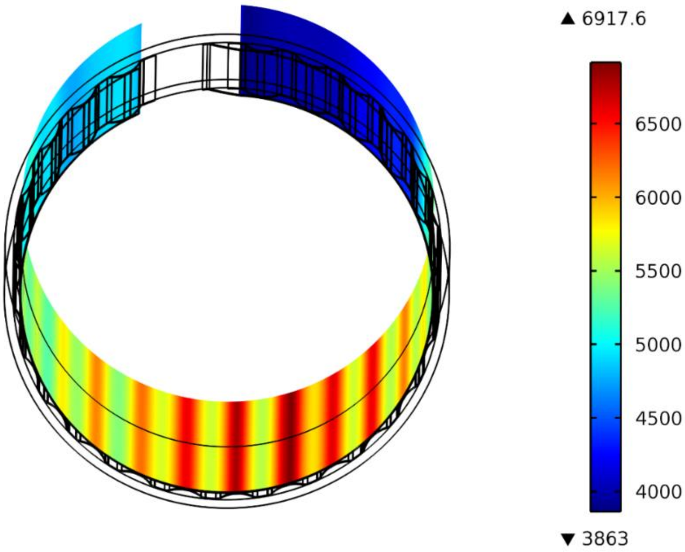

Figure 5.32: Estimated convective heat transfer coefficient on the bearing surface. The shaft speed is 30 krpm and the static radial load is 133 N. The unit is in [W/(m^{2}K)].

The heat convection coefficients for heat flux from the gas film into the shaft outer surface and topfoil inner surface are calculated by using the Reynolds-Colburn analogy between fluid friction and heat transfer as explained in detail in Section 3.3.2. Due to the variation in material properties of the fluid with respect to the temperature and pressure, the convection coefficients vary on different regions of the topfoil surface as illustrated in Figure 5.32. The peak values reach to 6917 W/m^2/K because of high relative velocities between operating surfaces and narrow film gaps in some regions.

5.2.2.2 Thermal contact properties

Modelling thermal contact is naturally challenging due to the thermal constriction and spreading of heat flux lines as well as the random distribution of asperities and the unknown boundary condition of micro-contacts. Various models are proposed in literature to predict the contact and joint conductance between nominally flat rough surfaces. In this study, the correlation developed by Cooper, Mikic and Yovanovich (CMY) is utilized to predict thermal conductance coefficients between contacting elements. The details of the model is already explained in detail in Section 3.6. The outer surface of topfoil and the inner surface of the bearing sleeve experience mechanical and thermal contact with the bump foil. The heat generated in the air film gap transported to the bearing sleeve through bump foil with a certain thermal resistance and related thermal conductivity of the contact region as illustrated in Figure 5.33. Figure 5.34 displays the predicted thermal conductance coefficients for the contacting regions of the bump foil and the sleeve. The shaft speed is 30 krpm and the radial load is 133 N for this case. The conductance coefficient is around 23 W/(m^2K) around the center of contact but decreasing steadily to null as the contact pressure declines. Similarly, predicted thermal conductance coefficients for the contact regions between the bump and topfoil structure are illustrated in Figure 5.35.

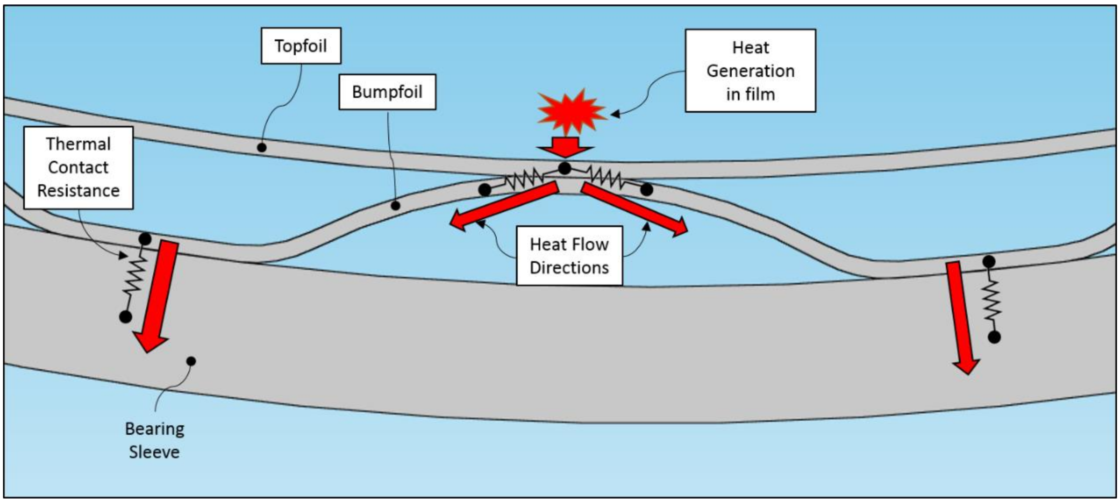

Figure 5.33: Illustration of the thermal contact resistances in topfoil-bump and bump-sleeve contact regions

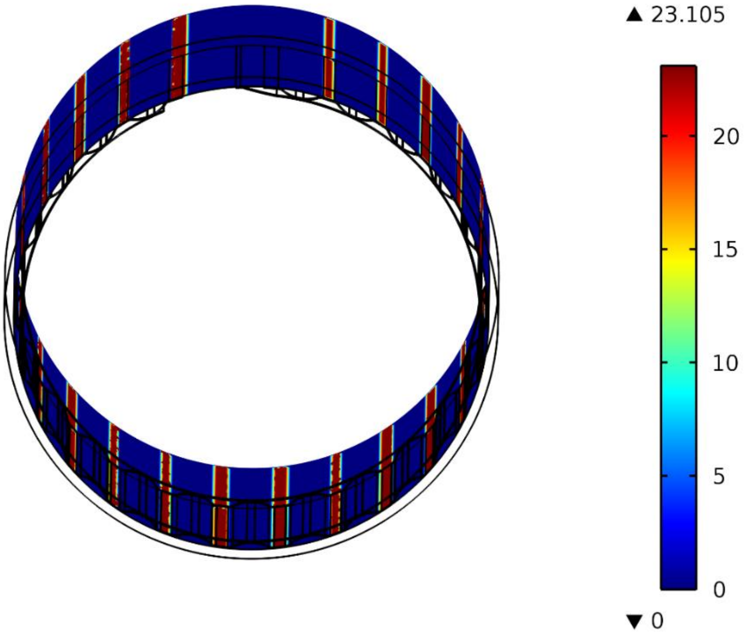

Figure 5.34: Predicted thermal conductance coefficients for the contact surfaces between the bumps and the sleeve surface. The shaft speed is 30 krpm and the static radial load is 133 N. The unit is in [W/(m^{2}K)].

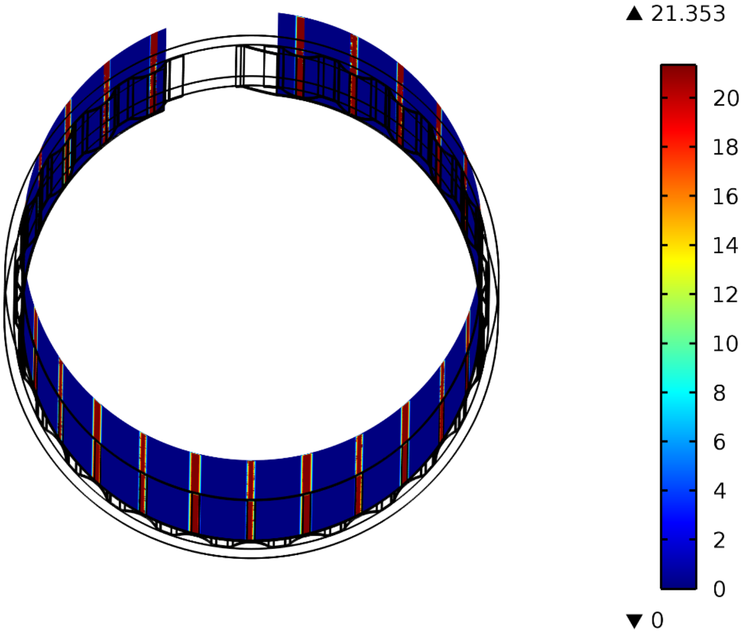

Figure 5.35: Predicted thermal conductance coefficient for the contact surfaces between the bumps and the topfoil surface. The shaft speed is 30 krpm and the static radial load is 133 N. The unit is in [W/(m^{2}K)].

5.2.3 Structural Parameters

5.2.3.1 Deformation

The compliant components such as bump-foil and topfoil of the foil bearing deform due to the combined effect of hydrodynamic pressure in the film and thermal expansions. The outstanding deformable property of the foils brings extra reliability and loading capacity to the bearing mechanism as previously explained. The behavior of the underlying mechanisms during various loading and surface speed conditions is investigated in this section.

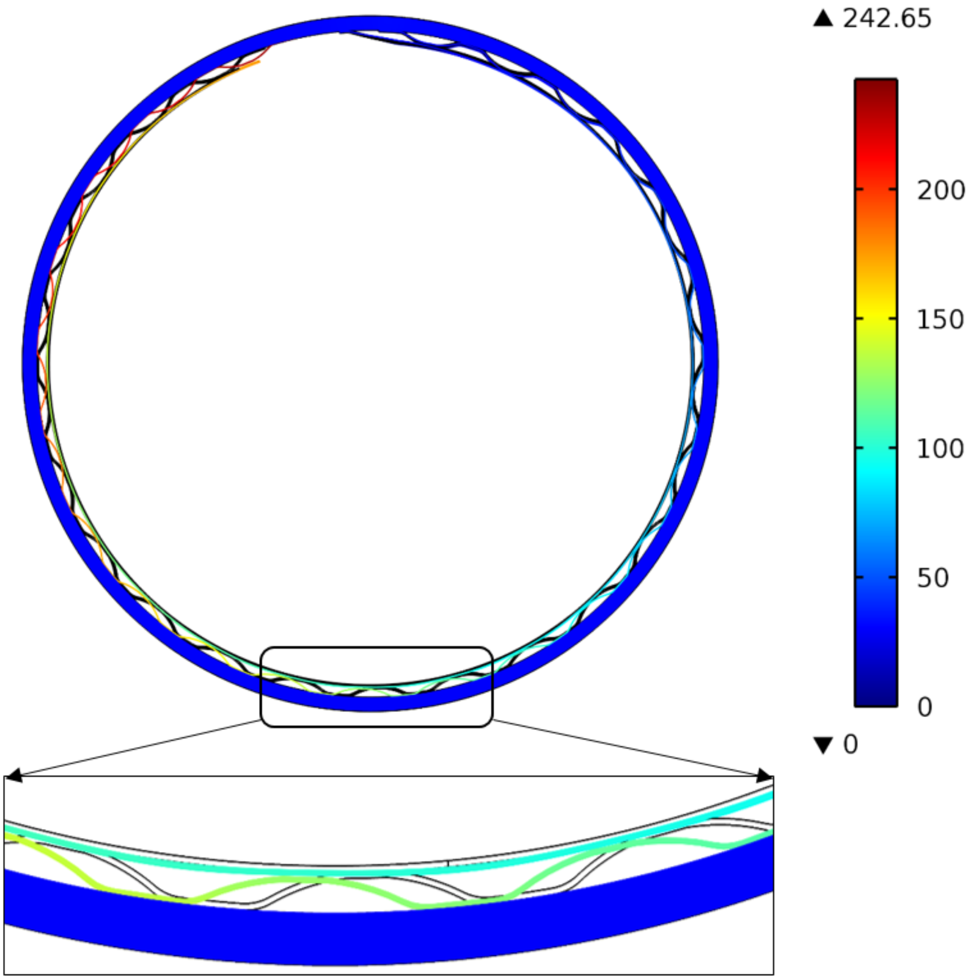

Figure 5.36: Total deformation of the bearing surface and underlying bump structure. The bump movement into the leading edge by sweeping between the topfoil structure and sleeve surface is displayed in the zoom image. The deformation is magnified with a scale factor of 20 to observe clearer. The shaft speed is 30 krpm and the static radial load is 133 N. The unit is in micrometers.

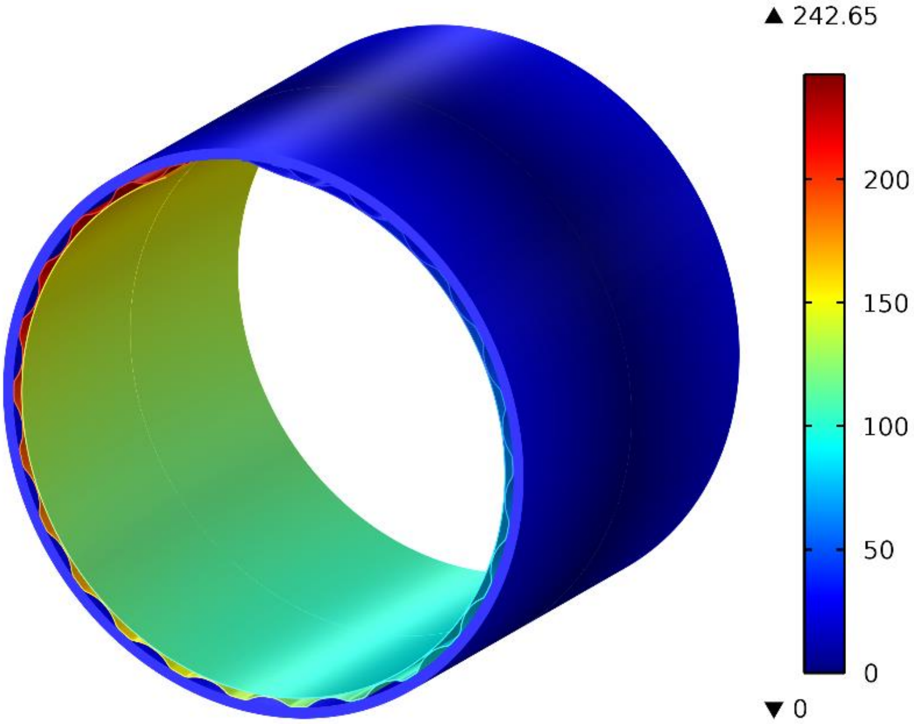

Figure 5.37: The deformation of the bearing surface and underlying bump structure from isometric view. The shaft speed is 30 krpm and the static radial load is 133 N. The unit is in micrometers.

Figure 5.36 and Figure 5.37 illustrate classical deformation characteristics of the bumps during operation. The shaft speed is 30 krpm and the radial load is 133 N for this case. The bumps close to the leading edge deform more since they are free at this end. Therefore, the deformation of the bumps increases from trailing edge to the leading edge in clock-wise direction. The bumps are squeezed between topfoil and sleeve surfaces with certain contact pressures in both side. The deformation in radial direction forces the bumps to sweep in tangential direction towards leading edge. Note that this tendency strictly depends on the position of the fixed or welded region of the bumps. If the bumps are fixed in center instead of the trailing edge, the sweep would occur in both directions by starting from the fixed region. Therefore, foil bearing designers must consider this mechanism to prevent possible failure modes due to undesired bump motions.

The thermal deformation of the bearing components in axial direction is shown in Figure 5.38. The amount of the deformation is equal in both sides due to the symmetry. The axial deformation may cause irregular sliding of the bumps over sleeve surface. This should be prevented by adding additional ribs between bump series (if exists) to preserve relative axial distances.

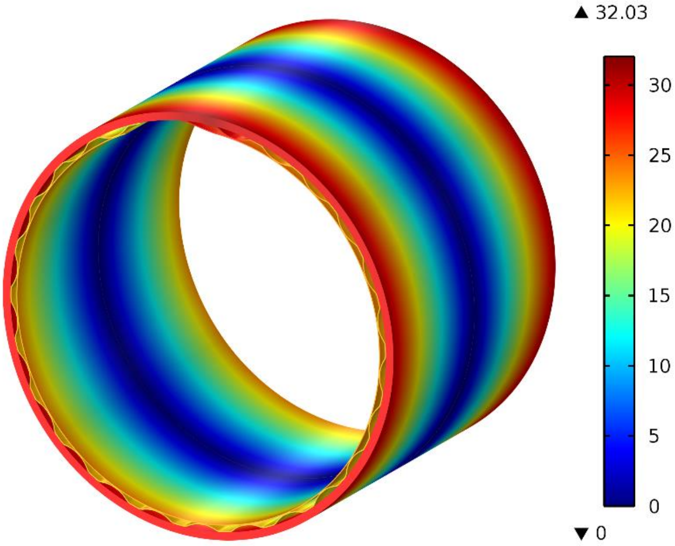

Figure 5.38: The deformation of the bearing in axial direction. The shaft speed is 30 krpm and the static radial load is 133 N. The unit is in micrometers.

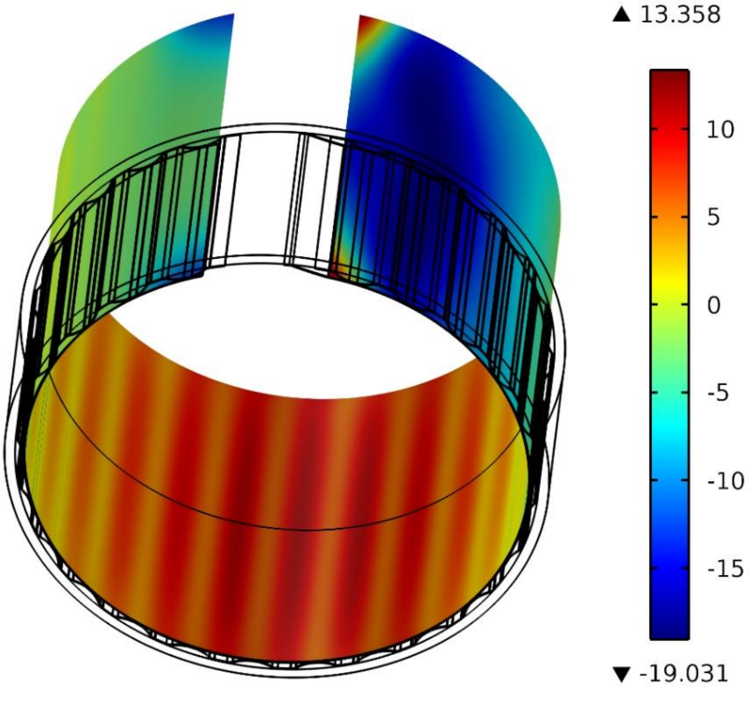

Figure 5.39: The deformation of the topfoil surface in radial direction from isometric view. The shaft speed is 30 krpm and the static radial load is 133 N. The unit is in micrometers.

The deformation of the topfoil surface in radial direction is displayed in Figure 5.39 for the same operation conditions. The foil is deflected more in high pressure zone as expected but with an exception near trailing and leading edges. The corners of topfoil are deflected outwards in trailing edge and inwards in leading edge. This provides evidence for the buckling of the topfoil structure because it is fixed in one edge and subjected to high pressures in the center. To overcome such problems, topfoil surface is split into several pieces in some foil bearing designs.

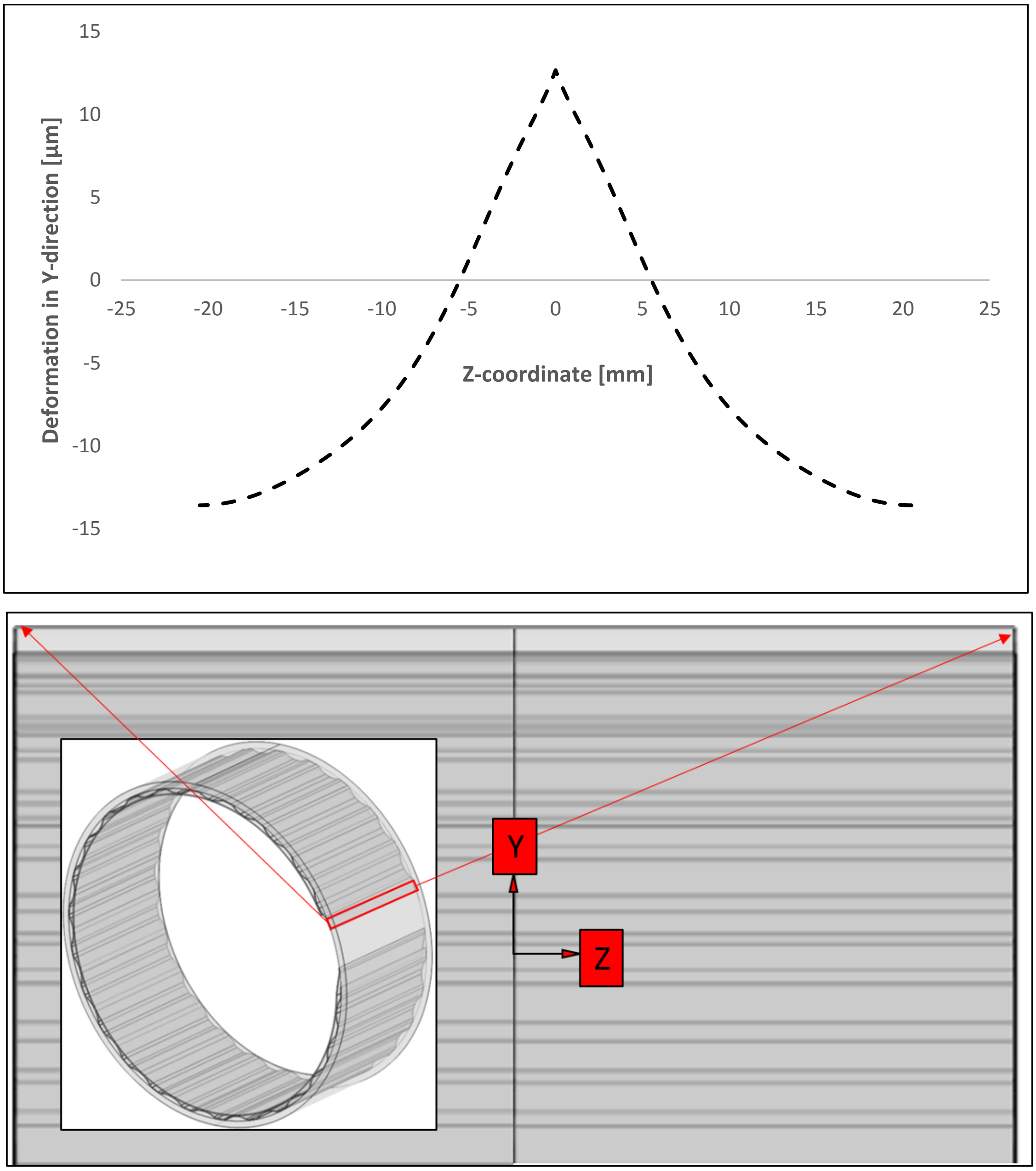

Figure 5.40: Radial deformation of the topfoil near weld region of the trailing edge. The y-direction shows the radial direction whereas the z-direction indicates the axial direction. The shaft speed is 30 krpm and the static radial load is 133 N.

The buckling of the topfoil is better observed in Figure 5.40 where the radial deformation of the topfoil close to the trailing edge is shown with respect to the axial direction. The topfoil deflects towards the shaft surface in edges but it deforms in the opposite direction at bearing center. Note that the nominal clearance is just 20 microns for this study and thus, a difference of almost 25 microns in radial position of the center and edges of the topfoil incurs the risk of mechanical contact with shaft surface which would damage the topfoil easily. Figure 5.41 depicts that this situation is not peculiar to the trailing/leading edges and also occurs in the center of the topfoil but with smaller amplitude. Also note that, the radial deformation of the topfoil more than 10 microns explains how foil bearings could operate with eccentricity ratios of more than unity. This compliant mechanism makes foil bearing unique in terms of sustaining high rates of radial distortions and misalignments.

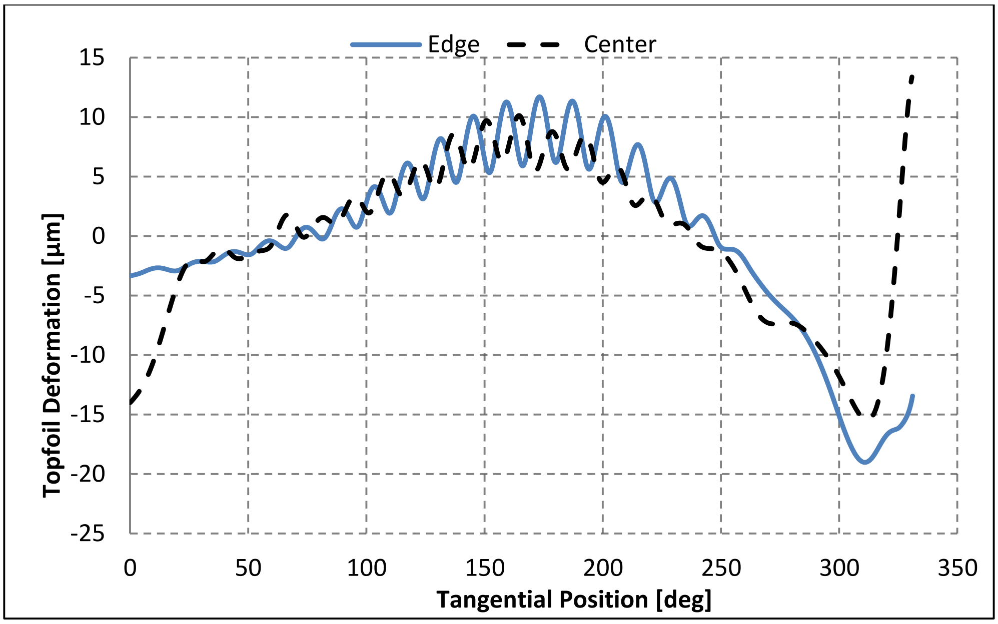

Figure 5.41: Comparison of the radial deformation of the topfoil in the midplane and edge in radial direction. The shaft speed is 30 krpm and the static radial load is 133 N.

The radial deformation profiles for the topfoil midplane along the circumferential direction for various shaft speeds and radial loading conditions are given in Figure 5.42 and Figure 5.43, respectively. The deformation is not affected significantly from the shaft speed change except in the vicinity of trailing and leading edges. Even so, the deformation is slightly decreases as the speed increases. On the other hand, the deformation is radically affected from loading conditions. Even though the profiles are very similar, the amount deformation increases as the load increases.

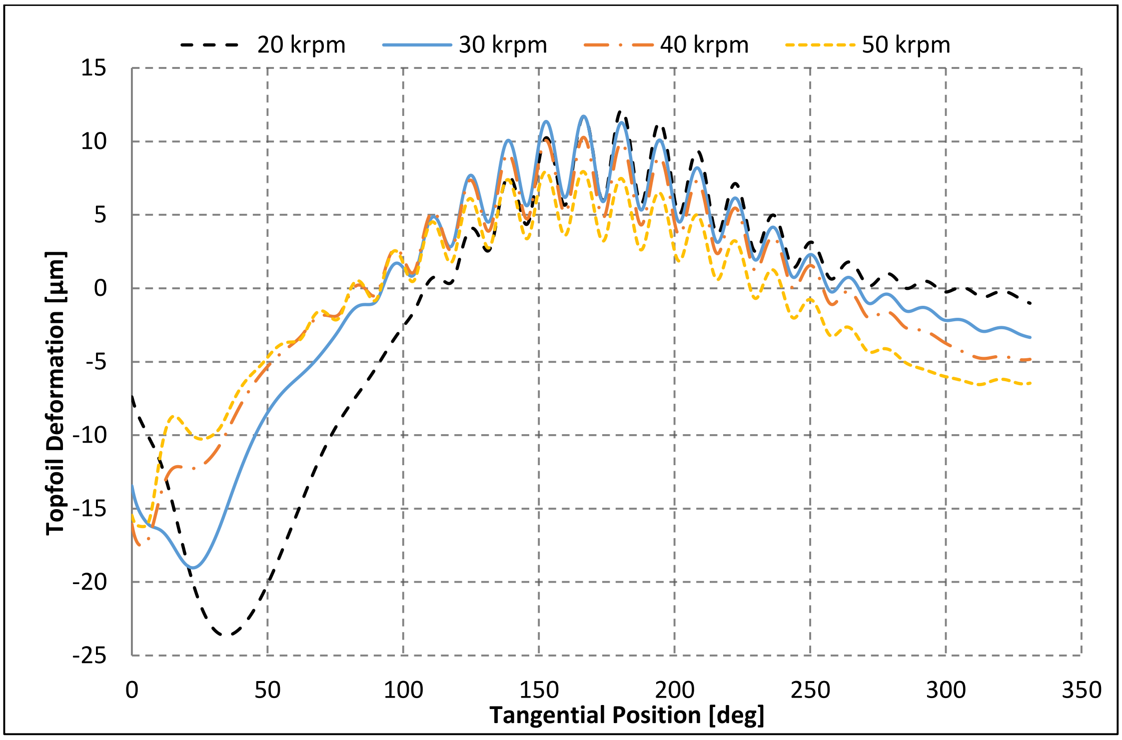

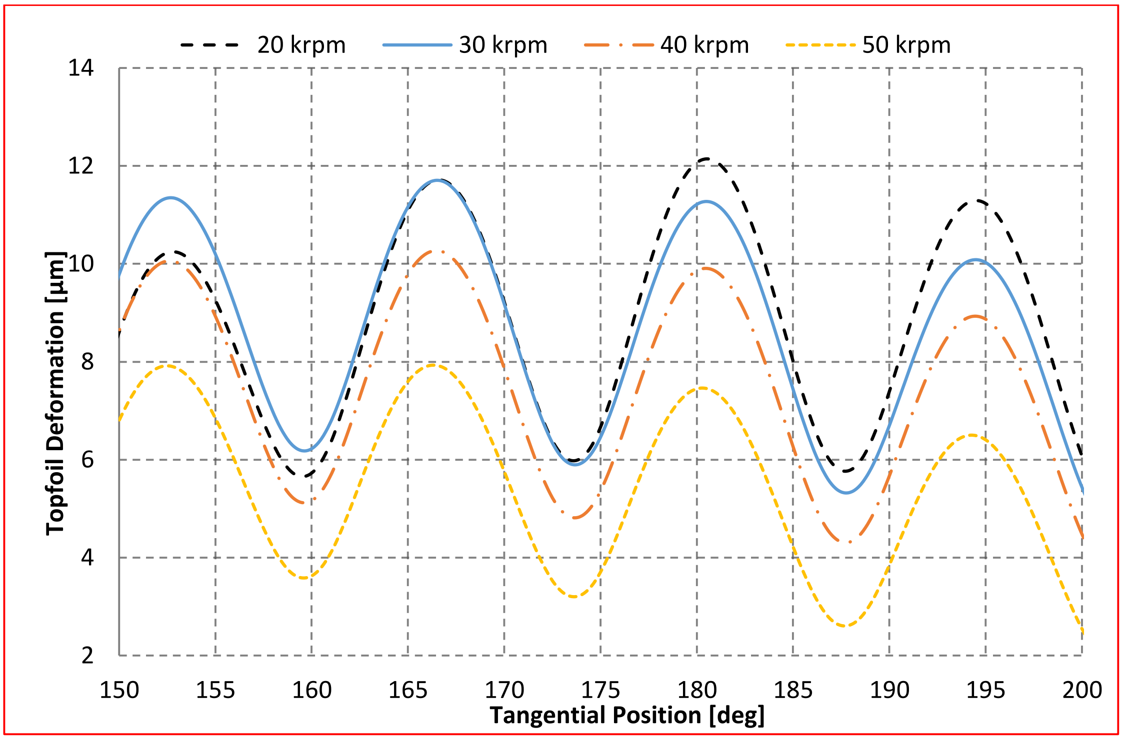

Figure 5.42: The radial deformation of the topfoil in the midplane for various shaft speeds. The static radial load is 133 N. The second figure displays the critical section along the circumferential position between 150 to 200 deg.

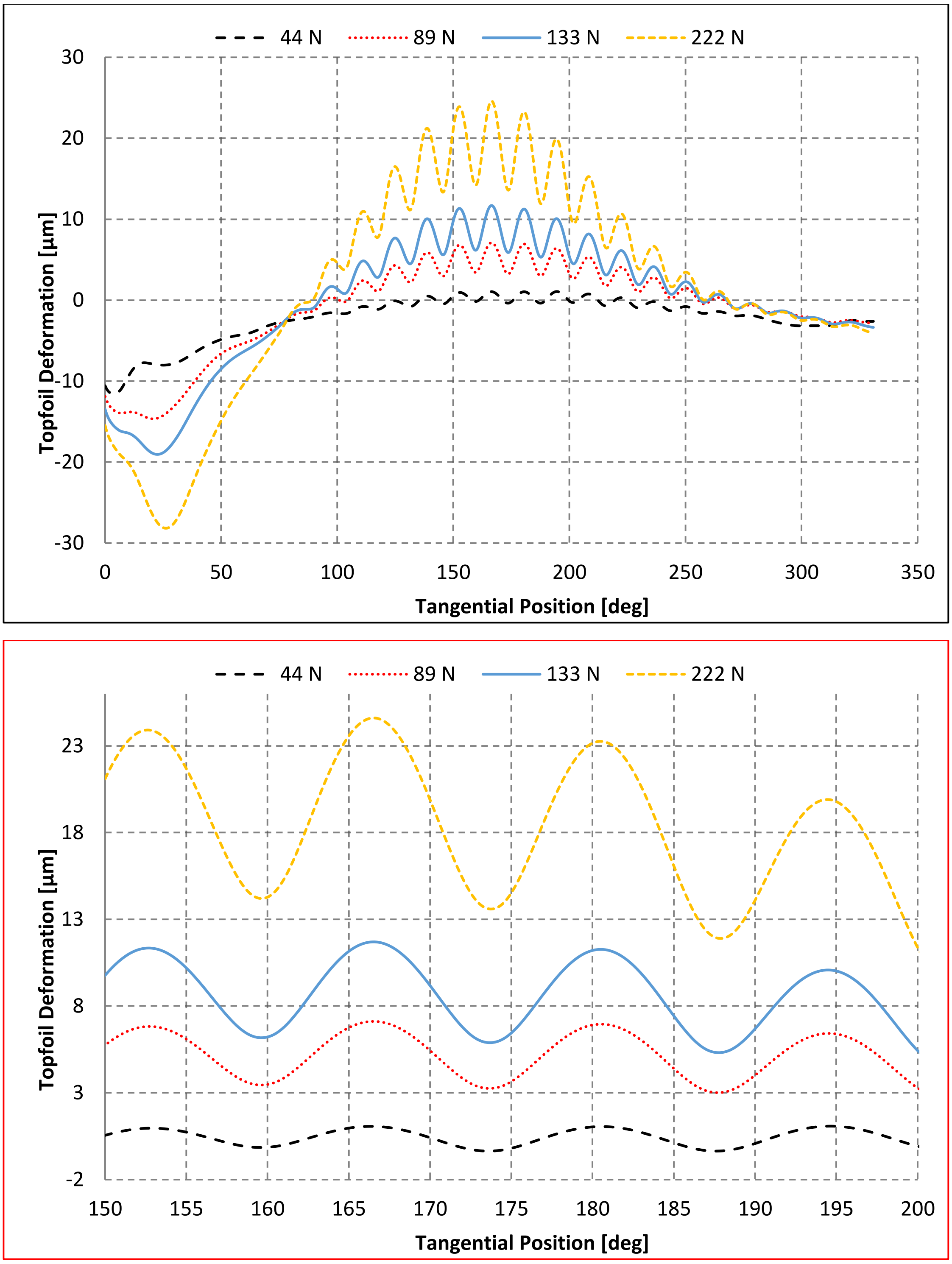

Figure 5.43: The radial deformation of the topfoil in the midplane for various radial loads. The shaft speed is 30 krpm. The second figure displays the critical section along the circumferential position between 150 to 200 deg.

5.2.3.2 Stress

To assess failure modes, an accurate stress analysis must be performed by estimating the largest stresses that occur at a critical point in the component [123]. Leaving the details of the underlying stress theory to the explanations in Section 3.4, the Von Mises stress results obtained from TEHD analysis are investigated in this section.

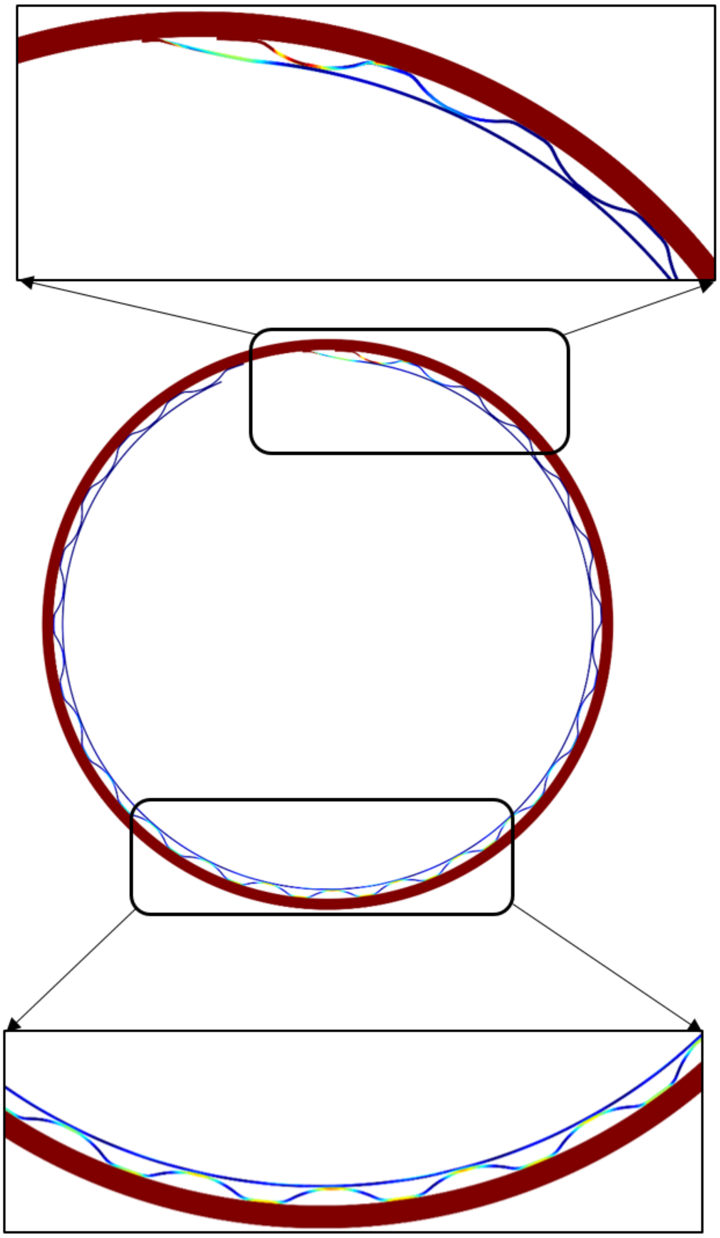

Figure 5.44: Von Mises stress distribution on the bumps and contact regions. The shaft speed is 30 krpm and the static radial load is 133 N.

Recall that top- and bump foil materials are defined as Inconel X-750, and Inconel 718 for the sleeve and shaft geometry in TEHD model. Temperature dependent material properties are given in Appendix A. The yield strength of Inconel X-750 is approximately 650 MPa for the temperature range of this study. The stress distribution on bearing components according to Von Mises stress theory is displayed in Figure 5.44. Maximum stress values are predicted in welded regions of both top- and bump foils as shown in Figure 5.45. The contact regions experience higher stress concentrations as well.

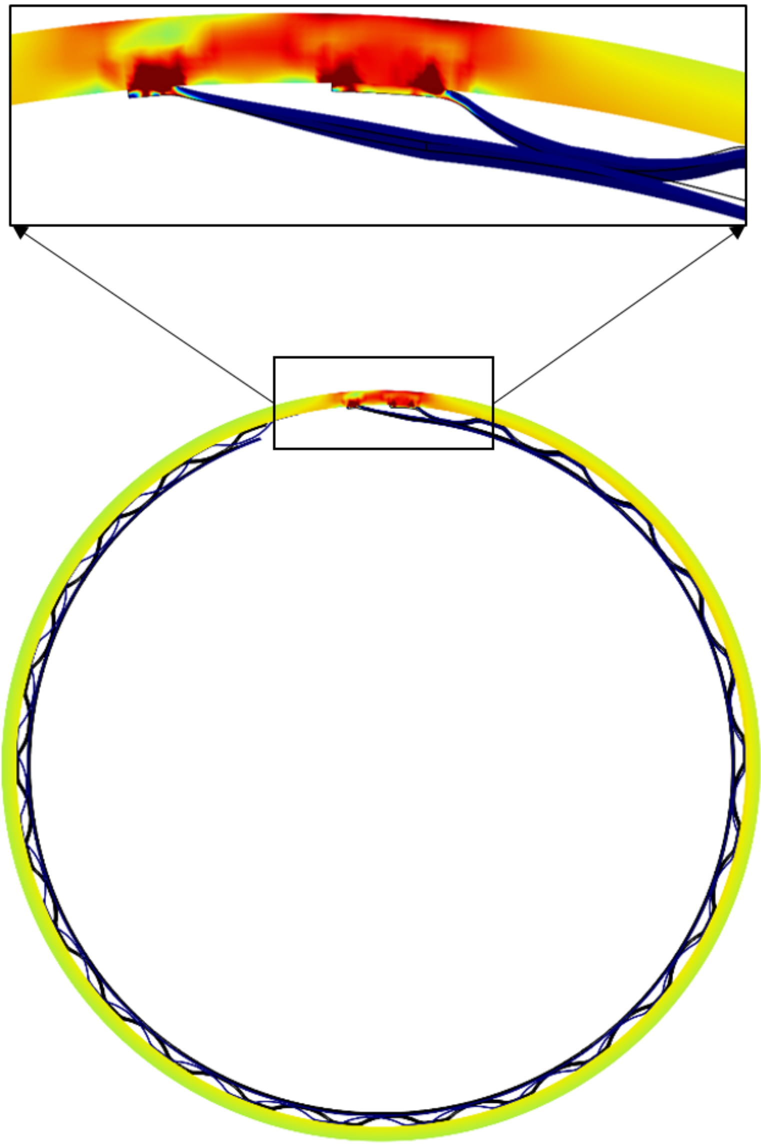

Figure 5.45: The stress concentration in welded regions of the topfoil and bump structure. The shaft speed is 30 krpm and the static radial load is 133 N.

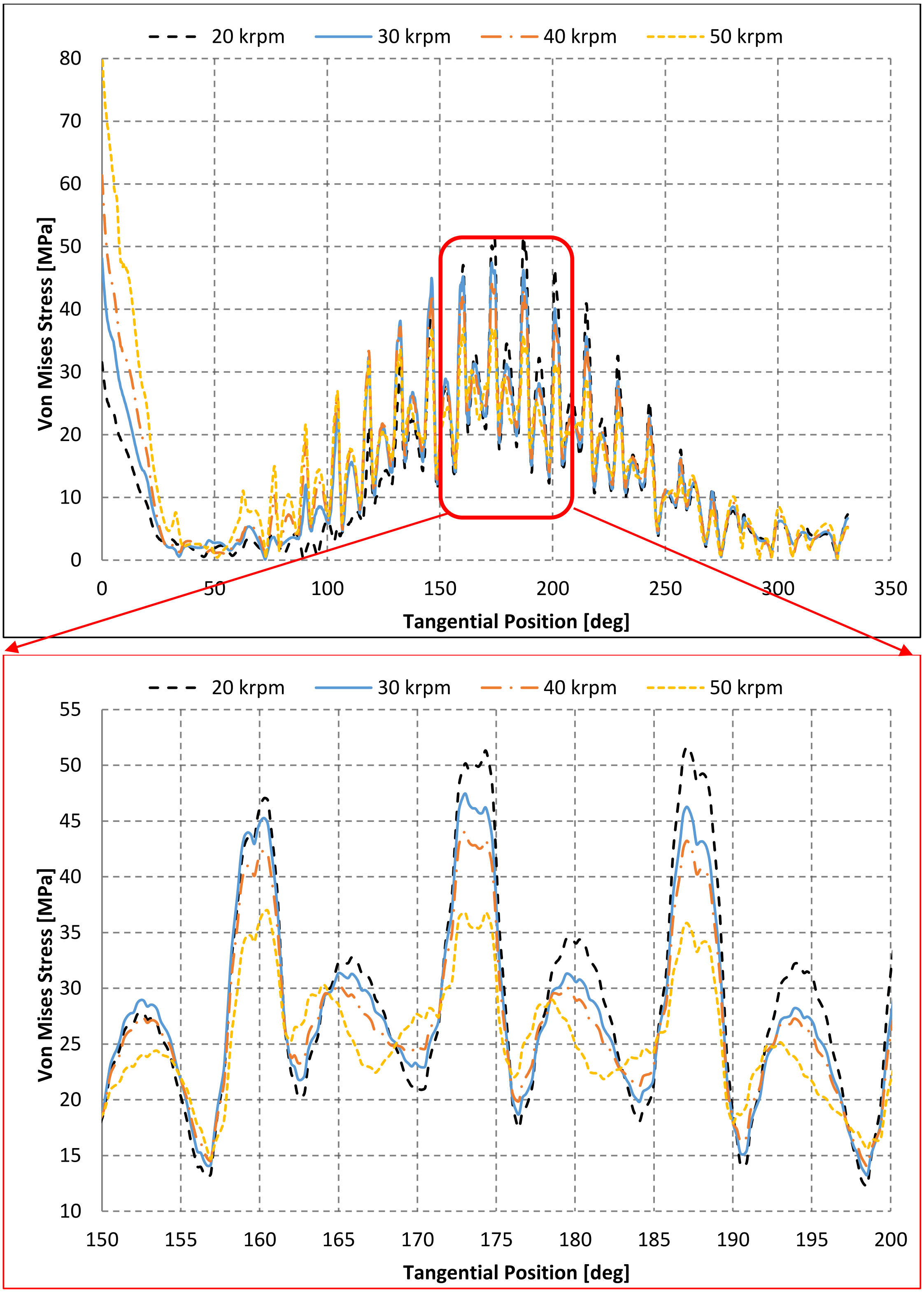

Figure 5.46: Von Mises stress on topfoil in the midplane for various shaft speeds. The radial load is 133 N. The second figure displays the critical section along the circumferential position between 150 to 200 deg.

The stress distribution in the midplane of the topfoil along the circumferential direction for various shaft speeds is shown in Figure 5.46. The static radial load is 133 N. The peak values in the second plot belong to the contact region between the topfoil and bumps where stress values reach 50 MPa for the shaft speed of 20 krpm. Note that, the stress predictions are higher at slower shaft speeds for the same radial load. The stress predictions are highest near trailing edge independent from the shaft speed as already stated before.

Figure 5.47 demonstrates the stress distribution on topfoil midplane for different loading conditions. The shaft speed is selected as 30 krpm for all cases. The radial load has more dramatic influence on stress values compared to shaft speed. As shown in Figure 5.6, the pressure profile changes with the radial load. Hence, the peak values for Von Mises stress predictions shifts as the load changes. Maximum pressure estimation for radial load of 222 N reaches to 85 MPa. Although this stress level individually appears to be far away from yield strength, it may be problematic for dynamic loading conditions in terms of fatigue failure. Note that, the stress level is oscillating along circumferential direction more than 65 MPa which is relatively high for an alternating load. Therefore, it would be wise for foil bearing designers to perform fatigue failure analysis especially when considering heavily loaded scenarios.

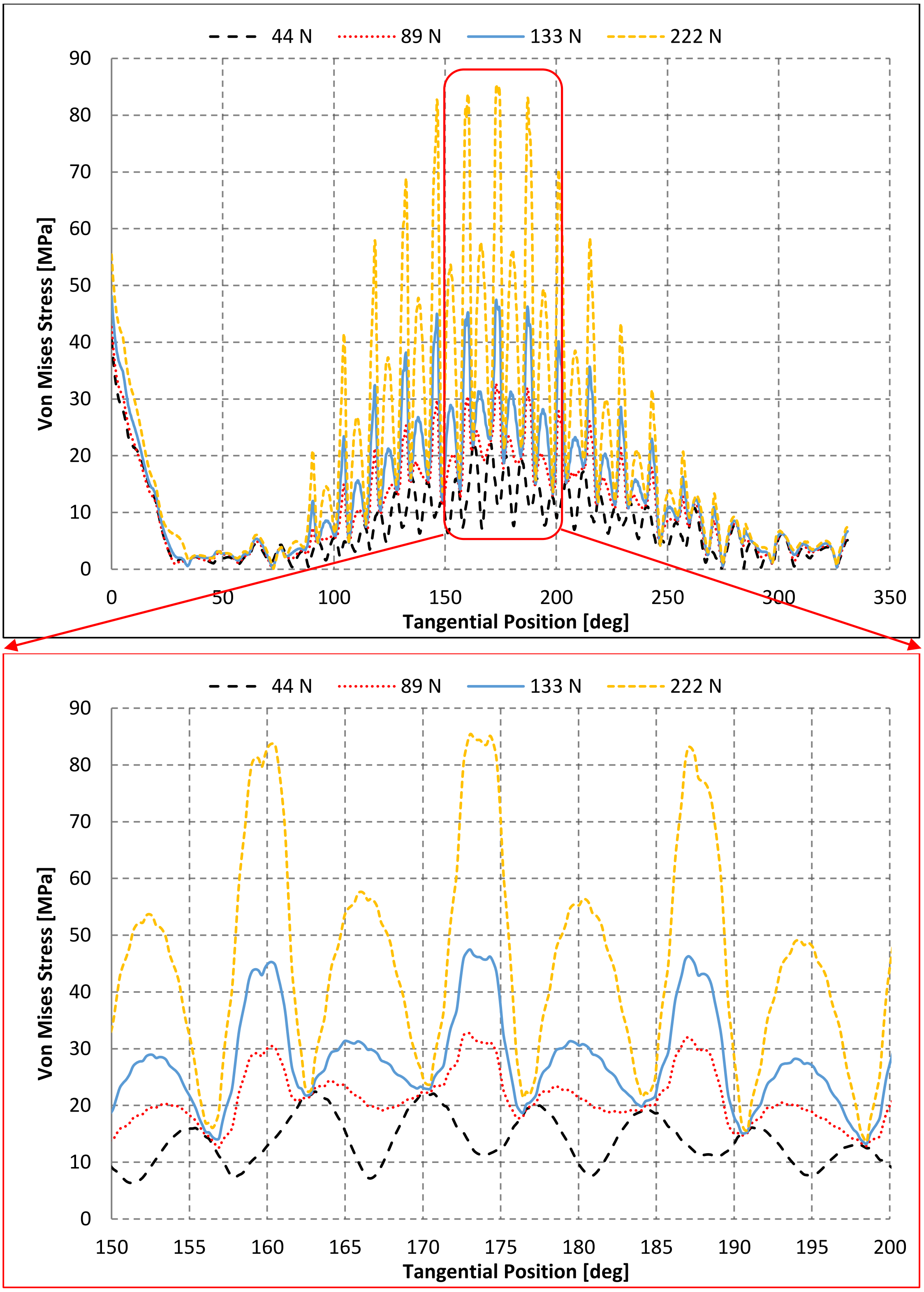

Figure 5.47: Von Mises stress distribution on topfoil in the bearing midplane for various radial loads. The shaft speed is 30 krpm. The second figure displays the critical section along the circumferential position between 150 to 200 deg.

5.2.3.3 Mechanical contact properties

The FEA solver of TEHD analysis utilizes an augmented Lagrangian penalty method for contact formulations. The contact pressures are estimated according to the distance between contacting surfaces. To prevent interpenetration of the surfaces, a type of penalty method is applied during calculations. The details of the contact formulation is already given in Section 3.5.

The penalized contact pressure estimations on the contact surfaces between the topfoil and bumps at a shaft speed of 30 krpm and radial load of 133 N is given in Figure 5.48. The numbering convention of the bumps are already given in Figure 5.1. The numbers are increasing from leading edge side towards trailing edge. The contact pressures rise as approached to the high pressure zone on topfoil surface. The z-coordinate corresponds to axial direction and starts from the center of the bearing. The contact pressures for many bumps around high pressure zone drop below zero near bearing edges which is the evidence of the separation of the contact between bumps and topfoil due to the deflection of the topfoil surface towards shaft surface in radial direction. The same behavior could be also observed in Figure 5.49. The contact gap becomes positive near bearing edge that shows contact separation. Also note that, the contact gaps for bump 16 and bump 17 are all positive in axial direction which proves that these bumps are not supporting the radial load. This is not efficient for the bearing performace and should be improved by tailoring the bump geometry to adjust the stiffness characteristics of the bearing. Actually, it is partially achieved in new generations of foil bearings by changing the bump geometry both in circumferential and axial directions to optimize the bearing capabilities.

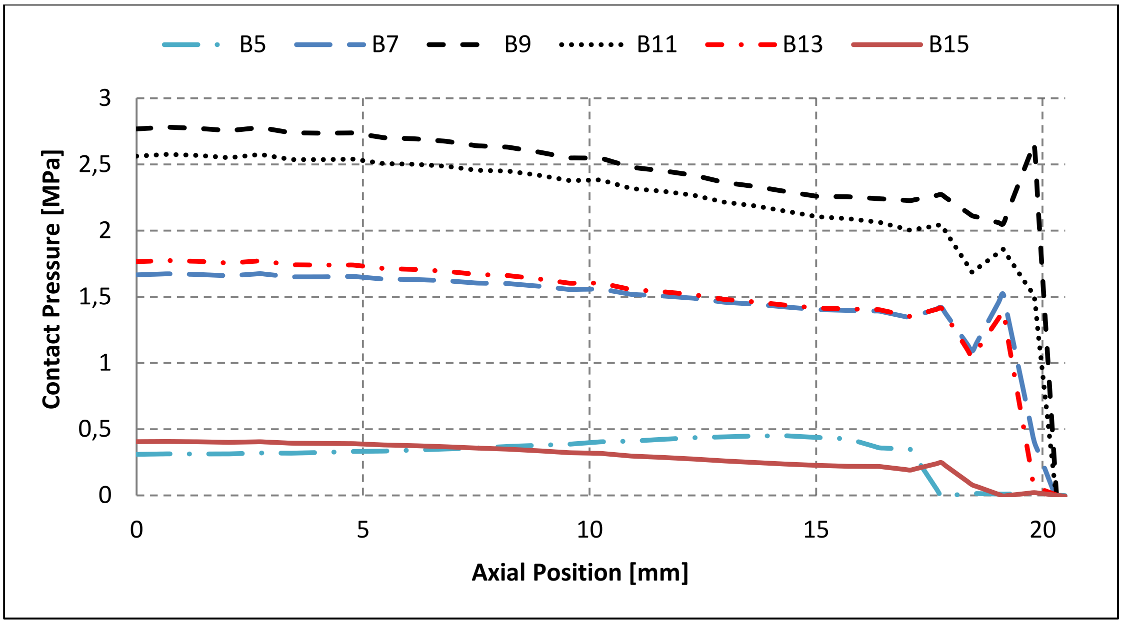

Figure 5.48: Predictions for the contact pressure on some contact surfaces between the topfoil and bumps in axial direction starting from the bearing center towards front edge. Numbering convention of the bumps are already given in previous sections. The shaft speed is 30 krpm and the radial load is 133 N.

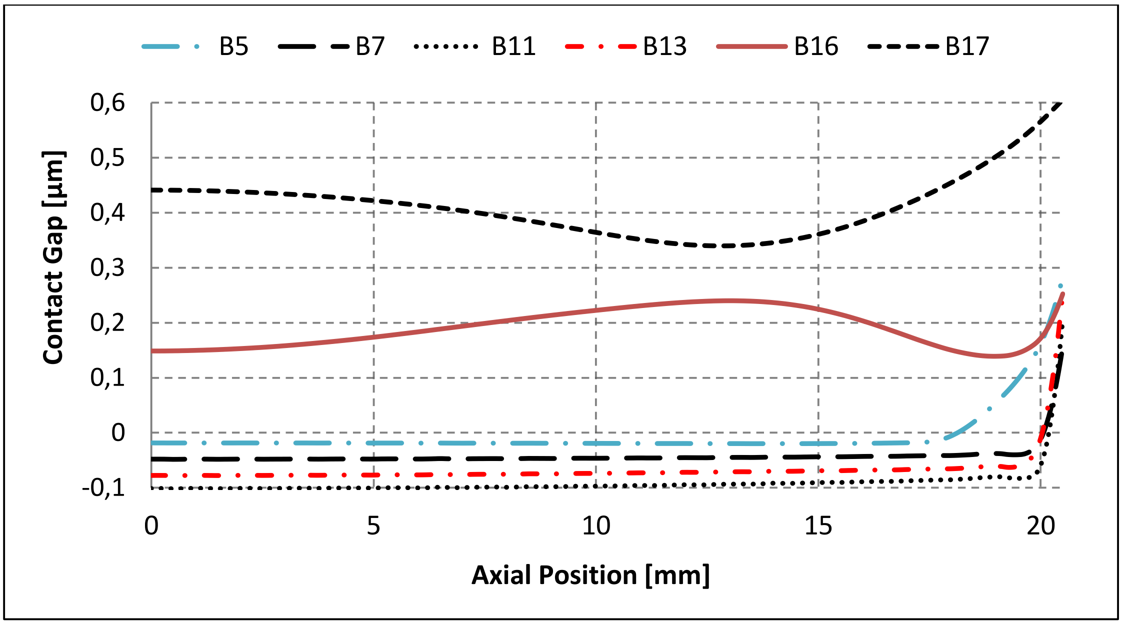

Figure 5.49: Predictions for the contact gaps on some contact surfaces between the topfoil and bumps in axial direction starting from the bearing center towards front edge. Numbering convention of the bumps are already given in previous sections. The shaft speed is 30 krpm and the static radial load is 133 N.

6 CONCLUSION

Compliant surface foil gas bearings are a class of hydrodynamic bearings that use ambient gas as their operating fluid. Therefore, they do not require any additional lubrication circuit. Their hydrodynamic pressure is generated between the moving shaft surface and a flexible bearing surface called as topfoil surface that is typically formed by numerous layers of sheet metal foils. To support radial or axial loads, foil bearings can be configured as journal or thrust bearings as in conventional oil-lubricated technologies. The main behavior of foil-gas bearings is that they float on a self-generated fluid film during normal operation but experience a short-term of dry sliding contact during low speed operation at start-up and shut-down. The bearing geometry and the fluid film thickness are shaped according to the equilibrium between the hydrodynamic film pressure, and the deformation of the foil surface and its underlying spring support structure.

Using compliant foil bearings in turbomachinery brings many advantages compared to the conventional rotor support technologies. The outstanding features of foil bearings involves improved reliability of the bearing mechanism, no requirement for scheduled maintenance, soft failure, elimination of lubrication system, environmental sustainability, high speed operation, capability at cryogenic and elevated temperatures, feasibility of operating with different process fluids and compensation for higher misalignment.

The operational feasibility of the compliant foil bearing has been demonstrated for different temperature, vibration and load conditions in a number of systems including air cycle machines, turbochargers, small scale gas turbines and cryogenic pumps.

The lubricant used in foil bearing applications is usually air that has a superior performance at elevated temperatures in terms of viscosity compared to the oil based lubricants. However, that property may result in thermal instability with increasing temperature. Some limitations also exist for the foil bearings due to the material property changes at some operation circumstances. The foils soften at high temperatures and the stiffness drops rigidly. The most crucial problem faced in experiments at high speeds or overload conditions is the high local temperature gradient that causes deformation of the foil surface and catastrophic failure of the bearing. Another important concern in terms of the thermal management is the weak conduction rate of the bearing due to the thin foil structure. The contact between the top foil and bumps occurs at localized small areas that resists the heat removal from the system. Inappropriate thermal management due to inadequate coatings and insufficient cooling techniques may produce ultimate deterioration of the rotor-bearing system. Even though some experimental research data are available in open literature, extended thermo-hydrodynamic analysis is required to advance and optimize the system performance at the design level. Comprehensive modeling of CFBs that is benchmarked to relevant test data will enable the widespread usage of CFBs into novel turbomachinery applications.

Conventional models include the bumps only as an equivalent stiffness uniformly distributed around the bearing circumference. More complex models couple directly the elastic deformations of the top foil to the bump mechanism as well as to the hydrodynamics of the gas film but by considerably simplifying the structural model. In the structure of an actual bump foil bearing, the role of the top foil is to generate air film force when the shaft rotates. Therefore, it is important that bending stiffness of the top foil is high enough to endure the pressure. However, the top foil surface that does not contact with the bump foil has practically little stiffness because the distributed load does not act partially on the top foil and more deflection occurs on the part which is not in contact with bumps. In many previous studies, this deflection of the top foil was ignored and extraction the damping characteristic due to the top foil deflection was impossible. However, the top foil deformations derived from many former experiments show the top foil deflection phenomenon which is called as sagging is radically affects the overall behavior of the bearing. The model explained in this work couples the structural deformation of the underlying structure with hyrodynamic pressure generated at the film gap by solving the Reynolds Equation and Duhamel-Hooke’s relation for structural deformation that are directly coupled by utilizing a commercial FEA code. The bending effects of the top foil are also investigated, considering energy dissipation due to deflection of top foil and bump foil. Furthermore, it accounts for temperature change in the film due to the viscous dissipation and compressibility of the fluid by solving the bulk flow energy equation in a custom written FDM that is iteratively coupled to the FEA code. The physical contacts between bearing assembly components are modeled by utilizing Augmented-Lagrangian contact model. The thermal contact is also included in the model with an advanced approach called CMY correlation. The model involves complete bearing mechanism as well as the interacting section of the shaft with the bearing. The thermal growth of the shaft, foil structure, bearing sleeve, and centrifugal growth of the shaft are also considered. From this aspect, this model is the most complete and advanced model in the open-literature for a bump-type compliant foil journal bearing. It aims to obtain a deep insight into the structural and thermal characteristics of a CFB during steady-state operation. The proposed model is first validated via the results available in the literature and then used to conduct a parametric study to investigate the the speed of the shaft surface and radial loading on structural and thermal properties of the bearing.

A bump-type foil journal bearing is used in the presented TEHD analysis. The topfoil consists of a single sheet welded to the sleeve from the so-called trailing edge and the other edge, which is called as leading edge, remains free. The shaft is not modeled fully in axial direction to avoid increase of the number of DOF in finite element model drastically. The modeled portion of the free part of the shaft is elongated one-bearing length in both directions.

All governing equations are utilized step-by-step to build a suitable format to be used in the developed algorithm. The three basic governing laws the conservation of mass, momentum, and energy are implemented in detail to deduce into useful forms for parameters including flow velocity, pressure, temperature, load etc. In addition to conservation laws, theories for structural deformation, contact algorithm and thermal contact behavior are also explained in separate sections. Finally, a new 4-point finite difference approximation is proposed to improve the accuracy of the solver algorithm. The applied non-dimensionalization techniques to normalize the Reynolds’ and energy equations are also given in related sections. Total Lagrangian formulation is used for structural analysis in COMSOL Multiphysics for both small and finite deformations. The contact problems are solved using an *augmented Lagrangian* method. This means that the code solves the system in a segregated way. In this study, the correlation developed by CMY is utilized to predict thermal conductance coefficients between contacting elements.

The model couples the structural deformation of the underlying structure with hyrodynamic pressure generated at the film gap by solving the Reynolds Equation and structural deformation that are directly coupled by utilizing a commercial FEA code.

The model involves complete bearing mechanism as well as the interacting section of the shaft with the bearing. The thermal growth of the shaft, foil structure, bearing sleeve, and centrifugal growth of the shaft are also considered.

The TEHD model developed in this study is benchmarked to the experimental work of Radil and Zeszotek [59] that presented measurements of temperature in a CFB for a number of speed and load conditions. The axial length of the tested CFB is 41 mm and the diameter is 50 mm. The model predictions match well with provided experimental data.

The predictions for hydrodynamic pressure, film thickness, flow velocity in the film gap, temperature distribution, thermal contact conductance, deformation of the geometry, stress distribution and mechanical contact properties are presented for various shaft speeds and radial loading conditions. The results are interesting in terms of providing a detailed insight to possible problems encountered in foil bearings during operation. Moreover, useful recommendations for bearing designers are provided by commenting on the outputs. This model can be further improved, as always, by including frictional effects at contacts and shaft transients. It can be also extended to cover new foil bearing generations.

In consequence, the contributions of the presented model to the literature can be summarized as follows:

- A fully coupled thermo-elasto-hydrodynamics (TEHD) model is developed that couples the flow effects in the film gap to the structural properties of the components including heat generation in the film and transfer of this energy to the foils as well as to the shaft.
- To solve 2D energy equation for the film flow, a finite difference code utilizing a robust direct solver is developed.
- To integrate the energy equation to the FEA solver code, a coupling code is developed.

- An advanced FEA model is developed to solve for Reynolds equation coupled with structural deformation of the geometry. This code also solves for the heat transfer on bearing components and hollow shaft.
- The derivation of the governing equations including conservation of mass, momentum and energy equations, elastic theory for structural deformation and stress, augmented Lagrangian formulation for mechanical contact properties, Cooper-Mikic-Yovanovich (CMY) correlation for thermal contact problem are presented in Section 3.
- Nickel-based superalloys are used as bearing material and temperature dependent thermo-mechanical properties are defined to the solver.
- A finite difference iterative solver for Reynolds Equation is provided as an option to the code in FEA solver.
- The results obtained from the proposed TEHD model are in good agreement with the experimental data.
- TEHD model predicts the real physics of foil bearings very well and could be utilized to design more advanced bearings.
- The model has a modular structure and could be improved to analyze magnetic, hydrostatic and leaf-type foil bearings with minor revisions.
- The frictional effects can be included in the model with a cost of computational expense.
- Transient behavior of the shaft can be simulated with this model by defining the motion profile to the FEA solver.
- The analysis can be repeated at high temperatures and/or shaft speeds considering the thermal properties of the materials.
- The model capabilities can be extended to cover cooling flow streams by coupling it with an additional CFD model.

7 REFERENCES

[1] Boyce MP. Gas turbine engineering handbook. 2002.

[2] Dowson D. History of tribology. 1998:443-507.

[3] Heshmat H, Walton II JF, Tomaszewski MJ. Demonstration of a turbojet using an air foil bearing. In: Proceedings of 2005 ASME turbo expo: power for land, sea & air, Reno, Nevada, 2005.

[4] Trivedi HK, Klenke CJ, Saba CS. Effect of formulation and temperature on boundary lubrication performance of polyphenylethers (5P4E). Tribology Letters. 2004;17(1):1-10.

[5] Agrawal GL. Foil air/gas bearing technology - An overview. In: International gas turbine & aeroengine congress & exhibition, Orlando, 1997;ASME Paper No. 97-GT-347.

[6] Swanson EE. Foil bearings versus other bearings. http://www.xdotea.com/services.foil_bearings.html. In: 03/03/2014.

[7] Dellacorte C, Bruckner RJ. Remaining technical challenges and future plans for oil-free turbomachinery. Journal of Engineering for Gas Turbines and Power. 2011;133:ASME Paper No 42502.

[8] Dellacorte C, Radil KC, Bruckner RJ, Howard SA. A preliminary foil gas bearing performance map. NASA/TM-2006-214343, 2006.

[9] Ku CR, Hesmat H. Structural stiffness and Coulomb damping in compliant foil journal bearings: Parametric studies. Tribology Transactions. 1994;37(3):455-62.

[10] Gross WA. A review of developments in externally pressurized gas bearing technology since 1959. Journal of LubricationTechnology. 1969;163.

[11] Dellacorte C. Oil-Free shaft support system rotordynamics: Past, present and future challenges and opportunities. Mechanical Systems and Signal Processing. 2012;29:67-76.

[12] Dellacorte C, Valco MJ. Oil-free turbomachinery technology for regional jet, rotorcraft and supersonic business jet propulsion engines. In: Proceedings of the 2003 ISABE conference, Cleveland, Ohio, 2003.

[13] Hesmat H, Salehi M, Walton JF, Tomaszewski MJ. Operation of a mesoscopic gas turbine simulator at speeds in excess of 700,000 rpm on foil bearings. Journal of Engineering for Gas Turbines and Power. 2007;129(1):170-79.

[14] Swanson EE, Heshmat H. Capabilities of large foil bearings. ASME paper no.2000-GT-0387. In: Proceedings of ASME turbo expo 2000, Munich, Germany, 2000.

[15] Hesmat H, Hermel P. Compliant foil bearing technology and their application to high speed turbomachinery. In: Proceedings of 19th Leeds-Lyon symposium on thin film in tribology - from micro meters to nano meters, Leeds, UK, 1993;559-75.

[16] Swanson EE, Hesmat H, Shin JS. The role of high performance foil bearings in an advanced, oil-free, integral permanent magnet motor Driven, high-speed turbo-compressor operating above the first bending critical speed. ASME paper no. GT-2002-30579. In: Proceedings of ASME turbo expo 2002, Amsterdam, The Netherlands, 2002.

[17] Walton JF, Hesmat H. Application of foil bearings to turbomachinery including vertical operation. Journal of Engineering for Gas Turbines and Power. 2002;124(4):1032-41.

[18] Hesmat H, Walton JF, Dellacorte C, Valco MJ. Oil-free turbocharger demonstration paves way to gas turbine applications. ASME paper no. 2000-GT-0620. In: Proceedings of ASME turbo expo 2000, Munich, Germany, 2000.

[19] Hesmat H. Analysis of compliant foil bearings with spatially variable stiffness. AIAA-91-2102. In: Proceedings of AIAA/SAE/ASME/ASEE 27th joint propulsion conference, Sacramento, CA, 1991.

[20] Hesmat H. A feasibility study on the use of foil bearings in cryogenic turbopumps. AIAA-91-2103. In: Proceedings of AIAA/SAE/ASME/ASEE 27th joint propulsion conference, Sacramento, CA, 1991.

[21] Walton II JF, Heshmat H, Tomaszewski MJ. Testing of a small turbocharger/turbojet sized simulator rotor supported on foil bearings. Journal of Engineering for Gas Turbines and Power. 2008;130:ASME Paper No 35001.

[22] Heshmat CA, Heshmat H. An analysis of gas-lubricated, multileaf foil journal bearings with backing springs. Journal of Tribology. 1995;117:437-43.

[23] Braun MJ, Choy FK, Dzodzo M, Hsu J. Two-dimensional dynamic simulation of a continuous foil bearing. Tribology International. 1996;29(1):61-8.

[24] Heshmat H. Advancements in the performance of aerodynamic foil journal bearings: high speed and load capacity. Journal of Tribology. 1994;116:287-95.

[25] Hesmat H, Walowit JA, Pinkus O. Analysis of gas-lubricated foil journal bearings. Journal of Lubrication Technology. 1983;105:647-55.

[26] San Andrés L. Turbulent flow foil bearings for cryogenic applications. Journal of Tribology. 1995;117:185-95.

[27] Dykas B, Howard SA. Journal design considerations for turbomachine shafts supported on foil air bearings. Tribology Transactions. 2004;47(4):508-16.

[28] Gross WA. Film lubrication-V. Infinitely long incompressible lubricating films of various shapes. In: 1958;Report No. RJ 117-5 69-70.

[29] Licht L, Branger M. Design, fabrication, and performance of foil journal bearings for the brayton rotating unit. In: Washington, D.C., 1973;NASA CR-2243.

[30] Klaas RF, Dellacorte C. The quest for oil-free gas turbine engines. SAE Paper No. 2006-01-3055. In: Proceedings of the power systems conference, New Orleans, LA, 2006.

[31] Lubel D, Dellacorte C, Stanford MK. Test evolution and oil-free engine experience of a high temperature foil air bearing coating. ASME Paper No. GT2006-90572. In: Proceedings of 2006 ASME turbo expo: power for land, sea, and air, Barcelona, Spain, 2006;1245-49.

[32] Walton II JF, Heshmat H. Compliant foil bearings for use in cryogenic turbopumps. NASA CP 3282, 1994.

[33] Radil KC, Dellacorte C. Foil bearing starting considerations and requirements for rotorcraft engine applications. Army research report no. ARL-TR-4873, 2009.

[34] Lee YB, Lee SH, Kim SJ. Vibration control and low power consumption of the combined smart bearings. Paper No. F-223. In: Proceedings of the Fourth World Tribology Congress, Kyoto, Japan, 2009.

[35] Dellacorte C, Radil KC, Bruckner RJ, Howard SA. Design, fabrication and performance of open source generation I and II compliant hydrodynamic gas foil bearings. NASA TM - 2007-214691, 2007.

[36] Iordanoff I. Analysis of an aerodynamic compliant foil thrust bearing: method for a rapid design. Journal of Tribology. 1999;121:816-22.

[37] Rubio D, San Andrés L. Bump-type foil bearing structural stiffness: experiments and predictions. J Eng Gas Turb Power. 2006;128(3):653-60.

[38] Walowit JA, Anno JN. Modern development in lubrication mechanics. London: Applied Science Publishers; 1975.

[39] Heshmat H, Walowit JA, Pinkus O. Analysis of gas-lubricated compliant thrust bearings. J Lubr Technol. 1983;105(4):638-46.

[40] Peng JP, Carpino M. Calculation of stiffness and damping coefficients for elastically supported gas foil bearings. Journal of Tribology. 1993;115(1):20-7.

[41] Peng JP, Carpino M. Coulomb friction damping effects in elastically supported gas foil bearings. Tribology Transactions. 1994;37(1):91-8.

[42] Peng JP, Carpino M. Finite element approach to the prediction of foil bearing rotor dynamic coefficients. Journal of Tribology. 1997;119:85-90.

[43] Carpino M, Medvetz LA, Peng JP. Effects of membrane stresses in the prediction of foil bearing performance. Tribology Transactions. 1994;37(1):43-50.

[44] Carpino M, Peng JP, Medvetz LA. Misalignment in a complete shell gas foil journal bearing. Tribology Transactions. 1994;37(4):829-35.

[45] Carpino M, Talmage G. A fully coupled finite element formulation for elastically supported foil journal bearings. Tribology Transactions. 2003;46:560-5.

[46] Carpino M, Talmage G. Prediction of rotor dynamic coefficients in gas lubricated foil journal bearings with corrugated sub-foils. Tribology Transactions. 2006;49(3):400-9.

[47] Heshmat CA, Xu DS, Heshmat H. Analysis of gas lubricated foil thrust bearings using coupled finite element and finite difference methods. Journal of Tribology. 2000;122(1):199-204.

[48] Lee YB, Park DJ, Kim CH. Numerical analysis for bump foil journal bearing considering top foil effect and experimental investigation. Paper-ID 229. In: Proceedings of 7th IFToMM conference on rotor dynamics, Vienna, Austria, 2006.

[49] Le Lez S, Arghir M, Frene J. Static and dynamic characterization of a bump-type foil bearing structure. Journal of Tribology. 2007;129:75-83.

[50] Le Lez S, Arghir M, Frene J. A new bump-type foil bearing structure analytical model. J Eng Gas Turb Power. 2007;129(4):1044-57.

[51] Dellacorte C, Valco MJ. Load estimation of foil air journal bearings for oil-free turbomachinery applications. Tribology Transactions. 2000;43:795-801.

[52] Radil KC, Howard SA, Dykas B. The role of radial clearance on the performance of foil air bearings. Tribology Transactions. 2002;45:485-90.

[53] Radil KC, Dellacorte C, Zeszotek M. Thermal management techniques for oil-free turbomachinery systems. Tribology Transactions. 2007;50(3):319-27.

[54] Peng ZC, Khonsari MM. On the limiting load-carrying capacity of foil bearings. Journal of Tribology. 2004;126:817-18.

[55] Kim TH, San Andrés L. Limits for high speed operation of gas foil bearings. Journal of Tribology. 2006;128(3):670-3.

[56] San Andrés L, Kim TH. Analysis of gas foil bearings integrating FE top foil models. Tribology International. 2009;42:111-20.

[57] Salehi M, Swanson EE, Heshmat H. Thermal features of compliant foil bearings-theory and experiments. Journal of Tribology. 2001;123.

[58] Peng ZC, Khonsari MM. A thermohydrodynamic analysis of foil journal bearings. Journal of Tribology. 2006;128:534-41.

[59] Radil KC, Zeszotek M. An experimental investigation into the temperature profile of a compliant foil air bearing. Tribology Transactions. 2004;47(4):470-9.

[60] Paulsen BT, Morosi S, Santos IF. Static, Dynamic, and Thermal Properties of Compressible Fluid Film Journal Bearings. Tribology Transactions. 2011;54:282-99.

[61] Feng K, Kaneko S. Thermohydrodynamic study of multiwound foil bearing using lobatto point quadrature. Journal of Tribology. 2009;131(2):021702-021702-9.

[62] Feng K, Kaneko S. A thermohydrodynamic sparse mesh model of bump-type foil bearings. J Eng Gas Turb Power. 2013;135:022501.

[63] San Andrés L, Kim TH. Thermohydrodynamic analysis of bump type gas foil bearings: a model anchored to test data. J Eng Gas Turb Power. 2010;132(4):042504.

[64] Kim D, Kim Y, Lee D, Ahn K. Comparison of thermo-hydrodynamic characteristics of airfoil bearings with different top foil geometries. In: Proceedings of the 8th IFToMM international conference on rotordynamics, Seoul, Korea, 2010.

[65] Kim TH, San Andrés L. Effect of side feed pressurization on the dynamic performance of gas foil bearings: a model anchored to test data. J Eng Gas Turb Power. 2009;131(1):012501.

[66] Sim K, Kim D. Thermohydrodynamic analysis of compliant flexure pivot tilting pad gas bearings. J Eng Gas Turb Power. 2008;130(3):032502.

[67] Lee D, Kim D. Thermo-Hydrodynamic analyses of bump air foil bearings with detailed thermal model of foil structures and rotor. Journal of Tribology. 2010;132(2):021704.

[68] Talmage G, Carpino M. Thermal structural effects in a gas-lubricated foil journal bearing. Tribology Transactions. 2011;54:701-13.

[69] Sim K, Kim TH. Thermohydrodynamic analysis of bump-type gas foil bearings using bump thermal contact and inlet flow mixing models. Tribology International. 2012;48:137-48.

[70] Kim TH, Song JW, Lee YB, Sim K. Thermal performance measurement of a bump type gas foil bearing floating on a hollow shaft for increasing rotating speed and static load. J Eng Gas Turb Power. 2011;134(2):024501.

[71] Kim D, Ki J, Kim Y, Ahn K. Extended three-dimensional thermo-hydrodynamic model of radial foil bearing: case studies on thermal behaviors and dynamic characteristics in gas turbine simulator. J Eng Gas Turb Power. 2012;134:052501.

[72] Kim TH, San Andrés L. Thermohydrodynamic model predictions and performance measurements of bump-type foil bearing for oil-free turboshaft engines in rotorcraft propulsion systems. Journal of Tribology. 2010;132:011701.

[73] Lee D, Kim D. Three-Dimensional thermo-hydrodynamic analyses of rayleigh step air foil thrust bearing with radially arranged bump foils. Tribology Transactions. 2011;54(3):432-48.

[74] Kim D, Lee D, Kim YC, Ahn K. Comparison of thermo-hydrodynamic characteristics of airfoil bearings with different top foil geometries. Paper No. WeD1-4. In: Proceedings of the 8th IFToMM international conference on rotordynamics, Seoul, Korea, 2010.

[75] Lee D, Kim D, Sadashiva RP. Transient thermal behavior of preloaded three-pad foil bearings: Modeling and experiments. Journal of Tribology. 2011;133(2):021703.

[76] Paouris LI, Bompos DA, Nikolakopoulos PG. Simulation of static performance of air foil bearings using coupled finite element and computational fluid dynamics techniques. J Eng Gas Turb Power. 2014;136:22503.

[77] Grassam NS. Proceedings of the third gas bearing symposium-contributions and discussions. In: Proceedings of the third gas bearing symposium, University of Southampton, 1967.

[78] Barnett MA, Silver A. Application of air bearings to high speed turbomachinery. SAE Paper. 1970:700720.

[79] Ruscitto D, McCormick J, Gray S. Hydrodynamic air lubricated compliant surface bearing for an automotive gas turbine engine, I-journal bearing performance. NASA CR-135368, 1978.

[80] Dellacorte C. Technical development path for foil gas bearings. No:71204. In: International joint tribology conference, Miami, FL, 2008.

[81] Gray S, Bhushan B. Support element for compliant hydrodynamic journal bearings. US patent number 4,274,683; 1981.

[82] Heshmat H. High load capacity compliant foil hydrodynamic journal bearing. US patent number 5,902,049; 1999.

[83] Special Metals Corporation. INCONEL® alloy X-750. Publication No. SMC-067; 2004.

[84] Special Metals Corporation. INCONEL® alloy 718. Publication No. SMC-045; 2007.

[85] Warsi ZUA. Fluid dynamics theoretical and computational approaches. 2nd ed. New York: CRC press; 1999.

[86] Using Continuum Elements. Getting started with Abaqus 610. Interactive ed. RI, USA: Dassault Systemes; 2010. p. 4-1.

[87] LeVeque RJ. Finite difference methods for ordinary and partial differential equations: Steady-state and time-dependent problems. 1st ed. Philadelphia, USA: SIAM; 2007. p. 61-2.

[88] Reynolds O. On the Theory of Lubrication and Its Application to Mr. Beauchamp Tower's Experiments, Including an Experimental Determination of the Viscosity of Olive Oil. Philosophical Transactions of the Royal Society of London. 1886;177:157-234.

[89] Khonsari MM, Booser ER. Applied tribology bearing design and lubrication. 2nd ed. West Sussex, England: John Wiley & Sons, Ltd.; 2008. p. 325.

[90] Theory for thin-film flow. CFD module user's guide - Comsol 42a: Comsol Inc.; 2013. p. 538-56.

[91] Gross WA. Fluid film lubrication. New York: Wiley Interscience; 1980.

[92] Incropera FP, Dewitt DP, Bergman TL, Lavine AS. Fundamentals of heat and mass transfer. 6th ed. New Jersey, US: John Wiley & Sons, Inc.; 2007. p. 350.

[93] Holman JP. Heat Transfer. 10th ed. New York: The McGraw-Hill Companies, Inc.; 2010. p. 241.

[94] Theory for the solid mechanics user interface. Structural mechanics module user's guide - Comsol 42a: Comsol Inc.; 2013. p. 137-89.

[95] Norton RL. Machine design an integrated approach. 2nd ed. New Jersey: Prentice-Hall Inc.; 2000. p. 258-60.

[96] Contact Technology Guide. ANSYS 14 documentation - Mechanical APDL: ANSYS Inc.; 2013.

[97] Cescotto S, Zhu YY. Large strain dynamic analysis using solid and contact finite elements based on a mixed formulation - application to metalforming. Journal of Metals Processing Technology. 1994;45:657-63.

[98] Bahrami M, Culham J, Yananovich MM, E SG. Review of thermal joint resistance models for nonconforming rough surfaces. Appl Mech Rev. 2006;59:1-12.

[99] Bhushan B. Introduction to tribology. New York: John Wiley & Sons, Inc.; 2002. p. 18.

[100] Mikic BB, Rohsenow WM. Thermal contact resistance. MIT Mech. Eng. Rep. DSR 74542-41, 1966.

[101] Cooper MG, Mikic BB, Yovanovich MM. Thermal contact conductance. International Journal of Heat Mass Transfer. 1969;12:279-300.

[102] Hegazy AA. Thermal joint conductance of conforming rough surfaces: effect of surface microhardness variation. Ontario, Canada: University of Waterloo; 1985.

[103] Lambert MA, Fletcher LS. Thermal contact conductance of spherical rough metals. ASME Journal of Heat Transfer. 1997;119:684-90.

[104] Yovanovich MM, DeVall JW, Hegazy AA. A statistical model to predict thermal gap conductance between conforming rough surfaces. In: AIAA-82-0888, AIAA/ASME 3rd joint thermophysics, St. Louis, MO, 1982.

[105] Song S, Yananovich MM. Relative contact pressure: Dependence on surface roughness and vickers microhardness. Journal of Thermophysics Heat Transfer. 1988;2(1):43-7.

[106] Sridhar MR, Yananovich MM. Empirical methods to predict vickers microhardness. Wear. 1996;193:91-8.

[107] Studies and Solvers - Stationary Solver. Comsol multiphysics reference manual: Comsol Inc.; 2013. p. 1101.

[108] Deuflhard P. Modified Newton Method for the Solution of Ill-conditioned Systems of Nonlinear Equations with Application to Multiple Shooting. Numerical Mathematics. 1974;22:289-315.

[109] What and where are the BLAS? http://www.netlib.org/blas/faq.html#1.2. In: 02/08/2014.

[110] Schenk O. Scalable parallel sparse lu factorization methods on shared memory multiprocessors. Zurich, Switzerland: ETH Zurich; 2000.

[111] Schenk O, Gaertner K. Fully coupled Newton-Raphson method. PARDISO user guide version 412 2011.

[112] Liu JWH. Modification of the minimum-degree algorithm by multiple elimination. Acm Transactions on Mathematical Software. 1985;11(2):141-53.

[113] Karypis G, Kumar V. A fast and highly quality multilevel scheme for partitioning irregular graphs. SIAM Journal on Scientific Computing. 1999;20(1):359-92.

[114] METIS - Serial graph partitioning and fill-reducing matrix ordering. http://glaros.dtc.umn.edu/gkhome/metis/metis/overview. In: 12/12/2013.

[115] Schenk O, Gaertner K, Fichtner W. Efficient sparse LU factorization with left-right looking strategy on shared memory multiprocessors. BIT. 2000;40(1):158-76.

[116] Schenk O, Gaertner K. On fast factorization pivoting methods for symmetric indefinite systems. Elec Trans Numer Anal. 2006;23:158-79.

[117] Yuan YX. Trust region algorithms for nonlinear equations. Information 1.1 p. 7-20, 1998.

[118] Powell MJD. A new algorithm for unconstrained optimization. In: Rosen JB, Mangasarian OL, Ritter K, editors. Nonlinear Programming. New York: Academic Press; 1970. p. 31-66.

[119] Dennis JE, Mei HHW. Two new unconstrained optimization algorithms which use function and gradient values. JOTA. 1979;28:453-82.

[120] Sun W, Yuan Y. Optimization theory and methods: Nonlinear programming. New York: Springer; 2005. p. 316.

[121] Kim TH, San Andrés L. Heavily loaded gas foil bearings: a model anchored to test data. GT2005-68486. In: ASME Turbo Expo 2005, Reno, Nevada, 2005.

[122] Mathematics linear equations - LU matrix factorization. MATLAB getting started 2012a: The Mathworks, Inc.; 2012.

[123] Collins JA, Busby H, Staab G. Mechanical design of machine elements and machines. 2nd ed. New Jersey: John Wiley & Sons, Inc.; 2010. p. 126.

APPENDIX A: Temperature Dependent Material Properties

A.1 Inconel X-750

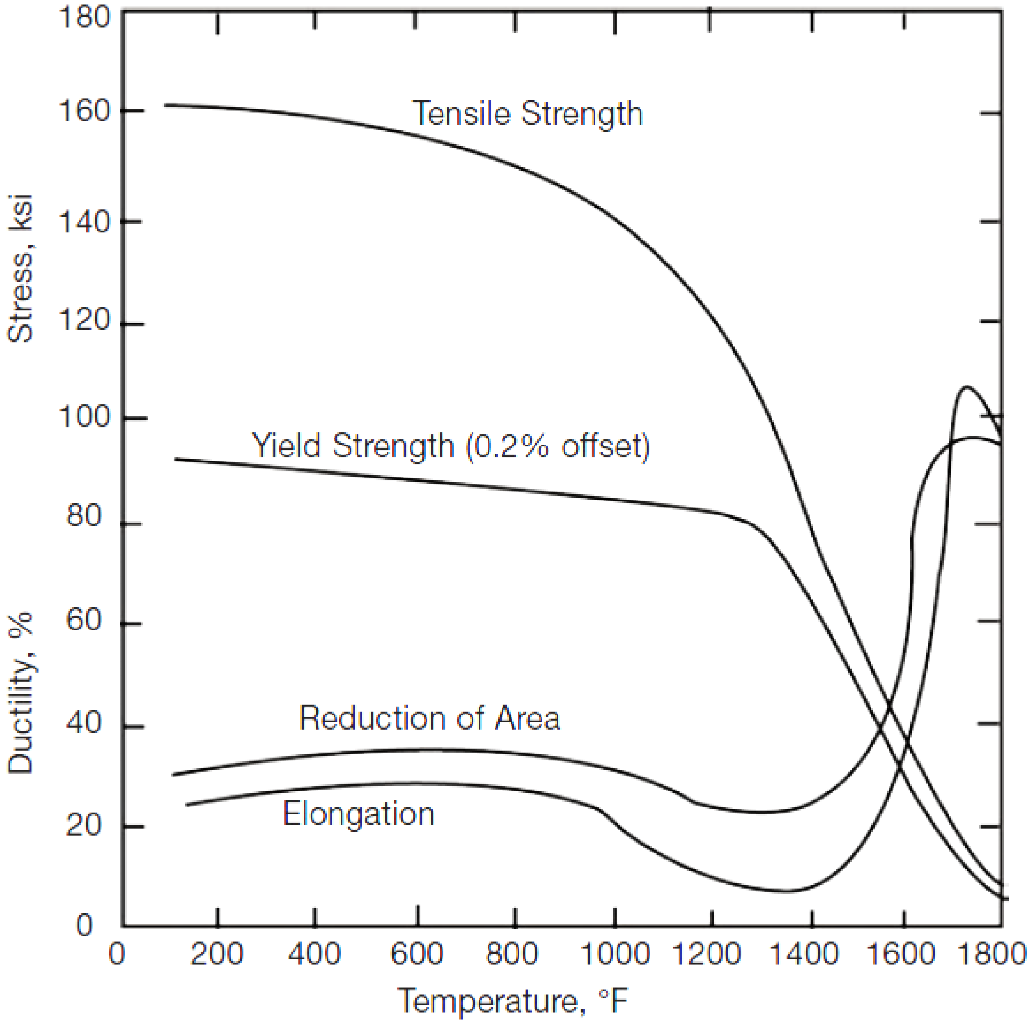

Figure A.1. The effect of temperature on tensile and yield strengths of INCONEL X-750 [83]

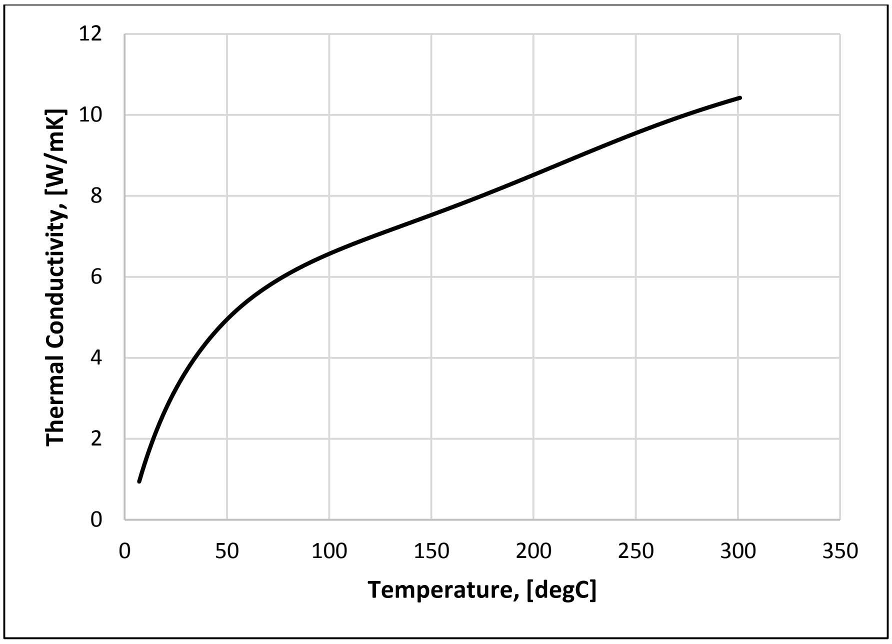

Figure A.2. The effect of temperature on thermal conductivity of INCONEL X-750 [83]

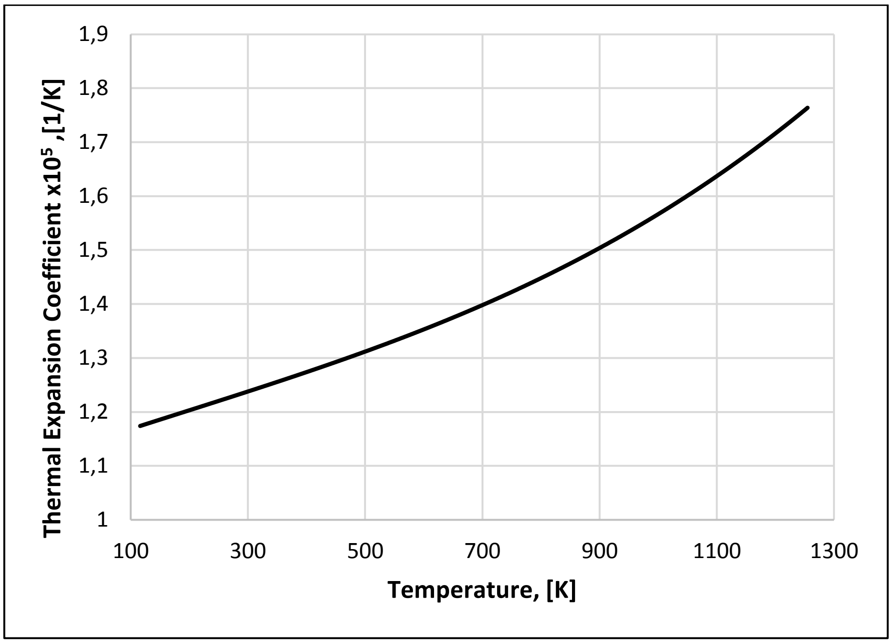

Figure A.3. The effect of temperature on thermal expansion coefficient of INCONEL X-750 [83]

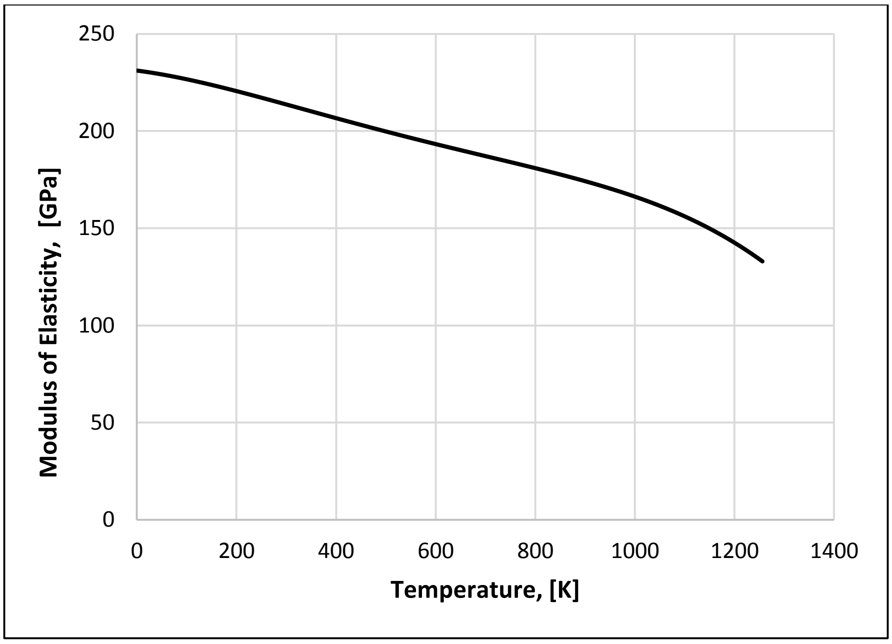

Figure A.4. The effect of temperature on modulus of elasticity of INCONEL X-750 [83]

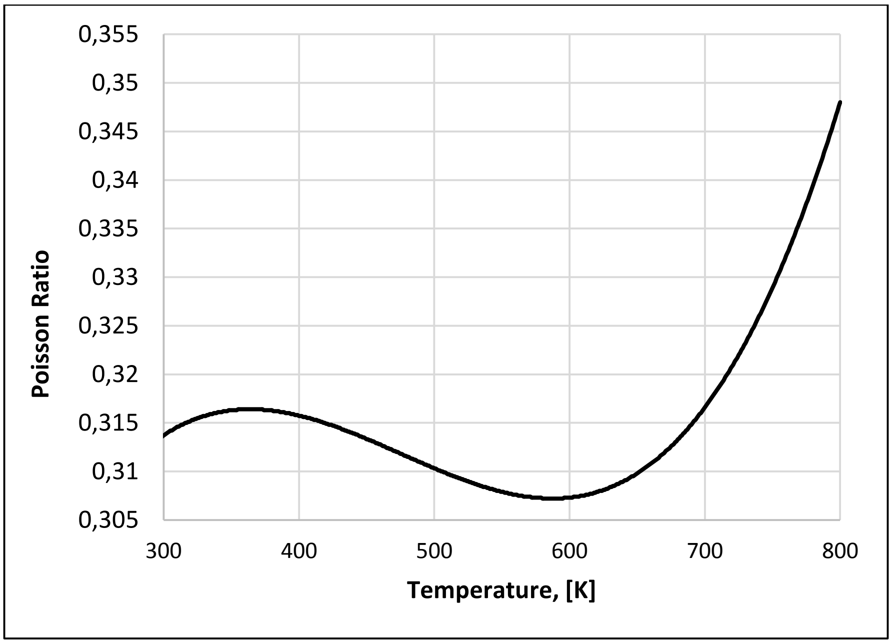

Figure A.5. The effect of temperature on Poisson ratio of INCONEL X-750 [83]

A.2 Inconel 718

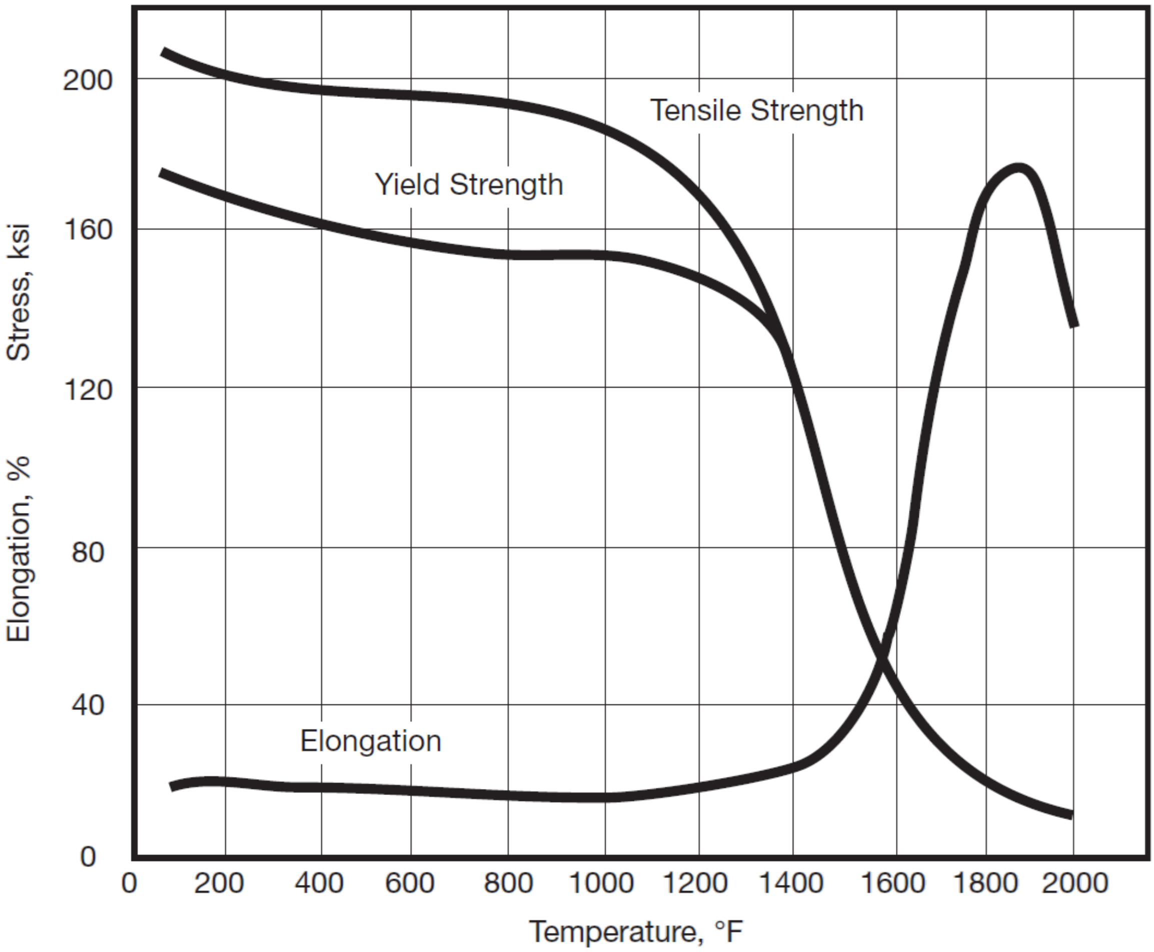

Figure A.6. The effect of temperature on thermal conductivity of INCONEL 718 [84]

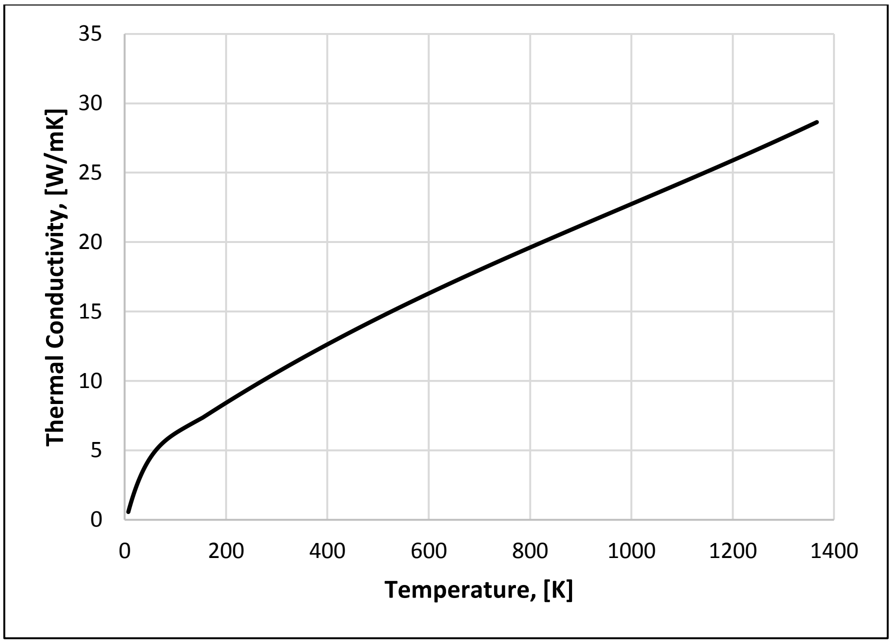

Figure A.7. The effect of temperature on thermal conductivity of INCONEL 718 [84]

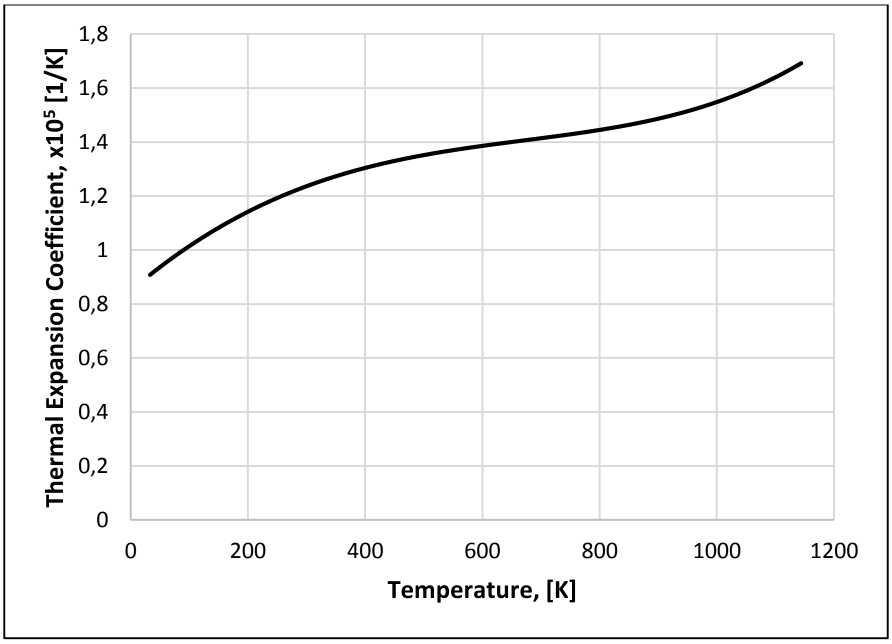

Figure A.8. The effect of temperature on thermal expansion coefficient of INCONEL 718 [84]

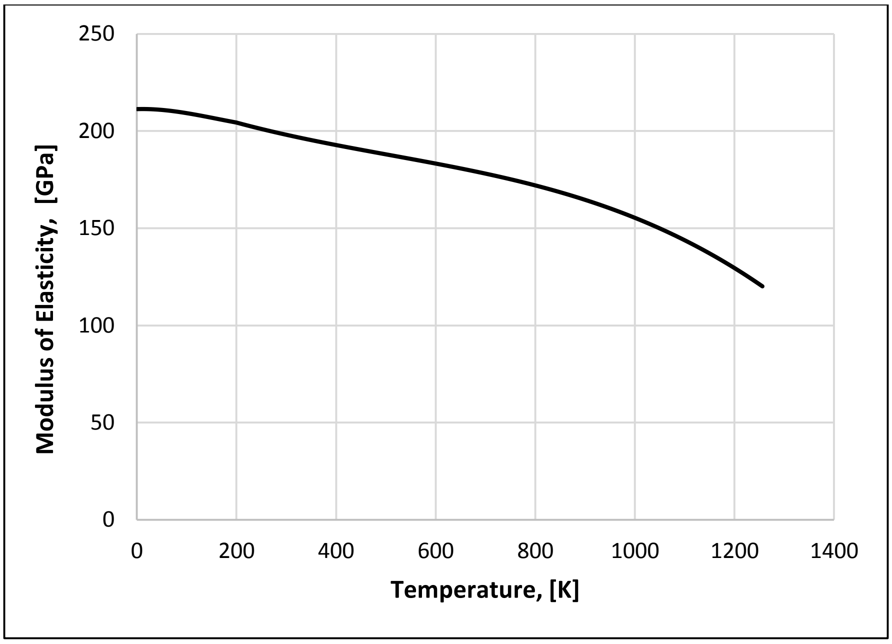

Figure A.9. The effect of temperature on modulus of elasticity of INCONEL 718 [84]

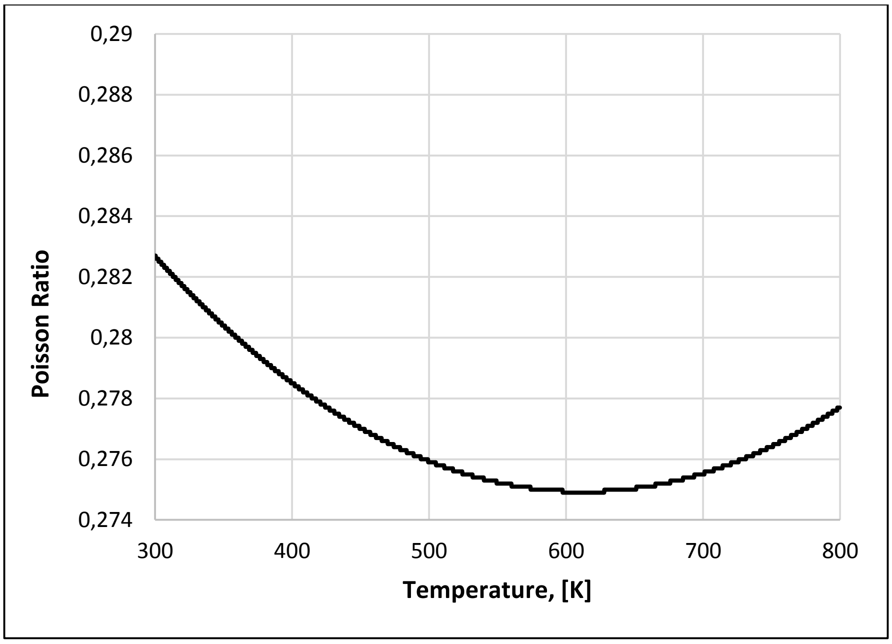

Figure A.10. The effect of temperature on Poisson ratio of INCONEL 718 [84]